

INFORMATION TO USERS

This manuscript has been reproduced from the microfilm master. UMI films the text directly from the original or copy submitted. Thus, some thesis and dissertation copies are in typewriter face, while others may be from any type of computer printer.

The quality of this reproduction is dependent upon the quality of the copy submitted. Broken or indistinct print, colored or poor quality illustrations and photographs, print bleedthrough, substandard margins, and improper alignment can adversely affect reproduction.

In the unlikely event that the author did not send UMI a complete manuscript and there are missing pages, these will be noted. Also, if unauthorized copyright material had to be removed, a note will indicate the deletion.

Oversize materials (e.g., maps, drawings, charts) are reproduced by sectioning the original, beginning at the upper left-hand corner and continuing from left to right in equal sections with small overlaps.

ProQuest Information and Learning
300 North Zeeb Road, Ann Arbor, MI 48106-1346 USA
800-521-0600



ADVANCES IN LOW-THRUST TRAJECTORY OPTIMIZATION AND FLIGHT MECHANICS

A Dissertation
presented to
the Faculty of the Graduate School
University of Missouri-Columbia

In Partial Fulfillment
of the Requirements for the Degree
Doctor of Philosophy

by
YANG GAO

Dr. Craig A. Kluever, Dissertation Supervisor

DECEMBER 2003

UMI Number: 3115547



UMI Microform 3115547

Copyright 2004 by ProQuest Information and Learning Company.
All rights reserved. This microform edition is protected against
unauthorized copying under Title 17, United States Code.

ProQuest Information and Learning Company
300 North Zeeb Road
P.O. Box 1346
Ann Arbor, MI 48106-1346

The undersigned, appointed by the Dean of the Graduate School, have examined the dissertation entitled

**ADVANCES IN LOW-THRUST TRAJECTORY
OPTIMIZATION AND FLIGHT MECHANICS**

presented by Yang Gao

a candidate for the degree of Doctor of Philosophy

and hereby certify that in their opinion it is worthy of acceptance.

Lee A. Klein

Steve D. Boggs

Dai-Teng

Zybelman

Dmitri Tse

ACKNOWLEDGEMENTS

I would like to express my sincere gratitude to my advisor, Prof. Craig Kluever, for his encouragement and support in every stage of my graduate study and research work. His insights and advice were invaluable to the production of this dissertation. His knowledge, kindness, patience, and openmindedness, have provided me with lifetime benefits.

I am grateful to the committee members of my doctoral program, Profs. Satish Nair, Frank Feng, VijaySekhar Chellaboina, Chun-Shin Lin, and Jinglu Tan, for their valuable comments and suggestions on the dissertation proposal.

I would like to thank my family and friends for supporting me through my Ph.D. education. Their encouragement and pride in my accomplishments has driven me to succeed at things I might not otherwise have attempted.

TABLE OF CONTENTS

ACKNOWLEDGEMENTS	ii
TABLE OF CONTENTS.....	iii
LIST OF TABLES	vi
LIST OF FIGURES.....	ix
ABSTRACT	xvii
CHAPTER 1 INTRODUCTION.....	1
1.1 Overview.....	1
1.2 Literature Review.....	4
1.3 Topics and Outline.....	8
CHAPTER 2 SPACECRAFT DYNAMICS.....	11
2.1 Equations of Motion	11
2.2 J2000 Earth Equatorial Coordinates and Heliocentric Ecliptic Coordinates	12
2.3 Equations of Motion Expressed by Different Coordinates	14
2.4 Escape at Sphere Of Influence and Planetary Capture	21
2.5 Gravity Assist.....	24
2.6 Dynamic Models for Perturbations.....	26
2.7 Essential Problem - How to Find the Optimal Control Steering	27
CHAPTER 3 HYBRID METHOD OBTAINED FROM TWO-POINT BOUNDARY-VALUE PROBLEM	29
3.1 Two-Point Boundary-Value Problem	30
3.2 Hybrid Method - Converting the TPBVP into Parameter Optimization.....	37
3.3 Costate Equations for the Hybrid Method	40
3.4 Perturbation Formulation in Costate Equations.....	44
3.5 Extended Multiple-Shooting Techniques for the Hybrid Method	45

3.6 Summary of Hybrid Method	50
CHAPTER 4 DIRECT-SHOOTING METHOD	52
4.1 Direct-Shooting Method	53
4.2 Direct Multiple Shooting Method.....	55
4.3 Collocation Method – Compared with the Direct-Shooting Method.....	59
CHAPTER 5 OPTIMAL ORBIT TRANSFERS USING HYBRID AND DIRECT-SHOOTING METHODS	63
5.1 Optimal Earth-Orbit Transfers.....	65
5.2 Optimal Lower-Thrust Earth-Orbit Transfers.....	69
5.3 Optimal Direct Transfers to Mercury, Venus and Mars	76
5.4 Multiple-Burn LEO-GEO Transfers Using the Hybrid Method.....	81
5.5 Optimal Earth-Mars 2-Burn Transfer with Venus Gravity Assist	88
5.6 Optimal Earth-Jupiter Orbit Transfers	93
5.7 Optimal Earth-Venus Transfer with Modulated Specific Impulse Using the Hybrid Method	98
5.8 Summary of the Hybrid and Direct-Shooting Methods.....	100
CHAPTER 6 OPTIMAL ORBIT TRANSFERS USING MULTIPLE SHOOTING TECHNIQUES	102
6.1 Optimal LEO-GEO Orbit Transfers Using Multiple Shooting.....	102
6.2 Optimal Earth-Mars Orbit Transfers Using Multiple Shooting.....	108
6.3 Optimal Earth-Jupiter Orbit Transfers Using Multiple Shooting	118
6.4 Conclusions.....	123
CHAPTER 7 INTERPLANETARY MISSION DESIGN USING NSTAR & NEXT ENGINES	125
7.1 Optimal Eros Sample Return Trajectories	125
7.2 The Pluto-Flyby Mission Using SEP and Engine-Switching Logic	139
CHAPTER 8 ALTERNATIVE FORMULATIONS FOR EQUATIONS OF MOTION.....	158
8.1 Transfers to Circular Orbits based on Inertial Frame Transformation	158
8.2 Trajectory Optimization Using Modified Equinoctial Elements	172

CHAPTER 9 LOW-THRUST GUIDANCE SCHEME FOR EARTH-CAPTURE TRAJECTORIES	189
9.1 Introductions	189
9.2 System Model	191
9.3 Capture Guidance Scheme.....	193
9.4 Numerical Results.....	203
9.5 Conclusions.....	213
CHAPTER 10 SUMMARY AND CONCLUSIONS	214
APPENDIX I: DERIVATIVES OF M, D WITH RESPECT TO WALKER'S EQUINOCTIAL ELEMENTS	218
APPENDIX II: DERIVATIVES OF M, D WITH RESPECT TO EQUINOCTIAL ELEMENTS USING NON-DIMENSIONAL ANGULAR MOMENTUM.....	222
LIST OF REFERENCES	225
VITA	233

LIST OF TABLES

Tables	Page
Table 5.1 Initial condition and terminal constraints for LEO-GEO orbit transfers	65
Table 5.2 Solutions for optimal single-burn LEO-GEO trajectories (hybrid method, direct-shooting method)	66
Table 5.3 Initial and terminal orbits for the Earth-orbit transfer with initial thrust-to-weight ratio of 10^{-3} (direct-shooting method).....	70
Table 5.4 Initial and terminal orbits for optimal LEO-GEO orbit transfer with initial thrust-to-weight ratio of 10^{-3} (hybrid method).....	72
Table 5.5 Optimal solutions of Earth-Mercury trajectories (hybrid method, direct-shooting method)	77
Table 5.6 Optimal solutions of Earth-Venus trajectories (hybrid method, direct-shooting method)	77
Table 5.7 Optimal solutions of Earth-Mars trajectories (hybrid method, direct-shooting method, collocation method)	77
Table 5.8 Optimal solutions of multiple-burn LEO-GEO trajectories (hybrid method) ..	81
Table 5.9 Optimal solution of Earth-Venus flyby trajectories (hybrid method, direct-shooting method)	88
Table 5.10 Optimal solution of Earth-Mars trajectory with Venus gravity assist	90
Table 5.11 Optimal solutions of Earth-Jupiter trajectories (hybrid method, direct-shooting method)	94
Table 5.12 Optimal solutions for Earth-Venus orbit transfers with modulated I_{sp} (hybrid method)	99
Table 6.1 State nodes for multiple shooting (LEO-GEO orbit transfers)	103
Table 6.2 Optimal solutions for LEO-GEO dual orbit transfers using the hybrid method and multiple-shooting technique with state nodes	103

Table 6.3 Optimal solutions for LEO-GEO dual orbit transfers using the direct-shooting method and multiple-shooting technique with state nodes	105
Table 6.4 State nodes for multiple shooting using the direct-shooting method (Earth-Mars orbit transfers).....	109
Table 6.5 Optimal solutions for Earth-Mars transfers using the direct-shooting method and multiple-shooting with state nodes.....	109
Table 6.6 Costate nodes for Earth-Mars transfer using multiple shooting (Earth-Mars orbit transfers).....	113
Table 6.7 Optimal solutions for Earth-Mars transfers using the direct-shooting method and multiple-shooting with costate nodes.....	113
Table 6.8 State and costate nodes for multiple shooting (Earth–Mars orbit transfer)	115
Table 6.9 Optimal solutions for Earh-mars transfers using the hybrid method and multiple-shooting technique with state and costate nodes.....	115
Table 6.10 State and costate nodes for multiple shooting (Earth-Jupiter orbit transfers)	119
Table 6.11 Optimal solutions for Earth-Jupiter transfers using the hybrid method and multiple-shooting technique with state and costate nodes	119
Table 7.1 I_{sp} and efficiency η of NSTAR engine.....	128
Table 7.2 Optimization results for optimal Eros sample return trajectories (parallel-burn, sequential-burn)	135
Table 7.3 Orbital Elements of Pluto	139
Table 7.4 I_{sp} and efficiency η of NEXT engine	145
Table 7.5 Optimal Pluto-flyby trajectories with maximized final mass using NSTAR engine.....	147
Table 7.6 Optimal Pluto-flyby trajectories with maximized final mass using NEXT engine.....	149
Table 7.7 Optimal Pluto-flyby trajectories with minimized transfer time using NSTAR engine.....	152
Table 7.8 Optimal Pluto-flyby trajectories with minimized transfer time using NEXT engine.....	154

Table 8.1 Terminal a , e , i , Ω and ω due to J_2 effect simulated in the J2000 frame.....	166
Table 8.2 Terminal a , e , i , Ω and ω due to J_2 effect simulated in the frame after transformation.....	166
Table 8.3 Initial orbital elements in different inertial frames	167
Table 8.4 Optimal solutions of LEO-GPS orbit transfers without J_2 perturbation	168
Table 8.5 Optimal solutions of LEO-GPS orbit transfers with J_2 perturbation	169
Table 8.6 Optimal solutions of LEO-GEO orbit transfers using modified set of equinoctial elements.....	185
Table 9.1 Initial spacecraft state for capture trajectory.....	204
Table 9.2 Initial capture trials with various guidance update frequencies.....	205
Table 9.3 Second guidance phase trials with various energy (radius) thresholds	209
Table 10.1 Mission types and suggested methods	216

LIST OF FIGURES

Figures	Page
Figure 2.1 J2000 Earth equatorial coordinate and heliocentric ecliptic coordinates	13
Figure 2.2 Cartesian coordinates.....	14
Figure 2.3 Spherical coordinates.....	16
Figure 2.4 Classical orbital elements	18
Figure 2.5 The hyperbolic Earth-escape orbit.....	22
Figure 3.1 Illustration of multiple shooting with state nodes	47
Figure 4.1 Illustration of the direct-shooting method	53
Figure 4.2 Illustration of direct multiple shooting	57
Figure 4.3 Illustration of Simpson's rule	60
Figure 5.1 Optimal single-burn LEO-GEO trajectories (hybrid method, direct-shooting method)	66
Figure 5.2 Time histories of control steering for optimal single-burn LEO-GEO trajectories (hybrid method, direct-shooting method)	67
Figure 5.3 Time histories of semi-major axis for optimal single-burn LEO-GEO trajectories (hybrid method, direct-shooting method)	67
Figure 5.4 Time histories of eccentricity for optimal single-burn LEO-GEO trajectories (hybrid method, direct-shooting method)	68
Figure 5.5 Time histories of inclination for optimal single-burn LEO-GEO trajectories (hybrid method, direct-shooting method)	68
Figure 5.6 Optimal Earth-orbit trajectory with initial thrust-to-weight ratio of 10^{-3} (direct-shooting method)	70

Figure 5.7 Time history of pitch angle for optimal Earth-orbit trajectory with initial thrust-to-weight ratio of 10^{-3} (direct-shooting method).....	71
Figure 5.8 Optimal LEO-GEO trajectory with initial thrust-to-weight ratio of 10^{-3} (hybrid method)	73
Figure 5.9 Time histories of control steering for optimal LEO-GEO trajectory with initial thrust-to-weight ratio of 10^{-3} (hybrid method).....	73
Figure 5.10 Time history of semi-major axis for optimal LEO-GEO trajectory with initial thrust-to-weight ratio of 10^{-3} (hybrid method).....	74
Figure 5.11 Time history of eccentricity for optimal LEO-GEO trajectory with initial thrust-to-weight ratio of 10^{-3} (hybrid method).....	74
Figure 5.12 Time history of inclination for optimal LEO-GEO trajectory with initial thrust-to-weight ratio of 10^{-3} (hybrid method).....	75
Figure 5.13 Optimal Earth-Mercury direct transfer trajectories (hybrid method, direct-shooting method)	78
Figure 5.14 Time histories of control steering for optimal Earth-Mercury direct transfer trajectories (hybrid method, direct-shooting method)	79
Figure 5.15 Optimal Earth-Venus and Earth-Mars direct transfer trajectories (hybrid method, direct-shooting method)	79
Figure 5.16 Time histories of control steering for optimal Earth-Venus direct transfer trajectories (hybrid method, direct-shooting method)	80
Figure 5.17 Time histories of control steering for optimal Earth-Mars direct transfer trajectories (hybrid method, direct-shooting method, collocation method).....	80
Figure 5.18 Time histories of semi-major axis for optimal 2, 3, 4, 5-burn LEO-GEO trajectories (hybrid method).....	82
Figure 5.19 Time histories of eccentricity for optimal 2, 3, 4, 5-burn LEO-GEO trajectories (hybrid method).....	83
Figure 5.20 Time histories of inclination for optimal 2, 3, 4, 5-burn LEO-GEO trajectories (hybrid method).....	83
Figure 5.21 Optimal 2-burn LEO-GEO trajectories (hybrid method)	84

Figure 5.22 Time histories of control steering for optimal 2-burn LEO-GEO trajectories (hybrid method)	84
Figure 5.23 Optimal 3-burn LEO-GEO trajectories (hybrid method)	85
Figure 5.24 Time histories of control steering for optimal 3-burn LEO-GEO trajectories (hybrid method)	85
Figure 5.25 Optimal 4-burn LEO-GEO trajectories (hybrid method)	86
Figure 5.26 Time histories of control steering for optimal 4-burn LEO-GEO trajectories (hybrid method)	86
Figure 5.27 Optimal 5-burn LEO-GEO trajectories (hybrid method)	87
Figure 5.28 Time histories of control steering for optimal 5-burn LEO-GEO trajectories (hybrid method)	87
Figure 5.29 Optimal Earth-Venus flyby trajectories (hybrid method, direct-shooting method)	89
Figure 5.30 Earth-Mars 675-day optimal trajectories (hybrid method #1, direct-shooting method)	91
Figure 5.31 Time histories of control steering for optimal Earth-Mars 675-day trajectories (hybrid method #1, direct-shooting method)	91
Figure 5.32 Alternative Earth-Mars 675-day optimal trajectory using hybrid method (hybrid method #2)	92
Figure 5.33 Time histories of control steering for alternative optimal Earth-Mars 675-day trajectory (hybrid method #2)	92
Figure 5.34 Optimal Earth-Jupiter 1-burn trajectories (hybrid method, direct-shooting method)	95
Figure 5.35 Time histories of control steering for optimal Earth-Jupiter 1-burn trajectories (hybrid method, direct-shooting method)	96
Figure 5.36 Optimal Earth-Jupiter 2-burn 600-day trajectories (hybrid method, direct-shooting method)	96
Figure 5.37 Time histories of control steering for optimal Earth-Jupiter 2-burn 600-day trajectories (hybrid method, direct-shooting method)	97

Figure 5.38 Time histories of eccentricities for optimal 1-burn and 2-burn 600-day Earth-Jupiter trajectories (hybrid method, direct-shooting method).....	97
Figure 5.39 Time histories of I_{sp} for optimal Earth-Venus transfers with different transfer times (hybrid method).....	99
Figure 5.40 Transfer time vs. final mass for optimal Earth-Venus transfers using modulated I_{sp} (hybrid method)	100
Figure 6.1 Optimal LEO-GEO optimal trajectories (hybrid method, multiple-shooting technique with state nodes).....	104
Figure 6.2 Time histories of control steering for optimal LEO-GEO trajectories (hybrid method, multiple- shooting technique with state nodes)	104
Figure 6.3 Time histories of control steering for optimal LEO-GEO trajectories (direct-shooting method, multiple-shooting technique with state nodes).....	106
Figure 6.4 LEO-GEO orbit transfers at the first iteration (direct-shooting method, multiple-shooting technique with state nodes)	106
Figure 6.5 Time histories of semi-major axis for LEO-GEO orbit transfers at the first iteration (direct-shooting method, multiple-shooting technique with state nodes).....	107
Figure 6.6 Time histories of eccentricity for LEO-GEO orbit transfers at the first iteration (direct-shooting method, multiple-shooting technique with state nodes).....	107
Figure 6.7 Time histories of inclination for LEO-GEO orbit transfers at the first iteration (direct-shooting method, multiple-shooting technique with state nodes).....	108
Figure 6.8 Earth-Mars trajectories at the first iteration (direct-shooting method, multiple shooting with state nodes).....	110
Figure 6.9 Time histories of semi-major axis for Earth-Mars trajectories at the first iteration (direct-shooting method, multiple shooting with state nodes)	110
Figure 6.10 Time histories of eccentricity for Earth-Mars trajectories at the first iteration (direct-shooting method, multiple shooting with state nodes).....	111
Figure 6.11 Time histories of input power for Earth-Mars trajectories at the first iteration (direct-shooting method, multiple shooting with state nodes).....	111
Figure 6.12 Earth-Mars trajectories at the first iteration (hybrid method, multiple-shooting technique with costate nodes)	114

Figure 6.13 Time histories of control steering for Earth-Mars trajectories at the first iteration (hybrid method, multiple-shooting technique with costate nodes).....	114
Figure 6.14 Earth-Mars trajectory at the first iteration (hybrid, multiple-shooting technique with state and costate nodes)	116
Figure 6.15 Time histories of control steering for Earth-Mars trajectory at the first iteration (hybrid, multiple-shooting technique with state and costate nodes)	116
Figure 6.16 Time histories of semi-major axis for Earth-Mars trajectories at the first iteration (hybrid method, multiple-shooting technique with state and costate nodes) ...	117
Figure 6.17 Time histories of eccentricity for Earth-Mars trajectories at the first iteration (hybrid method, multiple-shooting technique with state and costate nodes).....	117
Figure 6.18 Time histories of input power for Earth-Mars trajectories at the first iteration (hybrid method, multiple-shooting technique with state and costate nodes).....	118
Figure 6.19 Optimal Earth-Jupiter trajectory (hybrid method, multiple-shooting technique with state and costate nodes)	120
Figure 6.20 Time histories of control steering for optimal Earth-Jupiter trajectory (hybrid method, multiple-shooting technique with state and costate nodes).....	120
Figure 6.21 Earth-Jupiter trajectories at the first iteration (hybrid method, multiple-shooting technique with state and costate nodes)	121
Figure 6.22 Time histories of control steering for Earth-Jupiter trajectory at first iteration using multiple shooting with state and costate nodes	121
Figure 6.23 Time histories of semi-major axis for Earth-Jupiter trajectories at the first iteration (hybrid method, multiple-shooting technique with state and costate nodes) ...	122
Figure 6.24 Time histories of eccentricity for Earth-Jupiter trajectory at the first t iteration (hybrid method, multiple-shooting technique with state and costate nodes).....	122
Figure 6.25 Time histories of inclination for Earth-Jupiter trajectories at the first iteration (hybrid method, multiple-shooting technique with state and costate nodes).....	123
Figure 7.1 C_3 vs. delivered mass for Delta 7925	129
Figure 7.2 Final mass vs. P_0 with final mass maximized	133
Figure 7.3 Payload mass vs. P_0 with final mass maximized.....	134

Figure 7.4 Propellant masses vs. P_0 with final mass maximized	134
Figure 7.5 Optimal Eros sample return trajectory without gravity assist (parallel-burn)	136
Figure 7.6 Time histories of control steering for optimal Eros sample return trajectory without gravity assist (parallel-burn)	136
Figure 7.7 Optimal Eros sample return trajectory with Earth gravity assist (sequential-burn)	137
Figure 7.8 Time histories of control steering for optimal Eros sample return trajectory with Earth gravity assist (sequential-burn)	137
Figure 7.9 Payload mass vs. dropped mass (parallel-burn, sequential-burn)	138
Figure 7.10 C_3 vs. delivered mass for Delta IV 4450	141
Figure 7.11 Relation between thrust and input power	143
Figure 7.12 Engine-switching logic	144
Figure 7.13 NEXT engine I_{sp} vs. power	145
Figure 7.14 NEXT engine η vs. power	146
Figure 7.15 Control steering of optimal Pluto-flyby trajectories using NSTAR engine (maximum final mass)	148
Figure 7.16 Time histories of input power for optimal Pluto-flyby trajectories using NSTAR engine (maximum final mass)	148
Figure 7.17 Time histories of I_{sp} optimal Pluto-flyby trajectories using NSTAR engine (maximum final mass)	149
Figure 7.18 Time histories of control steering for optimal Pluto-flyby trajectories using NEXT engine (maximum final mass)	150
Figure 7.19 Time histories of input power for optimal Pluto-flyby trajectories using NEXT engine (maximum final mass)	150
Figure 7.20 Time histories of I_{sp} for optimal Pluto-flyby trajectories using NEXT engine (maximum final mass)	151
Figure 7.21 Time histories of control steering for optimal Pluto-flyby trajectories using NSTAR engine (minimum transfer time)	152

Figure 7.22 Time histories of input power for minimum-time Pluto-flyby trajectories using NSTAR engine (minimum transfer time).....	153
Figure 7.23 Time histories of I_{sp} for optimal Pluto-flyby trajectories using NSTAR engine (minimum transfer time)	153
Figure 7.24 Time histories of control steering for optimal Pluto-flyby trajectories using NEXT engine (minimum transfer time).....	154
Figure 7.25 Time histories of input power for optimal Pluto-flyby trajectories using NEXT engine (minimum transfer time).....	155
Figure 7.26 Time histories of I_{sp} for optimal Pluto-flyby trajectories using NEXT engine (minimum transfer time).....	155
Figure 7.27 3-D Pluto-flyby trajectories (NEXT, maximum final mass, switching logic II)	156
Figure 7.28 Pluto-flyby trajectory near the Earth (NEXT, maximum final mass, switching logic II)	156
Figure 8.1 Coordinate transformation.....	161
Figure 8.2 Time histories of a , e , i , Ω due to J_2 effect.....	166
Figure 8.3 Control steering for optimal LEO-GPS transfers (equinoctial elements)	169
Figure 8.4 Time histories of semi-major axis for optimal LEO-GPS transfers (equinoctial elements)	170
Figure 8.5 Time histories of eccentricity for optimal LEO-GPS transfers (equinoctial elements)	170
Figure 8.6 Time histories of inclination for optimal LEO-GPS transfers (equinoctial elements)	171
Figure 8.7 Time histories of RAAN for optimal LEO-GPS transfers (equinoctial elements)	171
Figure 8.8 Time histories of equinoctial element \dot{h}	185
Figure 8.9 Time histories of equinoctial elements f and g	186
Figure 8.10 Time histories of equinoctial elements h and k	186

Figure 8.11 Time histories of equinoctial elements L	187
Figure 8.12 Optimal LEO-GEO trajectory w/ J_2 solved by modified equinoctial elements	187
Figure 8.13 Optimal control steering solved by modified equinoctial elements	188
Figure 9.1 Perkins' low-thrust spiral solutions. (a) Velocity and spiral time (b) Flight-path angle.....	198
Figure 9.2 Perkins' low-thrust spiral solutions in energy-eccentricity space	199
Figure 9.3 Projected eccentricity at perigee for guidance parameter update trials.....	204
Figure 9.4 Guidance parameter λ update trials at start of second guidance phase.....	206
Figure 9.5 Predicted inclination rate for two update cycles in second guidance phase..	207
Figure 9.6 Guided trajectory from SOI to spiral target boundary.....	211
Figure 9.7 Time history of inclination	211
Figure 9.8 Steering program from SOI to spiral target boundary.....	212
Figure 9.9 The Earth-capture trajectories to Perkins' universal solution	212

ADVANCES IN LOW-THRUST TRAJECTORY OPTIMIZATION AND FLIGHT MECHANICS

Yang Gao

Dr. Craig A. Kluever, Dissertation Supervisor

ABSTRACT

The dissertation presents advances in trajectory optimization and flight mechanics of low-thrust spacecraft. The hybrid method and the direct-shooting method are described systematically. The system costates are employed to dictate optimal control in the hybrid method and the discrete nodes in the direct-shooting method are used to approximate the control steering. In both methods, the optimal control problems are converted into parameter optimization problems solved by sequential quadratic programming. Furthermore, with the aid of the extended multiple-shooting techniques with state and costate nodes, these two methods are utilized to solve a variety of optimal orbit transfer problems. Many optimal solutions including Earth-orbit and interplanetary orbit transfers are shown and comparisons are made between solutions using different dynamic models and optimization methods. New trajectory solutions for more complex interplanetary orbit transfers using solar electric propulsion (optimal Eros sample return and Pluto-flyby missions) are demonstrated, in which the operation and effects of multiple engines and engine switching logic are investigated. Alternative formulations of equations of motion are discussed, which include inertial frame transformation in terms of three Euler angles and a modified set of equinoctial elements using the non-dimensional angular momentum. Finally, a low-thrust Earth capture guidance scheme is presented, which

makes novel use of Perkins' low-thrust universal solution and thus doesn't require a stored reference trajectory or control. The simplicity and performance of this new guidance design makes it a viable candidate for onboard implementation.

CHAPTER 1 INTRODUCTION

1.1 Overview

Approximately a half century ago, human beings started research on aerospace technology, which is a relatively younger area compared to other modern engineering technologies. However, in the past fifty years, tremendous accomplishments have been achieved. The first man-made satellite was launched in 1957; the first manned space mission was successfully carried out in 1961; the unprecedented Apollo program landed humans on the Moon and brought them back safely in 1969. Since the 1970's, deep space explorations have helped people better understand the compositions of celestial bodies and the evolution of the solar system even the universe. These breakthroughs greatly encouraged scientists to put more emphasis on aerospace technology. Nowadays, more and more satellites have been launched to perform important tasks for many applications including telecommunications, scientific researches, meteorology, geography and others. At present, man-made spacecraft have visited eight planets in the solar system, all except Pluto. In recent years, the first asteroid exploration spacecraft, named NEAR, went into orbit of Eros 433 on February 14, 2000. In 2003, several Mars exploration spacecraft were launched and landing robots are ready to touch the surface of Mars. Also, the Pluto-flyby mission, named New Horizons, is recently under progress to visit the farthest and most mystical planet in our solar system.

Since the 1960's, much research work was started in the area of trajectory optimization of orbit transfers including Earth-orbit, Earth-Moon, and interplanetary trajectories. For most space missions, performance measures such as payload mass and trip time are crucial to the design of spacecraft and satellites. More payload mass or less trip time might result in reduced costs and more operational scientific discoveries. Therefore, optimization is indispensable in space mission design based on current hardware technologies.

The current orbit control technologies of spacecraft are principally based on the propulsion system. Since the beginning of the space age, chemical propulsion has been the primary option for spacecraft and satellites. It commonly represents the high-thrust trajectory design, in which burns are impulsive, and coast arcs are computed analytically. In recent decades, low-thrust propulsion, typically represented by electrical propulsion, has been a viable option. The characteristic of low-thrust is that the propulsion level is so low that the orbit transfers cannot be completed within a short powered period. Continuous powered arcs are needed for orbit transfers and numerical integration is necessary for trajectory computation. Although it seems that low-thrust propulsion results in technological complexity and longer transfer time, the existing research work has shown that significant payload advantages of low-thrust propulsion for orbit transfers are possible. Furthermore, low-thrust propulsion may provide superior mission design compared to conventional chemical propulsion.

Deep Space 1 (DS1) [1, 2] launched in 1998 demonstrated the first use of solar electric propulsion (SEP) as the primary propulsion mode for an interplanetary mission. In September 2003, Europe's first lunar spacecraft SMART-1 utilized electric propulsion

to boost the vehicle to escape the Earth and enter the orbit of the Moon. One of the main objectives of these two missions is to test solar electric propulsion, which is considered to be a viable option for near-term future interplanetary missions. Another example of low-thrust spacecraft is the solar sail [3-6], which is the spacecraft without an engine and is pushed directly by light particles from the sun, which reflect off giant mirror-like sails. Because it carries no fuel and keeps accelerating over almost unlimited distances, it is the only near-term technology that can one day carry a payload to the stars. NASA has a program to develop solar sail technology to a point where it can be used for new space exploration missions. A solar sail, named COSMOS 1, is supposed to be launched in 2004. However, solar electrical propulsion and solar sail also have drawbacks. For example, the thrust of solar sail is too low to perform a long-journey space mission in a short time frame; the solar electrical propulsion has difficulty to perform the rendezvous of planets far away from the sun such as Uranus, Neptune, and Pluto, due to the power loss from the sun. A newer technology, radioisotope electric propulsion [7, 8], may be useful for outer planetary missions because the power is not generated by solar energy. The electrical propulsion powered by other methods such as nuclear power can generate higher thrust and is expected and considered to be a good choice for outer planet missions. However, due to nuclear safety issues, its use is uncertain. Hybrid propulsion systems [9] were also investigated to take advantages of both high-thrust and low-thrust systems. One of the main differences between high-thrust and low-thrust propulsion is the specific impulse (I_{sp}), which measures the amount of thrust obtained from propellant burned in a time interval - the higher the number, the more efficient the engine. In general, high-thrust propulsion gives powerful acceleration to boost the spacecraft but the

energy change is limited due to limited fuel onboard and low I_{sp} (low efficiency) whereas the low-thrust propulsion would give continuous long-lasting small or large acceleration and higher I_{sp} (high efficiency) so the overall energy change might be larger.

In this dissertation, low-thrust propulsion is not specifically defined as spacecraft powered by either electrical propulsion or solar sail. Low-thrust trajectory optimization widely refers to the mission design with non-impulsive burn arcs and precise integration of the governing equations of motion. This dissertation principally presents the trajectory optimization and flight mechanics for the low-thrust spacecraft. An integrated view of dynamic models, trajectory optimization approaches, and mission design will be presented. The content of this dissertation is suitable for trajectories with any low-thrust propulsion system such as solar electrical propulsion and any general orbit transfer problem.

1.2 Literature Review

Recent low-thrust trajectory solutions include Earth-orbit, Earth-Moon, and interplanetary transfers. Trajectory optimization and mission design for low-thrust spacecraft present a range of challenging issues, including choosing a proper dynamic model, computing continuous powered arcs and continuous control functions (thrust steering), creating multiple burn and coast arcs, optimizing engine system parameters (I_{sp} , power), and utilizing realistic system models. The review of previous work falls into three categories: dynamical modeling, optimization methodologies, and mission designs.

The well-known two-body Keplerian equation in vector form is found in many texts [10-12] related to orbital mechanics. The Gauss planetary equations [10-12] were developed to indicate a variational form of spacecraft dynamics. In an actual orbit

transfer problem, a specific coordinate system should be adopted. Of course, the Cartesian coordinate frame is naturally used to express the equations of motion and is often employed in trajectory optimization problems. But other coordinate systems might be better for optimization. For example, Kluever [13, 14] used the spherical and two-dimensional spherical coordinate (polar) frames for Earth-Moon transfers. Broucke and Cefola [15], and Battin [12] introduced the equinoctial elements. Walker, Ireland, and Owens [16] developed another set of equinoctial elements, which accommodate all the conic orbits. Betts [17, 18] utilized this set of equinoctial elements to solve interplanetary and Earth-Moon trajectories. Kechichian [19-22] also developed a series of equinoctial elements to solve low-thrust Earth-orbit transfers. Both classical orbital elements and equinoctial elements give the variational forms for equations of motion so that it is easy to observe how the disturbing forces affect the orbits. The advantage of variational forms is that the orbital elements are changing slowly so that a large integration step size can be used. Furthermore, unlike classical orbital elements, equinoctial elements exhibit no singularity for orbits with zero eccentricity and zero inclination. Non-Keplerian orbits with perturbations [10-12] and displaced Keplerian orbits [23] were also investigated, which are extensions of the pure two-body dynamics.

With the existing dynamic models, one of the main objectives is to find optimal trajectories. Based on the optimal control theory and the calculus of variations, the well-known two-point bound-value problem (TPBVP) is established from the first-order necessary optimality condition. Kechichian [19-22] solved TPBVP of the Earth-orbit transfers using nonlinear programming (NLP) to minimize the terminal constraints. Chuang, Goodson and Hanson [24] also solved TPBVP problems that involve switching

functions. Hanson and Duckman [25] presented several multiple-burn trajectories using TPBVPs to solve each burn transfer. Solving a TPBVP (also called the indirect shooting method) means that the necessary optimal conditions are satisfied so that most solutions obtained are globally optimal. However, many researchers point out that the TPBVP problem is hard to solve directly due to the sensitivity of costate equations. Accurate guesses for the initial costates are required in order to obtain converged solutions. Therefore, how to generate the good guess of initial costates has become a common topic [26, 27] in solving TPBVPs. Since directly solving TPBVPs is not easy, other methods have been developed, and most of them utilized NLP. Ilgen [28] used NLP and the optimal condition of TPBVP to solve low-thrust trajectories. Zondervan, Wood and Caughey [29] used a hybrid method to study three-burn transfers with a large plane change. Kluever [13, 14] solved a series of Earth-Moon trajectories using a combined indirect/direct method. For these hybrid methods, the costate equations were developed but NLP was employed to optimize the desired performance. Recently, the relation between costates in different frames was also investigated [30].

At the same time, researchers also resorted to using direct methods instead of indirect or hybrid methods. Direct methods usually refer to methods that do not depend on Hamiltonian and costate equations, in which case only the governing state equations of motion are numerically integrated. The time histories of states and control steering are represented by discrete values, and a parameter optimization problem by NLP is created. Many applications of direct methods have been documented in trajectory optimization. Kluever [31] utilized control steering parameterization solving the interplanetary orbit transfers. Betts [17, 18, 32, 33] used direct transcription or collocation based on sparse

nonlinear programming to solve a series of optimal trajectories, including Earth-Mars transfers and Earth-Moon transfers. Tang and Conway [34] employed the collocation method to solve interplanetary trajectories. Herman and Conway [35] solved Earth-Moon trajectories using the collocation method, and later [36] they improved the collocation method with high-order Gauss-Lobbato rules. Herman and Spencer [37] used high-order collocation to deal with the low-thrust Earth-orbit transfers. Sheel and Conway [38] also demonstrated the parallel shooting method for two-dimensional low-thrust Earth-orbit transfers. Seywald [39], and Kuma and Seywald [40] introduced the differential inclusion concept, and Coverstone [41] used this method to solve the optimal interplanetary trajectories. Later, Conway and Larson [42] compared the collocation and differential inclusion methods.

Betts [43] summarized the different methods available to solve trajectory optimization problems. Hull [44] systematically summarized the conversion of optimal control problems into parameter optimization problems, which includes control steering parameterization, state and control parameterization, multiple direct shooting, and differential inclusion. These articles indicate that direct methods are commonly used in recent years.

In addition to direct parameterization of controls and states, other approaches are used to solve orbit transfer problems. Ilgen [45] used Lyapunov-based controller to guide the spacecraft to transfer between Earth orbits. Chang el al. [46] developed a Lyapunov-based controller using Laplace vector for transfers between elliptic orbits. Schaub et al. [47] also used Lyapunov-based controller for spacecraft formation flying. However, the Lyapunov-based controller is not optimal. Kluever and Oleson [48] utilized the extremal

rate of classical orbital elements to construct a blended optimal control for low-thrust orbit transfers. Spencer and Culp [49] employed a similar strategy to design low-Earth-orbit (LEO) to geostationary-Earth-orbit (GEO) transfers. Kechichian [50-52] also utilized this type of control for low-thrust orbit transfers. Fahroo and Ross [53] demonstrated direct trajectory optimization by a Chebyshev pseudospectral method. Jacobson [54, 55] presented a second-order algorithm using differential dynamic programming to solve optimal control problems but no orbit transfers were shown. Recently, genetic algorithm [56, 57] is employed in trajectory optimization but its capability to solve complex orbit transfers seems limited. Luo and Kluever [58] presented orbital rendezvous using fuzzy logic controller.

With more knowledge of trajectory optimization, many practical missions have been investigated and designed. The optimal trajectories have included Earth-orbit transfers [59-61], Earth-Moon transfers [62], interplanetary orbit transfers [63, 64], Earth escape and planetary capture orbits [65-67], and asteroid/comet missions [68, 69], and optimization of launch vehicle trajectories [70]. Low-thrust propulsion has also made it possible to perform new missions, such as atmosphere aero-assisted trajectories [71], optimal interceptions [72], and asteroid deflection [73].

1.3 Topics and Outline

This dissertation presents several advances in direct optimization approaches and flight mechanics for low-thrust orbit transfers. The direct methods in this work are those that do not solve the TPBVP directly. The hybrid method and the direct-shooting method are presented in subsequent chapters.

The outline of the dissertation is as follows. Chapter 2 deals with the orbit dynamics, including models for motion, perturbations, gravity assists, and escape/capture orbits. In Chapter 3, the hybrid method is introduced to solve trajectory optimization problems, which is obtained by combining the optimality condition from the TPBVP and NLP. Together with the extended multiple-shooting techniques, the hybrid method is designed to obtain general optimal orbit transfers. In Chapter 4, the direct-shooting method is described, where the time histories of states and control steering are directly parameterized as NLP design variables. The collocation method is also described and compared with the direct-shooting method. Chapter 5 presents examples of optimal trajectories using different methods. The solutions of optimal Earth-orbit and interplanetary orbit transfers using the hybrid and direct-shooting methods are presented and compared. The optimal orbit transfers using multiple shooting techniques is demonstrated in Chapter 6. In Chapter 7, two complex real missions (Eros sample return and Pluto-flyby missions) using realistic engine systems are obtained with real mission constraints. Some detailed problems, such as the operation of multiple engines and engine-switching logic, are also analyzed. These two mission designs also demonstrate the strength of the direct-shooting method. Alternative formulations for equations of motion are described in Chapter 8. The inertial frame transformation in terms of three Euler angles makes the terminal constraints simple if the final desired orbits are circular. The convergence performance of the hybrid method is improved using this transformation. A modified set of equinoctial elements is developed with non-dimensional angular momentum as the first element. In Chapter 9, a new low-thrust Earth-capture guidance scheme is presented. The maximum rates of classical orbital

elements are employed to construct onboard guidance scheme instead of finding optimal trajectories offline. The summary and conclusions are presented in Chapter 10.

The main contributions of this dissertation are stated as follows. An integrated and systematic implementation of the hybrid and direct-shooting methods is presented. Specifically, the hybrid and direct-shooting methods with multiple shooting techniques are developed to solve a variety of general orbit transfer problems. The hybrid method has been successfully applied in optimal interplanetary orbit transfers. Also, the sequential quadratic programming (SQP) is proved to be successful in solving optimal orbit transfer problems. The extended multiple shooting techniques with state nodes and costate nodes are shown to be more flexible and robust. The Eros sample return and Pluto-flyby optimal trajectories using realistic solar electric propulsion system are presented and can be considered candidate preliminary mission designs. These two missions are new and challenging to solve. The inertial frame transformation is presented as a technique to improve the convergence performance of the hybrid method. A modified set of equinoctial elements using non-dimensional angular momentum is a good alternative dynamic model. The low-thrust Earth capture guidance scheme presents a new solution concept by making novel use of Perkins' universal solution. This kind of guidance scheme is simple and does not require storing reference trajectories and control steering. Furthermore, the volume of the work for low-thrust guidance is limited, which is a challenging topic, especially for trajectories involving many revolutions.

CHAPTER 2 SPACECRAFT DYNAMICS

2.1 Equations of Motion

Spacecraft motion is modeled by the two-body dynamics, in which a general equation of two attractive bodies perturbed by each other was developed. Assuming that the attracting body (such as the sun, Earth or planet) is the origin of the two-body system, the equations of motion for spacecraft relative to the attracting body can be expressed in an inertial frame as follows:

$$\ddot{\mathbf{r}} + \frac{\mu_{body}}{r^3} \mathbf{r} = \mathbf{f}_T + \mathbf{f}_p \quad (2.1)$$

With the equation to express the mass-flow rate, we can rewrite the equations of motion with position and velocity vectors:

$$\dot{\mathbf{r}} = \mathbf{v} \quad (2.2)$$

$$\dot{\mathbf{v}} = -\frac{\mu_{body}}{r^3} \mathbf{r} + \frac{T}{m} \alpha + \mathbf{f}_p \quad (2.3)$$

$$\dot{m} = -\frac{T}{gI_{sp}} \quad (2.4)$$

where	\mathbf{r}	:	Position vector of spacecraft
	\mathbf{v}	:	Velocity vector of spacecraft
	m	:	Mass of spacecraft
	\mathbf{f}_T	:	Thrust acceleration
	\mathbf{f}_p	:	Perturbation acceleration

T	:	Thrust magnitude
α	:	Thrust acceleration direction unit vector
μ_{body}	:	Gravitational parameter of the attracting body
g	:	Earth sea-level gravitational acceleration
I_{sp}	:	Specific impulse

Equations (2.1)-(2.4) are found in many spacecraft dynamics texts [10-12]. For low-thrust orbit transfers, the thrust magnitude is modeled in two ways. The first type of model is

$$T = \frac{2\eta P}{c} = \frac{2\eta P}{gI_{sp}} \quad (2.5)$$

where $c = gI_{sp}$ is the exhaust velocity of propulsion system, η is the thruster efficiency, and P is the engine input power. The values of η , I_{sp} and P can be constant or variable with upper and lower boundaries. The mass-flow rate is related to the thrust magnitude and the exhaust velocity. The second expression for thrust magnitude is

$$T = (T/W)_0 \times m_0 g \quad (2.6)$$

where $(T/W)_0$ is the initial thrust-to-weight ratio and m_0 is the initial mass of spacecraft. Equation (2.6) gives constant thrust.

2.2 J2000 Earth Equatorial Coordinates and Heliocentric Ecliptic Coordinates

J2000 equatorial coordinates are defined by the mean orientation of the Earth's equator and ecliptic orbit at the beginning of the year 2000. The X-Y plane of the J2000 equatorial coordinates is the plane of the mean Earth's equator. The line, which is formed by intersection of the ecliptic orbit plane and the Earth's equatorial plane, defines the X-

axis. This line, on the first day of autumn, (starting from the sun to the center of the Earth) defines the positive direction of the X-axis, which is called the vernal equinox. The Z-axis is perpendicular to X-Y plane and points to the north. Y-axis completes Cartesian coordinate frame using the right-handed principle. The X-Y plane of the heliocentric ecliptic coordinates is the ecliptic plane of the Earth's revolution around the sun. The transformation from the J2000 Earth equatorial coordinates to the heliocentric ecliptic coordinates is a rotation about the X-axis. The rotation angle is the Earth's obliquity angle, and the rotation direction is counterclockwise. These two coordinate frames are shown in Fig. 2.1.

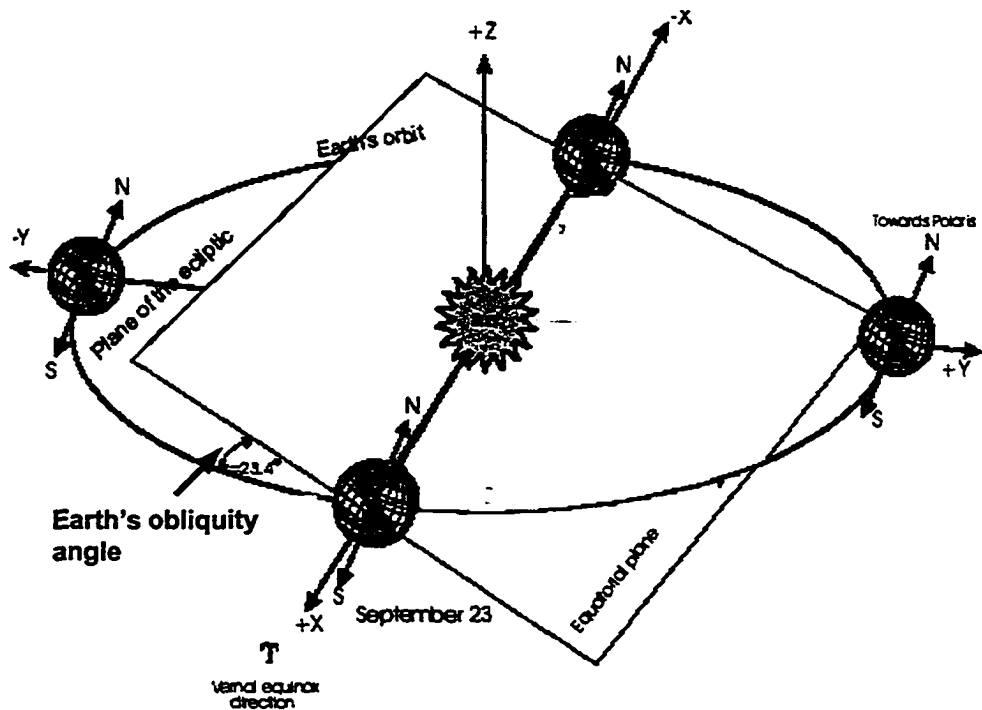


Figure 2.1 J2000 Earth equatorial coordinate and heliocentric ecliptic coordinates

For Earth-orbit transfers and interplanetary orbit transfers, these two types of inertial frames are commonly used. In this dissertation, the Jet Propulsion Laboratory

(JPL) solar system planet ephemeris is based on the J2000 inertial frame and is used for computing the interplanetary orbit transfer problems.

2.3 Equations of Motion Expressed by Different Coordinates

The basic equation of motion in vector form has been introduced in the previous section. In a practical trajectory optimization problem, we need to use three-dimensional coordinates or orbital elements for numerical computations. Cartesian and spherical coordinates are based on the position and velocity vectors of spacecraft. The expressions in terms of orbital elements give the variational forms.

2.3.1 Equations of Motion Expressed by Cartesian Coordinates

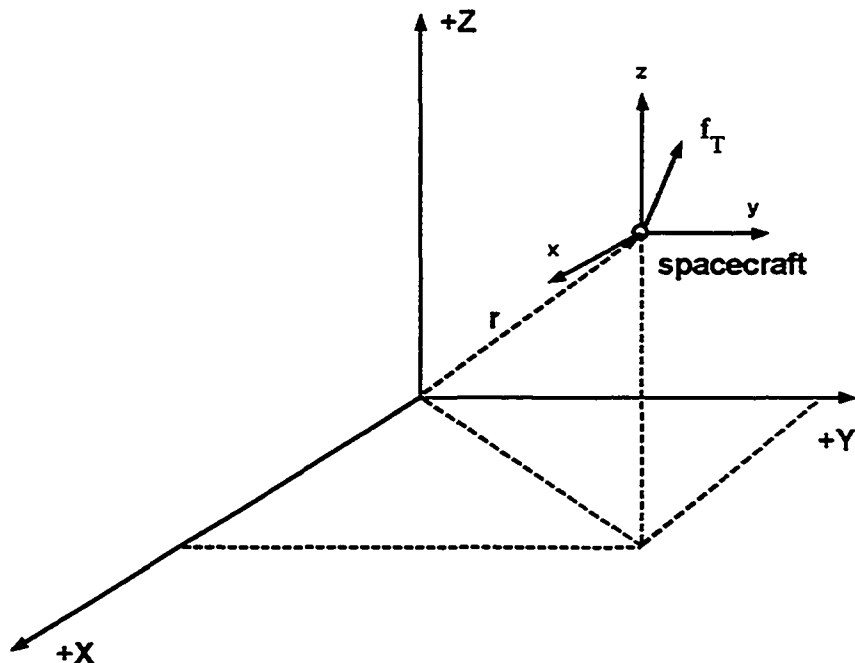


Figure 2.2 Cartesian coordinates

Cartesian coordinates presented in Fig. 2.2 are widely used in many research areas. It takes little effort to derive the equations of motion expressed by Cartesian coordinate

elements. Cartesian coordinate frame is a fixed frame and we usually assume that its axes are the same as those of inertial frame. The equations of motion in Cartesian coordinate are

$$\dot{x} = v_x \quad (2.7)$$

$$\dot{y} = v_y \quad (2.8)$$

$$\dot{z} = v_z \quad (2.9)$$

$$\dot{v}_x = -\frac{\mu}{x^2 + y^2 + z^2} \frac{x}{\sqrt{x^2 + y^2 + z^2}} + f_T \alpha_x + f_p, \quad (2.10)$$

$$\dot{v}_y = -\frac{\mu}{x^2 + y^2 + z^2} \frac{y}{\sqrt{x^2 + y^2 + z^2}} + f_T \alpha_y + f_p, \quad (2.11)$$

$$\dot{v}_z = -\frac{\mu}{x^2 + y^2 + z^2} \frac{z}{\sqrt{x^2 + y^2 + z^2}} + f_T \alpha_z + f_p, \quad (2.12)$$

where f_T is the thrust acceleration magnitude. α_x , α_y , and α_z are the components of the acceleration direction unit vector. f_{p_x} , f_{p_y} , and f_{p_z} are the three components of perturbation acceleration. Three position components are denoted by x , y , and z , and three velocity components are denoted by v_x , v_y , and v_z . This coordinate frame is usually used for few-revolution orbit transfers. For many-revolution orbit transfers, a small integration step size would be necessary to reduce the error produced by oscillation of the six states.

2.3.2 Equations of Motion Expressed by Spherical Coordinates

Spherical coordinates, shown in Fig. 2.3, is a rotating frame and is also used to express the equations of motion. For two-dimensional orbit transfers, the spherical

coordinates, or called polar frame, is convenient and is often used by researchers for demonstrating new algorithms.

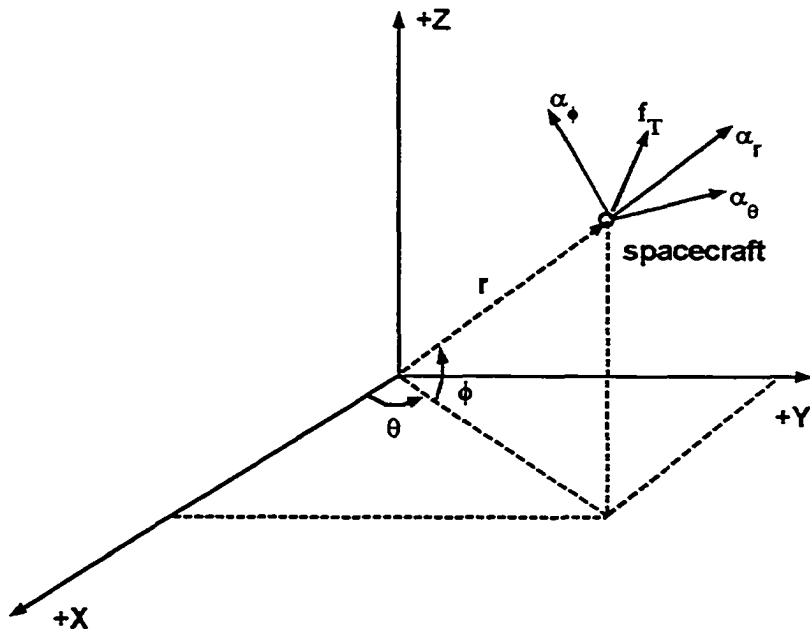


Figure 2.3 Spherical coordinates

The illustration of spherical coordinates is shown in Fig. 2.3 and the equations of motion are expressed as follows:

$$\dot{r} = v_r \quad (2.13)$$

$$\dot{\theta} = \frac{v_\theta}{r \cos \phi} \quad (2.14)$$

$$\dot{\phi} = \frac{v_\phi}{r} \quad (2.15)$$

$$\dot{v}_r = \frac{v_\theta^2}{r} + \frac{v_\phi^2}{r} - \frac{\mu}{r^2} + f_T \alpha_r + f_{p_r} \quad (2.16)$$

$$\dot{v}_\theta = -\frac{v_r v_\theta}{r} + \frac{v_\phi v_\theta}{r} \tan \phi + f_T \alpha_\theta + f_{p_\theta} \quad (2.17)$$

$$\dot{v}_\phi = -\frac{v_r v_\phi}{r} - \frac{v_\theta^2}{r} \tan \phi + f_r \alpha_r + f_{p_\phi} \quad (2.18)$$

where r is radius magnitude from the origin to spacecraft, and θ and ϕ are two position angles (defined in the Fig. 2.3). The three velocity components are denoted by v_r , v_θ , and v_ϕ . The direction of thrust is defined in a local rotating frame: α_r is along the radial direction, α_θ is perpendicular to α_r and parallel to X-Y plane, and α_ϕ is chosen according to right-handed principle.

2.3.3 Equations of Motion Expressed by Classical Orbital Elements

Compared with position and velocity vectors, orbital elements are more intuitive to describe an orbit. Six classical orbital elements, shown in Fig. 2.4, are defined as follows:

- a Semi-major axis
- e Eccentricity
- i Inclination
- Ω Right ascension of ascending node (RAAN)
- ω Argument of perigee
- θ True anomaly

Singularities occur when $e=0$ (circular orbit) and $i=0$ (equatorial orbit). If $e=0$, ω and θ are not defined, and if $i=0$, Ω is undefined. The energy of spacecraft is uniquely determined by semi-major axis and computed by

$$E = \frac{v^2}{2} - \frac{\mu}{r} = -\frac{\mu}{2a} \quad (2.19)$$

If $E = 0$ (escape conditions), α is undefined. So transfers to circular, equatorial, parabolic and hyperbolic orbits usually do not use the classic orbit elements for numerical integration.

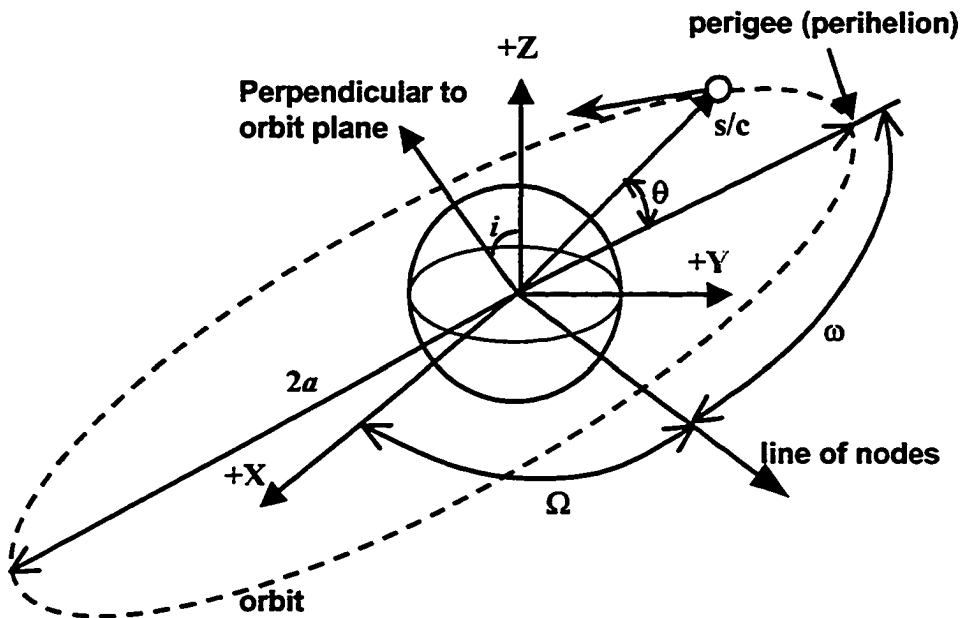


Figure 2.4 Classical orbital elements

Using all six classical orbit elements, a set of ordinary differential equations (2.20-2.25) is presented, which are also called the Gauss planetary equations [10-12].

$$\dot{a} = \frac{2a^2 e \sin \theta}{h} f_r + \frac{2a^2 p}{hr} f_t \quad (2.20)$$

$$\dot{e} = \frac{1}{h} p \sin \theta f_r + \frac{1}{h} [(p+r) \cos \theta + r e] f_t \quad (2.21)$$

$$\dot{i} = \frac{r \cos(\omega + \theta)}{h} f_n \quad (2.22)$$

$$\dot{\Omega} = \frac{r \sin(\omega + \theta)}{h \sin i} f_n \quad (2.23)$$

$$\dot{\omega} = -\frac{p \cos \theta}{he} f_r + \frac{(p+r) \sin \theta}{he} f_t - \frac{r \sin(\omega + \theta) \cos i}{h \sin i} f_n \quad (2.24)$$

$$\dot{M} = n + \frac{1}{a h e} [(p \cos \theta - 2re) f_r - (p+r) \sin \theta f_t] \quad (2.25)$$

where

$$p = a(1-e^2) \quad (2.26)$$

$$h = \sqrt{\mu p} \quad (2.27)$$

$$n = \sqrt{\frac{\mu}{a^3}} \quad (2.28)$$

$$r = \frac{p}{1+e \cos \theta} \quad (2.29)$$

M is the mean anomaly and is defined by $M = \psi - e \sin \psi$, where ψ is the eccentric anomaly. The relationship of true and eccentric anomalies is as follows:

$$\cos \psi = \frac{e + \cos \theta}{1 + e \cos \theta}, \quad \sin \psi = \frac{\sin \theta \sqrt{1 - e^2}}{1 + e \cos \theta} \quad (2.30)$$

$$\cos \theta = \frac{\cos \psi - e}{1 - e \cos \psi}, \quad \sin \theta = \frac{\sin \psi \sqrt{1 - e^2}}{1 - e \cos \psi} \quad (2.31)$$

The thrust acceleration direction in local radial-tangential-normal (RTN) rotating frame is defined by

$$[f_r \ f_t \ f_n]^T = \frac{T}{m} \alpha, \quad \text{where } \alpha = [\alpha_r \ \alpha_t \ \alpha_n]^T \quad (2.32)$$

Additionally, the direction unit vector can be expressed in terms of local pitch and yaw steering angles:

$$\alpha = [\sin \alpha \cos \beta \ \cos \alpha \cos \beta \ \sin \beta]^T \quad (2.33)$$

Pitch angle (α) is measured from the local horizon to the projection of the thrust vector onto the orbit plane, and yaw angle (β) is measured from the orbit plane to the thrust vector.

2.3.4 Equations of Motion Expressed by Equinoctial Elements

There exist singularities if the classical orbit elements are used for $e = 0$, and $i = 0$. A set of equinoctial elements described in Ref. [16] is utilized to avoid these singularities and accommodate all possible conic orbits except the case where $i = 180$ deg. The equinoctial elements can be obtained in terms of six classical orbital elements.

$$p = a(1 - e^2) \quad (2.34)$$

$$f = e \cos(\omega + \Omega) \quad (2.35)$$

$$g = e \sin(\omega + \Omega) \quad (2.36)$$

$$h = \tan(i/2) \cos \Omega \quad (2.37)$$

$$k = \tan(i/2) \sin \Omega \quad (2.38)$$

$$L = \Omega + \omega + \theta \quad (2.39)$$

The dynamic model based on equinoctial elements is shown below.

$$\dot{p} = \frac{2p}{w} \sqrt{\frac{p}{\mu}} f_i \quad (2.40)$$

$$\dot{f} = \sqrt{\frac{p}{\mu}} [f, \sin L + [(w+1)\cos L + f] \frac{f_i}{w} - (h \sin L - k \cos L) \frac{g \cdot f_n}{w}] \quad (2.41)$$

$$\dot{g} = \sqrt{\frac{p}{\mu}} [-f, \cos L + [(w+1)\sin L + g] \frac{f_i}{w} + (h \sin L - k \cos L) \frac{f \cdot f_n}{w}] \quad (2.42)$$

$$\dot{h} = \sqrt{\frac{p}{\mu}} \frac{s^2 f_n}{2w} \cos L \quad (2.43)$$

$$\dot{k} = \sqrt{\frac{p}{\mu}} \frac{s^2 f_n}{2w} \sin L \quad (2.44)$$

$$\dot{L} = \sqrt{\mu p} \left(\frac{w}{p} \right)^2 + \frac{1}{w} \sqrt{\frac{p}{\mu}} (h \sin L - k \cos L) f_n \quad (2.45)$$

where $w = 1 + f \cos L + g \sin L$. The thrust acceleration components are defined by Eq. (2.32).

2.4 Escape at Sphere Of Influence and Planetary Capture

2.4.1 Escape by Launch Vehicles

The spacecraft escape could be performed by launch vehicles, which can deliver the spacecraft to an Earth escape orbit with the desired energy (C_3). Another way to escape from the Earth's gravity is that the spacecraft uses its own engine. For example, SEP could deliver the spacecraft to an Earth escape orbit after many revolutions around the Earth. The starting point of the heliocentric orbit is the heliocentric position and velocity at the Earth's sphere of influence (SOI) where the Earth's gravity is "turned off". The heliocentric starting point at SOI is determined by the altitude, inclination, right ascension of the ascending node and longitude at burnout point, and C_3 . In Fig. 2.5, the relationship between energy of spacecraft at burnout point and at SOI is as follows:

$$\frac{v_o^2}{2} - \frac{\mu_{earth}}{r_o} = \frac{v_\infty^2}{2} - \frac{\mu_{earth}}{r_\infty} \quad (2.46)$$

C_3 is defined as

$$C_3 = v_\infty^2 \quad (2.47)$$

Suppose r_∞ is large enough, the velocity at burnout point could be estimated.

$$E = \frac{v_\infty^2}{2} - \frac{\mu}{r_\infty} \approx \frac{v_\infty^2}{2} = \frac{C_3}{2} \quad (2.48)$$

$$\frac{v_o^2}{2} - \frac{\mu_{earth}}{r_o} = \frac{v_\infty^2}{2} \quad (2.49)$$

$$v_o = \sqrt{v_\infty^2 + \frac{2\mu_{earth}}{r_o}} = \sqrt{C_3 + \frac{2\mu_{earth}}{r_o}} \quad (2.50)$$

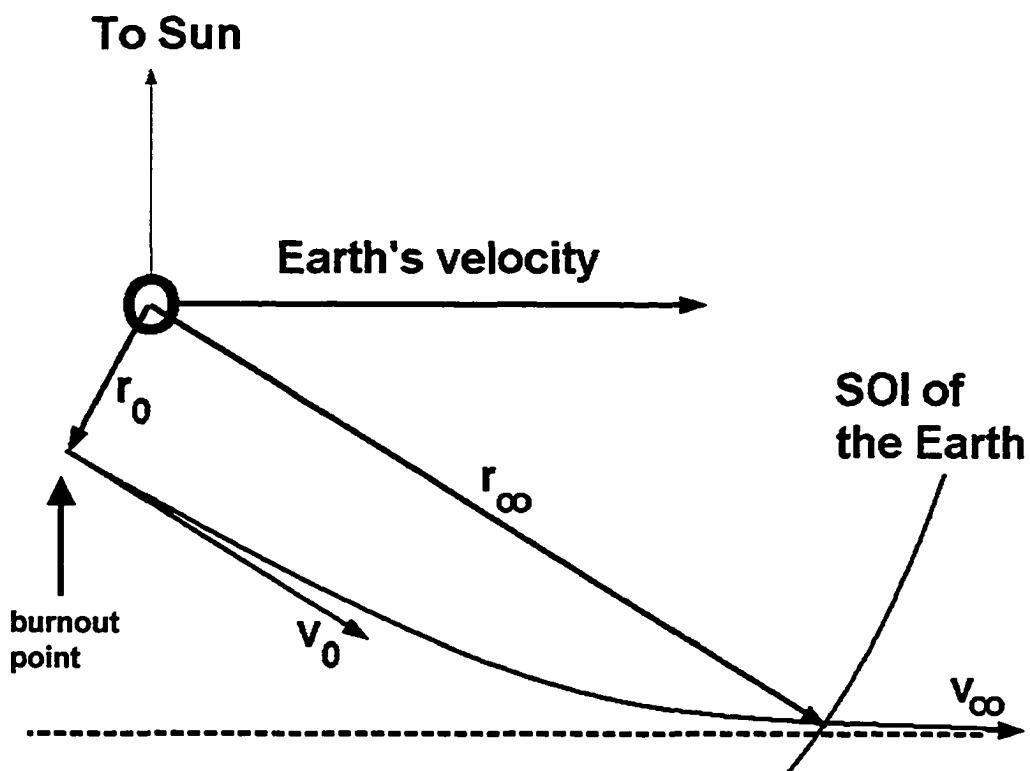


Figure 2.5 The hyperbolic Earth-escape orbit

Assuming that the flight-path angle at burnout point is zero, we can then get the eccentricity of the escape hyperbolic orbit.

$$h = r_o v_o \quad (2.51)$$

$$p = h^2 / \mu_{\text{earth}} \quad (2.52)$$

$$r_o = \frac{p}{1 + e \cos \theta} = \frac{p}{1 + e} \quad (2.53)$$

$$e = p/r_o - 1 \quad (2.54)$$

At SOI of the Earth

$$r_\infty = \frac{p}{1 + e \cos \theta_\infty} \quad (2.55)$$

$$\cos \theta_\infty = \frac{p/r_\infty - 1}{e} \approx \frac{-1}{e} \quad (2.56)$$

At Earth's SOI, semi-major axis $a = \frac{-\mu}{2E}$, eccentricity, inclination, right ascension of ascending node, argument of perigee (or longitude at burnout point), and true anomaly θ_∞ , are known. The classical orbital elements at Earth's SOI can be transformed into position and velocity of spacecraft. The initial conditions for an interplanetary transfer could be computed by a transformation from the equatorial coordinates to the heliocentric coordinates.

2.4.2 High-Thrust Planetary Capture

For high-thrust planetary capture with a chemical propulsion system, we need to assume a parking orbit with a capture perigee radius and apogee radius. The I_{sp} of a high-thrust propulsion system is known. The capture maneuver is approximated as impulsive Δv performed at perigee of the parking orbit. Before the impulsive Δv is performed, the velocity is computed as follows:

$$\frac{v_o^2}{2} - \frac{\mu_{\text{planet}}}{r_o} = \frac{v_\infty^2}{2} - \frac{\mu_{\text{planet}}}{r_\infty} \quad (2.57)$$

where v_∞ is velocity of spacecraft at planet SOI in planet-centered coordinate and is computed by $v_\infty = \|\mathbf{v}_{s/c} - \mathbf{v}_{planet}\|$, where $\mathbf{v}_{s/c}$ and \mathbf{v}_{planet} are velocity vector of spacecraft and planet in the heliocentric coordinates respectively.

$$v_o = \sqrt{v_\infty^2 + \frac{2\mu_{planet}}{r_o}} \quad (2.58)$$

The velocity after impulsive Δv performed at capture point is

$$v_{capture} = \sqrt{\frac{2\mu_{planet}}{r_p} - \frac{2\mu_{planet}}{r_a + r_p}} \quad (2.59)$$

Then the required impulsive Δv is computed as

$$\Delta v = v_{capture} - v_o \quad (2.60)$$

Equation (2.61) gives the relation between masses before and after capture maneuver.

$$m_{before} / m_{after} = e^{-\frac{\Delta v}{gI_p}} \quad (2.61)$$

2.4.3 Escape and Capture with Low Thrust

Instead of using launch vehicles, low-thrust propulsion could be used to propagate spacecraft to escape from a low Earth-orbit or from an approaching hyperbolic orbit to enter planets' low-altitude orbits with many-revolution spirals. Low-thrust escape and capture cannot be approximated analytically, which involve the trajectory optimization.

2.5 Gravity Assist

Planetary gravity assist is a technique used to speed up, slow down, or change the direction of spacecraft as it approaches a planet within the solar system. This technique

saves fuel that would otherwise have to be used to make these adjustments. This technique has been proved to be successful for practical missions.

2.5.1 Impulsive Δv Approximation

Planetary gravities can be modeled as instantaneous change in velocity without change in spacecraft's position [31]. This approximation is appropriate for a preliminary mission design. The gravity assist is defined by two free variables: the periapsis radius r_p for the planetary flyby, and a rotation angle θ , which defines the plane of the planetary flyby. To compute a gravity assist, the incoming position and velocity vector of the spacecraft relative to a planet is calculated.

$$\mathbf{v}_\infty^- = \mathbf{v}^- - \mathbf{v}_p \quad (2.62)$$

where \mathbf{v}^- is the heliocentric velocity of the spacecraft and \mathbf{v}_p is the heliocentric velocity of the planet. Then \mathbf{v}_∞^- is the velocity of the spacecraft on the approaching hyperbola relative to the planet. Given the periapsis radius r_p , the tuning angle δ is computed:

$$\delta = 2 \sin^{-1} \left[\frac{1}{1 + r_p v_\infty^2 / \mu_p} \right] \quad (2.63)$$

where μ_p is the gravitational parameter of the flyby planet. Next, we find the unit vector \mathbf{l} in planetary elliptic plane and perpendicular to \mathbf{v}_∞^- . The dot product of \mathbf{l} and spacecraft position vector should be greater than zero. The pole of flyby orbit plane is obtained by rotating vector \mathbf{l} by angle θ about the \mathbf{v}_∞^- vector. The departure hyperbolic velocity \mathbf{v}_∞^+ is obtained by rotating \mathbf{v}_∞^- about the pole by angle δ . Then the heliocentric velocity of the spacecraft after gravity assist is:

$$\mathbf{v}^+ = \mathbf{v}_p + \mathbf{v}_{\infty}^+ \quad (2.64)$$

The impulsive Δv is given by $\|\mathbf{v}^+ - \mathbf{v}^-\|$ and no position change is calculated during the gravity assist. No thrust is assumed during the gravity assist.

2.5.2 Precise Gravity Assist Simulation

Precise gravity assist simulation uses the accurate integration for the entire duration of gravity assists. As the spacecraft entering the SOI of a planet, the primary attractive body is changed from the sun to the planet. In the planet-centered coordinate, the position and velocity leaving the SOI of a planet can be computed analytically or by integrating the dynamics equation with or without thrust. To switch the primary attractive body also requires transformation between coordinates with different origins. Precise gravity assist simulation could be done after the preliminary solution of gravity assist is obtained by the impulsive Δv approximation method.

2.6 Dynamic Models for Perturbations

2.6.1 Earth Oblateness

The Earth oblateness potential function is expressed as

$$U_{J_2} = \frac{\mu}{r^3} R_E^2 J_2 \frac{1}{2} (3 \sin^2 \phi - 1) \quad (2.65)$$

$$\sin \phi = \frac{z}{r} \quad (2.66)$$

where J_2 is the second-order zonal harmonic coefficient. The angle ϕ is the same as that in spherical coordinates. Three components of J_2 perturbation expressed Cartesian coordinates can be obtained as follow:

$$f_{J_2,x} = -\frac{\partial U_{J_2}}{\partial x}, \quad f_{J_2,y} = -\frac{\partial U_{J_2}}{\partial y}, \quad f_{J_2,z} = -\frac{\partial U_{J_2}}{\partial z} \quad (2.67)$$

In spherical coordinates, we can get

$$f_{J_2,r} = -\frac{\partial U_{J_2}}{\partial r}, \quad f_{J_2,\theta} = -\frac{1}{r \cos \phi} \frac{\partial U_{J_2}}{\partial \theta}, \quad f_{J_2,\phi} = -\frac{1}{r} \frac{\partial U_{J_2}}{\partial \phi} \quad (2.68)$$

In the rotating RTN frame, three components of J_2 perturbation in terms of classical orbital elements are obtained as follows:

$$f_{J_2,r} = -\frac{\partial U_{J_2}}{\partial r}, \quad f_{J_2,i} = -\frac{1}{r} \frac{\partial U_{J_2}}{\partial (\omega + \theta)}, \quad f_{J_2,n} = -\frac{1}{r \sin(\omega + \theta)} \frac{\partial U_{J_2}}{\partial i} \quad (2.69)$$

2.6.2 Third-Body Gravitational Force

Suppose there exist perturbing gravitational forces of n bodies acting on the spacecraft, and then the total perturbation acceleration is computed as

$$\mathbf{f}_p = \sum_{j=1}^n \frac{\mu_n}{\|\mathbf{r}_n - \mathbf{r}\|^3} (\mathbf{r}_n - \mathbf{r}) \quad (2.70)$$

where \mathbf{r} is the inertial position vector of spacecraft, \mathbf{r}_n is the inertial position vector of the n^{th} body, and μ_n is the gravitational parameter of the n^{th} body.

2.7 Essential Problem - How to Find the Optimal Control Steering

A brief introduction to orbit dynamics has been presented in previous sections. The unforced spacecraft will follow a conic orbit defined by its initial position and velocity if we assume there is no perturbation. The problem of orbit transfers is how to propagate the spacecraft, change its initial state, and arrive at a desired target orbit. Moreover, the optimal trajectories are expected to minimize fuel consumption or transfer time.

We assume that the spacecraft is a point mass in space and the attitude control system works perfectly. The general problem statement for orbit transfers can be stated as follows:

Find an optimal control steering that minimizes performance index $J = \phi[\mathbf{x}(t_f), t_f]$, subject to differential equations of motion in the appropriate frame (such as Eq. (2.2-2.4)), and subject to equality constraints $\psi[\mathbf{x}(t_i), t_i] = 0$ and inequality constraints $\Omega[\mathbf{x}(t_j), t_j] \geq 0$ with the given initial condition t_0 and $\mathbf{x}(t_0) = \mathbf{x}_0$. The performance index is evaluated at the terminal time. Most performances are final mass, payload mass, or trip time. The term $\psi[\mathbf{x}(t_i), t_i] = 0$ is a general expression representing all the equality constraints such as final target orbits and gravity assists. The term $\Omega[\mathbf{x}(t_j), t_j] \geq 0$ represents all the inequality constraints such as the constrained launch date and trip time.

CHAPTER 3 HYBRID METHOD OBTAINED FROM TWO-POINT BOUNDARY-VALUE PROBLEM

The hybrid method is based on a two-point boundary-value problem (TPBVP) that results from optimal control theory. However, we do not intend to solve the TPBVP directly, but rather exploit the TPBVP structure and then use parameter optimization and NLP. Moreover, the costate equations and optimality condition derived from TPBVP are employed so that the hybrid method is a mixture of calculus of variations and parameter optimization.

Kechichian [19-22] utilized NLP to minimize the terminal constraints by satisfying all conditions of the TPBVP. Ilgen [28] used NLP and the optimal condition of the TPBVP to solve low-thrust trajectories. Zondervan, Wood, and Caughey [29] combined the direct approach and the TPBVP to solve the three-burn Earth-orbit transfers with a large plane change. Kluever [13, 14] employed the hybrid method to solve a series of optimal Earth-Moon trajectories. In this chapter, an integrated and systematic view of the hybrid method is presented. This method is capable of solving general, complex Earth-orbit and interplanetary orbit transfers with assumed flight sequences *a priori*. Furthermore, the multiple-shooting techniques with both state and costate nodes are developed to improve convergence properties for the hybrid method. The dynamic state and costate equations and the optimality conditions in three different coordinate frames are developed for numerical integration.

3.1 Two-Point Boundary-Value Problem

The two-point boundary-value problem (TPBVP) is based on the calculus of variations, which is widely utilized to obtain optimal control of continuous-time systems. The optimality condition of the TPBVP can be found in many texts on optimal control theory [74, 75]. TPBVP results from the necessary condition that the first-order variation of performance index (involving constraints using Lagrangian multipliers) be zero. The second-order variation of performance index is typically not investigated. TPBVP is briefly stated as below.

The general expression of a system dynamic model could be written as:

$$\dot{\mathbf{x}} = f(\mathbf{x}, \mathbf{u}, t), \quad t \geq t_0 \text{ and } t_0 \text{ fixed} \quad (3.1)$$

where \mathbf{x} is the system state vector, \mathbf{u} is the system input vector, and t_0 is the fixed initial time. The general performance index is defined as:

$$J = \phi[\mathbf{x}(t_f), t_f] + \int_{t_0}^{t_f} L(\mathbf{x}, \mathbf{u}, t) dt \quad (3.2)$$

where t_f is the final time and $t \leq t_f$. Also, for many optimal control problems there exist terminal state constraints, which are generally denoted as:

$$\psi[\mathbf{x}(t_f), t_f] = 0 \quad (3.3)$$

The problem statement is usually composed of Eqs. (3.1-3.3). Obtaining the optimal solution starts with the scalar Hamiltonian function, which is formed as:

$$H(\mathbf{x}, \mathbf{u}, t) = L(\mathbf{x}, \mathbf{u}, t) + \lambda^T f(\mathbf{x}, \mathbf{u}, t) \quad (3.4)$$

The derivative of the Hamiltonian with respect to the Lagrangian multiplier λ (costate) provides the state equations of motion.

$$\dot{\mathbf{x}} = \frac{\partial H}{\partial \lambda} = f(\mathbf{x}, \mathbf{u}, t) \quad (3.5)$$

The costate equation is the derivative of the Hamiltonian with respect to the states.

$$\dot{\lambda} = -\frac{\partial H}{\partial \mathbf{x}} = -\frac{\partial f^T}{\partial \mathbf{x}} \lambda - \frac{\partial L}{\partial \mathbf{x}}, \quad t \leq t_f \quad (3.6)$$

The optimality condition is computed by taking partial derivative of the Hamiltonian with respect to the control vector

$$\frac{\partial H}{\partial \mathbf{u}} = \frac{\partial f^T}{\partial \mathbf{u}} \lambda + \frac{\partial L}{\partial \mathbf{u}} = 0 \quad (3.7)$$

Boundary conditions are evaluated at both initial and final time. Obviously, $\mathbf{x}(t_0)$ is given at the initial time, and boundary conditions at the final time are as follows:

$$\left. \left(\frac{\partial \phi}{\partial \mathbf{x}} + \frac{\partial \psi^T}{\partial \mathbf{x}} \mathbf{v} - \lambda \right)^T \right|_{t_f} d\mathbf{x}(t_f) + \left. \left(\frac{\partial \phi}{\partial t} + \frac{\partial \psi^T}{\partial t} \mathbf{v} + H \right) \right|_{t_f} dt_f = 0 \quad (3.8)$$

Furthermore, if some control input $\mathbf{u}(t)$ is constrained, a more general stationary condition must be added to strengthen the stationary condition (3.7).

$$H(\mathbf{x}^*, \mathbf{u}^*, \lambda^*, t) \leq H(\mathbf{x}^*, \mathbf{u}^* + \delta \mathbf{u}, \lambda^*, t) \quad \text{For all admissible } \delta \mathbf{u} \quad (3.9)$$

where “*” denotes the optimal solutions. This is also called Pontryagin’s minimum principle.

Since most trajectory optimization problems belong to this category, we will employ optimal control theory to trajectory optimization. As we demonstrated in Chapter 2, position and velocity vectors or orbital elements can be used to express the system dynamic models. Therefore, these two expressions have different forms, and the corresponding Hamiltonian, costate equations, and optimal control also have different

forms. The derivations are given in the subsequent sections using Cartesian coordinates, spherical coordinates, and equinoctial elements.

3.1.1 TPBVP Expressed by Position and Velocity Vectors

The equations of motion of spacecraft can be expressed by position and velocity vectors, which are the same as Eqs. (2.1-2.3). A general performance index is given in terms of the terminal states and final time. The integral term is taken out from the general performance index because in almost all orbit transfer problems, only variables at the terminal time are considered. Therefore, our performance index is:

$$J = \phi[\mathbf{r}(t_f), \mathbf{v}(t_f), t_f] \quad (3.10)$$

According to the calculus of variations, the necessary condition of optimal control problem can be obtained from the Hamiltonian, which is formed as:

$$H = \lambda_r^T \mathbf{v} + \lambda_v^T \left(-\frac{\mu}{r^3} \mathbf{r} + \frac{T}{m} \boldsymbol{\alpha} + \mathbf{f}_p \right) - \lambda_m \frac{T}{gI_{sp}} \quad (3.11)$$

where $\lambda_r^T, \lambda_v^T, \lambda_m$ are Lagrangian multipliers (costates) associated with the states \mathbf{r}, \mathbf{v} , and m , respectively. The optimal thrust vector can be obtained by setting $\frac{\partial H}{\partial \boldsymbol{\alpha}} = 0$ with the constraint $\boldsymbol{\alpha}^T \boldsymbol{\alpha} = 1$. A simple expression for the optimal control is as follows, which only involves the costates associated with velocity vector.

$$\boldsymbol{\alpha}^* = -\frac{\lambda_v}{\|\lambda_v\|} \quad (3.12)$$

Assuming that the thrust magnitude and I_{sp} are not functions of \mathbf{r} and \mathbf{v} , taking partial derivative of the Hamiltonian with respect to the states, the costate equations are readily obtained.

$$\dot{\lambda}_r = -\frac{\partial H}{\partial r} = \left(\lambda_v \frac{\mu}{r^3} - \frac{3\lambda_v^T r}{r^5} r \right) - \frac{\partial f_p}{\partial r} \lambda_v \quad (3.13)$$

$$\dot{\lambda}_v = -\frac{\partial H}{\partial v} = (-\lambda_r) - \frac{\partial f_p}{\partial v} \lambda_v \quad (3.14)$$

$$\dot{\lambda}_m = -\frac{\partial H}{\partial m} = -\|\lambda_v\| \frac{T}{m^2} \quad (3.15)$$

In Eqs. (3.13) and (3.14), the terms in parenthesis pertain to the two-body dynamics, and terms $-\frac{\partial f_p}{\partial r} \lambda_v$ and $-\frac{\partial f_p}{\partial v} \lambda_v$ correspond to the perturbations. The terms pertaining to two-body dynamics could be derived in a specific coordinate system, and the terms related to perturbations depend on the perturbation dynamic models.

For a bounded thrust problem, Pontryagin's minimum principle states the Hamiltonian H must be minimized with respect to all admissible controls at all time. It is obvious that the Hamiltonian is linear in the thrust T . Therefore, the switching function is obtained:

$$H_T = \frac{\partial H}{\partial T} = \lambda_v^T \frac{1}{m} \alpha^* - \lambda_m \frac{1}{gI_{sp}} = -\frac{\|\lambda_v\|}{m} - \frac{\lambda_m}{gI_{sp}} \quad (3.16)$$

$$T = 0 \quad \text{if} \quad H_T > 0$$

$$T = T_{\max} \quad \text{if} \quad H_T < 0$$

$$0 < T < T_{\max} \quad \text{if} \quad H_T = 0$$

A general expression of equality constraints of a mission is as follows:

$$\psi[\mathbf{r}(t_f), \mathbf{v}(t_f)] = 0 \quad (3.17)$$

where t_f can represent the final time of orbit transfers. The function $\psi(\cdot)$ denotes the terminal constraints. The transversality conditions for the costates are:

$$\lambda_r(t_f) = \frac{\partial \phi}{\partial r} \Big|_{t=t_f} + v_r^T \frac{\partial \psi}{\partial r} \Big|_{t=t_f} \quad (3.18)$$

$$\lambda_v(t_f) = \frac{\partial \phi}{\partial v} \Big|_{t=t_f} + v_v^T \frac{\partial \psi}{\partial v} \Big|_{t=t_f} \quad (3.19)$$

$$\lambda_m(t_f) = \frac{\partial \phi}{\partial m} \Big|_{t=t_f} + v_m^T \frac{\partial \psi}{\partial m} \Big|_{t=t_f} \quad (3.20)$$

For the free transfer time, the variable-time condition exists:

$$\left[\frac{\partial \phi}{\partial t} + \left(\frac{\partial \psi}{\partial t} \right)^T v + H \right]_{t=t_f} = 0 \quad (3.21)$$

$$\text{where } v = [v_r \ v_v \ v_m]^T$$

Equation (3.12) is the optimal control steering, which is governed by the costate dynamic Eqs. (3.13-3.15). Equation (3.17) represents constraints for the mission, which must be satisfied for any feasible solution. Equations (3.18-3.21) are the necessary conditions from optimal control theory.

3.1.2 TPBVP in Terms of the Orbital Elements

The equations of motion expressed in classical orbital elements and equinoctial elements are in different forms compared with the governing equations in terms of position and velocity vectors. The general expression in matrix form is:

$$\dot{x} = M \left(\frac{T}{m} \alpha + f_p \right) + D \quad (3.22)$$

$$\dot{m} = -\frac{T}{gI_{sp}} \quad (3.23)$$

where the state variables could be the classical orbital elements, $\mathbf{x} = [a, e, i, \Omega, \omega, M]^T$, or equinoctial elements, $\mathbf{x} = [p, f, g, h, k, L]^T$. \mathbf{M} is a 6×3 matrix that represents the thrust and force perturbation term and \mathbf{D} is a 6×1 vector. The elements of matrices \mathbf{M} and \mathbf{D} for equinoctial elements are:

$$\begin{aligned} M_{11} &= 0, M_{12} = \frac{2p}{w} \sqrt{\frac{p}{\mu}}, M_{13} = 0 \\ M_{21} &= \sqrt{\frac{p}{\mu}} \sin L, M_{22} = \sqrt{\frac{p}{\mu}} [(w+1) \cos L + f] \frac{1}{w}, M_{23} = -\sqrt{\frac{p}{\mu}} [h \sin L - k \cos L] \frac{g}{w} \\ M_{31} &= -\sqrt{\frac{p}{\mu}} \cos L, M_{32} = \sqrt{\frac{p}{\mu}} [(w+1) \sin L + g] \frac{1}{w}, M_{33} = \sqrt{\frac{p}{\mu}} [h \sin L - k \cos L] \frac{f}{w} \\ M_{41} = M_{42} &= 0, M_{43} = \sqrt{\frac{p}{\mu}} \frac{s^2}{2w} \cos L \\ M_{51} = M_{52} &= 0, M_{53} = \sqrt{\frac{p}{\mu}} \frac{s^2}{2w} \sin L \\ M_{61} = M_{62} &= 0, M_{63} = \frac{1}{w} \sqrt{\frac{p}{\mu}} (h \sin L - k \cos L) \\ \mathbf{D} &= [0 \ 0 \ 0 \ 0 \ 0 \ D]^T, \quad D = \sqrt{\mu p} \left(\frac{w}{p} \right)^2 \end{aligned}$$

where \mathbf{D} is a natural kinematics term due to angular rotation (no force).

The Hamiltonian is easily formed as:

$$H = \lambda^T \mathbf{M} \left(\frac{T}{m} \boldsymbol{\alpha} + \mathbf{f}_p \right) + \lambda^T \mathbf{D} - \lambda_m \frac{T}{gI_{sp}} \quad (3.24)$$

The optimal thrust direction unit vector is obtained by setting $\frac{\partial H}{\partial \alpha} = 0$ with the constraint $\alpha^T \alpha = 1$.

$$\alpha^T \alpha = 1.$$

$$\alpha^* = -\frac{[\lambda^T \mathbf{M}]^T}{\|\lambda^T \mathbf{M}\|} \quad (3.25)$$

Taking the partial derivative of the Hamiltonian with respect to the states, the costate equations are determined. We can see that the first bracket term in Eq. (3.26) pertains to the two-body dynamics, and the second bracket term is related to the perturbation.

$$\dot{\lambda} = -\frac{\partial H}{\partial \mathbf{x}} = -\left(\lambda^T \frac{\partial \mathbf{M}}{\partial \mathbf{x}} \frac{T}{m} \alpha + \lambda^T \frac{\partial \mathbf{D}}{\partial \mathbf{x}} \right) - \left(\lambda^T \frac{\partial \mathbf{M}}{\partial \mathbf{x}} \mathbf{f}_p + \lambda^T \mathbf{M} \frac{\partial \mathbf{f}_p}{\partial \mathbf{x}} \right) \quad (3.26)$$

$$\dot{\lambda}_m = -\frac{\partial H}{\partial m} = \lambda^T \mathbf{M} \frac{T}{m^2} \alpha = -\|\lambda^T \mathbf{M}\| \frac{T}{m^2} \quad (3.27)$$

The transversality conditions are derived as follows:

$$\lambda(t_f) = \left. \frac{\partial \phi}{\partial \mathbf{x}} \right|_{t=t_f} + \nu^T \left. \frac{\partial \psi}{\partial \mathbf{x}} \right|_{t=t_f} \quad (3.28)$$

For the free transfer time, the variable-time condition exists:

$$\left[\frac{\partial \phi}{\partial t} + \left(\frac{\partial \psi}{\partial t} \right)^T \nu + H \right]_{t=t_f} = 0 \quad (3.29)$$

Pontryagin's Minimum Principle states the Hamiltonian H must be minimized with respect to all admissible controls at all time. It is obvious that the Hamiltonian is linear in the thrust T . Then the switching function is obtained readily as follows:

$$H_T = \frac{\partial H}{\partial T} = \lambda^T \mathbf{M} \frac{1}{m} \alpha^* - \lambda_m \frac{1}{gI_{sp}} = -\frac{\|\lambda^T \mathbf{M}\|}{m} - \frac{\lambda_m}{gI_{sp}} \quad (3.30)$$

$$T = 0 \quad \text{if} \quad H_T > 0$$

$$T = T_{\max} \quad \text{if} \quad H_T < 0$$

$$0 < T < T_{\max} \quad \text{if} \quad H_T = 0$$

3.2 Hybrid Method - Converting the TPBVP into Parameter

Optimization

Experience shows that it is difficult to solve the TPBVP for low-thrust orbit transfers directly. Solving the optimal control problem via TPBVP solution is also called the indirect method. The initial costates are very sensitive to boundary conditions and switching functions, and typically only a very accurate guess for the initial costates results in a converged solution. Therefore, we have developed other modified methods based on the TPBVP. The hybrid method is introduced in this chapter, which utilizes the optimal control steering from the TPBVP, but also converts the optimal control problem into a parameter optimization problem, which can be solved by NLP.

The reason we would like to convert optimal control problems into parameter optimization problems is twofold. First, the switching function indicates the flight sequence of burn and coast arcs. For a pure TPBVP, we have no a priori knowledge of the engine sequence. Many other researchers show that it is difficult to solve the TPBVP if the switching functions must be satisfied. In order to avoid this disadvantage, the flight sequence is assumed in advance. The trajectory is integrated following the assumed sequence of burn and coast arcs. Therefore, the nominal trajectory might include multiple stages with different dynamic models, and the variables determining each stage are considered to be free design variables in the NLP problem. Another aspect is that the initial costate guesses are sensitive to the transversality conditions and variable-time

condition. These additional constraints from the first-order necessary conditions are not modeled in the parameter optimization problem. Instead, the system performance index is optimized directly by NLP methods, and terminal equality and inequality constraints are evaluated by the NLP problem. Note that the inequality constraints are difficult to add to TPBVP. By converting optimal control problems into parameter optimization problems, the hybrid method can easily accommodate other system parameters and constraints, such as initial power, I_{sp} , for optimal engine configuration. These variables are difficult to handle by the TPBVP formulations whereas they would be design variables in the hybrid method. In summary, the hybrid method utilizes the optimality condition obtained by the TPBVP and costate equations to parameterize the control.

Suppose we employ orbital elements for numerical integration, the statement of parameter optimization for computing optimal trajectories is as follows. Find the optimal parameter vector

$$\mathbf{X} = [\lambda(t_0) \quad \lambda_m(t_0) \quad \beta]$$

that minimizes $J = \phi[\mathbf{x}(t_f), t_f] = \tilde{\phi}(\mathbf{X})$

subject to the dynamic equations

$$\dot{\mathbf{x}} = \mathbf{M} \frac{T}{m} \boldsymbol{\alpha} + \mathbf{D}$$

$$\dot{m} = -\frac{T}{g I_{sp}}$$

$$\dot{\lambda} = -\frac{\partial H}{\partial \mathbf{x}} = -\lambda^T \frac{\partial \mathbf{M}}{\partial \mathbf{x}} \frac{T}{m} \boldsymbol{\alpha} - \lambda^T \frac{\partial \mathbf{D}}{\partial \mathbf{x}}$$

$$\dot{\lambda}_m = -\frac{\partial H}{\partial m} = \lambda^T \mathbf{M} \frac{T}{m^2} \boldsymbol{\alpha} = -\|\lambda^T \mathbf{M}\| \frac{T}{m^2}$$

and subject to constraints

$$\psi[x(t_i), t_i] = 0$$

$$\Omega[x(t_j), t_j] \geq 0$$

$$x(t_0) = x_0 \text{ is given}$$

$\mathbf{X} = [\lambda(t_0) \ \lambda_m(t_0) \ \beta]$ is the design parameter vector for the NLP problem. Vector β is the part of design vector that contains non-control steering variables such as the burn durations, coast angles, and other system parameters (such as power) to be optimized. These discrete parameters are hard to handle in a TPBVP classic formulation. Initial costates $\lambda(t_0)$ are used to parameterize optimal control steering for each burn arc. The costate associated with mass $\lambda_m(t_0)$ is used to modify the Hamiltonian. In total, 7 initial costates need to be guessed for each burn arc; however, guessing a subset of the initial costates is also allowed, since certain costates might not affect the optimal control steering.

In summary, the hybrid method simply uses the costate equations and the optimality conditions from the TPBVP in order to parameter the control structure in an accurate and efficient manner. The NLP method optimizes the performance J subject to the desired equality and inequality constraints. The dynamic equations of states and costates can be integrated from the initial time to the final time explicitly using a fourth-order Runge-Kutta method or other accurate integration methods. The NLP method used in this work is sequential quadratic programming (SQP), which is a standard optimization method [76], and there exist many software versions that can be readily employed. Based on the gradient-search method, SQP iterates on the constraints and performance to adjust

system design variables to obtain better solutions. Although the hybrid method exhibits a larger radius of convergence compared to the classic TBPVP, SQP might fail to find a converged solution due to poor guesses of the initial costates and other free design variables. Trial-and-error is still needed for guessing the initial variables. Moreover, there are some techniques [26, 27] for obtaining reasonable guesses for initial costates.

3.3 Costate Equations for the Hybrid Method

It has been shown that the costate differential equations are needed for the hybrid method. Costate equations can be expressed in a variety of different coordinate systems, and each has different forms.

3.3.1 Derivation of the Costate Equations Expressed by Cartesian Coordinates

It is simple to express the costate equations if Cartesian elements are used. Using Eqs. (3.11), the Hamiltonian is expressed as:

$$H = \lambda_x v_x + \lambda_y v_y + \lambda_z v_z + \lambda_{v_x} \left(-\frac{\mu x}{r^3} + f_{T_x} + f_{p_x} \right) + \lambda_{v_y} \left(-\frac{\mu y}{r^3} + f_{T_y} + f_{p_y} \right) + \lambda_{v_z} \left(-\frac{\mu z}{r^3} + f_{T_z} + f_{p_z} \right) + \lambda_m \left(-\frac{T}{c} \right) \quad (3.31)$$

where $\lambda = [\lambda_x \ \lambda_y \ \lambda_z \ \lambda_{v_x} \ \lambda_{v_y} \ \lambda_{v_z} \ \lambda_m]^T$ is the costate vector with respect to Cartesian elements. Equations (3.32-3.28) are the costate equations expressed by Cartesian coordinate elements.

$$\dot{\lambda}_x = \lambda_{v_x} \frac{\mu}{r^3} - \frac{3\mu\lambda_{v_x} x^2}{r^5} - (\lambda_{v_x} \frac{\partial f_{p_x}}{\partial x} + \lambda_{v_y} \frac{\partial f_{p_y}}{\partial x} + \lambda_{v_z} \frac{\partial f_{p_z}}{\partial x}) \quad (3.32)$$

$$\dot{\lambda}_y = \lambda_{v_y} \frac{\mu}{r^3} - \frac{3\mu\lambda_{v_y} y^2}{r^5} - (\lambda_{v_x} \frac{\partial f_{p_x}}{\partial y} + \lambda_{v_y} \frac{\partial f_{p_y}}{\partial y} + \lambda_{v_z} \frac{\partial f_{p_z}}{\partial y}) \quad (3.33)$$

$$\dot{\lambda}_z = \lambda_{v_z} \frac{\mu}{r^3} - \frac{3\mu\lambda_{v_z} z^2}{r^5} - (\lambda_{v_x} \frac{\partial f_{p_x}}{\partial z} + \lambda_{v_y} \frac{\partial f_{p_y}}{\partial z} + \lambda_{v_z} \frac{\partial f_{p_z}}{\partial z}) \quad (3.34)$$

$$\dot{\lambda}_{v_x} = -\lambda_x - (\lambda_{v_x} \frac{\partial f_{p_x}}{\partial v_x} + \lambda_{v_y} \frac{\partial f_{p_x}}{\partial v_x} + \lambda_{v_z} \frac{\partial f_{p_x}}{\partial v_x}) \quad (3.35)$$

$$\dot{\lambda}_{v_y} = -\lambda_y - (\lambda_{v_x} \frac{\partial f_{p_y}}{\partial v_y} + \lambda_{v_y} \frac{\partial f_{p_y}}{\partial v_y} + \lambda_{v_z} \frac{\partial f_{p_y}}{\partial v_y}) \quad (3.36)$$

$$\dot{\lambda}_{v_z} = -\lambda_z - (\lambda_{v_x} \frac{\partial f_{p_z}}{\partial v_z} + \lambda_{v_y} \frac{\partial f_{p_z}}{\partial v_z} + \lambda_{v_z} \frac{\partial f_{p_z}}{\partial v_z}) \quad (3.37)$$

$$\dot{\lambda}_m = -\frac{\partial H}{\partial m} = -T/m^2(\sqrt{\lambda_{v_x}^2 + \lambda_{v_y}^2 + \lambda_{v_z}^2}) \quad (3.38)$$

where

$$r = \sqrt{x^2 + y^2 + z^2} \quad (3.39)$$

3.3.2 Derivation of the Costate Equations Expressed by Spherical Coordinates

The Hamiltonian in terms of spherical coordinate elements is

$$\begin{aligned} H = & \lambda_r v_r + \lambda_\theta \frac{v_\theta}{r^2 \cos\phi} + \lambda_\phi \frac{v_\phi}{r^2} + \lambda_{v_r} \left(\frac{v_\theta^2}{r} + \frac{v_\phi^2}{r} - \frac{\mu}{r^2} + f_{T_r} + f_{p_r} \right) \\ & + \lambda_{v_\theta} \left(-\frac{v_r v_\theta}{r} + \frac{v_\theta v_\phi}{r} \tan\phi + f_{T_\theta} + f_{p_\theta} \right) \\ & + \lambda_{v_\phi} \left(-\frac{v_r v_\phi}{r} - \frac{v_\theta v_\phi^2}{r} \tan\phi + f_{T_\phi} + f_{p_\phi} \right) + \lambda_m \left(-\frac{T}{c} \right) \end{aligned} \quad (3.40)$$

where $\lambda = [\lambda_r, \lambda_\theta, \lambda_\phi, \lambda_{v_r}, \lambda_{v_\theta}, \lambda_{v_\phi}, \lambda_m]^T$ is the costate vector with respect to spherical elements. The costate differential equations are

$$\begin{aligned}\dot{\lambda}_r = -\frac{\partial H}{\partial r} &= \lambda_\theta \frac{v_\theta}{r^2 \cos \phi} + \lambda_\phi \frac{v_\phi}{r^2} + \lambda_{v_r} \left(\frac{v_\theta^2}{r^2} + \frac{v_\phi^2}{r^2} - \frac{2\mu}{r^3} \right) \\ &\quad + \lambda_{v_\theta} \left(\frac{-v_r v_\theta}{r^2} + \frac{v_\theta v_\phi}{r^2} \tan \phi \right) + \lambda_{v_\phi} \left(\frac{-v_r v_\phi}{r^2} - \frac{v_\theta^2}{r^2} \tan \phi \right) \\ &\quad - \left(\lambda_{v_r} \frac{\partial f_{p_r}}{\partial r} + \lambda_{v_\theta} \frac{\partial f_{p_\theta}}{\partial r} + \lambda_{v_\phi} \frac{\partial f_{p_\phi}}{\partial r} \right)\end{aligned}\tag{3.41}$$

$$\dot{\lambda}_\theta = -\frac{\partial H}{\partial \theta} = -\left(\lambda_{v_r} \frac{\partial f_{p_r}}{\partial \theta} + \lambda_{v_\theta} \frac{\partial f_{p_\theta}}{\partial \theta} + \lambda_{v_\phi} \frac{\partial f_{p_\phi}}{\partial \theta} \right)\tag{3.42}$$

$$\begin{aligned}\dot{\lambda}_\phi = -\frac{\partial H}{\partial \phi} &= -\lambda_\theta \frac{v_\theta \sin \phi}{r \cos^2 \phi} + \lambda_{v_\theta} \left(\frac{-v_\phi v_\theta}{r} - \frac{v_\theta v_\phi}{r^2} \tan^2 \phi \right) + \lambda_{v_\phi} \left(\frac{v_\theta^2}{r^2} + \frac{v_\theta^2}{r^2} \tan \phi \right) \\ &\quad - \left(\lambda_{v_r} \frac{\partial f_{p_r}}{\partial \phi} + \lambda_{v_\theta} \frac{\partial f_{p_\theta}}{\partial \phi} + \lambda_{v_\phi} \frac{\partial f_{p_\phi}}{\partial \phi} \right)\end{aligned}\tag{3.43}$$

$$\dot{\lambda}_{v_r} = -\frac{\partial H}{\partial v_r} = -\lambda_r + \lambda_{v_\theta} \frac{v_\theta}{r} + \lambda_{v_\phi} \frac{v_\phi}{r} - \left(\lambda_{v_r} \frac{\partial f_{p_r}}{\partial v_r} + \lambda_{v_\theta} \frac{\partial f_{p_\theta}}{\partial v_r} + \lambda_{v_\phi} \frac{\partial f_{p_\phi}}{\partial v_r} \right)\tag{3.44}$$

$$\begin{aligned}\dot{\lambda}_{v_\theta} = -\frac{\partial H}{\partial v_\theta} &= -\lambda_\theta \frac{1}{r \cos \phi} - \lambda_{v_r} \frac{2v_\theta}{r} + \lambda_{v_\theta} \left(\frac{v_r}{r} - \frac{v_\phi}{r} \tan \phi \right) + \lambda_{v_\phi} \frac{2v_\theta}{r} \tan \phi \\ &\quad - \left(\lambda_{v_r} \frac{\partial f_{p_r}}{\partial v_\theta} + \lambda_{v_\theta} \frac{\partial f_{p_\theta}}{\partial v_\theta} + \lambda_{v_\phi} \frac{\partial f_{p_\phi}}{\partial v_\theta} \right)\end{aligned}\tag{3.45}$$

$$\begin{aligned}\dot{\lambda}_{v_\phi} = -\frac{\partial H}{\partial v_\phi} &= -\lambda_\phi \frac{1}{r} - \lambda_{v_r} \frac{2v_\phi}{r} - \lambda_{v_\theta} \frac{v_\theta}{r} \tan \phi + \lambda_{v_\phi} \frac{v_r}{r} \tan \phi \\ &\quad - \left(\lambda_{v_r} \frac{\partial f_{p_r}}{\partial v_\phi} + \lambda_{v_\theta} \frac{\partial f_{p_\theta}}{\partial v_\phi} + \lambda_{v_\phi} \frac{\partial f_{p_\phi}}{\partial v_\phi} \right)\end{aligned}\tag{3.46}$$

$$\dot{\lambda}_m = -\frac{\partial H}{\partial m} = \frac{T}{m^2} \left(\sqrt{\lambda_{v_r}^2 + \lambda_{v_\theta}^2 + \lambda_{v_\phi}^2} \right)\tag{3.47}$$

3.3.3 Derivation of the Costate Equations Expressed by Equinoctial Elements

Define equinoctial elements as

$$\mathbf{x} = [p, f, g, h, k, L]^T\tag{3.48}$$

The Hamiltonian is formed as:

$$H = \lambda^T \mathbf{M} \left[\frac{T}{m} \alpha + \mathbf{f}_p \right] + \lambda^T \mathbf{D} - \lambda_m \frac{T}{gI_{sp}} \quad (3.49)$$

Taking partial derivative of the Hamiltonian with respect to the states, costate equations are:

$$\dot{\lambda} = -\frac{\partial H}{\partial \mathbf{x}} = -\left(\lambda^T \frac{\partial \mathbf{M}}{\partial \mathbf{x}} \frac{T}{m} \alpha + \lambda^T \frac{\partial \mathbf{D}}{\partial \mathbf{x}} \right) - \left(\lambda^T \frac{\partial \mathbf{M}}{\partial \mathbf{x}} \mathbf{f}_p + \lambda^T \mathbf{M} \frac{\partial \mathbf{f}_p}{\partial \mathbf{x}} \right) \quad (3.50)$$

The costate equations in terms of the equinoctial elements are

$$\dot{\lambda}_p = -\frac{\partial H}{\partial p} = -\left(\lambda^T \frac{\partial \mathbf{M}}{\partial p} \frac{T}{m} \alpha + \lambda^T \frac{\partial \mathbf{D}}{\partial p} \right) - \left(\lambda^T \frac{\partial \mathbf{M}}{\partial p} \mathbf{f}_p + \lambda^T \mathbf{M} \frac{\partial \mathbf{f}_p}{\partial p} \right) \quad (3.51)$$

$$\dot{\lambda}_f = -\frac{\partial H}{\partial f} = -\left(\lambda^T \frac{\partial \mathbf{M}}{\partial f} \frac{T}{m} \alpha + \lambda^T \frac{\partial \mathbf{D}}{\partial f} \right) - \left(\lambda^T \frac{\partial \mathbf{M}}{\partial f} \mathbf{f}_p + \lambda^T \mathbf{M} \frac{\partial \mathbf{f}_p}{\partial f} \right) \quad (3.52)$$

$$\dot{\lambda}_g = -\frac{\partial H}{\partial g} = -\left(\lambda^T \frac{\partial \mathbf{M}}{\partial g} \frac{T}{m} \alpha + \lambda^T \frac{\partial \mathbf{D}}{\partial g} \right) - \left(\lambda^T \frac{\partial \mathbf{M}}{\partial g} \mathbf{f}_p + \lambda^T \mathbf{M} \frac{\partial \mathbf{f}_p}{\partial g} \right) \quad (3.53)$$

$$\dot{\lambda}_h = -\frac{\partial H}{\partial h} = -\left(\lambda^T \frac{\partial \mathbf{M}}{\partial h} \frac{T}{m} \alpha + \lambda^T \frac{\partial \mathbf{D}}{\partial h} \right) - \left(\lambda^T \frac{\partial \mathbf{M}}{\partial h} \mathbf{f}_p + \lambda^T \mathbf{M} \frac{\partial \mathbf{f}_p}{\partial h} \right) \quad (3.54)$$

$$\dot{\lambda}_k = -\frac{\partial H}{\partial k} = -\left(\lambda^T \frac{\partial \mathbf{M}}{\partial k} \frac{T}{m} \alpha + \lambda^T \frac{\partial \mathbf{D}}{\partial k} \right) - \left(\lambda^T \frac{\partial \mathbf{M}}{\partial k} \mathbf{f}_p + \lambda^T \mathbf{M} \frac{\partial \mathbf{f}_p}{\partial k} \right) \quad (3.55)$$

$$\dot{\lambda}_L = -\frac{\partial H}{\partial L} = -\left(\lambda^T \frac{\partial \mathbf{M}}{\partial L} \frac{T}{m} \alpha + \lambda^T \frac{\partial \mathbf{D}}{\partial L} \right) - \left(\lambda^T \frac{\partial \mathbf{M}}{\partial L} \mathbf{f}_p + \lambda^T \mathbf{M} \frac{\partial \mathbf{f}_p}{\partial L} \right) \quad (3.56)$$

The costate associated with mass is

$$\dot{\lambda}_m = -\frac{\partial H}{\partial m} = \lambda^T \mathbf{M} \frac{T}{m^2} \alpha^* = -\|\lambda^T \mathbf{M}\| \frac{T}{m^2} \quad (3.57)$$

The partial derivatives of matrices \mathbf{M} and \mathbf{D} with respect to equinoctial elements are presented in Appendix I.

3.4 Perturbation Formulation in Costate Equations

We can see that the costate equations (3.13) and (3.14) are composed of two parts, the term corresponding to thrust acceleration, and the term corresponding to perturbation accelerations. In Cartesian and spherical frames, the formulation of perturbation in costate equations is

$$\dot{\hat{\lambda}}_r = -\frac{\partial \mathbf{f}_p}{\partial r} \lambda_v \quad (3.58)$$

$$\dot{\hat{\lambda}}_v = -\frac{\partial \mathbf{f}_p}{\partial v} \lambda_v \quad (3.59)$$

If the state equations are expressed by orbital elements and equinoctial elements,

$$\dot{\hat{\lambda}} = -\left(\lambda^T \frac{\partial \mathbf{M}}{\partial \mathbf{x}} \mathbf{f}_p + \lambda^T \mathbf{M} \frac{\partial \mathbf{f}_p}{\partial \mathbf{x}} \right) \quad (3.60)$$

Any analytical expression of perturbation accelerations in RTN frame can be included in the costate equations if perturbation accelerations are functions of the state vector. If perturbations have a minor effect on optimal trajectories, their formulations in the costate equations can be neglected, and the optimal control dictated by costates without regarding the perturbations is most likely a good approximation of the optimal solutions. Of course, if we incorporate the perturbation in the costate equations, the solution is also accurate with respect to the “real dynamics”. For example, the gravity forces of other planets in an interplanetary mission are difficult to model in the costate if the accurate planetary ephemeris is employed because the gravity forces do not explicitly depend on the states themselves. By incorporating perturbative gravity forces in the state equations

and neglecting their formulations in the costate equation, the hybrid method can provide near-optimal solutions.

3.5 Extended Multiple-Shooting Techniques for the Hybrid Method

The optimal control using the hybrid method is governed by the costate equations, and the initial values of the respective costates are converted into SQP design variables. The advantage of the hybrid method is the relatively smaller number of SQP variables in NLP problem and smoother control steering profiles compared with other direct methods to be discussed in Chapter 4. Using the hybrid method only requires guesses of the initial costates for each burn arc, and we can guess a total of seven costates or a small number because some costates might not affect the control. However, it is known that using the collocation method or direct parameterization of the controls would yield a large number of SQP design variables for the optimization method because these methods need many discrete nodal values for states and controls. For example, solving any continuous-burn transfer requires at most seven costates to dictate the optimal control steering, while using other direct approaches would require a large number of discrete nodes of states or controls depending on the time duration of the burn arc. Another advantage of using hybrid method is the high accuracy of the solution. This is because the control steering is dictated by the true optimal expression derived from the TPBVP, and the costate equations are precisely integrated.

On the other hand, no matter what methods are used, simply guessing the unknown SQP design variables might not produce a converged solution. For the hybrid method, although it exhibits improved convergence characteristics compared with the TPBVP solution, simple initial guesses may not result in the converged solutions. The

initial costates still exhibit sensitivity to terminal constraints. However, the sensitivity can be alleviated by employing multiple shooting techniques, or parallel shooting. The parallel shooting method is introduced and employed by Sheel and Conway [38] to solve planar low-thrust orbit transfers using direct shooting methods. In this work, the multiple-shooting techniques are introduced, which are found to be more robust and flexible when combined with the hybrid method. This strategy includes multiple shooting with state nodes, multiple shooting with costate nodes and multiple shooting with both state and costate nodes.

3.5.1 Multiple Shooting with State Nodes

Time histories of the states can be divided into several segments. In this work, discrete state nodes are inserted during a powered arc integration process. For each burn phase, the initial time is denoted as t_0 and the terminal time t_f . The state nodes can be coordinate elements themselves, or classical orbital elements. A total of n nodes are inserted between t_0 and t_f , and the intermediate time points are denoted by t_1, t_2, \dots, t_n .

Figure 3.1 presents multiple shooting for two states. Three state nodes at time points t_1, t_2, t_3 for a (semi-major axis) and e (eccentricity) are equally inserted between t_0 and t_f . The values of these nodes must be equal to the values of a and e at time nodes t_1, t_2, t_3 obtained by integrating the governing equations from t_0 to t_1 , t_1 to t_2 and t_2 to t_3 , respectively. Therefore six additional equality constraints are generated if multiple shooting with three state nodes is used. At each time point, the coordinate states are transformed into classical orbital elements. Have recording the differences between computed values from numerical integration and guessed values, a (semi-major axis) and

e (eccentricity) are replaced by the guessed values and transformed to coordinate states, after with the integration keeps going to next node with the same procedures applied. Of course, the nodal values could be coordinate elements so that the transformation to and from classical orbital elements is not necessary. However, guessing the state nodes as classical orbital elements may be more intuitive.

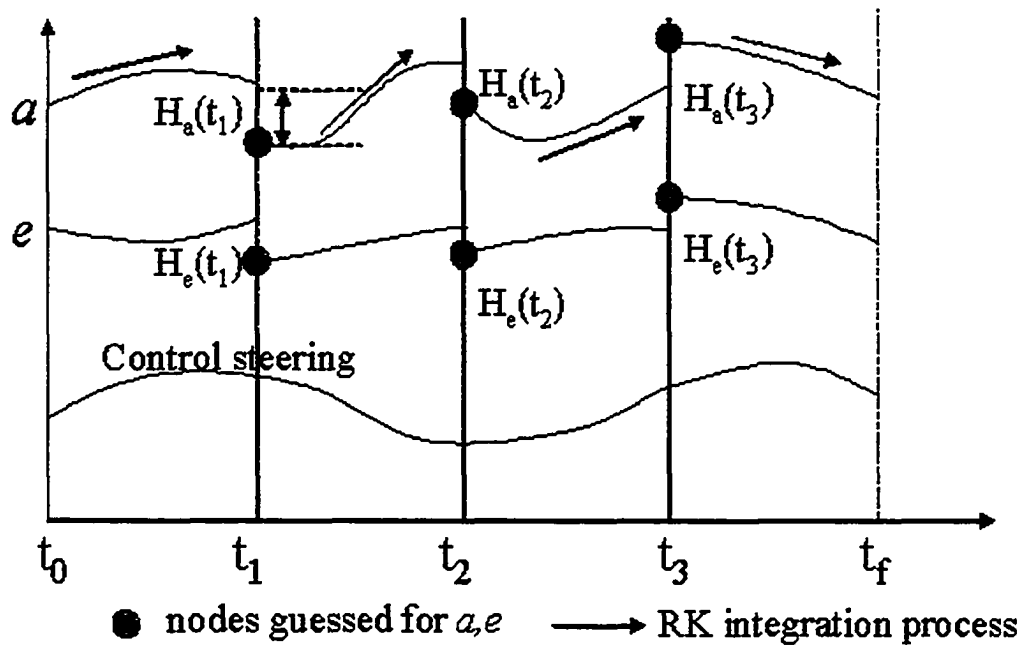


Figure 3.1 Illustration of multiple shooting with state nodes

We can readily summarize the multiple-shooting technique with state nodes. For a single burn arc, suppose n state nodes are inserted

$$\tilde{\mathbf{x}}(t_1), \tilde{\mathbf{x}}(t_2), \dots, \tilde{\mathbf{x}}(t_n) \quad (3.61)$$

The corresponding values of $\tilde{\mathbf{x}}(t_1), \tilde{\mathbf{x}}(t_2), \dots, \tilde{\mathbf{x}}(t_n)$ determined by numerically integrating the equations of motion are

$$\tilde{\mathbf{x}}'(t_1), \tilde{\mathbf{x}}'(t_2), \dots, \tilde{\mathbf{x}}'(t_n) \quad (3.62)$$

Then the equality constraints at each node point could be written as

$$H_{ms}(t_i) = \tilde{\mathbf{x}}'(t_i) - \tilde{\mathbf{x}}(t_i), \quad i = 1, 2, \dots, n \quad (3.63)$$

In NLP problem, $\tilde{\mathbf{x}}(t_1), \tilde{\mathbf{x}}(t_2), \dots, \tilde{\mathbf{x}}(t_n)$ are additional SQP free design variables to be optimized, and $H_{ms}(t_i)$ (such as $H_a(t_i)$ and $H_e(t_i)$ in Fig. 3.1) are formulated as additional SQP equality constraints. For a single burn arc, if p states or orbital elements are inserted, additional $p \times n$ SQP design variables and $p \times n$ equality constraints are created. The state nodes are not necessarily equally spaced between t_0 and t_f , however, equally spaced nodes are easier to implement and give good performance for most orbit transfer problems.

3.5.2 Multiple Shooting with Costate Nodes

Following the same idea as multiple shooting with state nodes, the costate time histories could also be divided into segments. The same type of additional constraints is generated. The costates are related to the control expression in the hybrid method. We can easily summarize the multiple-shooting technique with costate nodes. For a single burn arc, suppose m costate nodes are inserted

$$\tilde{\lambda}(t_1), \tilde{\lambda}(t_2), \dots, \tilde{\lambda}(t_m) \quad (3.64)$$

The corresponding values of $\tilde{\lambda}(t_1), \tilde{\lambda}(t_2), \dots, \tilde{\lambda}(t_m)$ determined by numerically integrating the equations of motion are

$$\tilde{\lambda}'(t_1), \tilde{\lambda}'(t_2), \dots, \tilde{\lambda}'(t_m) \quad (3.65)$$

Then the additional equality constraints are

$$H_{mcs}(t_i) = \tilde{\lambda}'(t_i) - \tilde{\lambda}(t_i), \quad i = 1, 2, \dots, m \quad (3.66)$$

For a single burn arc, if q costates are inserted, then a total of $q \times m$ extra SQP design variables and $q \times m$ extra equality constraints are created. Guessing the costate nodes may be intuitive. We may be able to use other methods to generate the approximate costate time histories, which provide good initial guess for costate nodes.

3.5.3 Multiple Shooting with both State and Costate Nodes

Extending the idea in last two sections, both state and costate nodes could be inserted during the burn process. However, the numbers of states and costates nodes are not necessarily the same. Actually, state and costate nodes are dealt with separately.

$$\tilde{\mathbf{x}}(t_1), \tilde{\mathbf{x}}(t_2), \dots, \tilde{\mathbf{x}}(t_n) \quad \tilde{\lambda}(t_1), \tilde{\lambda}(t_2), \dots, \tilde{\lambda}(t_m) \quad (3.67)$$

The corresponding values of $\tilde{\mathbf{x}}(t_1), \tilde{\mathbf{x}}(t_2), \dots, \tilde{\mathbf{x}}(t_n)$ and $\tilde{\lambda}(t_1), \tilde{\lambda}(t_2), \dots, \tilde{\lambda}(t_m)$ determined by numerically integrating the equations of motion are

$$\tilde{\mathbf{x}}'(t_1), \tilde{\mathbf{x}}'(t_2), \dots, \tilde{\mathbf{x}}'(t_n) \quad \tilde{\lambda}'(t_1), \tilde{\lambda}'(t_2), \dots, \tilde{\lambda}'(t_m) \quad (3.68)$$

Then the equality constraints are

$$H_{ms}(t_i) = \tilde{\mathbf{x}}'(t_i) - \tilde{\mathbf{x}}(t_i), \quad i = 1, 2, \dots, n \quad (3.69)$$

$$H_{mc}(t_i) = \tilde{\lambda}'(t_i) - \tilde{\lambda}(t_i), \quad i = 1, 2, \dots, n \quad (3.70)$$

For a single burn arc, if p states or orbital elements and q costates are inserted into the burn duration, there are a total of $p \times n + q \times m$ extra SQP design variables and $p \times n + q \times m$ extra equality constraints.

For certain optimization problems, using multiple-shooting technique with state nodes or costate nodes may result in improved convergence. The advantage of separating the use of state and costate nodes is that a smaller number of design variables are

optimized and the computation burden can be reduced. Additionally, we can choose a subset of state and costate nodes to reduce the number of design variables. The feature of extended multiple-shooting techniques can be summarized:

1. Multiple shooting is used together with the integration of state and costate equation so that the accurate solutions are obtained.
2. We can use the nodal values in classic orbit elements for state nodes, which is intuitive. We can also use the nodal values in coordinate elements.
3. We can use state and costate multiple shooting method separately or together.
4. We can guess part of state and costate histories, or all of them.
5. The nodes could be equally spaced or unequally spaced.
6. The numbers of state nodes and costate nodes are not necessarily the same due to their respective sensitivities.

3.6 Summary of Hybrid Method

By converting the TPBVP into a parameter optimization problem, the hybrid method could be employed to solve general optimal orbit transfer problems. The optimal control steering is analytically expressed in three frames and the costate equations are numerically integrated. Thus the optimal control obtained is differentiable and exhibits smooth profiles. Besides optimizing the control steering, the hybrid method can optimize system parameters, which are of great importance in mission and vehicle system design. Compared with the TPBVP solution, the hybrid method has a larger domain of convergence. Furthermore, with the aid of extended multiple shooting techniques, the convergence performance is further improved. Examples of orbit transfer problems with the hybrid method will be presented in subsequent chapters. Prior research has shown that

application of the hybrid method has been somewhat limited. Interplanetary orbit transfers will be successfully solved by the hybrid method and results will be presented in later chapters.

CHAPTER 4 DIRECT-SHOOTING METHOD

Instead of using the optimality conditions derived from the TPBVP, direct methods directly parameterize the time histories of states and controls. The drawback of the TBPVP (and hybrid method) is the necessity of deriving the costate differential equations and the sensitivity of the initial costate guesses. Direct methods only require integrating state equations.

Kluever [31] demonstrated an explicit state integration and control steering parameterization method to solve interplanetary orbit transfer problems. The collocation method [32-35] is a direct method that uses implicit numerical integration. Discrete nodes are used to determine both states and controls, and the states are approximated by different curve-fitting methods. Tang and Conway [34] used this method to solve an Earth-Mars transfer problem. Herman and Conway [36] developed a high-order collocation method. The differential inclusion technique is another direct method studied by Seywald [39], which is suitable for problems where the control steering can be expressed explicitly by states and the time-rate of states. These direct methods all convert optimal control problems into parameter optimization problems. A summary was discussed by David [44], who presented four cases of direct methods. In this chapter, only the direct-shooting method is presented, which explicitly integrates the state equations and parameterizes the control steering by NLP method. In addition, multiple-shooting techniques can be used with the direct-shooting method. A comparison will be

made between the direct-shooting method and collocation methods. These two methods are all capable of solving general, complex orbital transfer problems.

4.1 Direct-Shooting Method

The method used by Kluever in Ref. [31] is the direct-shooting method, and it is discussed in this section. Only the time histories of the control steering for burn phases are represented by a finite number of discrete nodes. The nodal values of the control steering are converted into the design variables of the parameter optimization problem. An illustration of the direct-shooting method is shown in Fig. 4.1.

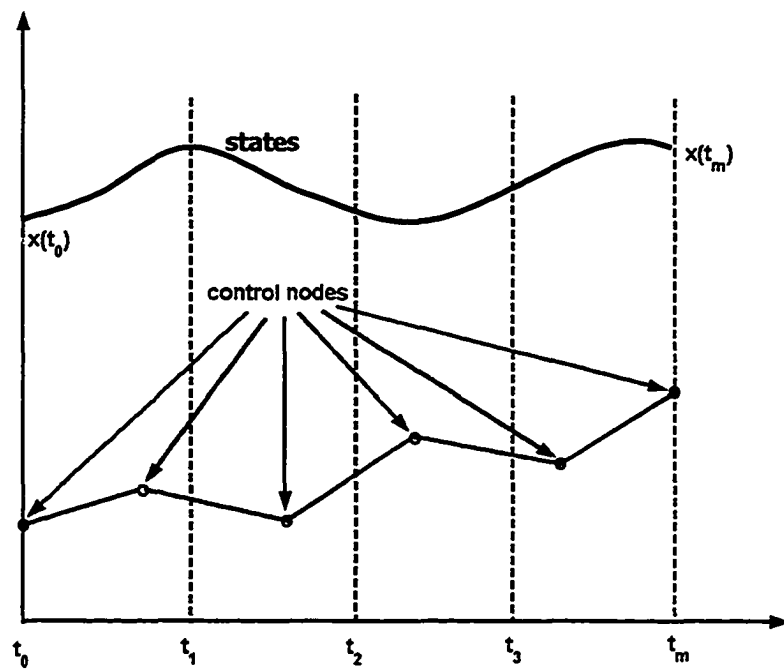


Figure 4.1 Illustration of the direct-shooting method

In Fig. 4.1, the continuous time histories of control steering can be approximated by using linear or spline interpolation. The NLP technique, SQP, adjusts the values of

nodes and therefore the entire time histories of the control steering in order to obtain the optimal performance. The flight sequence (such as burn, coast, or gravity assist) is also specified a priori. This strategy is the same as that in the hybrid method, which avoids considering the switching function.

Let vector \mathbf{X} denote the design variables of the NLP parameter optimization problem.

$$\mathbf{X} = [\alpha(t_0) \alpha(t_1) \dots \alpha(t_i) \dots \alpha(t_m) \beta]^T \quad (4.1)$$

where t_m is the terminal time for a burn arc. There are a total of $m+1$ nodes for the control steering profile where $\alpha(t_0)$ is the control steering at initial time and $\alpha(t_m)$ at final time for a single burn arc. The vector β contains the other necessary design parameters, such as burn time durations, coast angles, flyby variables, and engine system parameters.

The nodal values of $\alpha(t_i)$ can be three direction cosines, or two angles (pitch and yaw). The trajectory is integrated using the explicit fourth-order Runge-Kutta method from the initial time to the final time for each burn arc. The time histories of states and control steering are also saved to evaluate any interior point constraint. Compared with the hybrid method, only state equations are integrated in the direct-shooting method. The NLP problem is stated as follows.

Find optimal $\mathbf{X} = [\alpha(t_0) \alpha(t_1) \dots \alpha(t_i) \dots \alpha(t_m) \beta]^T$ that minimizes

$$J = \phi[\mathbf{x}(t_f), t_f] = \tilde{\phi}(\mathbf{X})$$

subject to state equations $\dot{\mathbf{x}} = f(\mathbf{x}, \mathbf{u}, t)$

 equality constraints $\psi[\mathbf{x}(t_i), t_i] = 0$

inequality constraints $\Omega[\mathbf{x}(t_j), t_j] \geq 0$

with initial condition $\mathbf{x}(t_0) = \mathbf{x}_0$ is given

There are several advantages of the direct-shooting method. The design variables are more intuitive since the initial control steering profile is to be guessed. Many optimization problems converge easily even with a simple initial guess, such as pure tangential steering. Direct shooting methods exhibit a larger convergence domain compared with TPBVP methods. Since only a finite number of nodes are used to represent the entire control time history, the number of nodes could be increased to obtain better performance. We can use a small number of nodes to quickly obtain converged solutions, and then increase the number of nodes to improve the performance.

Of course, there are some drawbacks for using the direct-shooting method. The number of design variables required for accuracy becomes larger if the burn duration becomes longer. The accuracy of the direct-shooting method is only as good as the interpolation method used with a finite number of nodes. Using additional nodes to improve performance will increase the computation burden. Furthermore, the control steering profile may not be smooth due to linear interpolation, and the direct-shooting method often converges to a local minimum.

4.2 Direct Multiple Shooting Method

In the direct-shooting method, the trajectory is integrated from the initial time to the final time. If the initial guess for the control steering is not close to the optimal solution, we may still have difficulties obtaining a converged solution. One idea to ease this difficulty is to divide the burn arc trajectories into several segments. Scheel and

Conway [38] employed a parallel-shooting method to solve two very-low-thrust planar orbit transfer problems. Tangential thrust or thrust along the velocity vector can raise the orbital altitude while keeping the eccentricity low. That is to say, tangential thrust or thrust along the velocity vector is a good guess for very-low-thrust circle-circle planar transfers. Optimal control is easily obtained using NLP method by casting control nodes as the SQP design variables. Due to long transfer time for very-low-thrust transfers, either direct-shooting method or parallel-shooting method will require a larger number of design variables. Conversely, for higher-thrust orbit transfers, a simple tangential-thrust guess for control steering may not provide a desirable trajectory. For these cases, the multiple-shooting techniques are useful to improve convergence characteristics. Wirthman et al. [77] implemented a parallel-shooting method on a parallel computer. Hull [44] also described this idea in a summary of parameter optimization method, but no numerical examples were presented.

The multiple-shooting techniques in this chapter differ from prior work in some aspects. The numbers of state and control nodes are not necessarily to be the same, and they are dealt separately. Not all state nodes need to be guessed as SQP design variables, since some states do not interest us. Another improvement is that the state nodes can be a subset of the classical orbital elements so that they are more intuitive to guess.

Using the same technique for the hybrid method in Chapter 3, state nodes could be inserted during the burn process. Each segment in each burn can be integrated from the initial time to the final time of this segment to get the final states, which are used to compare with guessed states. The integrated terminal states and guessed states of each segment are forced to be equal by the NLP optimization method. Of course, the nodal

values of states could be coordinate elements themselves or classic orbital elements (see Fig. 4.2) that are more intuitive to be guessed.

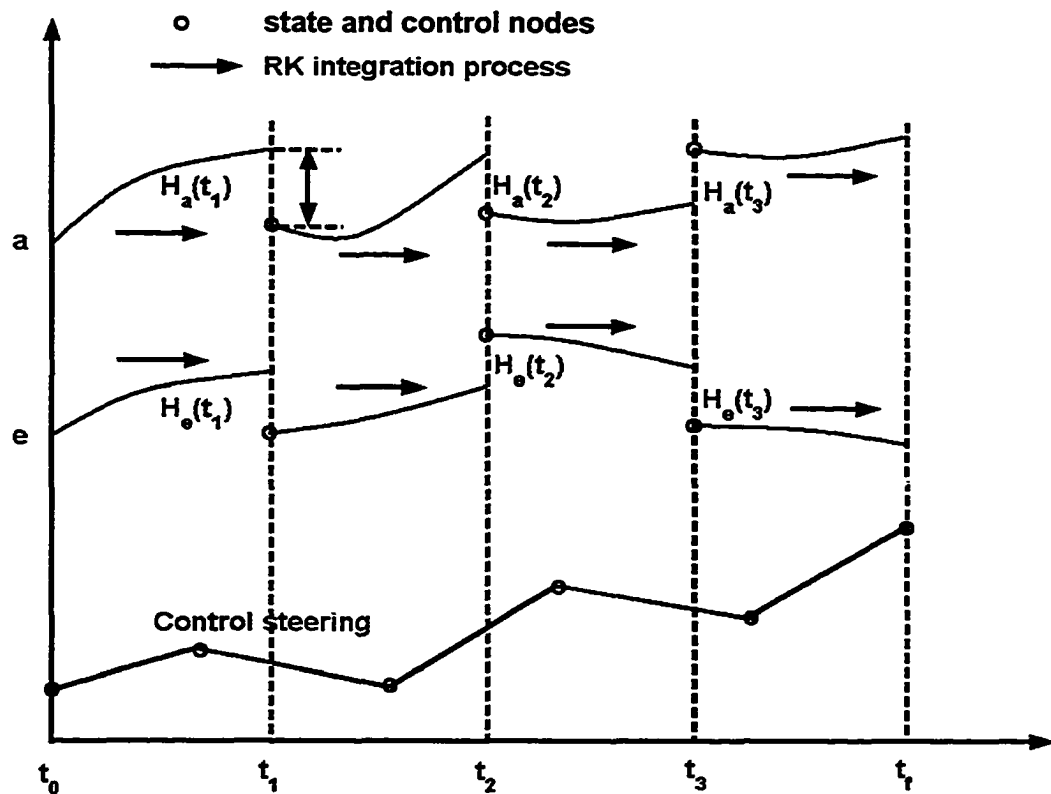


Figure 4.2 Illustration of direct multiple shooting

The direct multiple shooting method can be readily summarized. For a single burn process, suppose n state nodes are inserted at $t_1, t_2 \dots t_f$.

$$\tilde{\mathbf{x}}(t_1), \tilde{\mathbf{x}}(t_2), \dots, \tilde{\mathbf{x}}(t_n) \quad (4.2)$$

The corresponding values of $\tilde{\mathbf{x}}(t_1), \tilde{\mathbf{x}}(t_2), \dots, \tilde{\mathbf{x}}(t_n)$ determined by numerically integrating the equations of motion are

$$\tilde{\mathbf{x}}'(t_1), \tilde{\mathbf{x}}'(t_2), \dots, \tilde{\mathbf{x}}'(t_n) \quad (4.3)$$

Then the equality constraints at each node point could be written as

$$H_{ms}(t_i) = \tilde{x}'(t_i) - \tilde{x}(t_i), \quad i = 1, 2, \dots, n \quad (4.4)$$

In the NLP problem, $\tilde{x}(t_1), \tilde{x}(t_2), \dots, \tilde{x}(t_n)$ are additional free SQP design variables to be optimized, and $H_{ms}(t_i)$ (such as $H_a(t_i)$ and $H_e(t_i)$ in Fig. 4.2) are formulated as additional equality constraints. For a single burn arc, if p states or classic orbital elements are inserted, an extra total $p \times n$ SQP design variables and $p \times n$ equality constraints are created. The state nodes are not necessarily equally spaced between t_0 and t_f ; however, equally spaced nodes are easier to implement and give good performance for most orbital transfer problems. Let \mathbf{X} to be parameter vector in the NLP problem.

$$\mathbf{X} = [\alpha(t'_0) \alpha(t'_1) \dots \alpha(t'_i) \dots \alpha(t'_n) \tilde{x}(t_1) \tilde{x}(t_2) \dots \tilde{x}(t_i) \dots \tilde{x}(t_n) \beta] \quad (4.5)$$

The trajectory is integrated using the explicit fourth-order Runge-Kutta method for each segment $[t_k, t_{k+1}]$. The superscript “ $'$ ” means that the time points of nodes for the control steering and the states are not necessarily to be the same. The NLP problem is stated as follows: Find optimal design variables

$$\mathbf{X} = [\alpha(t'_0) \alpha(t'_1) \dots \alpha(t'_i) \dots \alpha(t'_n) \tilde{x}(t_1) \tilde{x}(t_2) \dots \tilde{x}(t_i) \dots \tilde{x}(t_n) \beta]$$

that minimizes $J = \phi[\mathbf{x}(t_f), t_f] = \tilde{\phi}(\mathbf{X})$

subject to state equations $\dot{\mathbf{x}} = f(\mathbf{x}, \mathbf{u}, t)$

system terminal equality constraints $\psi[\mathbf{x}(t_f), t_f] = 0$

equality constraints from multiple shooting $H_{ms}(t_i) = \tilde{x}'(t_i) - \tilde{x}(t_i)$

system inequality constraints $\Omega[\mathbf{x}(t_k), t_k] \geq 0$

with initial condition $\mathbf{x}(t_0) = \mathbf{x}_0$ is given

It is obvious that the direct multiple shooting method increases the number of design variables since the state nodes also need to be guessed. If only one segment is specified for each burn arc, it is actually the direct-shooting method. These two methods could be used to solve a variety of orbit transfer problems.

4.3 Collocation Method – Compared with the Direct-Shooting Method

The trajectories using the direct-shooting method are integrated explicitly. The collocation method uses implicit integration methods on the dynamic equation of motion. Considering the numerical integration, the approximation of $\Delta x(t_k) = x(t_{k+1}) - x(t_k)$ could be computed by Eq. (4.6), which is called rectangular rule.

$$\int_{t_k}^{t_{k+1}} dx(t) = x(t_{k+1}) - x(t_k) = \int_{t_k}^{t_{k+1}} f(x, t) dt \approx \Delta t_k f(x_k, t_k) \quad (4.6)$$

In the rectangular rule, the value of states $x(t_{k+1})$ is uniquely computed by states at t_k . This property is the same as that in the Runge-Kutta method where the future state is only depends on previous states. There are other approximations of $\Delta x(t_k)$ using both states at t_k and t_{k+1} . Equation (4.7) is called second-order trapezoid rule and Equation (4.8) is called fourth-order Simpson rule.

$$\int_{t_k}^{t_{k+1}} dx(t) \approx \frac{\Delta t_k}{2} [f(x_k, t_k) + f(x_{k+1}, t_{k+1})] \quad (4.7)$$

$$\int_{t_k}^{t_{k+1}} dx(t) \approx \frac{\Delta t_k}{6} [f(x_k, t_k) + 4f(x_m, t_m) + f(x_{k+1}, t_{k+1})] \quad (4.8)$$

where t_m, x_m are located between t_k, x_k and t_{k+1}, x_{k+1} . Usually the middle point between t_k, x_k and t_{k+1}, x_{k+1} are used. Figure 4.3 is an illustration of Simpson's rule.

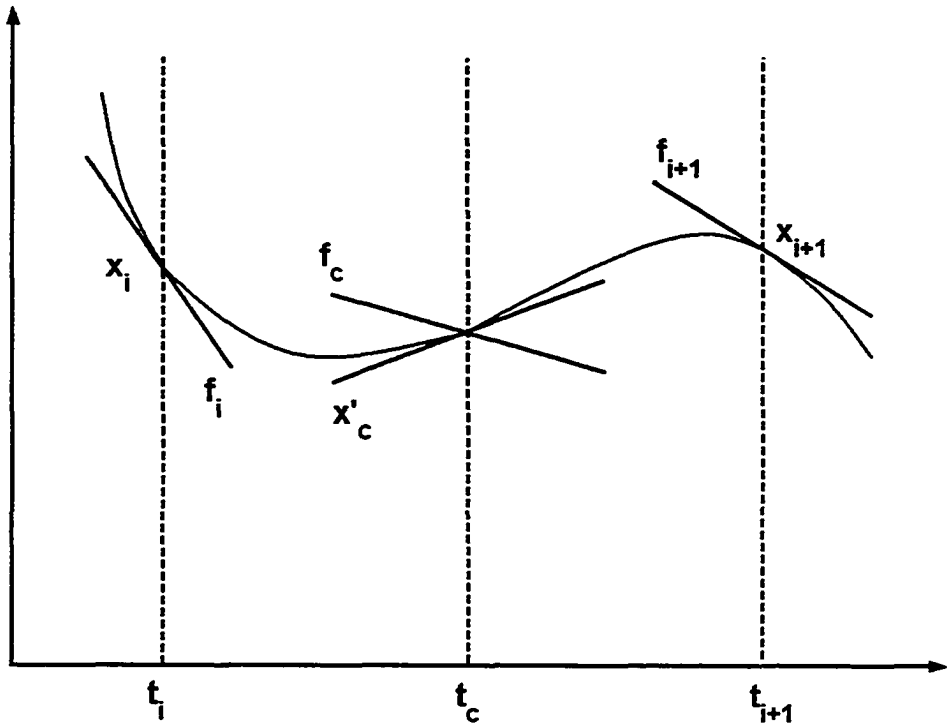


Figure 4.3 Illustration of Simpson's rule

The error $E(t_k) = x(t_{k+1}) - \bar{x}(t_{k+1})$ is expected to be as small as possible, where $\bar{x}(t_{k+1})$ is the accurate values of the states at t_{k+1} . This idea could be employed into orbit transfer problems. We can guess the states and control steering at each nodal time point. For each interval from t_k and t_{k+1} , by the Simpson rule, the $x(t_{k+1})$ can be computed by Eq. (4.7) and $\bar{x}(t_{k+1})$ is considered the state we have guessed. By constraining $E(t_k)$ to zero, we can get the entire trajectory. The high-order collocation method was described by Conway [36], which produces more accurate solution with the same number of segments. Then the design variables could be denoted as follows.

$$\mathbf{X} = [\alpha(t_0) \alpha(t_1) \dots \alpha(t_i) \dots \alpha(t_n) \mathbf{x}(t_1) \mathbf{x}(t_2) \dots \mathbf{x}(t_j) \dots \mathbf{x}(t_n) \beta]^T \quad (4.9)$$

Except the mission constraints, additional equality constraints are produced by the collocation method, which is denoted as:

$$\mathbf{C}(\mathbf{X}) = \begin{bmatrix} E(t_1) \\ E(t_2) \\ \dots \\ E(t_{n-1}) \end{bmatrix} = 0 \quad (4.10)$$

The optimal control problem could be stated as follows using nonlinear programming.

Find optimal design variables

$\mathbf{X} = [\alpha(t_0) \alpha(t_1) \dots \alpha(t_i) \dots \alpha(t_n) \mathbf{x}(t_1) \mathbf{x}(t_2) \dots \mathbf{x}(t_j) \dots \mathbf{x}(t_n) \beta]^T$ that minimizes

$$J = \phi[\mathbf{x}(t_f), t_f] = \phi'(\mathbf{X})$$

subject to the state equations $\dot{\mathbf{x}} = f(\mathbf{x}, \mathbf{u}, t)$

equality constraints $\psi[\mathbf{x}(t_i), t_i] = 0$

inequality constraints $\Omega[\mathbf{x}(t_j), t_j] \geq 0$

collocation defects $\mathbf{C}(\mathbf{X}) = 0$

with initial condition $\mathbf{x}(t_0) = \mathbf{x}_0$ is given

Based on the description of the collocation method, it is obvious that the collocation method uses the idea of the implicit numerical integration, unlike the direct multiple shooting method that integrates forward. In the collocation method, the time intervals for states and control steering must be the same. The direct multiple-shooting method is not limited to this requirement. Collocation methods do not need explicit integration methods, such as a Runge-Kutta method, but the method does need to employ some curve-fitting methods for computing states at t_c , either in lower order or higher order. Usually collocation methods yield a larger number of design variables since nodes

for both states and control steering need to be guessed even for simple problems. For a complex orbit transfer problem, collocation methods must be run on high performance computers due to the extremely large number of free variables. Also, the accuracy of solutions obtained by the collocation method still needs to be verified by explicit numerical integration. Meanwhile, the solutions obtained by the direct-shooting method are considered more accurate since explicit integration is utilized in the optimization process.

CHAPTER 5 OPTIMAL ORBIT TRANSFERS USING HYBRID AND DIRECT-SHOOTING METHODS

As discussed in the Chapter 1, trajectory optimization methods fall into two main categories: indirect and direct approaches. The hybrid method presented in Chapter 3 and the direct-shooting method presented in Chapter 4 are all considered direct approaches in this dissertation since parameter optimization using NLP methods is employed. Based on hybrid and direct-shooting methods, two sets of FORTRAN programs were developed by the author. The purpose of this chapter is to present optimal orbit transfers obtained by these two methods. DTOM (Direct Trajectory Optimization Methods) is a FORTRAN program that computes low-thrust optimal interplanetary orbit transfers. EOTD (Earth-Orbit Trajectory via Direct methods) is a FORTRAN program that computes low-thrust optimal Earth-orbit transfers. The primary features of these two packages are described as follows:

Easy to use: Several input files are required to run DTOM/EOTD, in which many flags can be setup by the user. Since DTOM/EOTD converts the trajectory optimization problems into NLP problems, a user can set a variety of performance indices, equality, and inequality constraints. Users also have the option to build new input files, or use a restart solution from a previous run. This feature is helpful for solving difficult problems.

Hybrid method and direct-shooting method: Two optimization approaches are used in DTOM/EOTD - the hybrid and the direct-shooting methods described in Chapters 3 and 4. The hybrid method requires the user to guess the initial costates for each burn

phase and the direct-shooting method requires the user to guess the nodal values of the control steering.

Multiple-shooting techniques: The strategy of multiple shooting is also included in DTOM/EOTD and it is extended to multiple shooting with state nodes, costate nodes, or both state and costate nodes. Furthermore, the multiple-shooting techniques can be employed in both the hybrid and direct-shooting methods. Convergence characteristics are improved by the multiple-shooting techniques.

Three coordinate frames: Three coordinate frames are used in DTOM/EOTD (Cartesian frame, spherical frame, and equinoctial elements). All appropriate state and costate equations are derived and coded. The user can choose a coordinate frame to run the optimization, and then compare the results obtained with solutions obtained with another frame. For certain orbit transfer problems, using a specific coordinate frame might be helpful.

Numerical integration methods: In DTOM/EOTD, the state equations and costate equations are numerically integrated forward using a fourth-order Runge-Kutta method with fixed step size or variable step size. For variable step size, the user can set the error tolerance to obtain more accurate solutions.

Nonlinear programming: The sequential quadratic programming is utilized in DTOM/EOTD.

JPL ephemeris: DTOM uses the JPL planetary ephemeris and DASTCOM (Database of ASTeroids and COMets) database for asteroids and comets. The user also can set arbitrary bodes according to specific format, or a set of static terminal constraints.

Multiple dynamic stages: Complex trajectories might have several flight phases such as power arcs, coast arcs, or gravity assists. In DTOM/EOTD, users can assume the flight sequence a priori. The parameters for each stage are converted into SQP design variables to be optimized.

5.1 Optimal Earth-Orbit Transfers

In this section, it is intended to show the application of the hybrid and direct-shooting methods to solve the Earth-orbit transfers. The first example is low-Earth-orbit (LEO) to Geostationary-Earth-orbit (GEO) transfer with initial thrust-to-weight ratio of 2×10^{-2} . The I_{sp} is 3800 seconds, and it is constant during the transfer. The initial mass is 6100 kg. The initial condition and terminal constraints are shown in Table 5.1. The flight sequence is assumed as a coast arc followed by a burn arc. This assumption means that the location (longitude angle) of the burn start is to be optimized since the plane change exists. The final mass is to be maximized. There are no perturbations included in this case.

Table 5.1 Initial condition and terminal constraints for LEO-GEO orbit transfers

Orbital elements	Initial condition	Terminal constraints
a (Re)	1.047	6.6107
e	10^{-6}	10^{-6}
i (deg)	28.5	0.0
Ω (deg)	0.0	n/a
ω (deg)	0.0	n/a
θ (deg)	0.0	n/a

For the hybrid method, equations of motion are integrated in spherical coordinate so that five initial costates ($\lambda_r, \lambda_\phi, \lambda_{\nu_r}, \lambda_{\nu_\phi}, \lambda_{\nu_\theta}$) are guessed to dictate the optimal control. The costate λ_θ is set constant at zero and it is not SQP design variable because $\dot{\lambda}_\theta = 0$.

For the direct-shooting method, 21 nodes are used to parameterize the control steering for each of the direction cosines, or RTN components. Also, the coast angle and the burn time duration are SQP design variables for both methods. The optimization results are summarized in Table 5.2. The total transfer time includes duration of the coast. The optimal trajectories and time histories of control steering, semi-major axis, eccentricity and inclination are shown in Figs. 5.1-5.5.

Table 5.2 Solutions for optimal single-burn LEO-GEO trajectories (hybrid method, direct-shooting method)

Optimal solutions	Hybrid, spherical	Direct, equinoctial
Transfer time (hours)	9.0707	9.0745
Burn duration (hours)	8.8037	8.8063
Final mass (kg)	5082.4706	5082.1818
Longitude (deg)	63.6964	64.0046

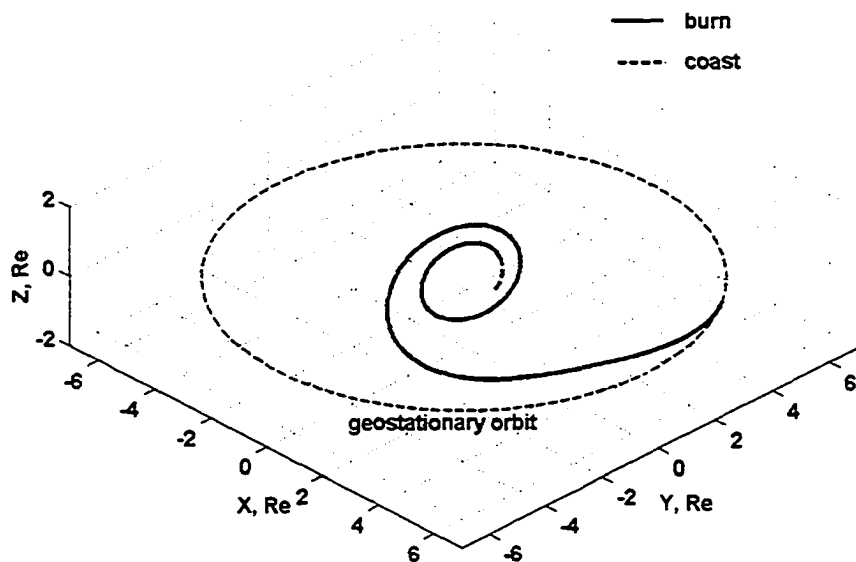


Figure 5.1 Optimal single-burn LEO-GEO trajectories (hybrid method, direct-shooting method)

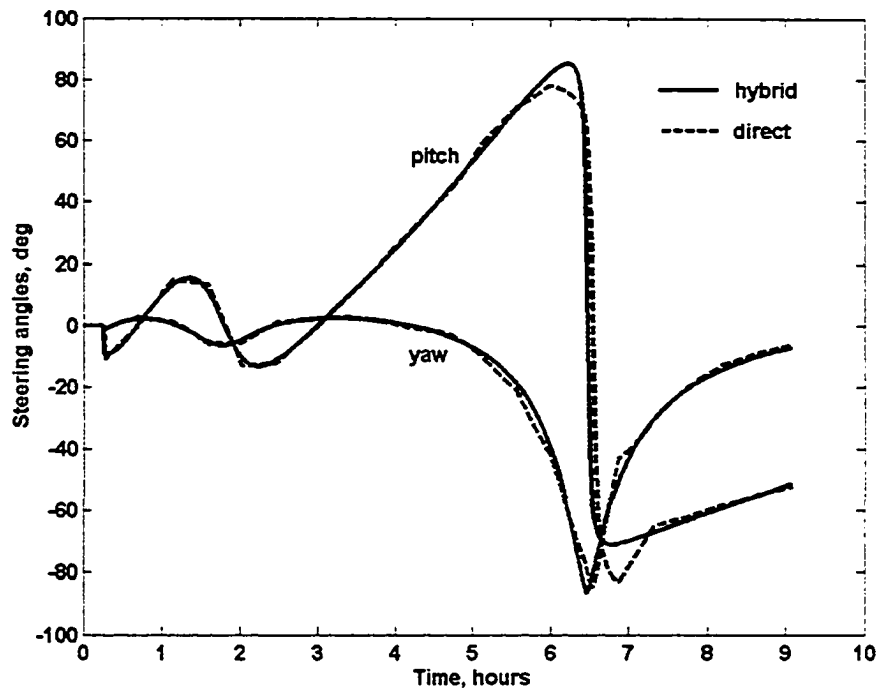


Figure 5.2 Time histories of control steering for optimal single-burn LEO-GEO trajectories (hybrid method, direct-shooting method)

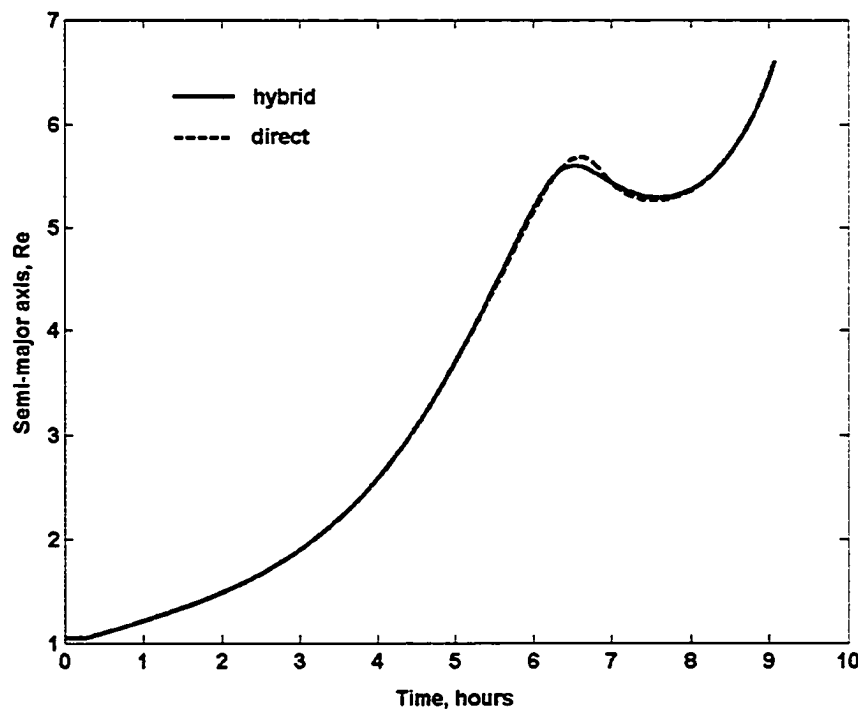


Figure 5.3 Time histories of semi-major axis for optimal single-burn LEO-GEO trajectories (hybrid method, direct-shooting method)

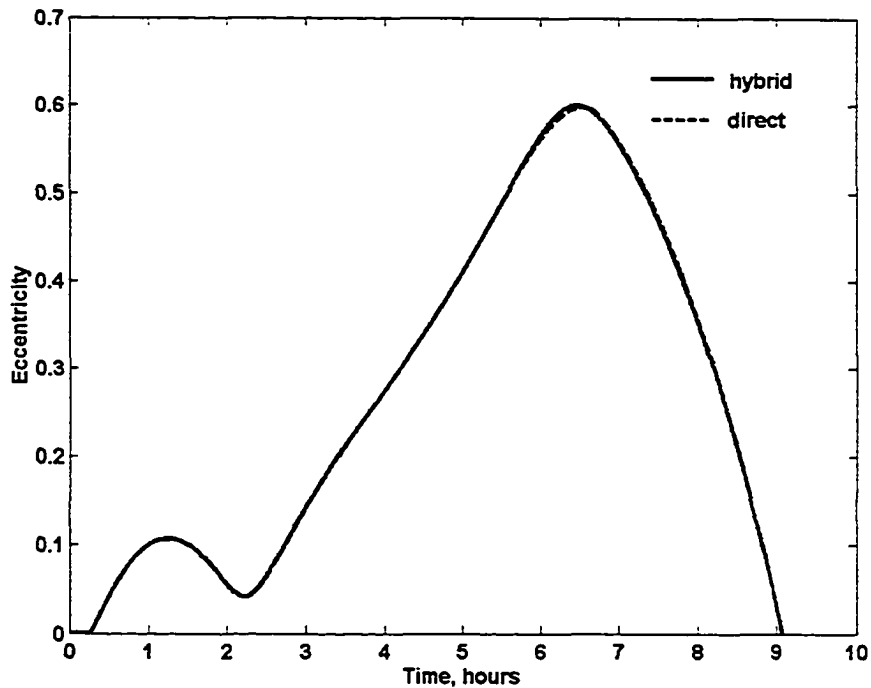


Figure 5.4 Time histories of eccentricity for optimal single-burn LEO-GEO trajectories (hybrid method, direct-shooting method)

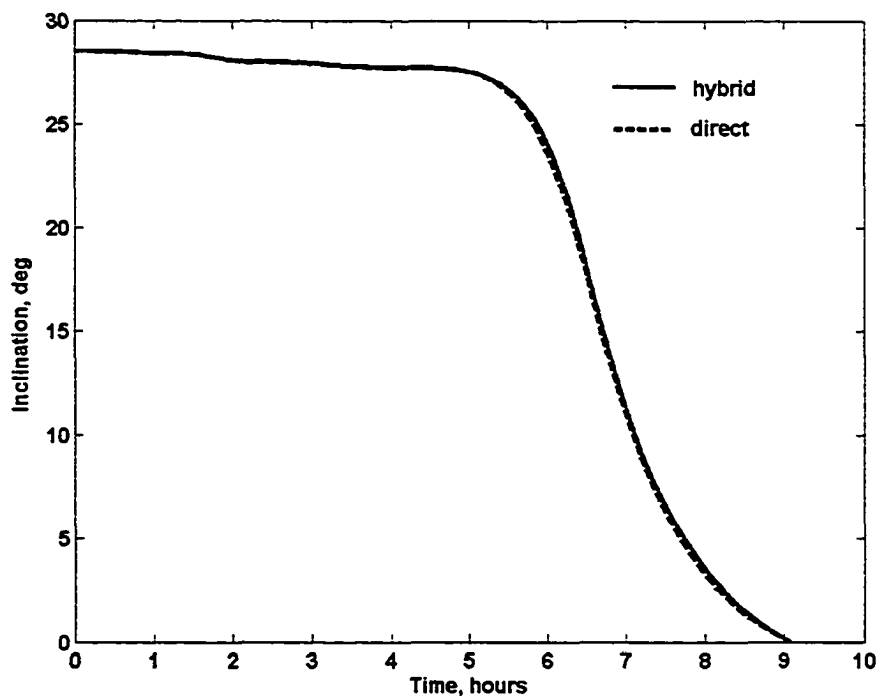


Figure 5.5 Time histories of inclination for optimal single-burn LEO-GEO trajectories (hybrid method, direct-shooting method)

The solutions obtained by the hybrid and direct-shooting methods are very close. To be expected, the hybrid method exhibits slightly better performance. Figure 5.1 presents the optimal trajectories (essentially identical) obtained by the two methods. And the first coast arcs are included since the optimal burn start point is desired to change the orbit plane more efficiently. Figure 5.2 indicates that the control steering obtained by the hybrid method has a smoother profile than that obtained by the direct-shooting method. The reason is that the optimal control is governed by costate differential equations for the hybrid method and is parameterized as discrete nodal values for the direct-shooting method. The accuracy of solutions computed by the direct-shooting method is only as good as interpolation between the discrete nodes. The time histories of orbital elements (see Fig. 5.3, 5.4 and 5.5) obtained by the two methods are only slightly different. The semi-major continuously increases during the first six hours, and the eccentricity and inclination decrease to zero within the final three hours.

5.2 Optimal Lower-Thrust Earth-Orbit Transfers

5.2.1 Low-Thrust Orbit Raising Using the Direct-Shooting Method

In this case, the initial thrust-to-weight ratio is set to a lower level of 10^{-3} . Only final semi-major axis and eccentricity are constrained at 4 Earth radii and 10^{-6} , respectively. Due to the lower thrust level, transfer time becomes significantly longer and the transfer trajectory has many revolutions around the Earth. Therefore, the direct-shooting method requires a larger number of nodes for control steering and the numerical integration takes much more time for computation. We selected 201 nodes for the pitch angle with all initial guesses set at zero deg (yaw angle is not employed). Reasonable

transfer times need to be guessed. Equinoctial elements are employed for numerical integration, and the total number of integration steps is 5000. Since J_2 perturbation becomes significant for low-thrust orbit transfers, it is modeled in the equations of motion expressed by equinoctial elements. The initial mass is 5100 kg, and constant I_{sp} is 3800 seconds. The final mass is to be maximized. The optimization results show that the optimal final mass is 4629.6983 kg, and the optimal transfer time is 4.0558 days (97.33 hours). The initial and terminal orbits are shown in Table 5.3. The coast is not included in this case since no plane change exists.

Table 5.3 Initial and terminal orbits for the Earth-orbit transfer with initial thrust-to-weight ratio of 10^{-3} (direct-shooting method)

Orbital elements	Initial orbit	Final orbit
Semi-major axis (Re)	1.047	3.999998
Eccentricity	10^{-7}	$2.5662(10^{-4})$
Inclination (deg)	28.50	28.4840
RAAN (deg)	0.0	353.18
Argument of perigee (deg)	0.0	103.25

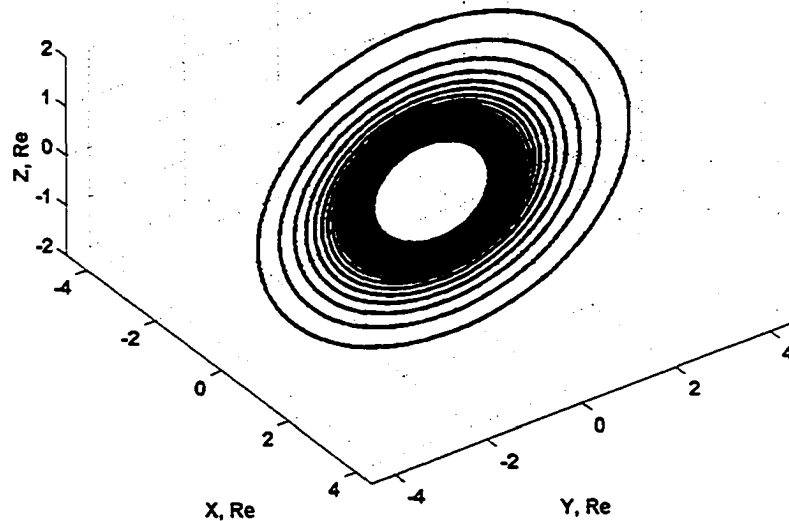


Figure 5.6 Optimal Earth-orbit trajectory with initial thrust-to-weight ratio of 10^{-3} (direct-shooting method)

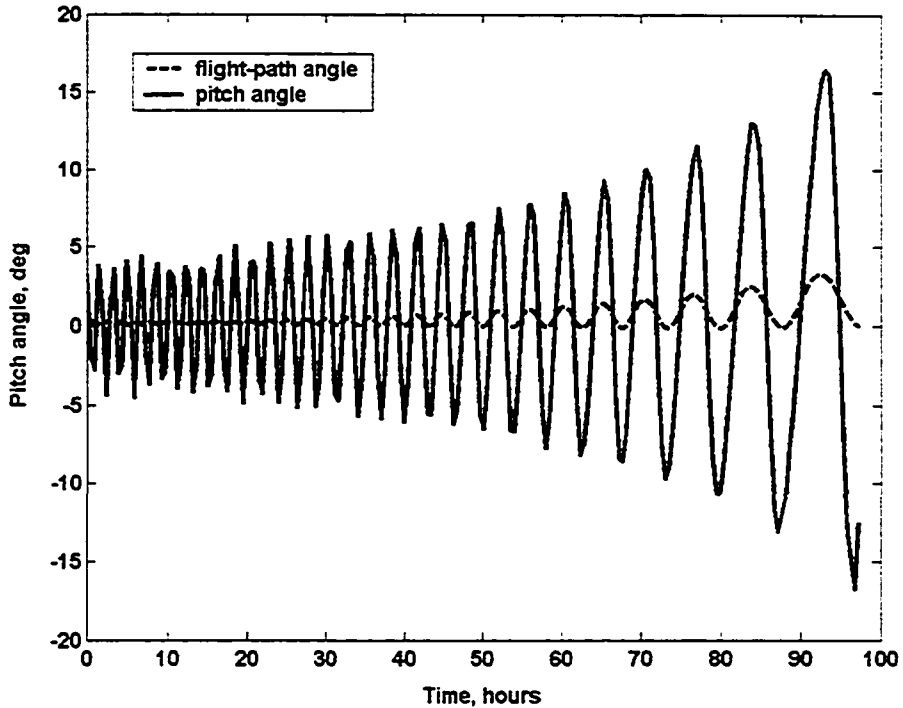


Figure 5.7 Time history of pitch angle for optimal Earth-orbit trajectory with initial thrust-to-weight ratio of 10^{-3} (direct-shooting method)

Figure 5.6 presents the optimal transfer trajectory with about 30 revolutions. The pitch angle and flight-path angle are presented in Fig. 5.7. Both of them are in the near-tangential direction, and oscillate about mean values.

The thrust-to-weight ratio level might be much lower than the previous case, such as 10^{-5} or 10^{-6} . The direct-shooting method encounters the difficulty in very-low-thrust orbit transfers. In order to obtain accurate solutions, a large number of control nodes are necessary. The increasing number of integration steps increases the computational time for the optimization method. This is also a drawback of other direct methods. As an example, Tang and Conway [34] used collocation method to solve low-thrust Earth-Mars transfers using 918 variables and 728 constraints. The stated execution time is about 5 hours on a Convex C240. Betts [18] employed direct transcription to solve low-thrust

Earth-Moon transfer using 211,031 variables and 146,285 constraints. In another article by Betts [33], the very-low-thrust trajectory optimization using a direct SQP method employed 416,123 variables and 249,674 constraints. However, for very-low-thrust planar transfer with tangential thrust or thrust along velocity vector, the semi-major axis is continuously raised and the eccentricity remains low. For a circle-circle planar transfer, tangential thrust or thrust along velocity vector may be close to optimal control, SQP could eventually obtain optimal solution after tremendous computation.

5.2.2 Low-Thrust LEO-GEO Orbit Transfer Using the Hybrid Method

The lower-thrust three-dimensional LEO-GEO transfer is solved by hybrid method. The initial thrust weight ratio is also set to 10^{-3} . The initial mass is 6100 kg and constant I_{sp} is 3800 seconds. The numerical integration is implemented in spherical coordinate with 10000 steps. J_2 perturbation is included in both state and costate equations. No coast is allowed during the transfer. The initial orbit and final orbit is given in Table 5.4. The optimization results indicate that the final mass is 5225.2028 kg and transfer time is 151.3766 hours. The trajectory, control and time histories of orbital elements are shown in Figs. 5.8-2.12.

Table 5.4 Initial and terminal orbits for optimal LEO-GEO orbit transfer with initial thrust-to-weight ratio of 10^{-3} (hybrid method)

Orbital elements	Initial orbit	Final orbit
Semi-major axis (Re)	1.047	6.61070000
Eccentricity	10^{-7}	$5.9903(10^{-12})$
Inclination (deg)	28. 5	0.0
RAAN (deg)	0.0	n/a
Argument of perigee (deg)	0.0	n/a

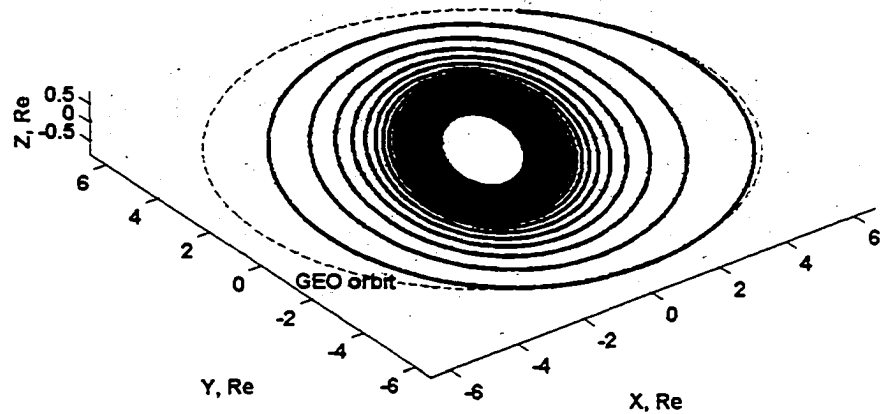


Figure 5.8 Optimal LEO-GEO trajectory with initial thrust-to-weight ratio of 10^{-3} (hybrid method)

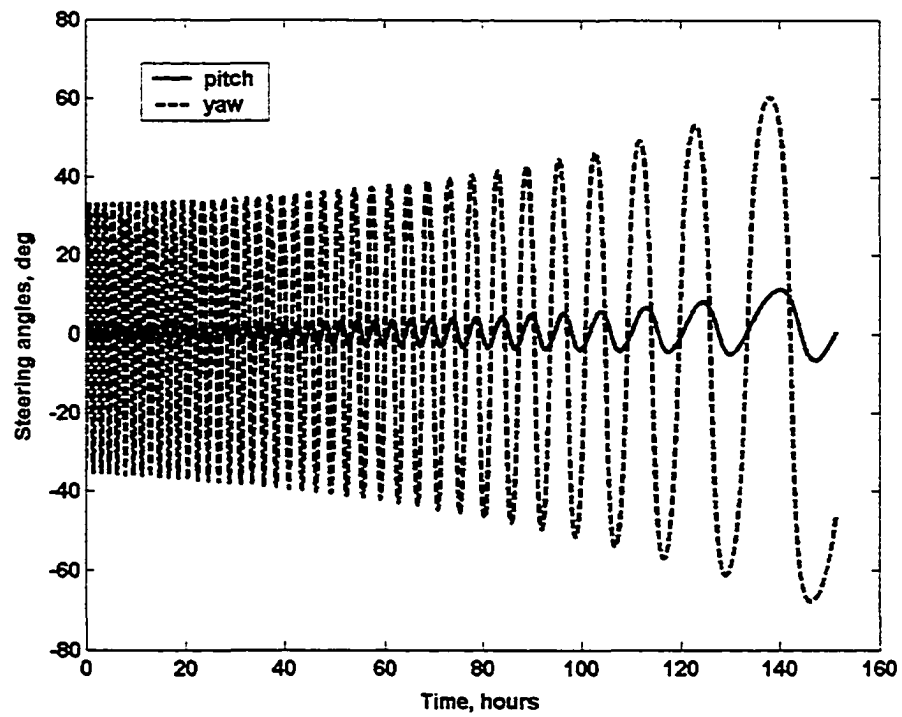


Figure 5.9 Time histories of control steering for optimal LEO-GEO trajectory with initial thrust-to-weight ratio of 10^{-3} (hybrid method)

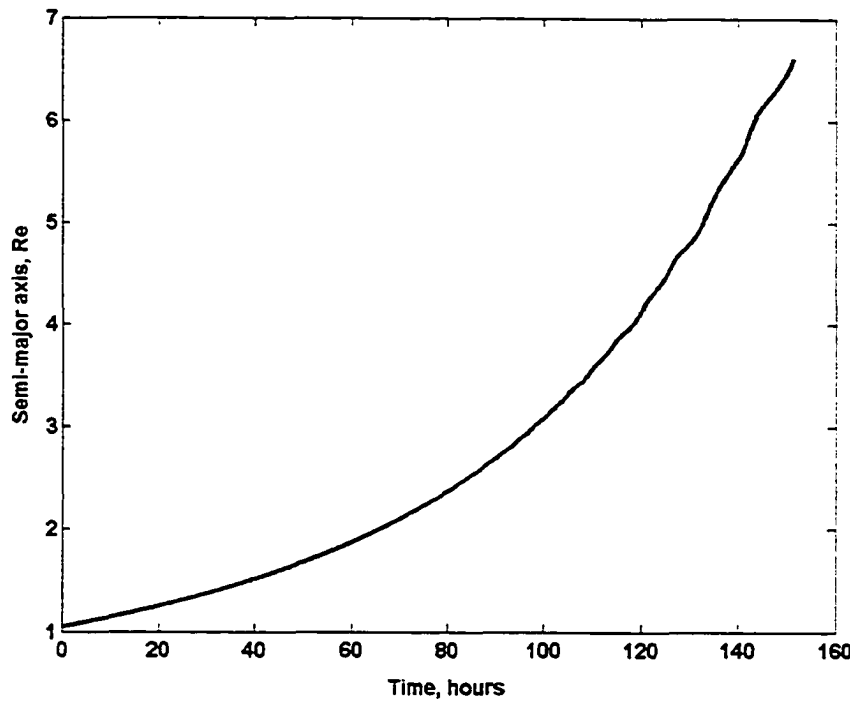


Figure 5.10 Time history of semi-major axis for optimal LEO-GEO trajectory with initial thrust-to-weight ratio of 10^{-3} (hybrid method)

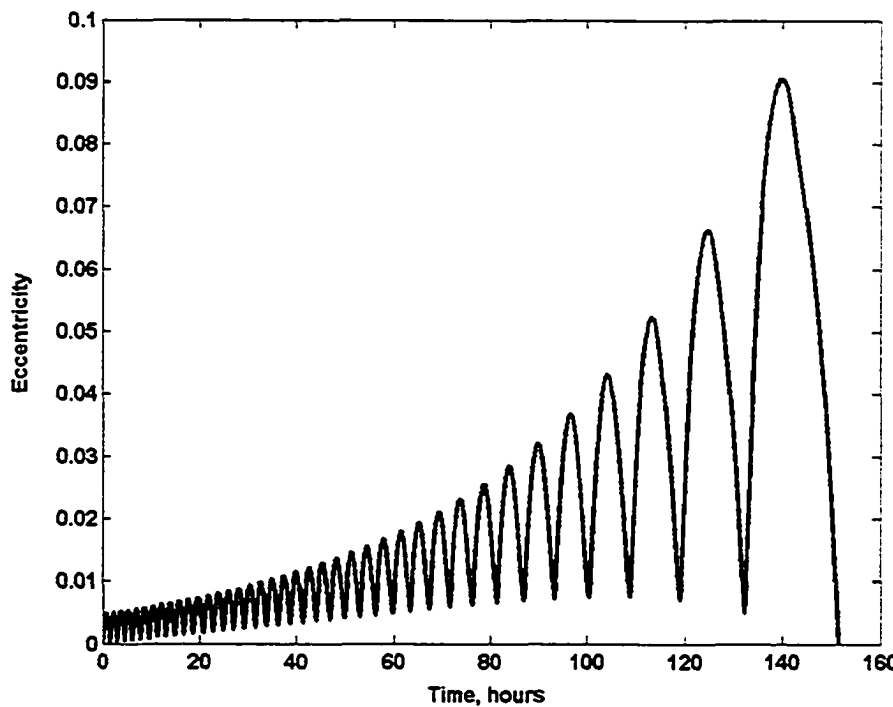


Figure 5.11 Time history of eccentricity for optimal LEO-GEO trajectory with initial thrust-to-weight ratio of 10^{-3} (hybrid method)

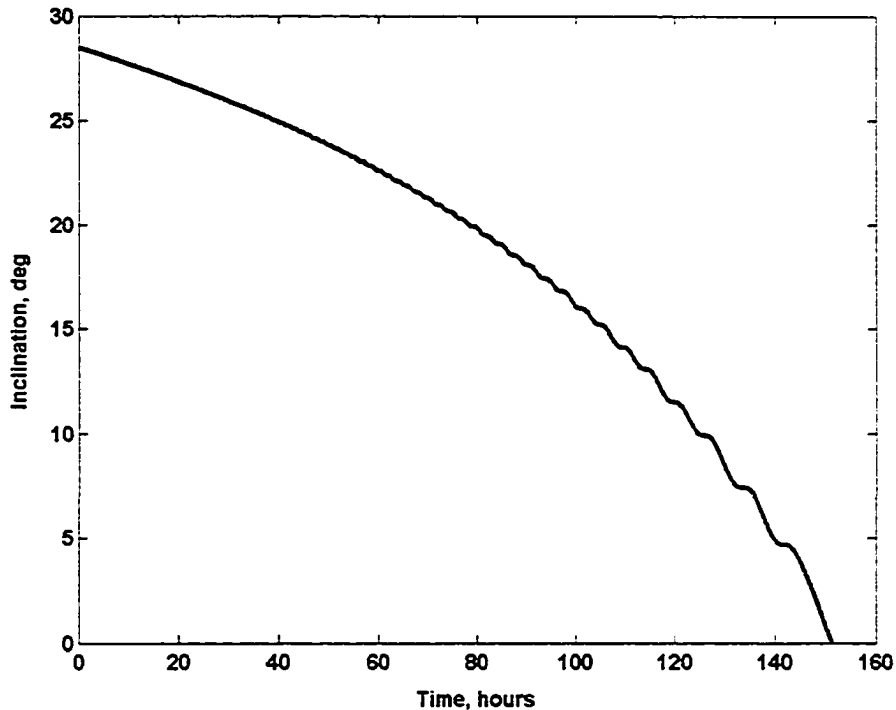


Figure 5.12 Time history of inclination for optimal LEO-GEO trajectory with initial thrust-to-weight ratio of 10^{-3} (hybrid method)

The optimal transfer trajectory (presented in Fig. 5.8) consists of approximate 40 revolutions due to low thrust level. The control steering (pitch and yaw) is presented in Fig. 5.9 where the pitch steering is in near-tangential direction, and the yaw thrust is relatively larger due to the existence of a large plane change. The semi-major axis and inclination (presented in Fig. 5.10 and 5.12) continuously change to the desired target values in a monotonic fashion, while the eccentricity (presented in Fig. 5.11) oscillates about a mean value and deceases to zero at the final phase. This is a significant property for very-low-thrust orbit transfers.

Like the direct-shooting method, the hybrid method has the same problem for solving very-low-thrust orbit transfer problems. The precise numerical integration takes a great deal of computation time. Although the hybrid method only requires (at most) 7

initial costates to dictate the optimal control profile, the initial costates become more difficult to guess for many-revolution transfers. Perturbations also become dominant during transfers and cannot be ignored. However, some time-vary perturbations are hard to analytically derive and include in the costate differential equations. Since the hybrid method employs NLP instead of TBPVP to solve the optimal control problem, the costate equations that involve two-body dynamics only still may be used to achieve a sub-optimal control.

The orbital averaging technique is an alternative approach for computing many-revolution transfers. This technique assumes the orbital elements are constant for a single revolution, which allows large integration steps for the mean rates of change. Orbital averaging is described in Ref. [31] and not presented in this dissertation.

5.3 Optimal Direct Transfers to Mercury, Venus and Mars

In this section, the optimal direct transfers to Mercury, Venus and Mars, are presented. Direct transfers mean that no intermediate gravity assist is employed, and no coast arc allowed. The planet-rendezvous problems are proposed, and the spacecraft is only propelled by low-thrust SEP. For all trajectories, the final mass is to be maximized. The solar array power at 1 astronomic unit (AU), P_0 , is 6.5 kW and the maximum power is also 6.5 kW. The available array power (P) follows inverse-square relation with distance to the sun ($P = P_0/r^2$ where r is in AU). The initial mass is 1200 kg. The constant I_{sp} is 3100 seconds and the thruster efficiency is 0.65. We also assume that position and velocity of spacecraft are the same as those of the Earth at launch date ($C_3 = 0$). This case is intended to compare the use and performance of the hybrid, direct-shooting, and

collocation methods for solving the interplanetary trajectories in different coordinate systems. The optimization results are summarized in Tables 5.5-5.7.

Table 5.5 Optimal solutions of Earth-Mercury trajectories (hybrid method, direct-shooting method)

Solution methods	Launch date	Final mass (kg)	Trip time (days)	No. of SQP variables	No. of SQP constraints
Direct, equinoctial	Feb 3, 2009	620.0449	734.1564	92	6
Direct, cartesian	Feb 3, 2009	620.0819	734.1096	92	6
Direct, spherical	Feb 3, 2009	620.0463	734.1547	92	6
Hybrid, equinoctial	Feb 3, 2009	620.1625	734.0076	8	6
Hybrid, cartesian	Feb 3, 2009	620.1905	733.9721	8	6
Hybrid, spherical	May 11, 2009	622.4134	732.4532	7	6

Table 5.6 Optimal solutions of Earth-Venus trajectories (hybrid method, direct-shooting method)

Solution methods	Launch date	Final mass (kg)	Trip time (days)	No. of SQP variables	No. of SQP constraints
Direct, equinoctial	Oct 23, 2008	985.7550	271.2094	35	6
Direct, cartesian	Oct 23, 2008	985.7498	271.2161	35	6
Direct, spherical	Oct 23, 2008	985.7462	271.2206	35	6
Hybrid, equinoctial	Oct 23, 2008	985.7599	271.2033	8	6
Hybrid, cartesian	Oct 23, 2008	985.7600	271.2031	8	6
Hybrid, spherical	Oct 23, 2008	985.7600	271.2031	7	6

Table 5.7 Optimal solutions of Earth-Mars trajectories (hybrid method, direct-shooting method, collocation method)

Solution methods	Launch date	Final mass (kg)	Trip time (days)	No. of SQP variables	No. of SQP constraints
Direct, equinoctial	July 25, 2009	959.5011	490.6422	35	6
Hybrid, equinoctial	July 25, 2009	959.4958	490.7975	8	6
Collocation, spherical	July 23, 2009	964.7637	495.4184	107	76

Table 5.5 summarizes the optimal solutions of Earth-Mercury transfers. We can see that the solutions using the two methods in three different coordinates are very close only except last one. This also indicates that the NLP method has found a local optimum. The optimal solutions for Earth-Venus transfers (see Fig. 5.6) are also very close. For Earth-Mars direct transfers, the solution obtained by the collocation method (Simpson's rule) is compared with the solutions obtained with the other two methods in Table 5.7. For collocation method, the total 105 SQP design variables include 70 state nodes

(including mass) with 10 for each, 33 nodes of control steering (with 11 for each direction cosine), launch date and transfer time. However, using the direct-shooting method, the 70 state nodes are not necessary. The collocation uses implicit numerical integration so the number of segments of states and control steering will affect the solution accuracy.

The optimal trajectories and steering for Earth-Mercury, Earth-Veuns and Earth-Mars are shown in following Figs. 5.13-5.17. It is shown that the Earth-Mercury trajectory has more revolutions because spacecraft is closer to the sun. For Earth-mercury and Earth-Venus transfers, the pitch angle is always near 180 degree to decrease the energy (see Fig. 5.14 and 5.16). Figure 5.17 presents control steering obtained with three methods. The hybrid method exhibits a smoother control profile than the other two methods.

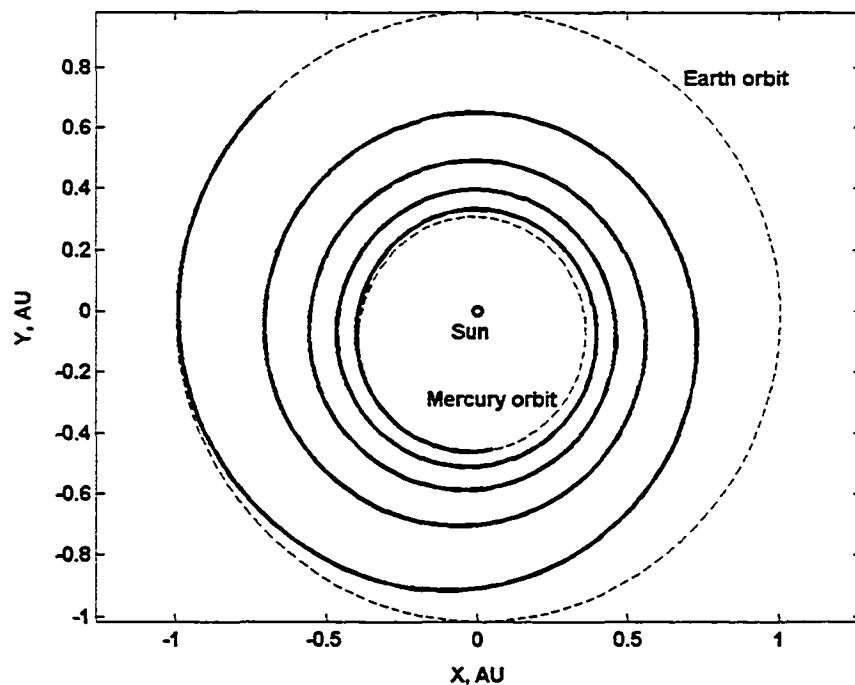


Figure 5.13 Optimal Earth-Mercury direct transfer trajectories (hybrid method, direct-shooting method)

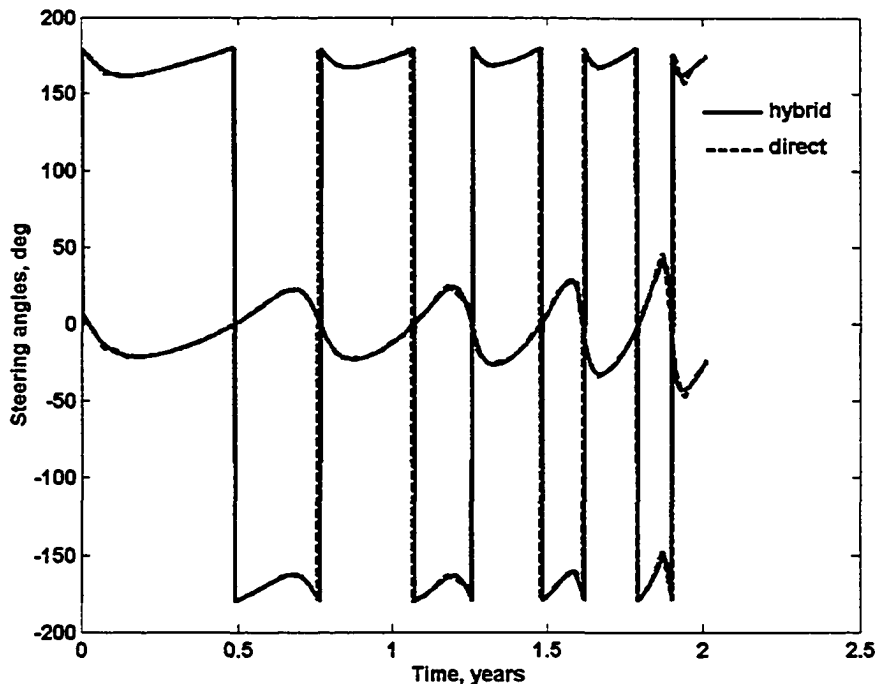


Figure 5.14 Time histories of control steering for optimal Earth-Mercury direct transfer trajectories (hybrid method, direct-shooting method)

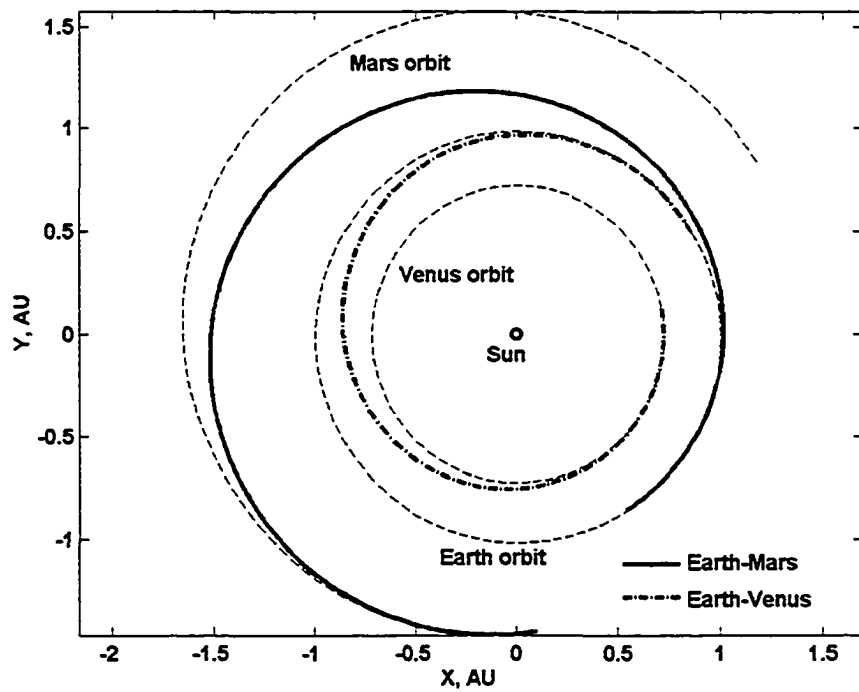


Figure 5.15 Optimal Earth-Venus and Earth-Mars direct transfer trajectories (hybrid method, direct-shooting method)

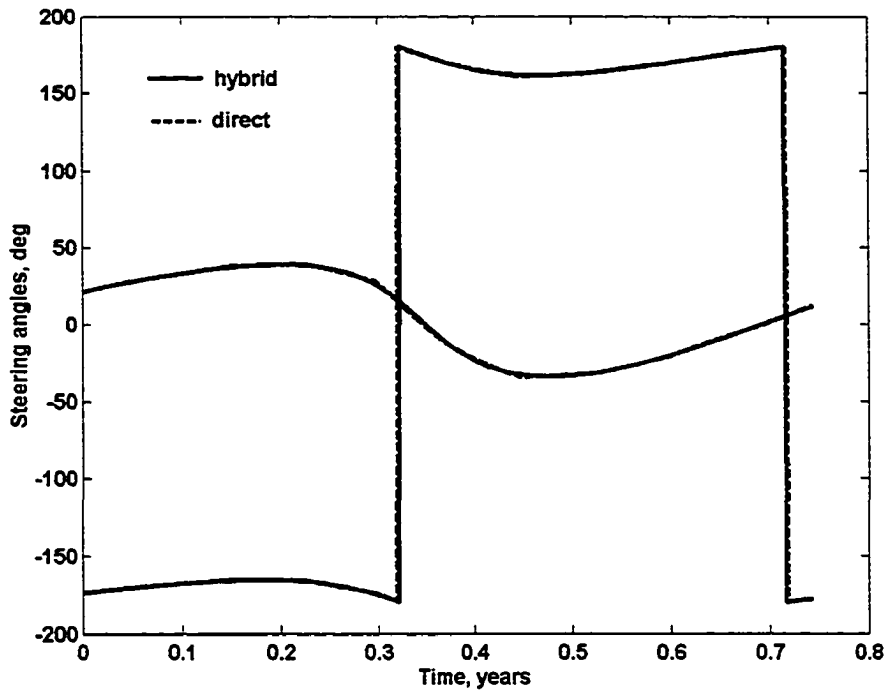


Figure 5.16 Time histories of control steering for optimal Earth-Venus direct transfer trajectories (hybrid method, direct-shooting method)

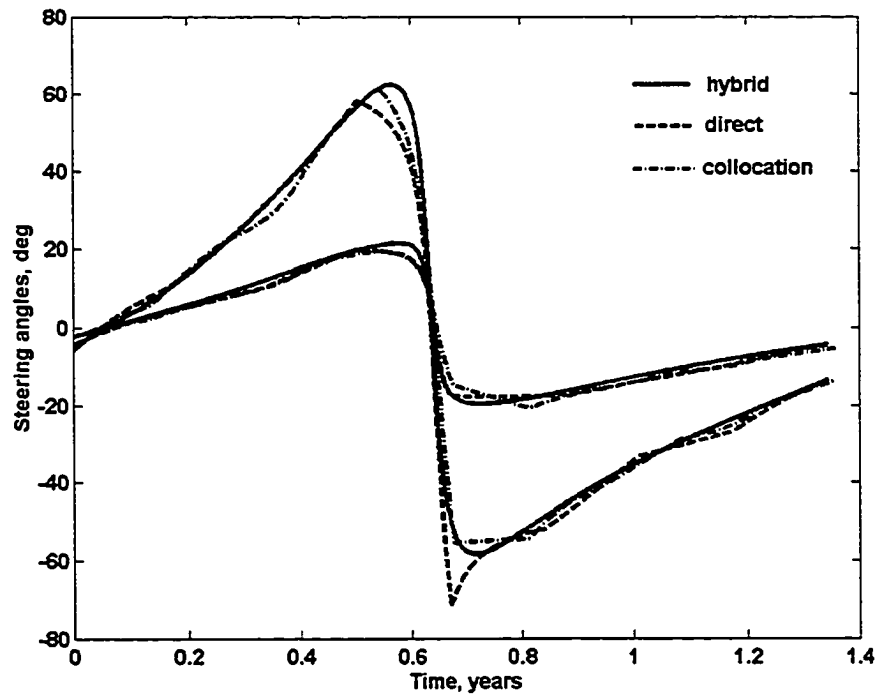


Figure 5.17 Time histories of control steering for optimal Earth-Mars direct transfer trajectories (hybrid method, direct-shooting method, collocation method)

In this section, single-burn trajectories are investigated in order to compare the different solution methods. However, for actual few-revolution interplanetary orbit transfers, single-burn trajectories usually do not provide the best performance. A coast or planetary gravity assist is always considered during the mission-planning phase. Typically, multiple-burn trajectories might have better performance than single-burn trajectories. Gravity assist can provide large energy change with expending fuel, but the feasibility of using gravity assists depends on the relative geometry position of the planets and the spacecraft.

5.4 Multiple-Burn LEO-GEO Transfers Using the Hybrid Method

Recently, researchers have investigated Earth-orbit transfers with multiple burns in order to improve payload mass [25, 78]. In this section, the multiple-burn LEO-GEO orbit transfers obtained by the hybrid method are presented. The spacecraft parameters for the single-burn LEO-GEO trajectories in section 5.1 are used in this section. However, the flight sequence of burn and coast arcs are specified a priori for four cases and optimal LEO-GEO orbit transfers with up to 5 burns are obtained. The departure true anomaly is optimized, and the coast duration is counted in transfer time of optimal trajectories. In these cases, the J_2 perturbation is included. The equations of motion are integrated in spherical coordinates.

Table 5.8 Optimal solutions of multiple-burn LEO-GEO trajectories (hybrid method)

No. of burns	Total burn time (hours)	Final mass (kg)
2-burn	12.3718	5308.7294
3-burn	14.3876	5343.3217
4-burn	13.8858	5359.6062
5-burn	16.6576	5389.2463

Summaries of the optimal solutions are presented in Table 5.8. The orbital elements (semi-major axis, eccentricity and inclination) are presented in Fig. 5.18-5.20, in which the flat lines are coast arcs where three orbital elements are constant. Figures 5.18-5.20 also indicates that the semi-major axis is consciously raised during each burn arc, the eccentricity builds up and decreases only during the final burn arc, and the most inclination change occurs within the last burn arc. The optimal trajectories and control steering are presented in Fig. 5.21-5.28. The first coast arcs are included. The trajectories consist of the final near-apogee burn and the other near-perigee burns. The control steering for the final burn, which has a relatively larger out-plane component, eventually propagates the spacecraft to reach the target orbit.

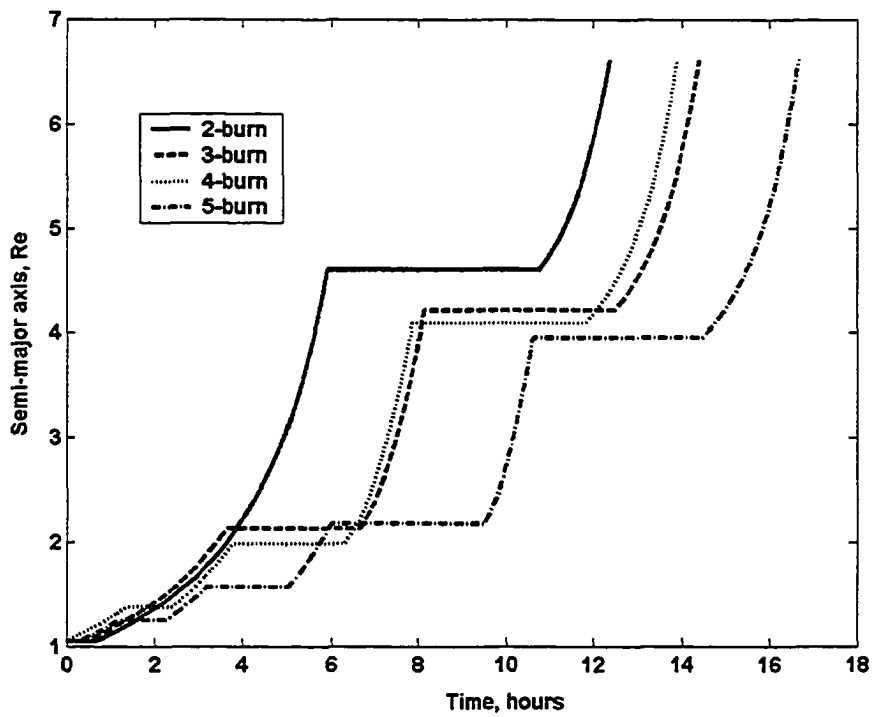


Figure 5.18 Time histories of semi-major axis for optimal 2, 3, 4, 5-burn LEO-GEO trajectories (hybrid method)

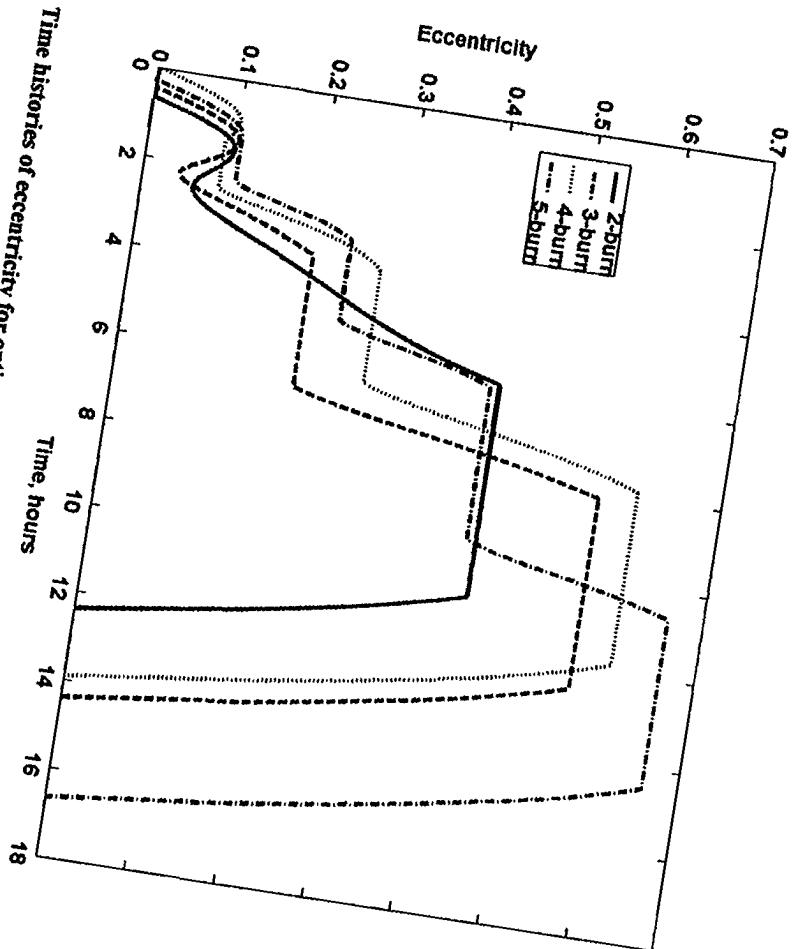


Figure 5.19 Time histories of eccentricity for optimal 2, 3, 4, 5-burn LEO-GEO trajectories (hybrid method)



Figure 5.20 Time histories of inclination for optimal 2, 3, 4, 5-burn LEO-GEO trajectories (hybrid method)

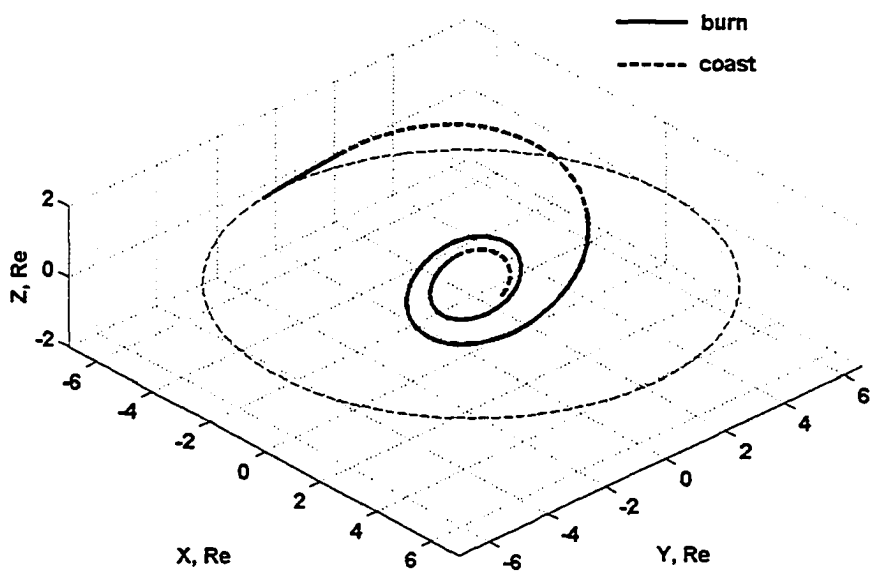


Figure 5.21 Optimal 2-burn LEO-GEO trajectories (hybrid method)

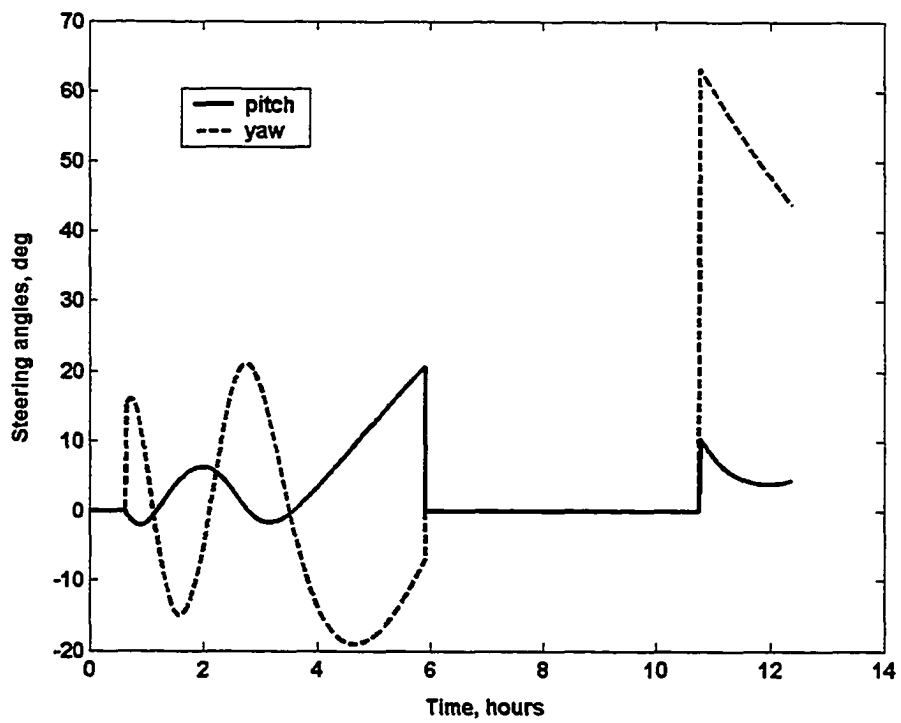


Figure 5.22 Time histories of control steering for optimal 2-burn LEO-GEO trajectories (hybrid method)

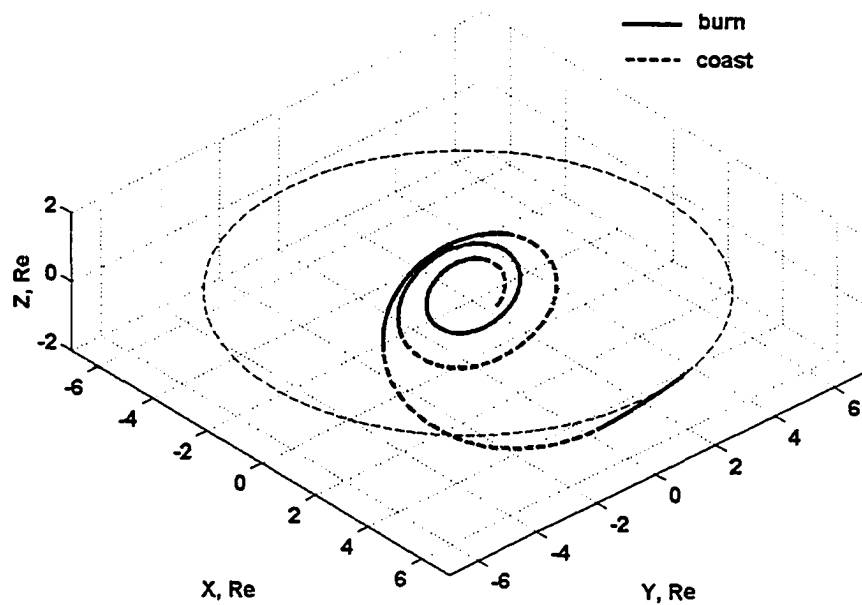


Figure 5.23 Optimal 3-burn LEO-GEO trajectories (hybrid method)

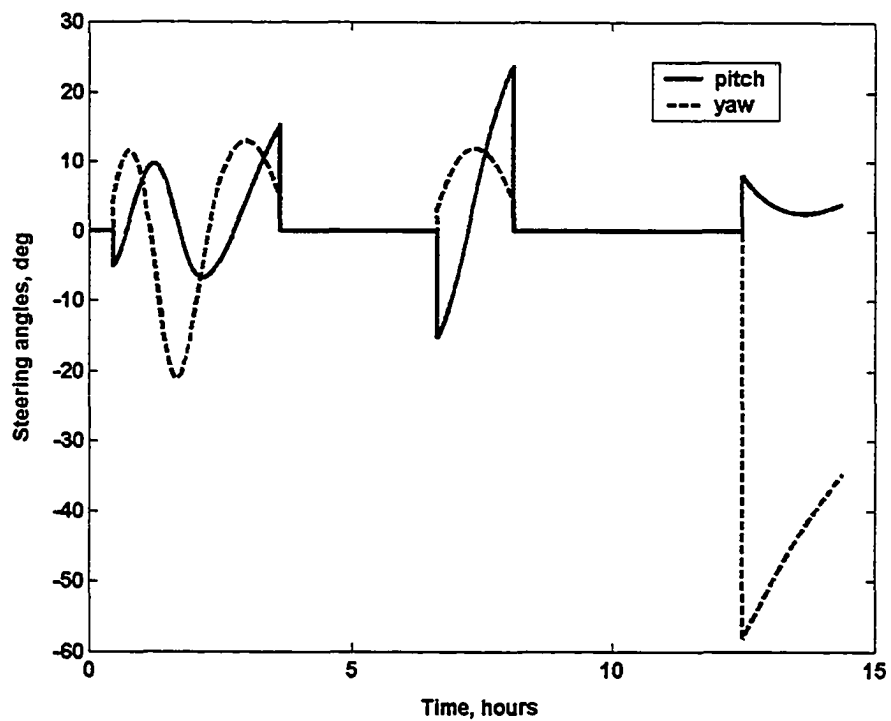


Figure 5.24 Time histories of control steering for optimal 3-burn LEO-GEO trajectories (hybrid method)

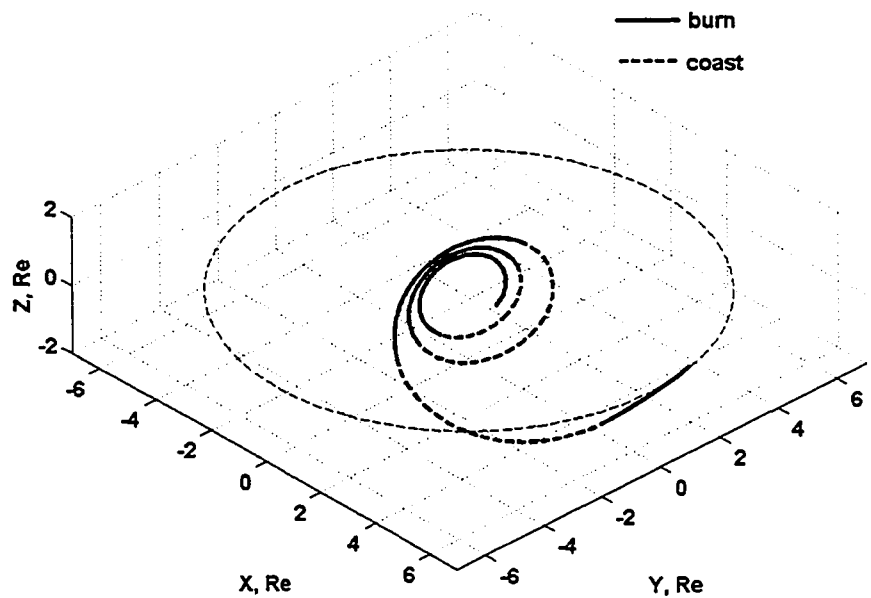


Figure 5.25 Optimal 4-burn LEO-GEO trajectories (hybrid method)

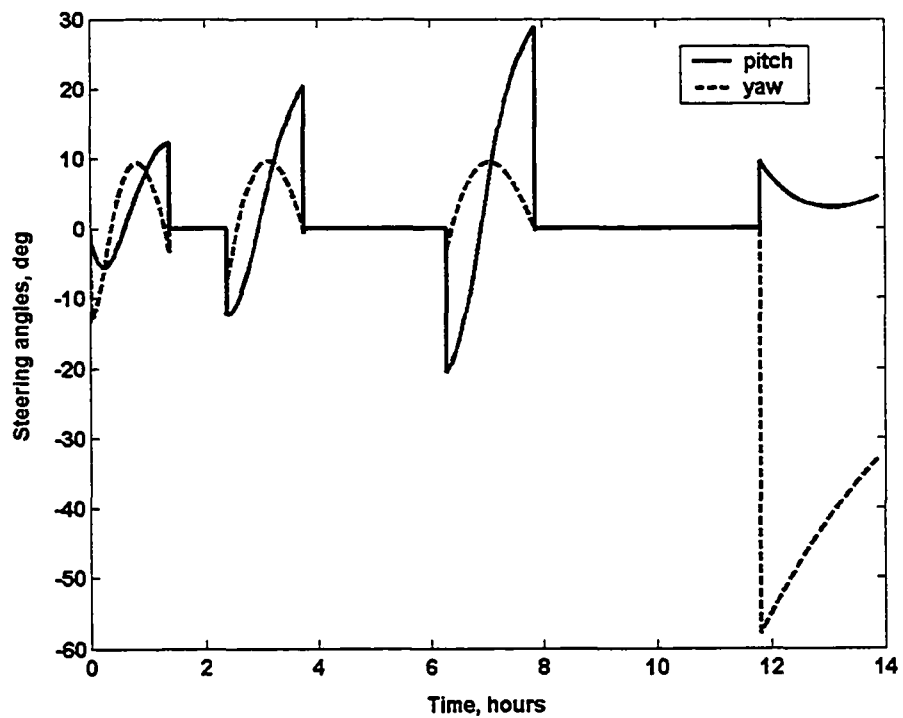


Figure 5.26 Time histories of control steering for optimal 4-burn LEO-GEO trajectories (hybrid method)

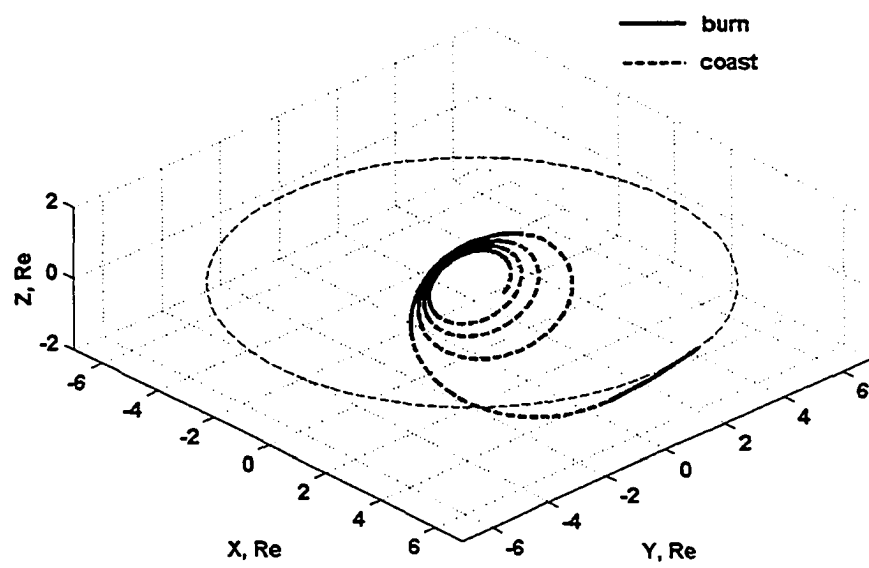


Figure 5.27 Optimal 5-burn LEO-GEO trajectories (hybrid method)

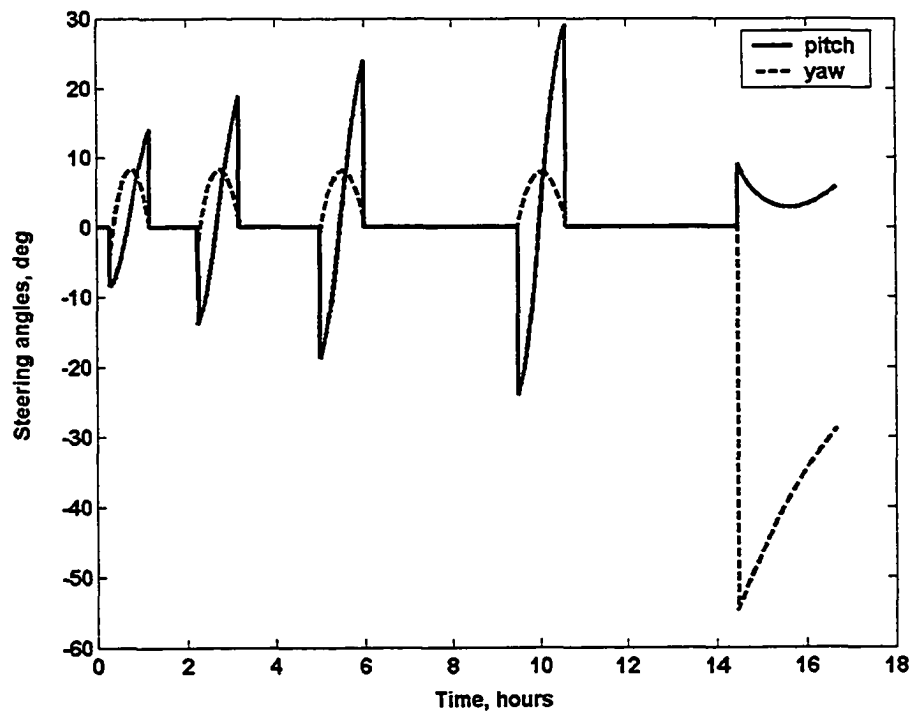


Figure 5.28 Time histories of control steering for optimal 5-burn LEO-GEO trajectories (hybrid method)

5.5 Optimal Earth-Mars 2-Burn Transfer with Venus Gravity Assist

In this case, we will duplicate an optimal Earth-Mars two-burn transfer with Venus gravity assist. Betts [17] originally solved this problem using the direct transcription method. Kluever [31] also duplicated this trajectory using a direct shooting method. The final mass is to be maximized. The thrust is constant at 306 N and I_{sp} is 10,000 seconds. The spacecraft departs on December 1, 2010 and trip time is fixed at 675 days. We assume that the position and velocity at Earth departure are the same as those of the Earth on December 1, 2010. The purpose of this case is to show how to start from a simple initial guess and eventually obtain the optimal trajectories. The first stage of the optimal trajectory is from Earth to the Venus gravity assist, and we assume the flight sequence is a burn and coast arc. The target constraint is the planetary position so that the sub-problem is an Earth-Venus flyby problem. The performance goal is to maximize final mass. Using the direct-shooting method, the converged solution is easily obtained from a simple tangential steering initial guess (6 nodes for each direction cosine) and equinoctial elements. The flyby problem is also solved using the hybrid method, and the converged solution is obtained from following guesses with $\lambda_p = 1$, $\lambda_f = 0$, $\lambda_g = 0$, $\lambda_h = 0$, $\lambda_k = 0$, and $\lambda_L = 0$. In addition, reasonable values for the duration of burn and coast arc are also necessary for obtaining the converged solution.

Table 5.9 Optimal solution of Earth-Venus flyby trajectories (hybrid method, direct-shooting method)

Solution methods	Arrival date	Final mass (kg)	Trip time (days)
Direct, equinoctial	June 19, 2011	373785.8351	200.0377
Hybird, equinoctial	June 19, 2011	373785.8677	200.0390

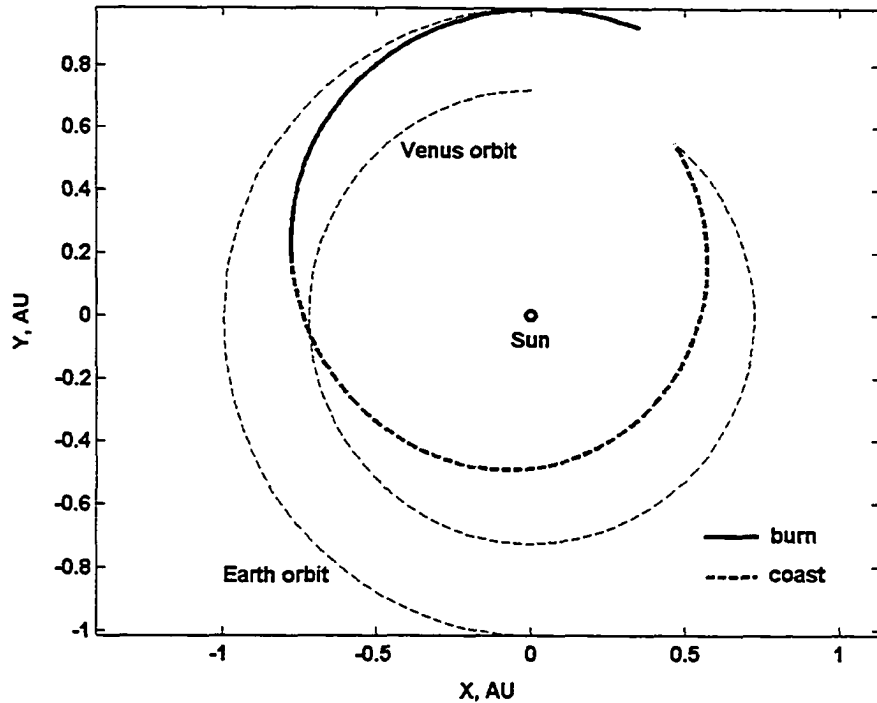


Figure 5.29 Optimal Earth-Venus flyby trajectories (hybrid method, direct-shooting method)

The optimization results are summarized in Table 5.8. The solutions obtained by the two methods are essentially identical. The optimal Venus-flyby trajectories are presented in Fig. 5.29.

After solutions of Earth-Venus flyby trajectories are obtained, we need to reset the flight sequence (burn-coast-flyby-coast-burn) to complete the entire trajectory to Mars. The target also needs to be set at Mars, and the rendezvous problem is desired. Because the gravity assist exists, two parameters for Venus-flyby should be added, which are flyby altitude and rotation angle. Betts [17] and Kluever [31] fixed the flyby altitude at 2 Venus radii and rotation angle at zero. The time duration for the second burn and the second coast also need to be guessed. We also need to add control nodes (tangential steering with 6 nodes for each direction cosine for the direct-shooting method) or initial

costates ($\lambda_p = 1$, $\lambda_f = 0$, $\lambda_g = 0$, $\lambda_h = 0$, $\lambda_k = 0$, and $\lambda_L = 0$ for the hybrid method) for the second burn. For Venus gravity assist, the initial flyby altitude is set at 350 km, and the rotation angle is set at zero. Optimizing the penalty function (norm of all equality and inequality constraints) readily results in a converged solution, which is a feasible trajectory for the Earth-Mars transfer. By optimizing the final mass based on the feasible solutions, better performance for the final mass is readily obtained, which is the optimal solution with free transfer time. Next, we can get the optimal solution with fixed transfer time (optimize the penalty function and then the final mass). The comparison of optimal solutions is in Table 5.10. The solutions obtained by the direct-shooting method and the hybrid method (#1) are essentially identical, and exhibit better final masses (compared with Betts' and Kluever's solutions) since the Venus-flyby parameters are free.

Table 5.10 Optimal solution of Earth-Mars trajectory with Venus gravity assist

Trajectories	Final mass (kg)	Trip time (days)	No. of SQP variables	No. of SQP constraints
675-day transfer, Betts	294,749	675	n/a	n/a
675-day transfer, Kluever	299,248	675	n/a	n/a
675-day transfer, direct	303,657	675	42	9
675-day transfer, hybrid (#1)	303,667	675	18	9
675-day transfer, hybrid (#2)	320,032	675	18	9

The optimal trajectories and the control steering computed by the direct-shooting method and the hybrid method (#1) are presented in Figs. 5.30 and 5.31. Another 675-day trajectory and the control steering computed by the hybrid method (#2) are shown in Figs. 5.32 and 5.33. This solution is obtained based on different initial guess of SQP design variables using the hybrid method.

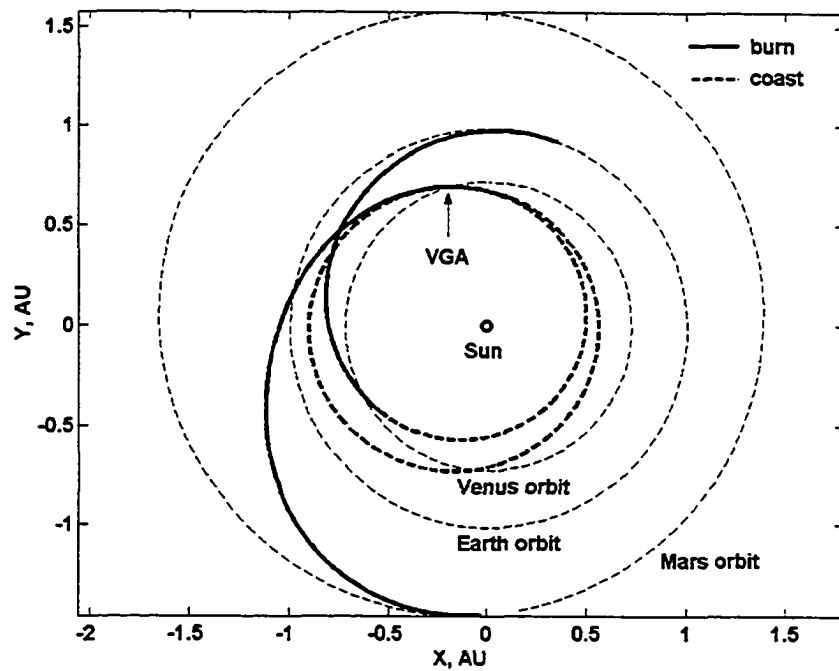


Figure 5.30 Earth-Mars 675-day optimal trajectories (hybrid method #1, direct-shooting method)

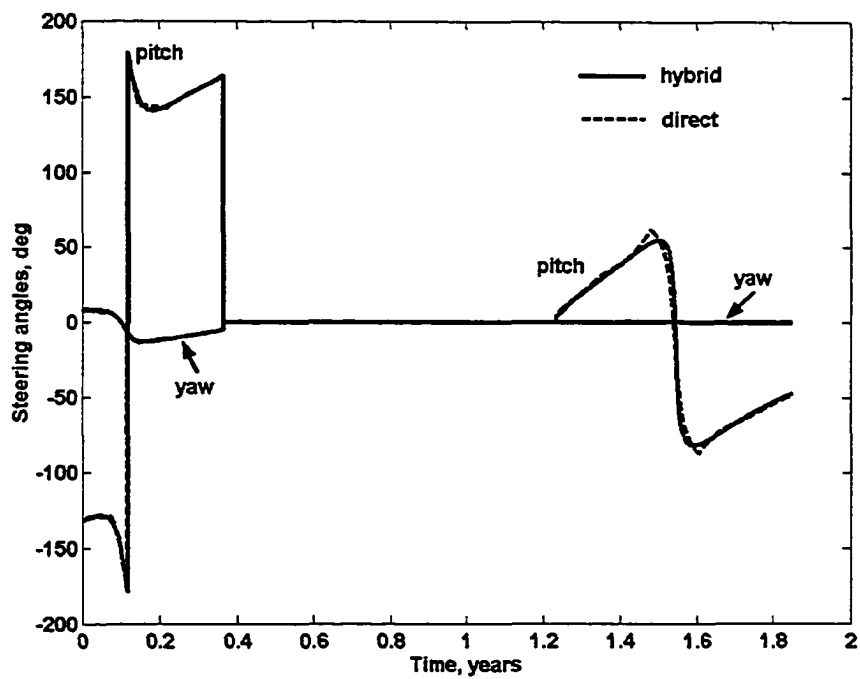


Figure 5.31 Time histories of control steering for optimal Earth-Mars 675-day trajectories (hybrid method #1, direct-shooting method)

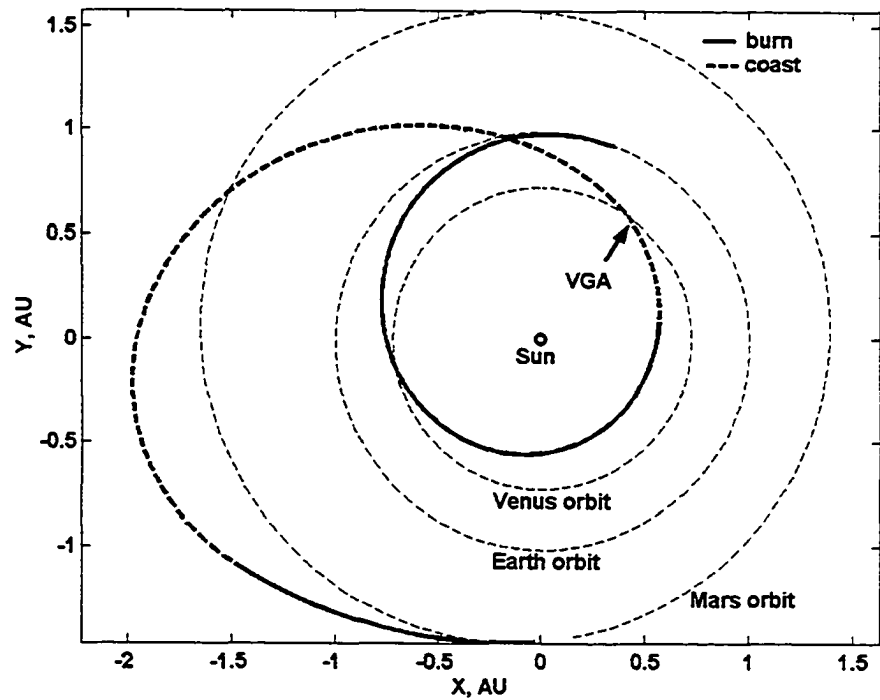


Figure 5.32 Alternative Earth-Mars 675-day optimal trajectory using hybrid method (hybrid method #2)

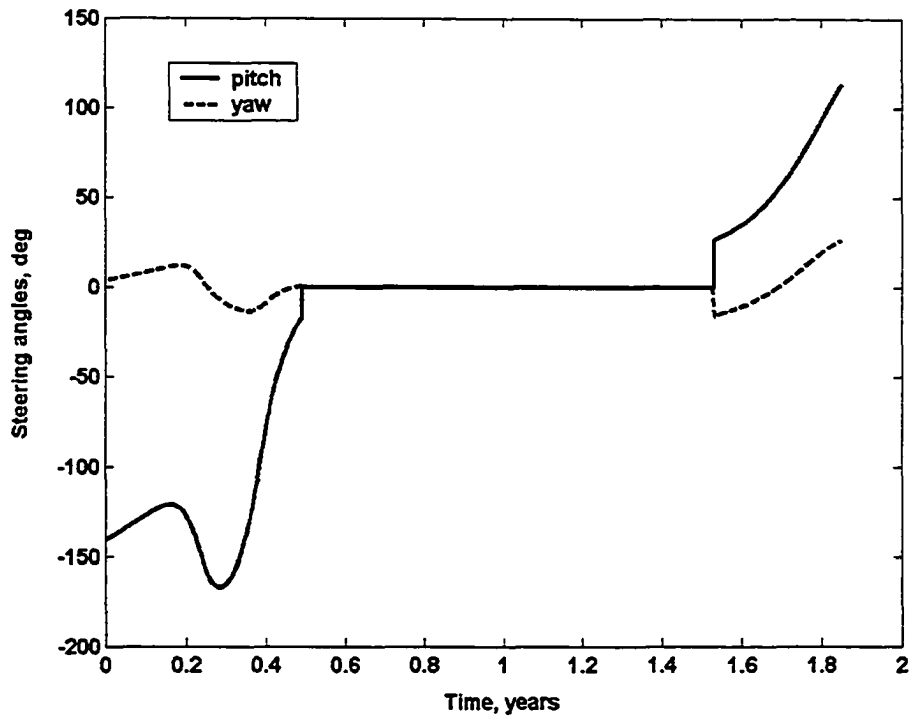


Figure 5.33 Time histories of control steering for alternative optimal Earth-Mars 675-day trajectory (hybrid method #2)

The alternative solution obtained by the hybrid method (#2) is different and exhibits better performance. After gaining energy from the Venus gravity assist, the spacecraft is accelerated beyond Mars circular orbit. We can conclude that both the direct-shooting method and the hybrid method (#1) locate local minimum solutions. Therefore, Betts' solution in Ref. [17] is not a global minimum. For interplanetary orbit transfers with multiple dynamic stages, local minima are easy to obtain since multiple dynamic stages make the problem more nonlinear. Furthermore, the sequence of multiple dynamic stages will also affect the solutions. For low-thrust interplanetary orbit transfer, gravity assists need to be investigated for better payload performance.

5.6 Optimal Earth-Jupiter Orbit Transfers

This problem was first investigated by Coverstone [41], who used a differential inclusion method. Later, Kluever [31] used the direct-shooting method to verify this solution. Since the original departure date (the year 2000) is in the past, the launch date is changed to be 2009 in this section. The other spacecraft parameters are not changed. The constant power is 115kW, and constant I_{sp} is 4000 seconds. The initial mass is 10000 kg. The position and velocity of spacecraft at departure are assumed to be the same as those of the Earth on the launch date. The optimal free-time 1-burn and 2-burn trajectories with maximum final mass are solved using the hybrid and direct-shooting methods.

In order to solve the 2-burn Earth-Jupiter transfer, we start by solving the 1-burn trajectory, which could be solved by using simple guesses for control steering. With the direct-shooting method, the converged solution is readily obtained from a tangential control initial steering (15 nodes for each direction cosine). Also using the hybrid method, the converged solution is obtained from a simple initial guesses with $\lambda_p = 1.0$,

$\lambda_f = 1.0$, $\lambda_g = 1.0$, $\lambda_h = 0$, $\lambda_k = 0$, and $\lambda_L = 0$. The strategy of obtaining optimal 2-burn trajectories is to split the burn duration of the 1-burn solution. For the direct-shooting method the control nodes are divided into two parts, and for the hybrid method the time histories of costates are divided into two segments. After separating the burn phase, we simply add a coast phase, and the angle for coast arc is set to a very small value. Then, this set of initial guesses for the NLP problem variables is close to a feasible solution with a very short coast arc. Based on this good initial guesses, SQP increases the length of the coast arc and optimizes the final mass.

Table 5.11 Optimal solutions of Earth-Jupiter trajectories (hybrid method, direct-shooting method)

Trajectories	Launch date	Arrival date	Final mass (kg)	Trip time (Days)
1-burn, direct	Feb 8, 2009	July 29, 2011	3084.5496	535.4762
1-burn, hybrid	Mar 17, 2009	Sept 2, 2011	3109.5114	533.5434
2-burn 600-day, direct	Feb 8, 2009	Oct 1, 2011	4562.8020	600.
2-burn 600-day, hybrid	Mar 18, 2009	Nov 8, 2011	4625.3162	600.
2-burn 700-day, direct	Feb 6, 2009	Jan 7, 2012	5714.1784	700.
2-burn 700-day, hybrid	Mar 16, 2009	Feb 14, 2012	5747.5885	700.
2-burn 800-day, direct	Feb 5, 2009	Apr 16, 2012	6316.7944	800.
2-burn 800-day, hybrid	Mar 15, 2009	May 23, 2012	6332.1454	800.
2-burn 900-day, direct	Feb 5, 2009	July 25, 2012	6629.7393	900.
2-burn 900-day, hybrid	Mar 16, 2009	Sept 1, 2012	6636.8877	900.
2-burn free time, direct	Feb 10, 2009	Feb 1, 2013	6792.8547	1086.2644
2-burn free time, hybrid	Mar 19, 2009	Mar 19, 2013	6805.2998	1095.5262

In Table 5.11, we can see that the solutions obtained by the hybrid method are slightly better than those obtained by the direct-shooting method. The launch dates computed by the hybrid method is about 40 days later than those computed by the direct-shooting method. From Table 5.11, it is obvious that 2-burn solutions are better than 1-burn solution. The performance (final mass) improves with increasing transfer time. The 1-burn solution is also a minimum-time transfer.

The optimal 1-burn trajectories and control steering are presented in Fig. 5.34 and 5.35, and the optimal 2-burn 600-day trajectories and control steering are presented in Fig. 5.36 and 5.37. From the Fig. 5.38 we can see that the eccentricity exceeds 1 (escape) for the 1-burn trajectory while remains below 1 for the 2-burn trajectory. Since the first equinoctial element is not the semi-major axis, there is no singularity during the numerical integration.

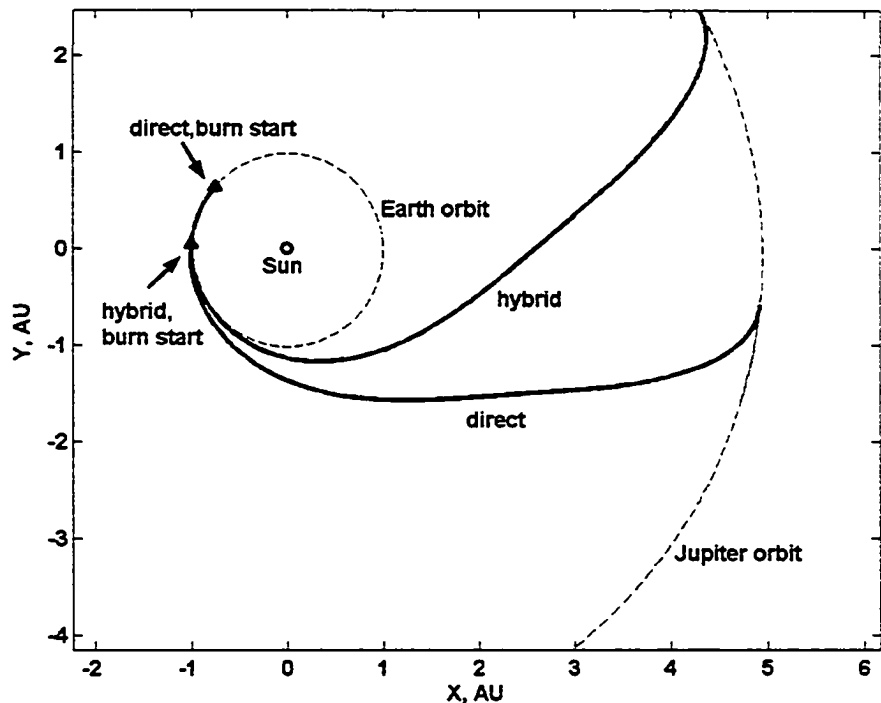


Figure 5.34 Optimal Earth-Jupiter 1-burn trajectories (hybrid method, direct-shooting method)

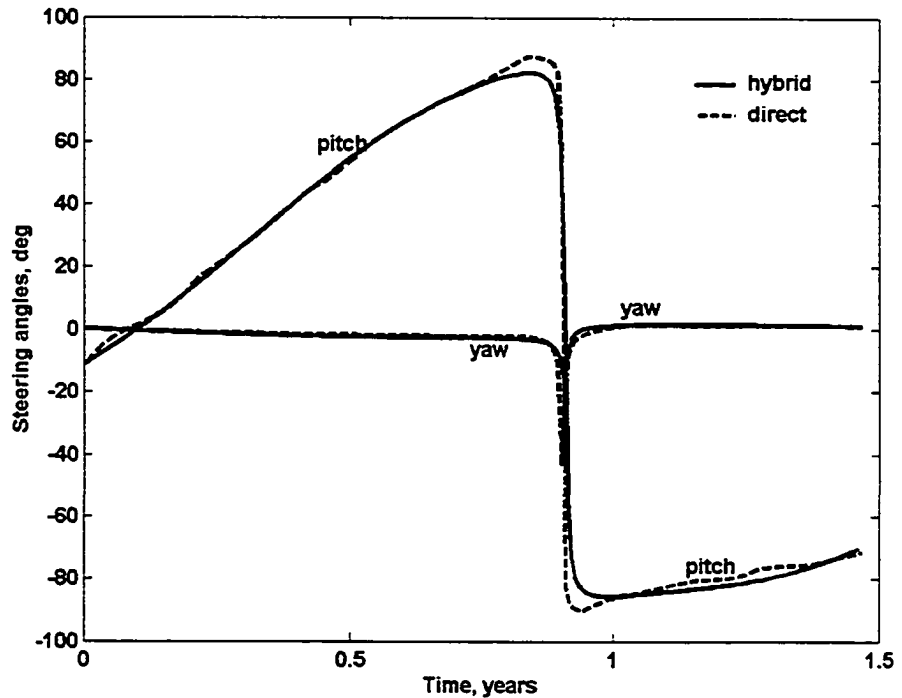


Figure 5.35 Time histories of control steering for optimal Earth-Jupiter 1-burn trajectories (hybrid method, direct-shooting method)

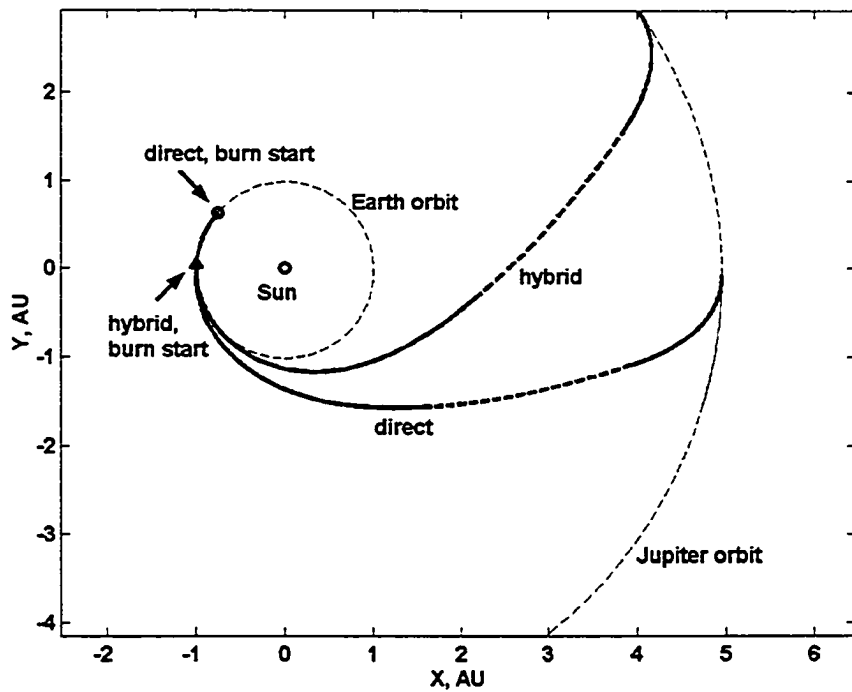


Figure 5.36 Optimal Earth-Jupiter 2-burn 600-day trajectories (hybrid method, direct-shooting method)

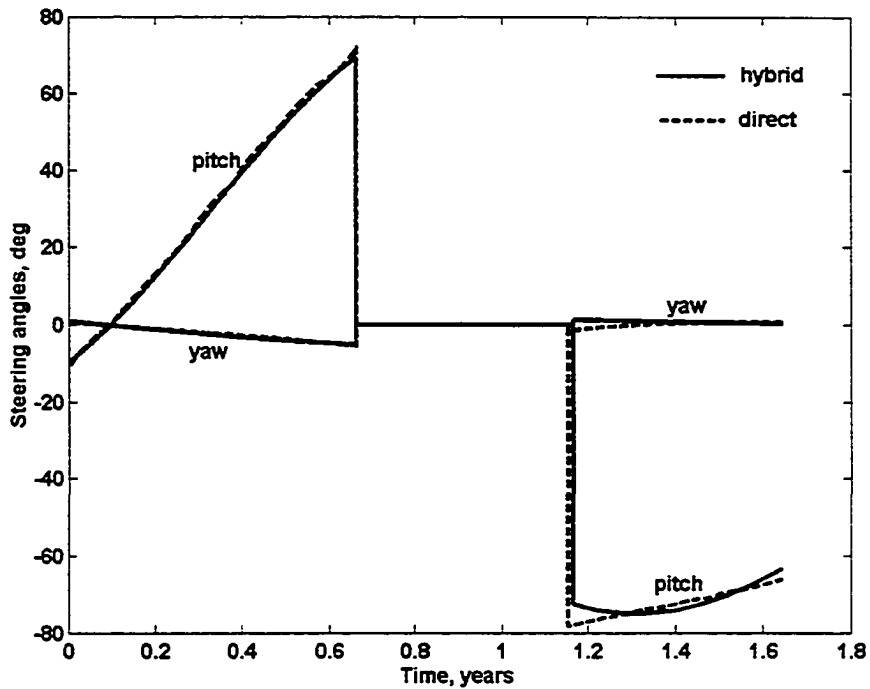


Figure 5.37 Time histories of control steering for optimal Earth-Jupiter 2-burn 600-day trajectories (hybrid method, direct-shooting method)

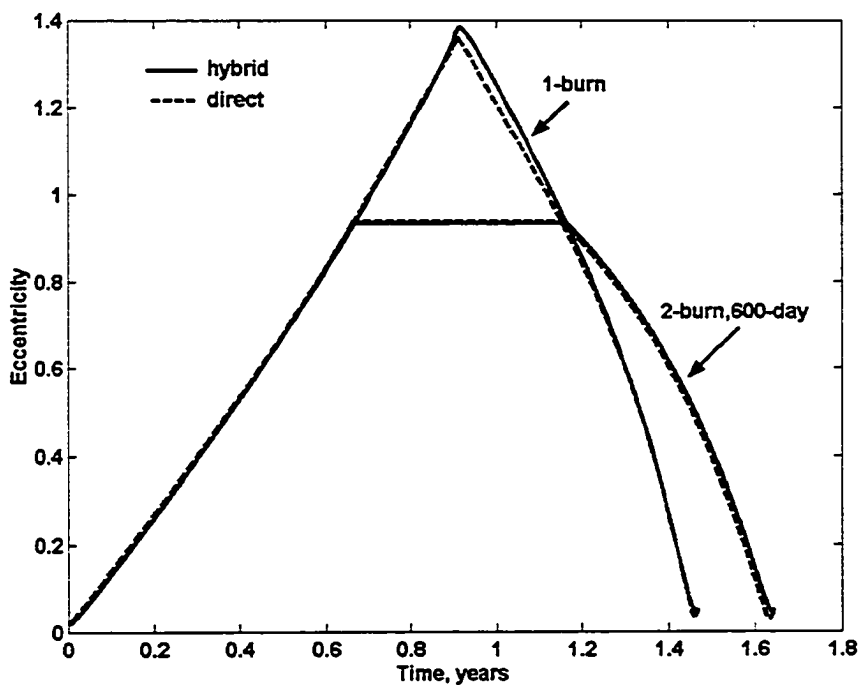


Figure 5.38 Time histories of eccentricities for optimal 1-burn and 2-burn 600-day Earth-Jupiter trajectories (hybrid method, direct-shooting method)

5.7 Optimal Earth-Venus Transfer with Modulated Specific Impulse

Using the Hybrid Method

Recently, variable specific impulse (or variable engine throttle) can be employed to gain better mission performance [79]. This case is intended to show how the hybrid method can be used in tandem with system parameter optimization. For electric engines, the value of I_{sp} can be variable, and modulating I_{sp} might give better performance. Usually I_{sp} -modulation is analyzed for missions with fixed transfer time. This case is an Earth-Venus transfer based on the solution with maximum final mass presented in section 5.3. The nominal value of I_{sp} is 3100 seconds, and it is assumed that for this case the upper and lower limit of I_{sp} is 3400 and 2800 seconds. The hybrid method is utilized, and numerical integration is performed in Cartesian coordinates. In the SQP, 30 additional discrete nodes are used to parameterize time history of I_{sp} , and the continuous value of I_{sp} is computed using linear interpolation between discrete nodes. The transfer time is fixed at several values. A series of solutions with variable I_{sp} are obtained, and results are summarized in Table 5.12. For solution with minimum transfer time, the I_{sp} is always 2800 seconds and for solution with maximum final mass, the I_{sp} is always 3400 seconds. For the solutions in section 5.3 (using constant I_{sp}), the minimum trip time is 271 days, and the final mass is 986 kg. With I_{sp} -modulation, the minimum trip time is 244 days with minimum I_{sp} , and maximum final mass is 1009 kg with maximum I_{sp} .

Table 5.12 Optimal solutions for Earth-Venus orbit transfers with modulated I_{sp} (hybrid method)

Transfer time (days)	Final mass (kg)
243.7264 (min. trip time)	946.1906
245	952.3729
250	966.6087
260	980.6810
270	990.1095
280	998.0005
290	1004.1132
300	1008.0071
307.4235 (max. final mass)	1009.4849

Figure 5.39 presents the time histories of I_{sp} for solutions with different trip times.

The number labels in the figure indicate the trip time (days). The curve of final mass vs. trip time is presented in Fig. 5.40. It is obvious that with increasing trip time, the final mass improves, and the values of I_{sp} tend to the upper limit and vice versa.

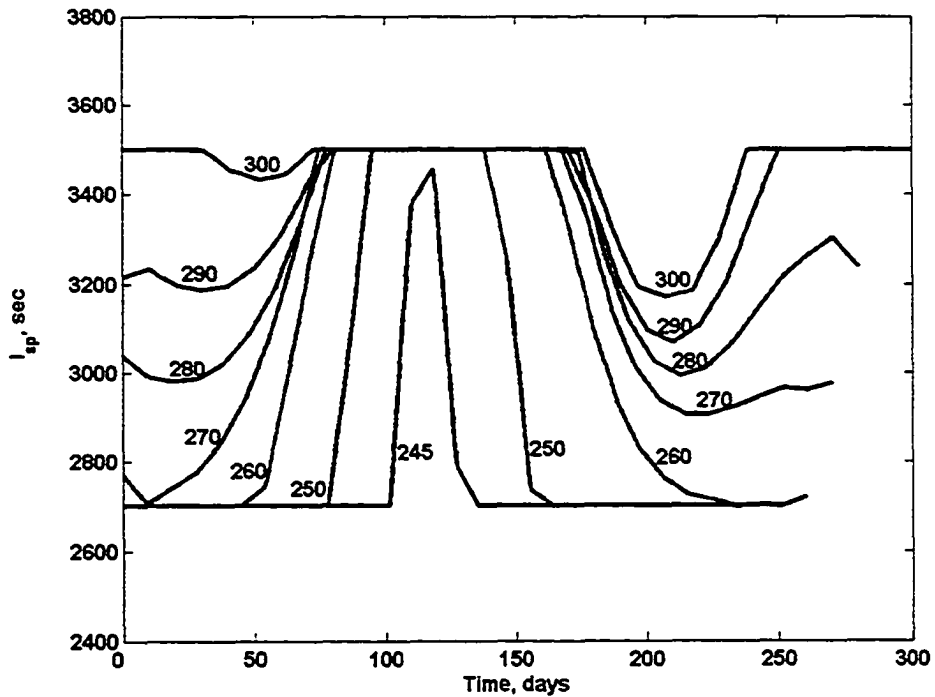


Figure 5.39 Time histories of I_{sp} for optimal Earth-Venus transfers with different transfer times (hybrid method)

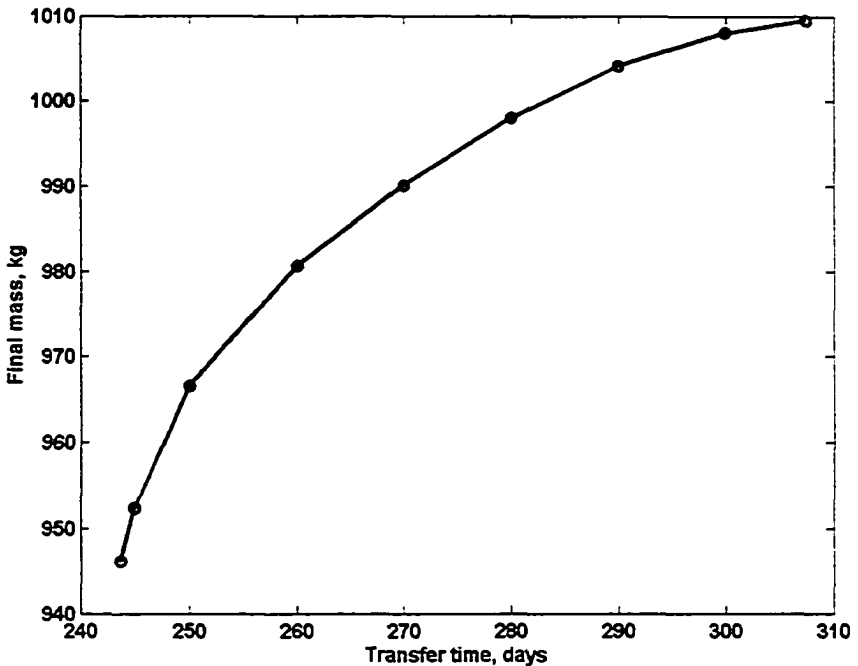


Figure 5.40 Transfer time vs. final mass for optimal Earth-Venus transfers using modulated I_{sp} (hybrid method)

5.8 Summary of the Hybrid and Direct-Shooting Methods

Optimal orbit transfers using the hybrid and direct-shooting methods have been presented in this chapter. According to previous published work, direct methods have been widely used, while the application of hybrid method is somewhat limited and has not been applied to interplanetary transfers. These two methods could be used to design a wide range of low-thrust Earth-orbit and interplanetary missions. Many system discrete parameters could be incorporated in the NLP problem so that complex missions can be designed. Because trajectory optimization is converted to parameterization by SQP, it is easy to change the objective function, design variables, constraints, design variable limits, etc. The drawback of these two methods is that the sequence of flight phases needs to be assumed *a priori*. How to automatically find a good flight sequence, especially for

interplanetary orbital transfers, is still an unsolved difficulty. Good convergence from simple initial guesses is obtained for these two methods (validated against published trajectory results) and relatively few design variables are employed in SQP. Usually the direct-shooting method starts from simple tangential steering. For hybrid method, trial-and-error is needed to find good guess of initial costates, but it is not as hard as TBPVP. However, the local minimum is also easier to be located by these two methods. Compared to the direct-shooting method, the hybrid method leads to more trials for initial guesses to find a global optimum since fewer NLP design variables results in much less computation time. For most transfers, the solutions obtained by the hybrid method are slightly better than those obtained by the direct-shooting method. This is because only linear interpolation is used to find the continuous control in the direct-shooting method while the optimal control is dictated by costate differential equation in the hybrid method.

CHAPTER 6 OPTIMAL ORBIT TRANSFERS USING MULTIPLE SHOOTING TECHNIQUES

In this chapter, multiple shooting techniques are employed to obtain optimal trajectories. As introduced in Chapters 3 and 4, the extended multiple-shooting techniques include multiple shooting with state nodes, costate nodes, or both state and costate nodes. Optimal LEO-GEO, Earth-Mars, and Earth-Jupiter orbit transfers are presented in order to illustrate the multiple-shooting techniques. The optimization results demonstrate that multiple shooting improves convergence properties of the NLP problems.

6.1 Optimal LEO-GEO Orbit Transfers Using Multiple Shooting

6.1.1 Multiple Shooting with State Nodes Using the Hybrid Method

The optimal LEO-GEO orbit transfer in section 5.1 is reconsidered. All the spacecraft parameters remain the same, and the final mass is to be maximized. The purpose of this section is to show how multiple shooting increases the convergence domain. Five initial costates are guessed simply ($\lambda_{v_g} = -1$, and other initial costates are zeros except λ_θ), the first coast angle is guessed as 0.1 rad and the burn time duration is guessed as 0.3 days (7.2 hours). Running EOTD shows that no converged solution was obtained. If multiple shooting with state nodes is employed, 5 nodes for semi-major axis, eccentricity, and inclination are equally inserted during the burn duration (see Table 6.1). The initial nodes for semi-major axis and inclination are simple, and the initial

eccentricity nodes are constant. Therefore, the SQP design variables include 5 initial costates, a burn time duration, and additional 15 state nodes for multiple shooting. The SQP constraints include additional 15 equality constraints for multiple shooting besides 3 terminal constraints. The optimal solution presented in Table 6.2 is obtained with the same guesses for the initial costates and the burn duration.

Table 6.1 State nodes for multiple shooting (LEO-GEO orbit transfers)

States	Initial guess for nodes
Semi-major axis (Re)	2.0, 3.0, 4.0, 5.0, 6.0,
Eccentricity	0.01, 0.01, 0.01, 0.01, 0.01
Inclination (radian)	0.48, 0.46, 0.44, 0.4, 0.2

Furthermore, the dual (mirror) transfer is readily obtained by adding $\pm\pi$ to the optimal longitude and switching the signs of costates λ_ϕ and λ_{ν_e} . There is no optimization for the dual transfer. The transfer time includes the coast arc duration.

Table 6.2 Optimal solutions for LEO-GEO dual orbit transfers using the hybrid method and multiple-shooting technique with state nodes

Final state and optimized longitude	Trajectory #1 (Multiple Shooting)	Trajectory #2 (Dual transfer)
Semi-major axis (Re)	6.61070027	6.6107048
Eccentricity	4.0524(10^{-5})	1.4560(10^{-5})
Inclination (deg)	1.2074(10^{-5})	2.4452(10^{-5})
Transfer time (hours)	11.3328	9.0720
Final mass (kg)	5082.4708	5082.4708
Longitude optimized (deg)	243.6800	63.6800

The LEO-GEO trajectory has its dual solution (see Fig. 6.1) where the burns start at the other side of LEO. This is because that optimized longitude of the burn start point exists for orbit transfers with plane changes. It is shown in Fig. 6.2 that the pitch steering of two transfers are essentially the same, and the yaw steering is exactly in opposite directions.

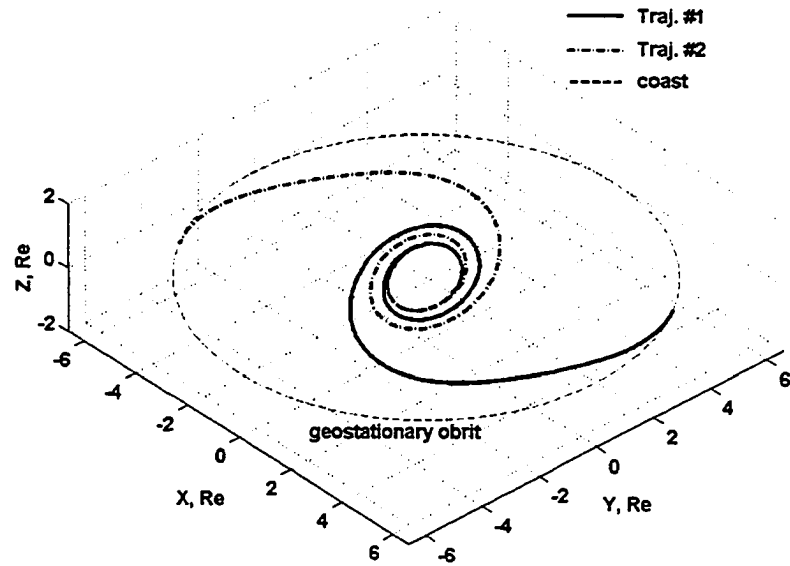


Figure 6.1 Optimal LEO-GEO optimal trajectories (hybrid method, multiple-shooting technique with state nodes)

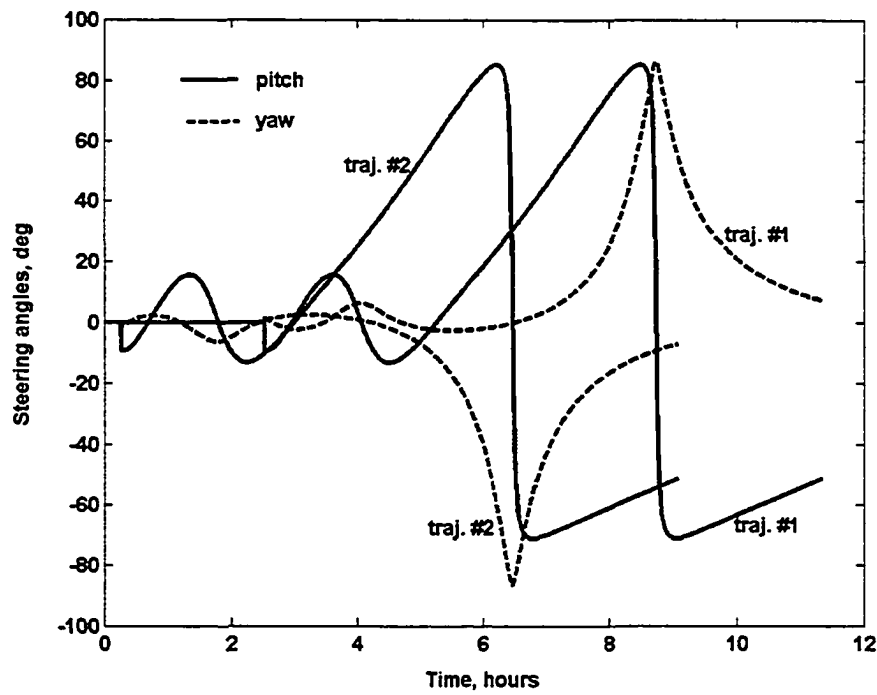


Figure 6.2 Time histories of control steering for optimal LEO-GEO trajectories (hybrid method, multiple-shooting technique with state nodes)

6.1.2 Multiple Shooting with State Nodes Using the Direct-Shooting Method

If the direct-shooting method is employed, 63 total nodes for the direction cosines (with 21 for each) are used. The initial guess of control is in tangential direction. The first coast angle is guessed as 0.1 rad and the burn time duration is guessed as 0.2 days (4.8 hours). Running EOTD shows no converged solution from the simple initial guesses with tangential steering. If the state nodes in Table 6.1 are used, the problem converged using the state node multiple-shooting method.

The optimal solutions are summarized in Table 6.3. Furthermore, the dual transfer is readily obtained without optimization by adding $\pm\pi$ to the optimal longitude and switching the sign of the normal direction cosine α_n . The optimal solutions in this section and in Table 6.2 are very close.

Table 6.3 Optimal solutions for LEO-GEO dual orbit transfers using the direct-shooting method and multiple-shooting technique with state nodes

Final state and optimized longitude	Trajectory #1 (Multiple Shooting)	Trajectory #2 (Dual transfer)
Semi-major axis (Re)	6.6106998	6.6107042
Eccentricity	1.0470(10^{-6})	1.2506(10^{-6})
Inclination (deg)	8.0274(10^{-5})	5.4052(10^{-5})
Transfer time (hours)	8.8045	8.8045
Final mass (kg)	5082.3764	5082.3764
Longitude optimized (deg)	63.6800	243.6800

In this case, only the burn time is counted so that the transfer time of dual trajectories are the same (see Fig. 6.3). The control steering obtained by the direct-method is not smooth enough as discussed in previous chapters. Furthermore, the hybrid method exhibits a slightly better performance for the final mass.

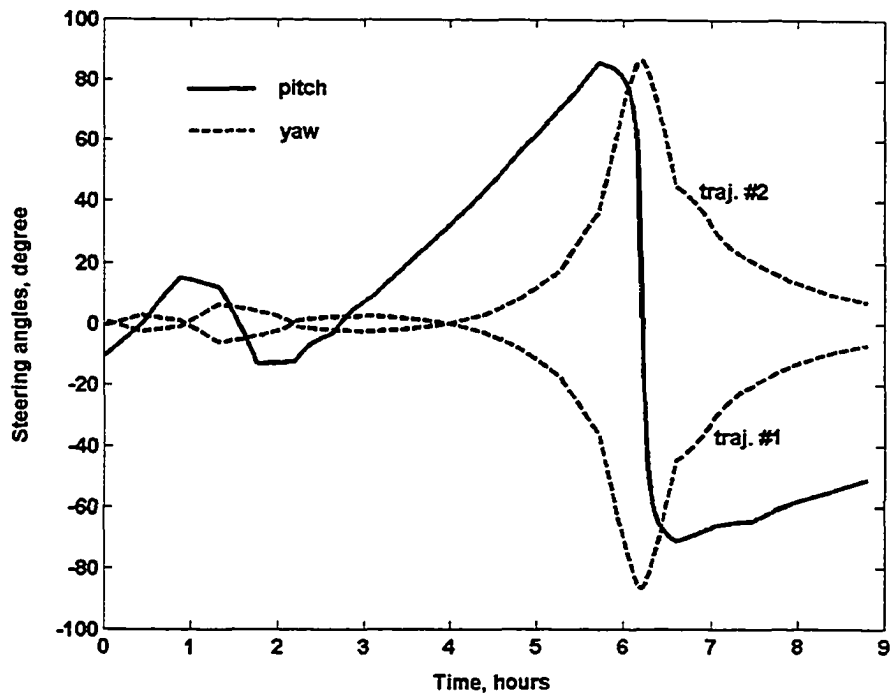


Figure 6.3 Time histories of control steering for optimal LEO-GEO trajectories (direct-shooting method, multiple-shooting technique with state nodes)

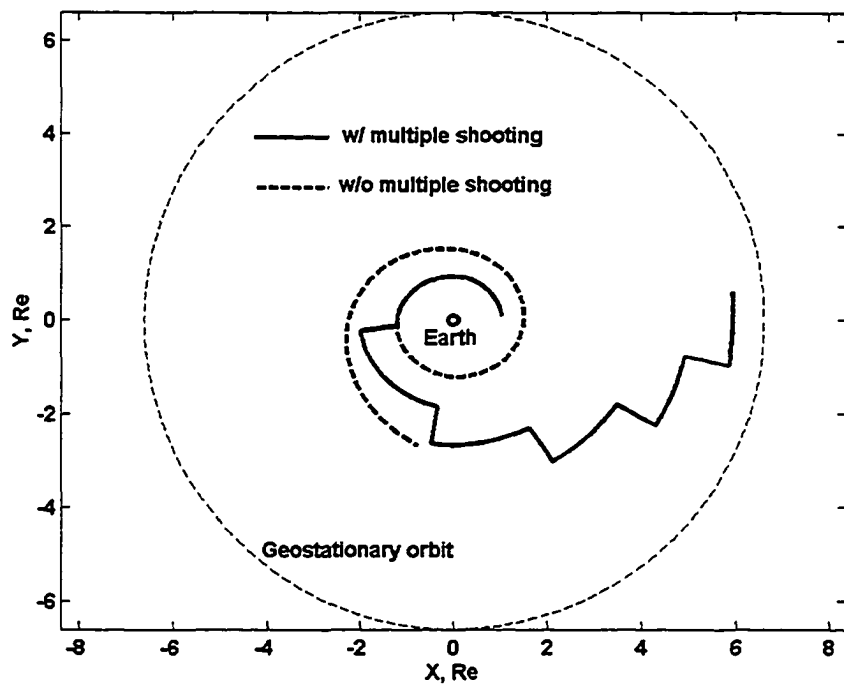


Figure 6.4 LEO-GEO orbit transfers at the first iteration (direct-shooting method, multiple-shooting technique with state nodes)

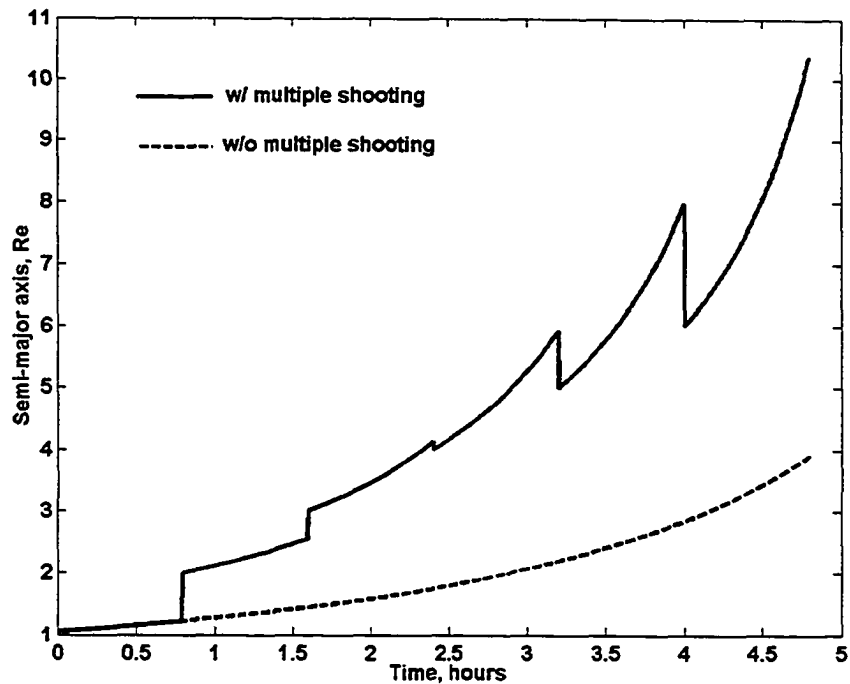


Figure 6.5 Time histories of semi-major axis for LEO-GEO orbit transfers at the first iteration (direct-shooting method, multiple-shooting technique with state nodes)

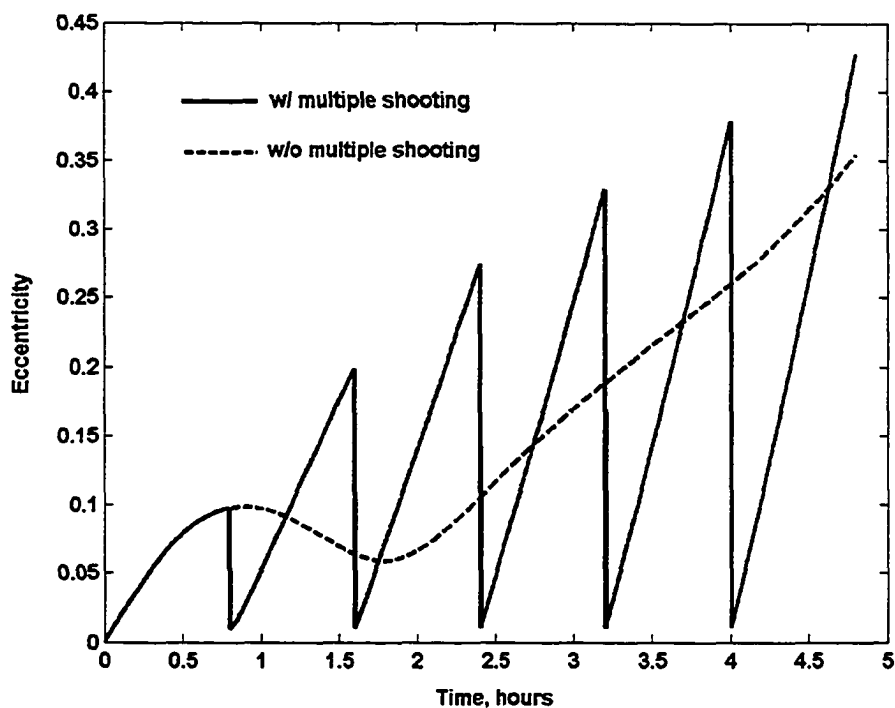


Figure 6.6 Time histories of eccentricity for LEO-GEO orbit transfers at the first iteration (direct-shooting method, multiple-shooting technique with state nodes)

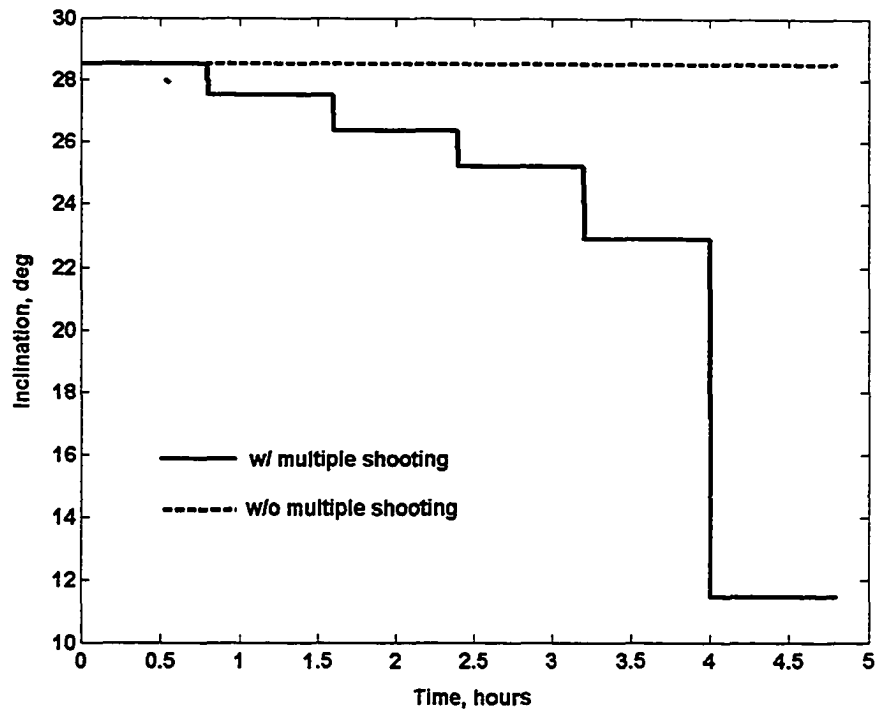


Figure 6.7 Time histories of inclination for LEO-GEO orbit transfers at the first iteration (direct-shooting method, multiple-shooting technique with state nodes)

In Figs. 6.4-6.7, the trajectory, semi-major axis, eccentricity and inclination profiles at the first iteration are shown. We can see that the multiple shooting forces the trajectory and orbital elements closer to the target orbit (see Fig. 6.4). At the first iteration, inclination (see Fig. 6.7) is not changed since the yaw angle is set to zero, and multiple shooting forces it closer to the desired value. The discontinuities (“gaps”) between orbital elements are formulated as equality constraints in NLP problem and eventually disappear as the optimal solutions are obtained.

6.2 Optimal Earth-Mars Orbit Transfers Using Multiple Shooting

In this section, multiple shooting is employed to obtain Earth-Mars single-burn transfers with maximum final mass. The spacecraft parameters are the same as those in section 5.3.

6.2.1 Multiple Shooting with State Nodes Using the Direct-Shooting Method

The tangential direction is always employed as the initial guess for the control steering. A total of 60 nodes are used to parameterize the optimal control (with 20 for each direction cosine). The initial departure time is January 1, 2009, and the initial transfer time is set to 3 years. The equinoctial elements are used for numerical integration. Running DTOM indicated that no converged solution was obtained without multiple shooting. Tangential control steering always increases the orbital energy. Therefore, if the initial guess of some parameter (e.g. burn time) is not good enough, it is easy to propagate the spacecraft far from the target condition. This drawback could be overcome by the multiple-shooting method with state nodes. Five nodes of semi-major axis and eccentricity (see Table 6.4) are equally inserted between the initial and terminal times. Thus, an extra 10 design variables and 10 equality constraints are created in the NLP problem. As a result, the converged solution in Table 6.5 is obtained with the multiple-shooting method.

Table 6.4 State nodes for multiple shooting using the direct-shooting method (Earth-Mars orbit transfers)

States	Initial guess for nodes
Semi-major axis (AU)	1.1, 1.2, 1.3, 1.4, 1.5
Eccentricity	0.01, 0.01, 0.01, 0.01, 0.01

Table 6.5 Optimal solutions for Earth-Mars transfers using the direct-shooting method and multiple-shooting with state nodes

Launch date	Arrival date	Final mass (kg)	Trip time (days)
July 24, 2009	Nov 28, 2010	959.0290	491.9355

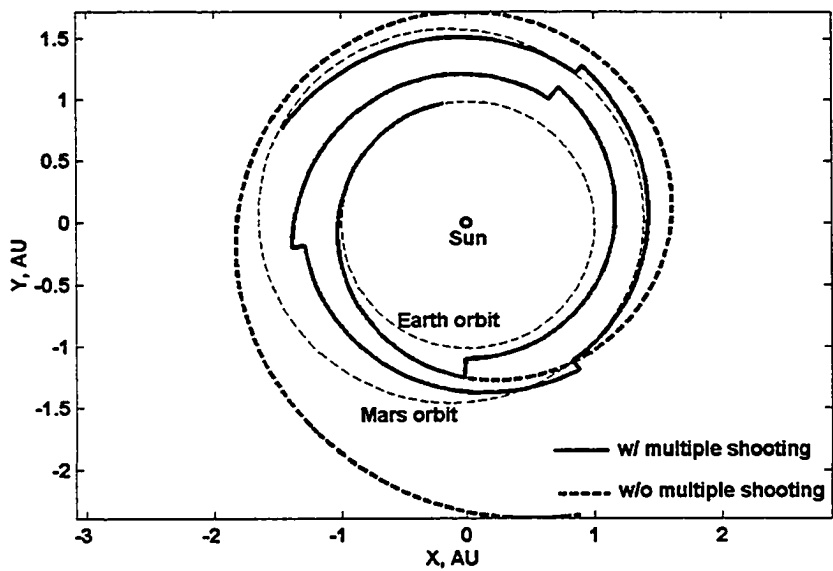


Figure 6.8 Earth-Mars trajectories at the first iteration (direct-shooting method, multiple shooting with state nodes)

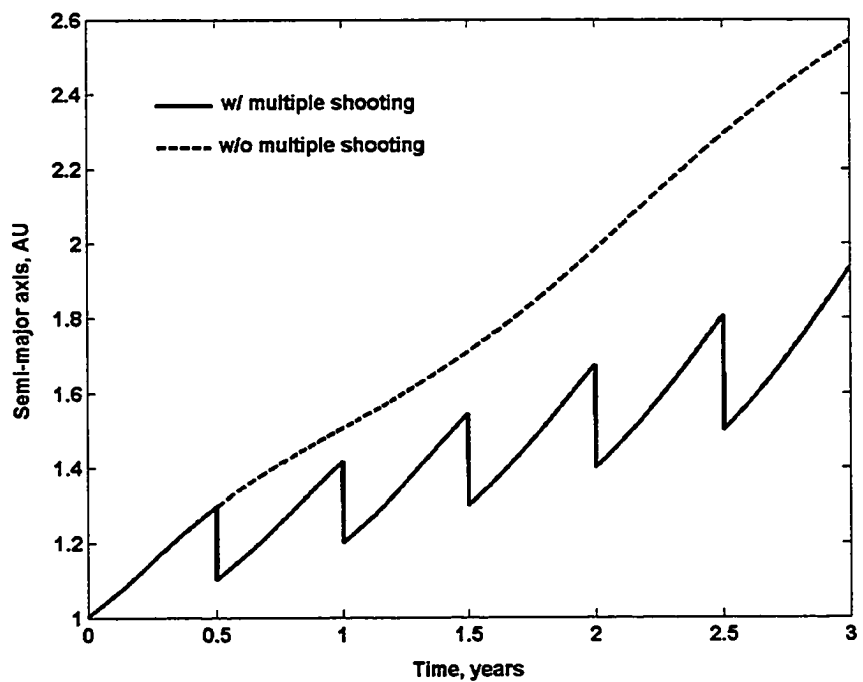


Figure 6.9 Time histories of semi-major axis for Earth-Mars trajectories at the first iteration (direct-shooting method, multiple shooting with state nodes)

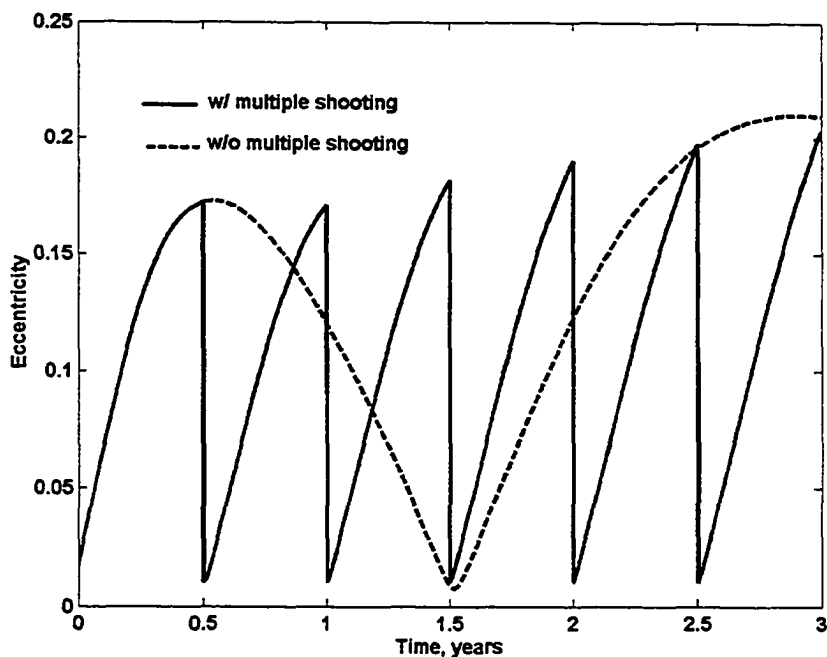


Figure 6.10 Time histories of eccentricity for Earth-Mars trajectories at the first iteration (direct-shooting method, multiple shooting with state nodes)

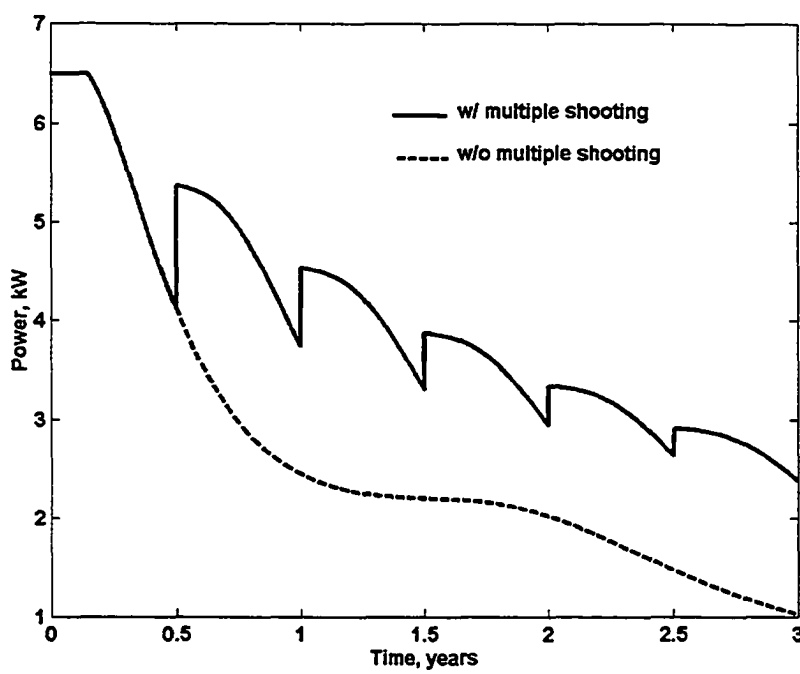


Figure 6.11 Time histories of input power for Earth-Mars trajectories at the first iteration (direct-shooting method, multiple shooting with state nodes)

In Figs. 6.8, it is obvious that the multiple shooting prevents the trajectory from deviating too far away from the Mars target orbit. The semi-major axis overshoots the target without multiple shooting, and is restrained to reasonable values with multiple shooting (see Fig. 6.9). The nodes for the eccentricity (see Fig. 6.10) force the trajectory in a near-circular orbit. In Fig. 6.11, there are no nodes used for power, but power depends on the distance to the sun, which changes with the semi-major axis and eccentricity. Those discontinuous “gaps” eventually disappear when the equality constraints in SQP are satisfied.

6.2.2 Multiple Shooting with Costate Nodes Using the Hybrid Method

In this section, multiple shooting with costate nodes is presented. Since the hybrid method is used, the costate equations are included. The spherical coordinate elements are utilized for numerical integration. As introduced in Chapter 3, the time history of costates could be divided into segments. The initial costates are set as $\lambda_r = 0, \lambda_\theta = 0, \lambda_\phi = 0,$ $\lambda_{v_r} = 0, \lambda_{v_\theta} = -1,$ and $\lambda_{v_\phi} = 0.$ The initial departure time is January 1, 2009, and the initial transfer time is set 1 year. If the multiple shooting is not used, running DTOM shows that no converged solution was obtained. If multiple shooting is employed, 10 nodes for the costates $\lambda_{v_r}, \lambda_{v_\theta}$ and λ_{v_ϕ} (shown in Table 6.6), are equally inserted between the initial and final times. It is obvious that not all costates are needed as nodes, and the optimal control steering is directly affected by the costates $\lambda_{v_r}, \lambda_{v_\theta}$ and $\lambda_{v_\phi}.$ Thus, an extra 30 design variables and 30 equality constraints are created. The converged solution is obtained with multiple shooting and summarized in Table 6.7.

Table 6.6 Costate nodes for Earth-Mars transfer using multiple shooting (Earth-Mars orbit transfers)

Costates	Initial guess for nodes
λ_{v_r}	0. 0. 0. 0. 0. 0. 0. 0. 0. 0.
λ_{v_θ}	-1.0 -1.0 -1.0 -1.0 -1.0 -1.0 -1.0 -1.0 -1.0 -1.0
λ_{v_ϕ}	0. 0. 0. 0. 0. 0. 0. 0. 0.

Table 6.7 Optimal solutions for Earth-Mars transfers using the direct-shooting method and multiple-shooting with costate nodes

Launch date	Arrival date	Final mass (kg)	Trip time (days)
July 25,2009	Nov 28, 2010	959.5072	490.6545

By inserting free nodes into time histories of costates, the control steering is constrained since the optimal control is determined by the costates. Without multiple shooting, these the costates “drift” due to poor initial guess; and multiple shooting allows λ_{v_r} , λ_{v_θ} and λ_{v_ϕ} to “reset” back to reasonable values. Therefore, the control (presented in Fig. 6.13) is constrained in the near-tangential direction with multiple shooting. At the first iteration, the spacecraft lose the orbital energy without multiple shooting due to the poor guess of the initial costates, which result in anti-tangential pitch steering (see Fig. 6.12).

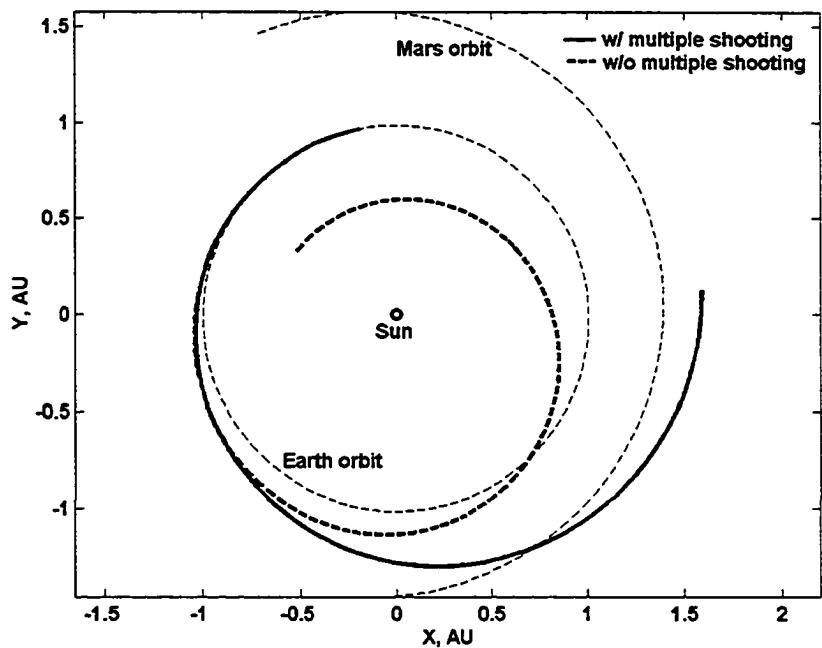


Figure 6.12 Earth-Mars trajectories at the first iteration (hybrid method, multiple-shooting technique with costate nodes)

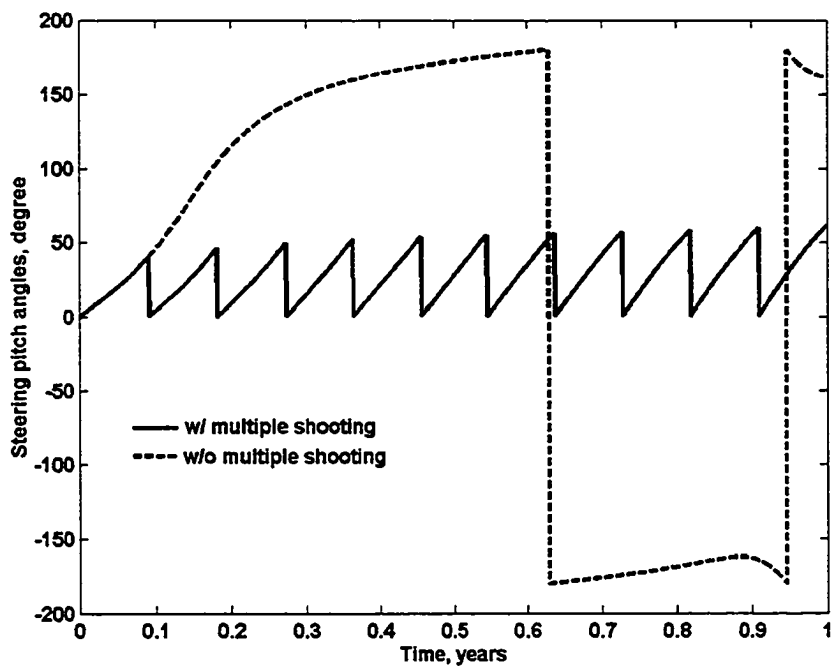


Figure 6.13 Time histories of control steering for Earth-Mars trajectories at the first iteration (hybrid method, multiple-shooting technique with costate nodes)

6.2.3 Multiple Shooting with both State and Costate Nodes Using the Hybrid Method

For the case in which the equinoctial elements are used, the initial costates are set as $\lambda_p = -1, \lambda_f = 0, \lambda_g = 0, \lambda_h = 0, \lambda_k = 0$, and $\lambda_L = 0$. The initial departure time is January 1, 2009, and the initial transfer time is set 1.0 year. If the multiple-shooting method is not used, running DTOM doesn't converge. If multiple shooting is employed, 10 nodes for λ_p, λ_f and λ_g are equally spaced during the time histories of the costates, and 5 nodes for semi-major axis and eccentricity are equally spaced during the time histories of the states (see Table 6.8). An extra 40 design variables and 40 constraints are created in the NLP problem. It is obviously that not all states and costates are employed as nodes. The converged solution is obtained with multiple shooting and is summarized in Table 6.9. The trajectory, control, semi-major axis, eccentricity and input power at the first iteration are shown in Figs.6.14-6.18. Due to free nodes for states and costates, the states (semi-major axis, eccentricity) and control (pitch angle) are all discontinuous for the first iteration.

Table 6.8 State and costate nodes for multiple shooting (Earth–Mars orbit transfer)

Costates or states	Initial guess for nodes
λ_p	-1.0 -1.0 -1.0 -1.0 -1.0 -1.0 -1.0 -1.0 -1.0 -1.0
λ_f	0. 0. 0. 0. 0. 0. 0. 0. 0. 0.
λ_g	0. 0. 0. 0. 0. 0. 0. 0. 0. 0.
Semi-major axis (AU)	1.1, 1.2, 1.3, 1.4, 1.5
Eccentricity	0.01, 0.01, 0.01, 0.01, 0.01

Table 6.9 Optimal solutions for Earth–mars transfers using the hybrid method and multiple-shooting technique with state and costate nodes

Trajectories	Launch date	Arrival date	Final mass (kg)	Trip time (days)
Equinoctial, costate	July 25,2009	Nov 28, 2010	959.5002	490.6073

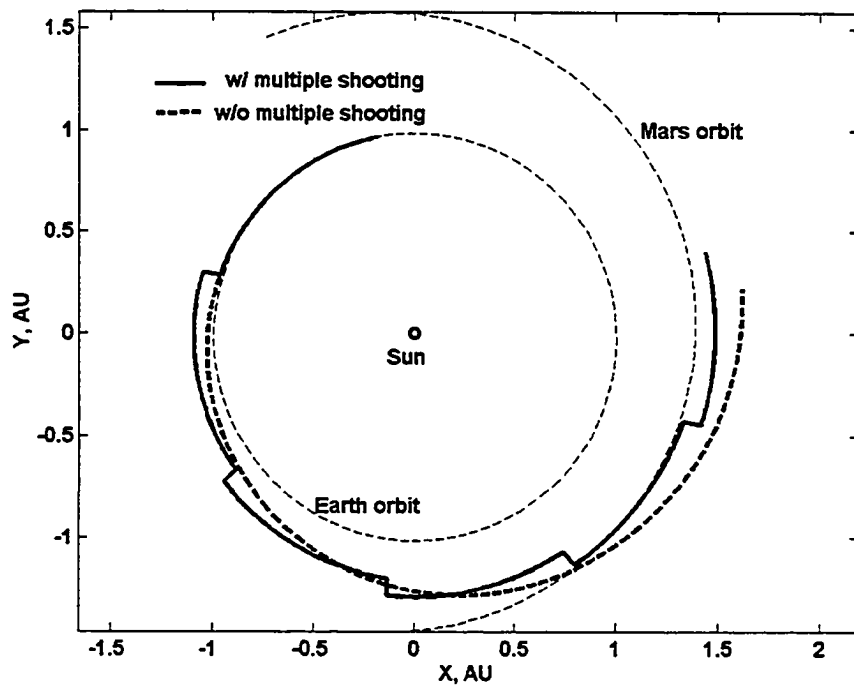


Figure 6.14 Earth-Mars trajectory at the first iteration (hybrid, multiple-shooting technique with state and costate nodes)

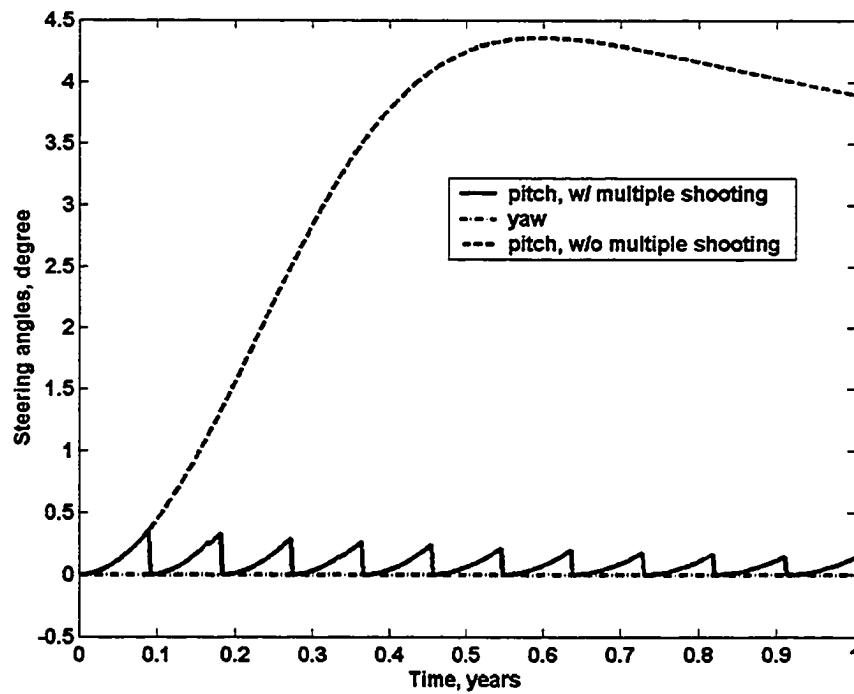


Figure 6.15 Time histories of control steering for Earth-Mars trajectory at the first iteration (hybrid, multiple-shooting technique with state and costate nodes)

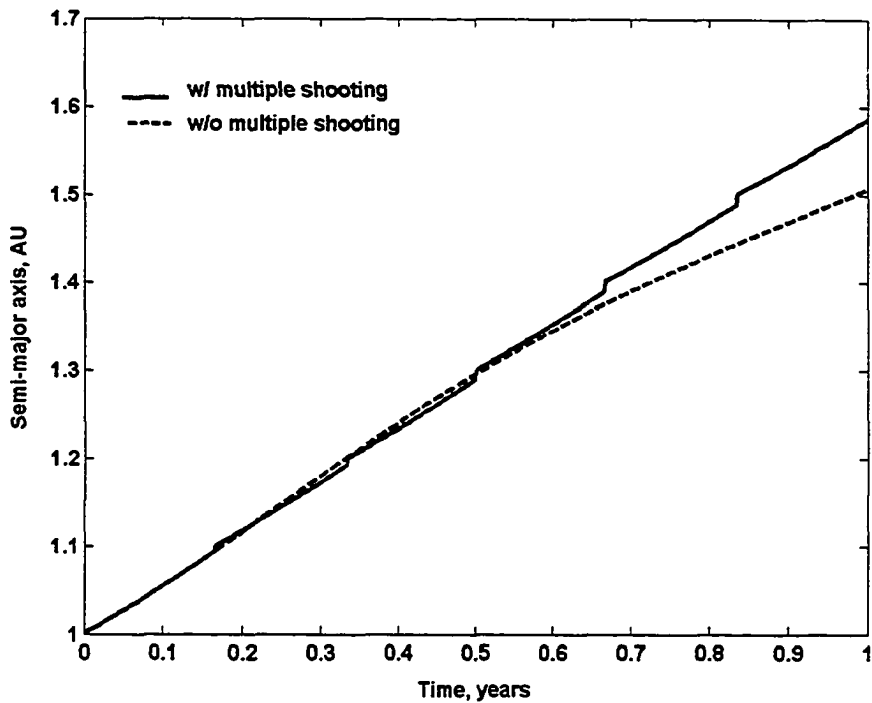


Figure 6.16 Time histories of semi-major axis for Earth-Mars trajectories at the first iteration (hybrid method, multiple-shooting technique with state and costate nodes)

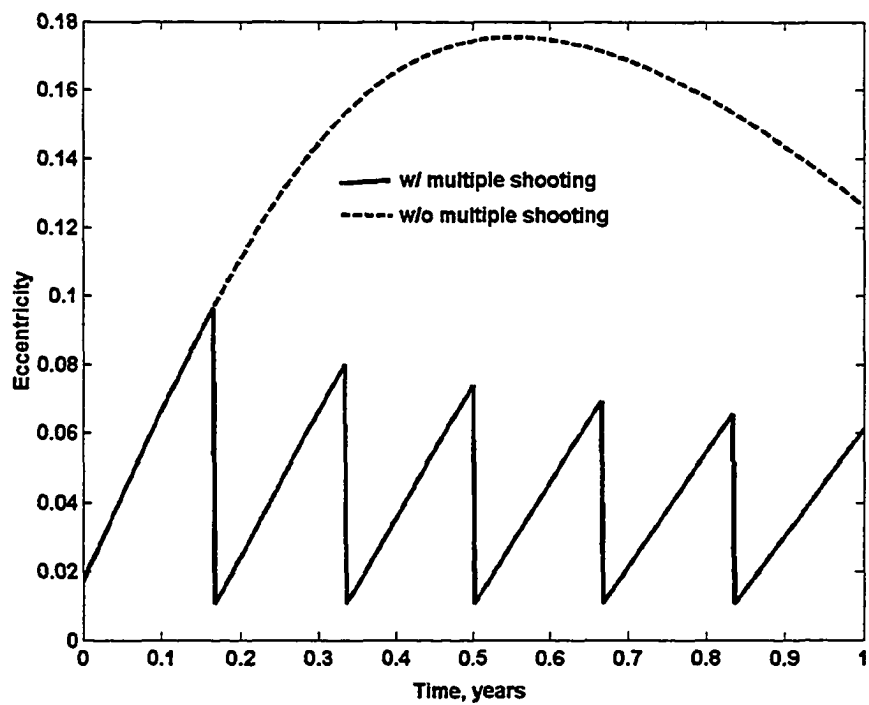


Figure 6.17 Time histories of eccentricity for Earth-Mars trajectories at the first iteration (hybrid method, multiple-shooting technique with state and costate nodes)

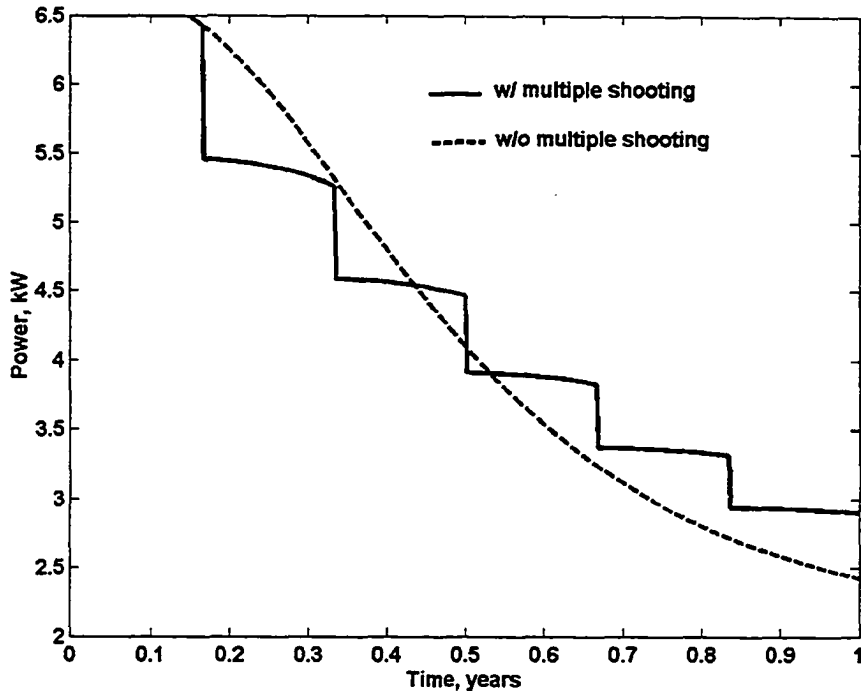


Figure 6.18 Time histories of input power for Earth-Mars trajectories at the first iteration (hybrid method, multiple-shooting technique with state and costate nodes)

The multiple-shooting method with both state and costate nodes constrains not only the states but also the control steering. However, the number of nodes for the states and costates are not necessarily to be the same.

6.3 Optimal Earth-Jupiter Orbit Transfers Using Multiple Shooting

In this section, the multiple-shooting method is used to solve optimal Earth-Jupiter single-burn problems with multiple revolutions and large eccentricity change, which make the problem harder to solve. The power at 1 astronomic unit (AU) is 1.0 kW, which represents the power level of radioisotope electric propulsion (REP) [7, 8] and is constant during the transfer. The constant I_{sp} is 3000 seconds and the engine efficiency is set as 1.0. We also assume the launch mass is fixed as 1200 kg and $C_3 = 0$. The final

mass is to be maximized. For the case in which the equinoctial elements are used, the initial costates are set as $\lambda_p = -1$, $\lambda_f = 0$, $\lambda_g = 0$, $\lambda_h = 0$, $\lambda_k = 0$, and $\lambda_L = 0$. The initial departure time is January 1, 2009, and the initial transfer time is set 1.0 year. If the multiple shooting is not used, the running doesn't converge. 10 nodes for costates λ_p , λ_f and λ_g , and 5 nodes for semi-major axis and eccentricity (shown in Table 5.16), are equally inserted between initial and final time. Therefore, an extra 40 design variables and extra 40 equality constraints are created. The converged solution is obtained with the same guess of the initial costates with multiple shooting. The optimal solution is summarized in Table 6.10.

Table 6.10 State and costate nodes for multiple shooting (Earth-Jupiter orbit transfers)

Costates and states	Initial guess for nodes
λ_p	-1.0 -1.0 -1.0 -1.0 -1.0 -1.0 -1.0 -1.0 -1.0 -1.0
λ_f	0.0 0.0 0.0 0.0 0.0 0.0 0.0 0.0
λ_g	0.0 0.0 0.0 0.0 0.0 0.0 0.0 0.0
Semi-major axis (AU)	2.0, 2.5, 3.0, 3.5, 4.0, 4.5
Eccentricity	0.01, 0.01, 0.01, 0.01, 0.01, 0.01

Table 6.11 Optimal solutions for Earth-Jupiter transfers using the hybrid method and multiple-shooting technique with state and costate nodes

Trajectories	Launch date	Arrival date	Final mass (kg)	Trip time (days)
Equinoctial elements	Aug 11,2007	Mar 7, 2016	574.9446	3130.8238

The optimal trajectory and control steering are presented in Figs. 6.19 and 6.20. Fig.6.21 presents the trajectory at the first iteration. The time histories of control steering, semi-major axis, eccentricity and inclination at the first iteration are shown in Figs.6.22-6.25.

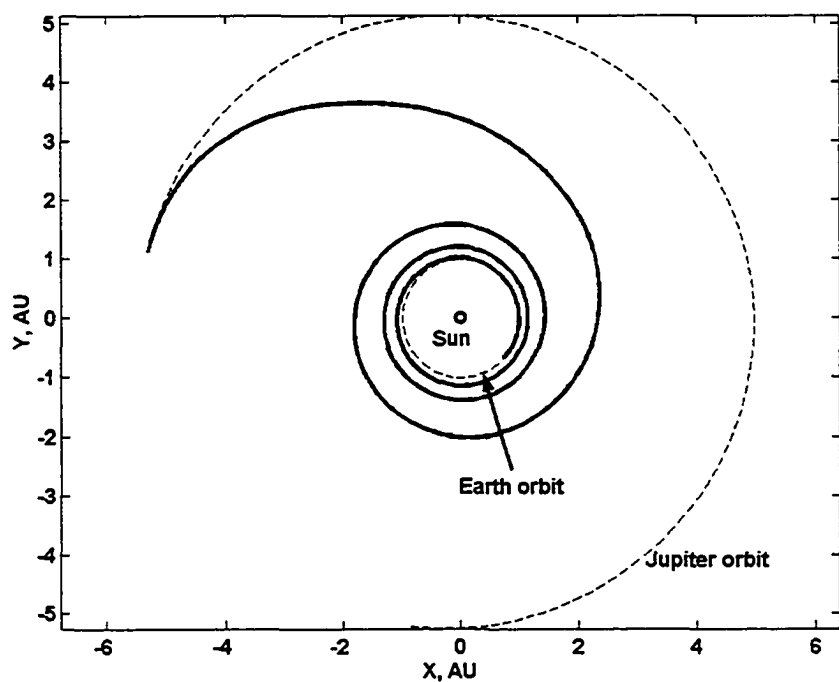


Figure 6.19 Optimal Earth-Jupiter trajectory (hybrid method, multiple-shooting technique with state and costate nodes)

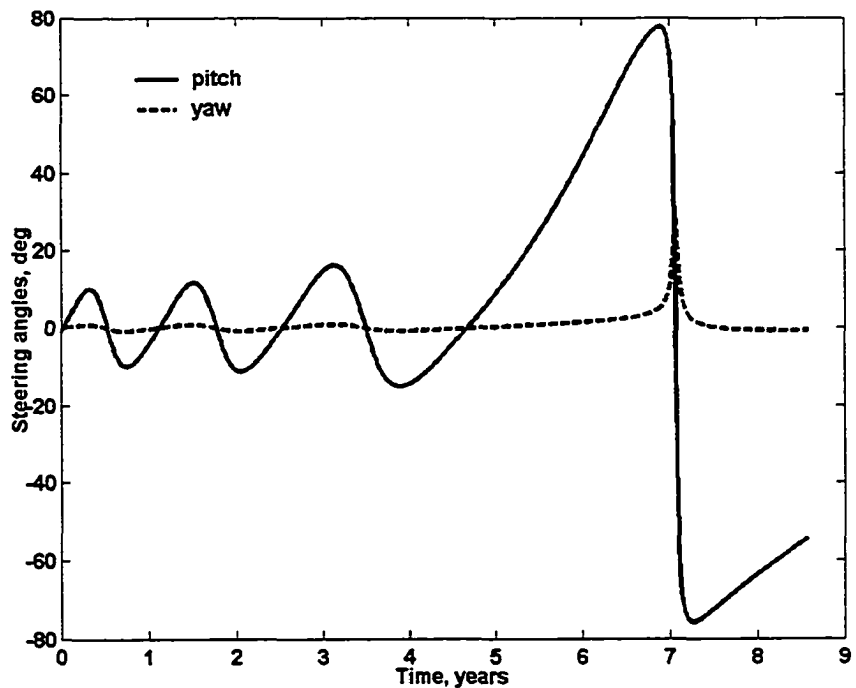


Figure 6.20 Time histories of control steering for optimal Earth-Jupiter trajectory (hybrid method, multiple-shooting technique with state and costate nodes)

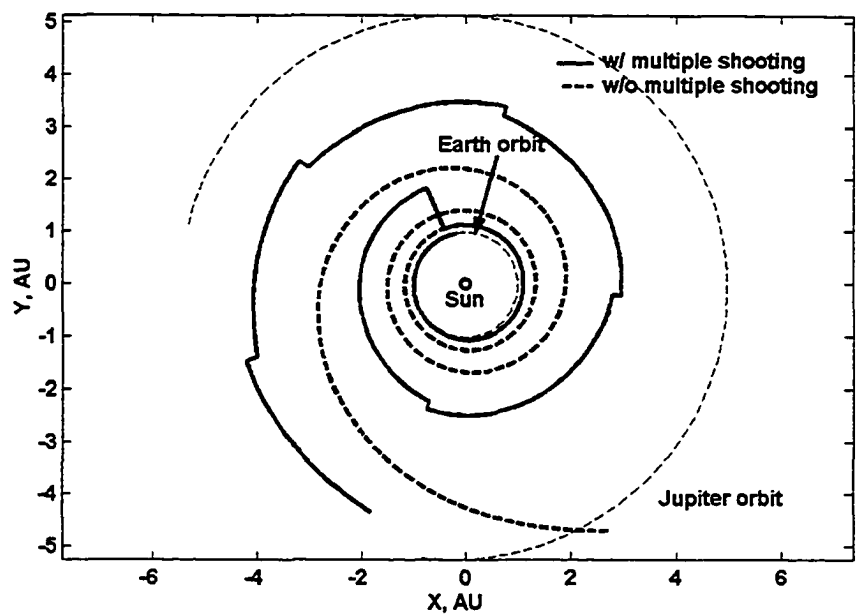


Figure 6.21 Earth-Jupiter trajectories at the first iteration (hybrid method, multiple-shooting technique with state and costate nodes)

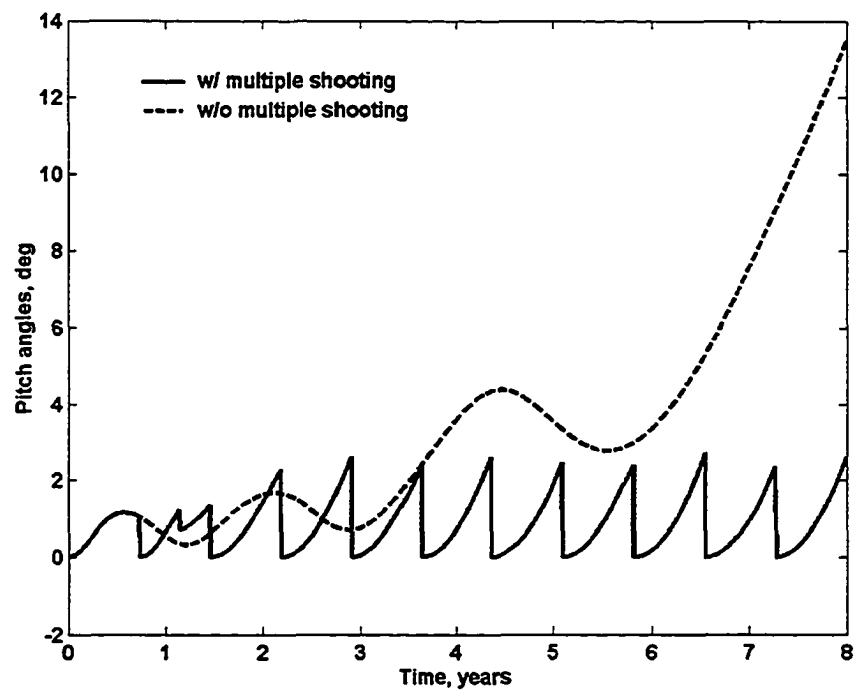


Figure 6.22 Time histories of control steering for Earth-Jupiter trajectory at first iteration using multiple shooting with state and costate nodes

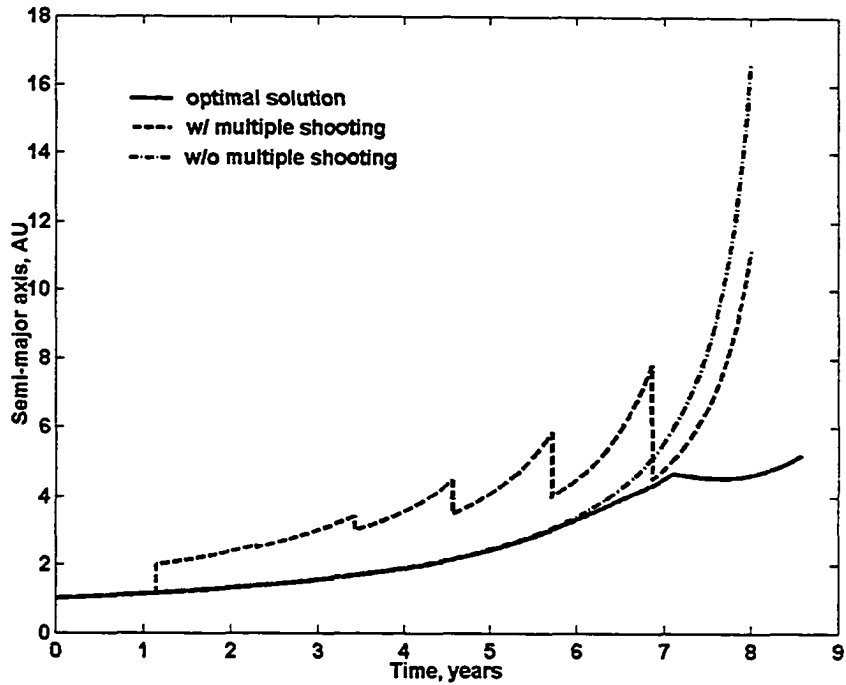


Figure 6.23 Time histories of semi-major axis for Earth-Jupiter trajectories at the first iteration (hybrid method, multiple-shooting technique with state and costate nodes)

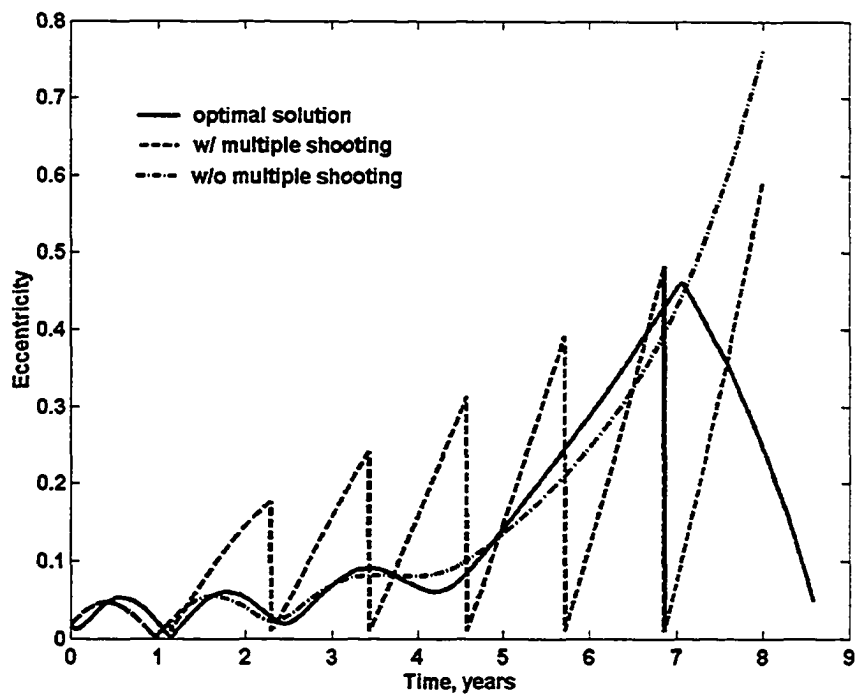


Figure 6.24 Time histories of eccentricity for Earth-Jupiter trajectory at the first iteration (hybrid method, multiple-shooting technique with state and costate nodes)

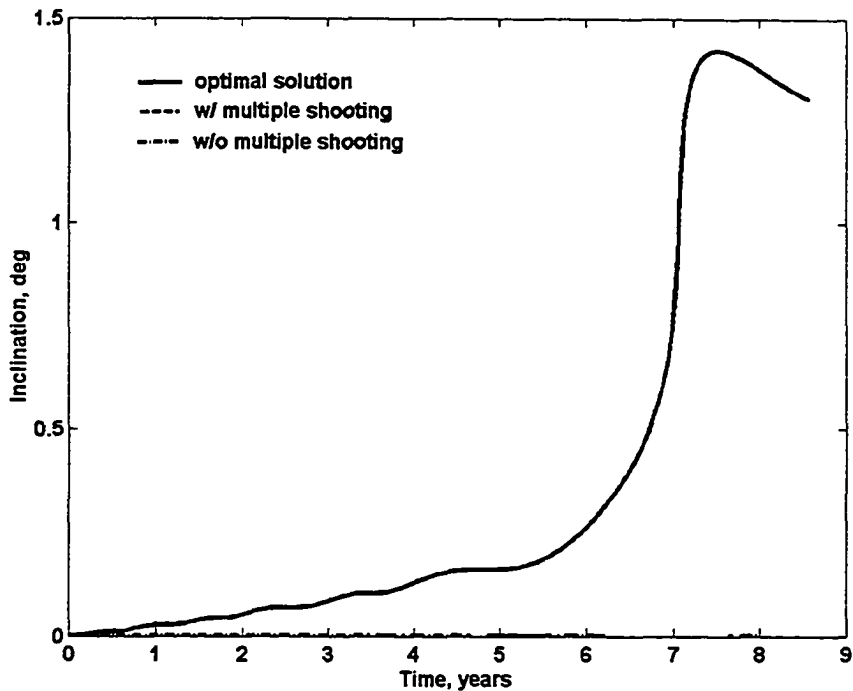


Figure 6.25 Time histories of inclination for Earth-Jupiter trajectories at the first iteration (hybrid method, multiple-shooting technique with state and costate nodes)

The optimal semi-major axis, eccentricity and inclination are also presented in Fig. 6.23-6.25. At the first iteration, the semi-major axis overshoots too much without multiple shooting, and thus the spacecraft is in a highly eccentric orbit (see Fig. 6.23 and 6.24). This drawback is avoided using the multiple-shooting technique with both state and costate nodes.

6.4 Conclusions

Multiple shooting techniques have been successfully applied for both the hybrid and direct-shooting methods. The convergence properties are apparently improved using the multiple-shooting techniques. The techniques are more flexible since not all the state or costate are required to be divided into segments. Therefore, certain state equations and

costate equations are integrated forward in one pass. The major strength of the multiple-shooting techniques is that they create fewer number of free nodes compared with the general collocation method, parallel-shooting method and indirect multiple shooting method (with TPBVP).

CHAPTER 7 INTERPLANETARY MISSION DESIGN USING NSTAR & NEXT ENGINES

In this chapter, two preliminary interplanetary missions, optimal Eros sample return and Pluto-flyby trajectories, are designed using realistic electric engines. Engine configurations such as NSTAR (NASA Solar Electric Power Technology Application Readiness) and NEXT (NASA Evolutionary Xenon Thruster), are utilized for these two missions. A new issue for SEP missions is the operation of multiple engines onboard, and this is taken into consideration in this chapter. The design of optimal Eros sample return trajectories is based on sequential or parallel operation of multiple engines. For the Pluto-flyby mission, engine-switching logic is employed to improve the efficiency of operating multiple engines. These two missions also demonstrate the successful application of the direct-shooting method in designing complex optimal interplanetary orbit transfers.

7.1 Optimal Eros Sample Return Trajectories

7.1.1 Introduction

On February 17, 1996, the NEAR Shoemaker spacecraft was launched from Cape Canaveral Air Station. On February 12, 2001, the NEAR spacecraft touched down on asteroid Eros [80]. This summarizes the near Earth asteroid rendezvous (NEAR) mission, designed as the first asteroid orbiter, which captured images of Eros at extremely high resolution. This one-way mission was not designed to return samples from Eros. Therefore, the next step might be a sample return mission, which makes it possible to bring Eros samples back to Earth.

The current sample return mission, MUSES-C managed by Japan's Institute of Space and Astronautical Science (ISAS) and NASA, should be the first space mission to collect asteroid surface samples and return them to Earth for detailed compositional analyses. MUSES-C is the temporary name (Mu Space Engineering Spacecraft-C) given to the mission prior to launch. The MUSES-C spacecraft was supposed to be launched in December 2002. After an earth swingby in May 2004, the spacecraft will rendezvous with near-Earth asteroid 1998 SF36 in June 2005. After a stay of about five months, MUSES-C will return to Earth in June 2007 with an asteroid surface sample of a few grams.

In this section, the study is focused on computing optimal Eros sample return trajectories. The primary propulsion system is the solar electric propulsion NSTAR engine due to the fact that the spacecraft performing near-Earth missions can take advantage of solar energy. Two types of trajectories are presented, the parallel-burn case and the sequential-burn case. In the first case, three SEP engines are fired simultaneously throughout the mission, and only one engine is fired at a time in the second case. Due to the smaller thrust level in the sequential-burn case, an Earth gravity assist is employed so that the total transfer time increases. However, the payload mass delivery seems also satisfactory, and both cost and technical complexity could be reduced if only one engine is operated at a time. The optimal trajectories presented in this chapter are candidate preliminary designs for a future Eros sample return mission.

7.1.2 System Dynamics

The equinoctial elements (2.33)-(2.38) are utilized to avoid singularities during numerical integration. The equations of motion are described by Eqs. (2.39)-(2.44), and the thrust magnitude is modeled as:

$$T = \frac{2\eta P}{gI_{sp}} \times \text{duty cycle} \quad (7.1)$$

where $c = gI_{sp}$ is the engine exhaust velocity, η is the thruster efficiency, and P is the engine input power. The *duty cycle* is considered for coast arcs required for navigation and is simply modeled to be a constant factor in thrust computation. In a real mission, the duty cycle approximates coasts during burn arcs (i.e., 0.90 means thrust is on 90% of burn durations and is off on 10% of burn durations). The thrust magnitude is not constant for spacecraft using SEP in an interplanetary mission. The power is dependant on the performance of solar array, which is commonly referred to as the relation between power generated and the distance to the sun. The total available power is expressed by Eq. (7.2) in an inverse-square relation.

$$P_{total} = P_0 / r^2 \quad \text{and} \quad P_{total} \leq P_0 \quad (7.2)$$

where r is in AU, and P_0 is the power at 1 AU. The total power will be distributed to the engines onboard. The input power for a single engine should be within the engine's operating range. Suppose \bar{P}_i is the power allocated to the i^{th} engine, the actual input power for the i^{th} engine P_i is as follows:

$$P_i = \begin{cases} 0 & \text{if } \bar{P}_i \leq P_{\min} \\ \bar{P}_i & \text{if } P_{\min} \leq \bar{P}_i \leq P_{\max} \\ P_{\max} & \text{if } \bar{P}_i > P_{\max} \end{cases} \quad (7.3)$$

where P_{\max} and P_{\min} are the maximum and minimum input power for each single engine.

The engine exhaust velocity I_{sp} and thruster efficiency η are determined by the power P_i .

For the Eros sample return mission, the NSTAR engine is used, in which case the values of I_{sp} and η are determined by 16 discrete values of input power P_i shown in Table 7.1.

In trajectory optimization process, linear interpolation is used to compute the continuous values of I_{sp} and η . The specific impulse I_{sp} essentially controls the mass-flow rate.

Table 7.1 I_{sp} and efficiency η of NSTAR engine

Power (kW)	I_{sp} (sec.)	η
0.47	1972	0.420
0.60	2376	0.472
0.74	2671	0.487
0.86	2836	0.527
0.97	2935	0.554
1.09	3002	0.574
1.21	3058	0.590
1.33	3067	0.596
1.44	3109	0.611
1.57	3136	0.618
1.70	3177	0.626
1.82	3189	0.631
1.94	3174	0.628
2.06	3185	0.630
2.17	3157	0.624
2.29	3120	0.618

For the Eros sample return mission, the performance index is either the final mass or payload mass, depending on the specific tasks expected. Power at 1AU, P_0 , is either selected at different power levels or is to be optimized by the NLP method. It is assumed there are three engines equipped onboard, and they are operated in two modes - burning sequentially or in parallel. The minimum and maximum input power of a single NSTAR

engine is 0.47 kW and 2.29 kW, respectively so that the total maximum usable input power is 2.29 kW for burning sequentially and 6.87 kW for burning in parallel. For burning in parallel, the available power is equally distributed to each engine, and then no engine switching is employed. Obviously, simultaneously operating three NSTAR engines provides greater thrust, but simultaneously operating multiple engines increases the technical complexity. Single engine operation is technically easier, but mission duration increases.

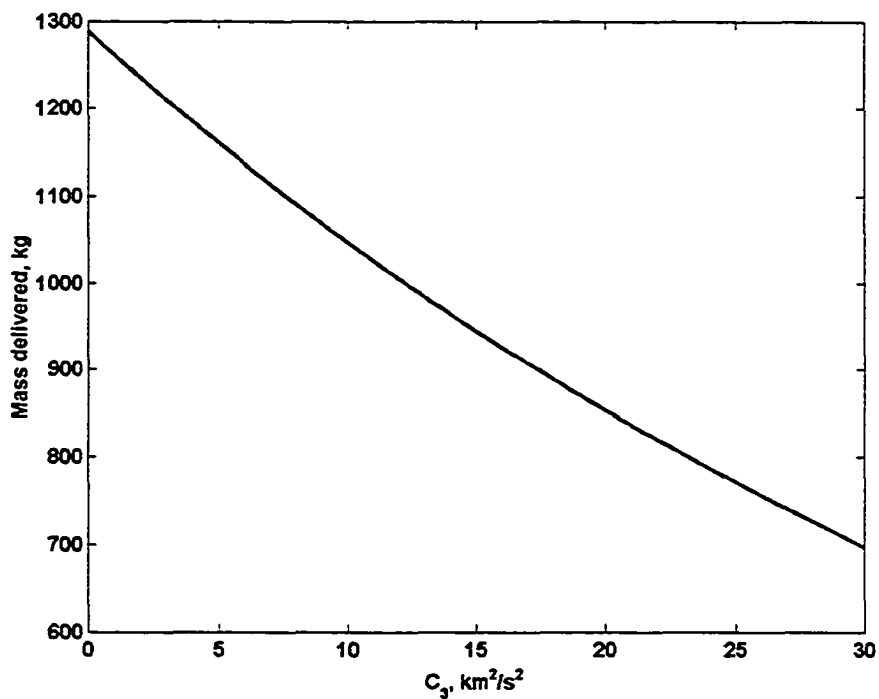


Figure 7.1 C_3 vs. delivered mass for Delta 7925

The spacecraft is assumed to be launched by a Delta 7925, which is a medium-sized launch vehicle also used for the 1996 NEAR mission. The launch altitude is 185 km, and the launch inclination is 28.5 deg. The curve for delivered mass and C_3 (energy) is approximated as a fifth-order polynomial, which is shown in Fig. 7.2.

The period of staying at Eros is constrained in three time windows. They are May 18, 2010 to October 2, 2010; May 20, 2011 to November 7, 2011; and February 20, 2012 to July 7, 2012. The stay time is constrained by seasonal lighting condition for landing.

7.1.3 Maximum Payload Computation Using SEP

In this mission scenario, the maximized payload mass is desired. The calculation of payload of SEP system is presented in this section. Suppose that m_0 is the delivered mass, which is determined by a launch vehicle (see Fig. 7.1), m_f is the final mass, m_{fuel} is the total mass of fuel (with reserved portion), and m_{sep} is the total mass of the SEP system. The launch mass consists of payload mass, fuel mass, and total mass of the SEP system.

$$m_0 = m_{P/L} + m_{fuel} + m_{sep} \quad (7.4)$$

The total mass of the SEP system can be divided into the fixed SEP mass \bar{m}_{sep} and the variable SEP mass \tilde{m}_{sep} .

$$m_{sep} = \tilde{m}_{sep} + \bar{m}_{sep} \quad (7.5)$$

The total dry (no fuel) and wet masses (with fuel) are defined as:

$$m_{total_dry} = m_{P/L} + m_{sep} = m_{P/L} + \bar{m}_{sep} + \tilde{m}_{sep} \quad (7.6)$$

$$m_{total_wet} = m_{P/L} + m_{sep} + m_{fuel} = m_{P/L} + \bar{m}_{sep} + \tilde{m}_{sep} + m_{fuel} \quad (7.7)$$

The SEP dry and wet masses are

$$m_{sep_dry} = m_{sep} = \bar{m}_{sep} + \tilde{m}_{sep} \quad (7.8)$$

$$m_{sep_wet} = m_{sep} + m_{fuel} = \bar{m}_{sep} + \tilde{m}_{sep} + m_{fuel} \quad (7.9)$$

The total wet mass is actually the launch mass m_0 , and the SEP dry mass is m_{sep} . The fixed mass \bar{m}_{sep} is given for a specific SEP system, and \tilde{m}_{sep} is composed of the mass of the fuel tank m_{tank} (dependant on amount of fuel), mass of solar array $m_{s/a}$ (dependant on the system initial power at 1 AU), mass of structure m_{st} relative to the wet mass of the SEP system, and mass of harness m_h relative to dry mass of SEP system.

$$\tilde{m}_{sep} = m_{tank} + m_{s/a} + m_{st} + m_h \quad (7.10)$$

Each part of the variable SEP mass is defined as follows:

$$m_{tank} = K_t m_{fuel} \quad (7.11)$$

$$m_{s/a} = \alpha_{power} P_0 \quad (7.12)$$

$$m_{st} = K_{st} (m_{sep} + m_{fuel}) = K_{st} (\bar{m}_{sep} + \tilde{m}_{sep} + m_{fuel}) \quad (7.13)$$

$$m_h = K_h m_{sep} = K_h (\bar{m}_{sep} + \tilde{m}_{sep}) \quad (7.14)$$

where K_t , α_{power} , K_{st} and K_h are coefficients for computing m_{tank} , $m_{s/a}$, m_{st} and m_h , respectively. It is easy to compute the mass of fuel as:

$$m_{fuel} = (m_0 - m_f - m_{drop})(1 + K_{res}) \quad (7.15)$$

where m_{drop} is the mass dropped during transfers, and K_{res} is the factor of the reserved mass for the fuel. The variable mass of SEP system can be expressed as:

$$\tilde{m}_{sep} = K_t m_{fuel} + \alpha_{power} P_0 + K_{st} (\tilde{m}_{sep} + \bar{m}_{sep} + m_{fuel}) + K_h (\tilde{m}_{sep} + \bar{m}_{sep}) \quad (7.16)$$

$$(1 - K_{st} - K_h) \tilde{m}_{sep} = K_t m_{fuel} + \alpha_{power} P_0 + K_{st} (\bar{m}_{sep} + m_{fuel}) + K_h \bar{m}_{sep} \quad (7.17)$$

$$\tilde{m}_{sep} = \frac{\alpha_{power} P_0 + (K_t + K_{st}) m_{fuel} + (K_{st} + K_h) \bar{m}_{sep}}{1 - K_h - K_{st}} \quad (7.18)$$

The payload mass is computed as:

$$m_{P/L} = m_0 - m_{sep} - m_{fuel} = m_0 - \bar{m}_{sep} - \tilde{m}_{sep} - m_{fuel} \quad (7.19)$$

$$m_{P/L} = m_0 - \bar{m}_{sep} - \frac{\alpha_{power} P_0 + (K_t + K_{st}) m_{fuel} + (K_{st} + K_h) \bar{m}_{sep}}{1 - K_h - K_{st}} - m_{fuel} \quad (7.20)$$

In this case, the fixed SEP mass \bar{m}_{sep} is 257 kg. The other coefficients are $K_t = 0.025$, $K_{st} = 0.09$, $K_h = 0.05$, $\alpha_{power} = 5.7471$ kW/kg, and $K_{res} = 0$.

7.1.4 Numerical Results

The direct-shooting method is utilized for the Eros sample return trajectory optimization. For the mode of burning in parallel, the flight sequence (burn-coast-burn-loiter-burn-coast-burn-burn-coast) is specified a priori. The design variables in the NLP problem are described as follows. There are a total of 138 design variables, where 126 nodes are used for control steering (expressed by direction cosines) with 7 nodes for each burn, except the second burn with 21 nodes. The other design variables include durations for four burns, durations for three coasts, launch date, escape energy C_3 , right ascension of ascending node and longitude angle at burnout point, and number of days to stay at Eros. The launch date is constrained within the year 2008. The period to stay at Eros must be greater than 90 days and less than 365 days. The Eros latest arrival date is July 2, 2010, and the Eros earliest leaving date is August 18, 2010. The total maximum propellant mass is 360 kg (120 kg for each engine). For the mode of burning sequentially, the sequence of burn-flyby-burn-loiter-burn-coast is assumed in advance. The design variables in nonlinear programming SQP are as follows. There are a total of 74 design variables where 63 nodes are used for control steering (expressed by direction cosines) with 7 nodes for each burn. The other design variables include two parameters for Earth-

flyby, durations for three burns, duration for one coast, launch date, escape energy C_3 , right ascension of ascending node and longitude angle at burnout point, and days to stay at Eros. The launch date is constrained in late 2009 and early 2010. The Eros period to stay at Eros must be greater than 90 days and less than 365 days. The Eros latest arrival date is April 7, 2012, and the Eros earliest leaving date is May 21, 2012. The maximum propellant mass is 360 kg (120 kg for each engine).

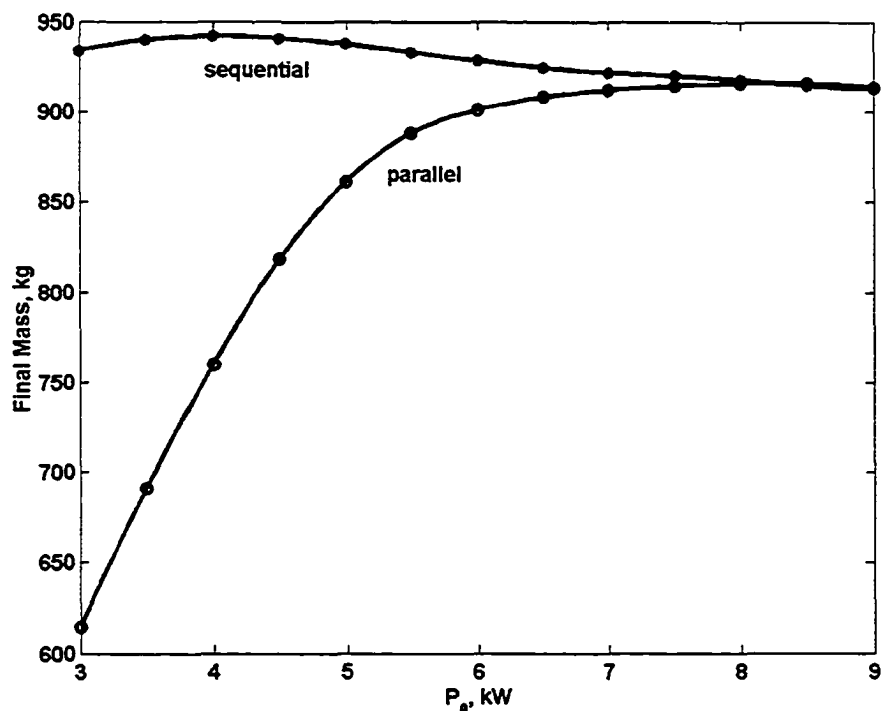


Figure 7.2 Final mass vs. P_0 with final mass maximized

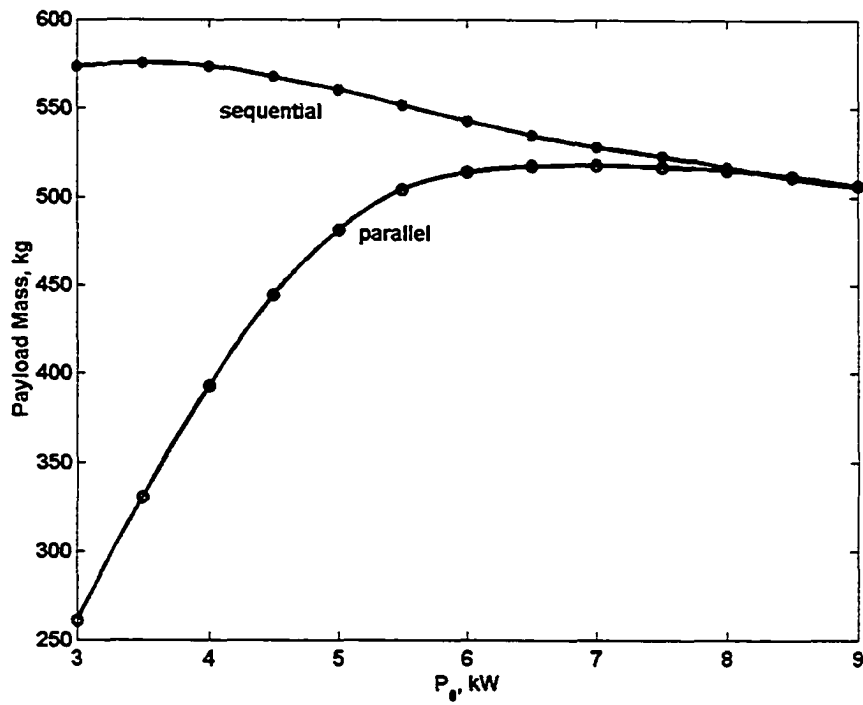


Figure 7.3 Payload mass vs. P_e with final mass maximized

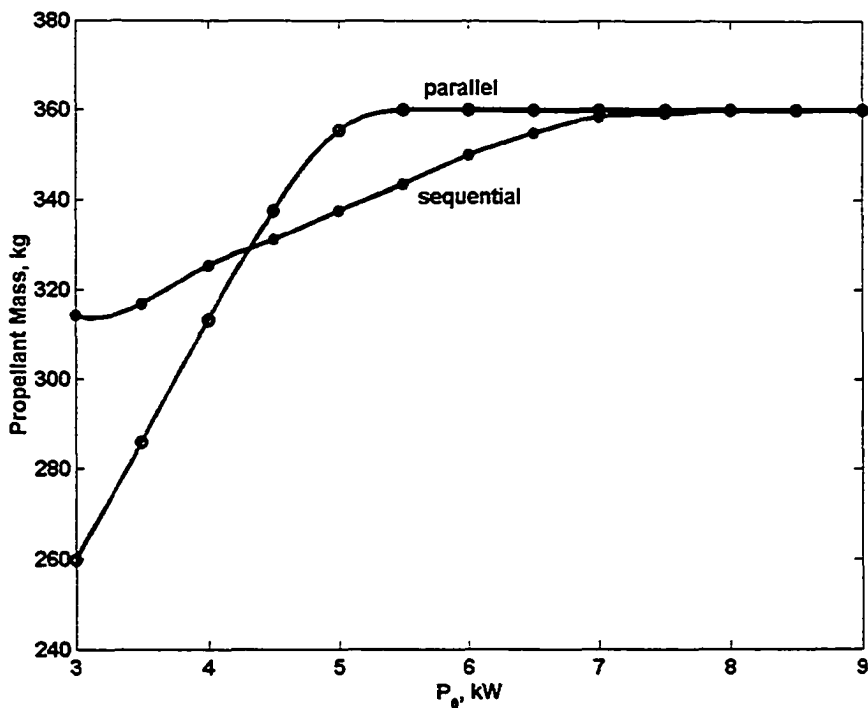


Figure 7.4 Propellant masses vs. P_e with final mass maximized

Figures 7.2, 7.3 and 7.4 show the relations between final mass, payload mass, and propellant mass vs. initial power level with maximized final mass. Based on these solutions, the payload mass is to be maximized around 3.5 kW for burning sequentially and around 7 kW for burning in parallel. Thus, initial power at 1 AU, P_0 , is to be optimized. The optimization results are summarized in Table 7.2. The trajectories and control steering are presented in Figs. 7.5-7.8. The trajectory in the parallel-burn case has no gravity assist, and the trajectory in the sequential-burn case has an Earth gravity assist.

Table 7.2 Optimization results for optimal Eros sample return trajectories (parallel-burn, sequential-burn)

Solutions	Parallel-burn	Sequential-burn
Launch date	July 30, 2008	October 17, 2008
Earth return date	January 26, 2012	January 23, 2015
Eros arrival date	June 12, 2010	March 23, 2012
Eros leaving date	September 10, 2010	June 21, 2012
Stay time on Eros (days)	90 days	90
Launch mass (kg)	1271.72	1256.94
Final mass (kg)	911.72	940.19
Propellant mass (kg)	360.00	316.74
Payload mass (kg)	518.38	575.61
C_3 (km^2/s^2)	0.624	1.182
RAAN at burnout point	110.92 deg	119.45 deg
Longitude angle at burnout point	-81.82 deg	223.30 deg
Earth GA date	n/a	January 20, 2010
Earth GA Δv (km/s)	n/a	7.412
Earth GA r_p	n/a	350
Earth GA rotation angle	n/a	-138.38
V_∞ at Earth return (km/s)	7.45	6.34
Optimized P_0 (kW)	6.939	3.500

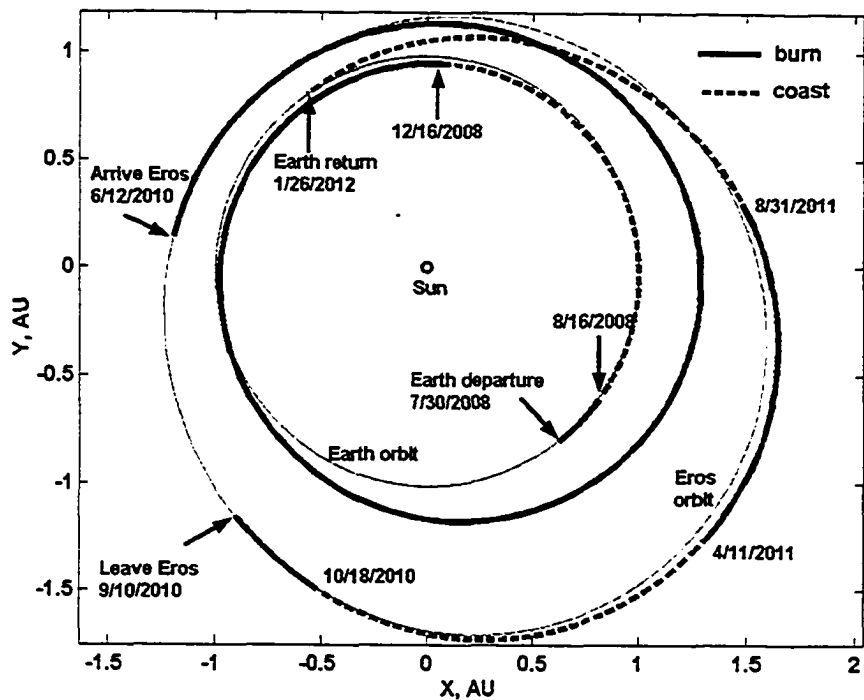


Figure 7.5 Optimal Eros sample return trajectory without gravity assist (parallel-burn)

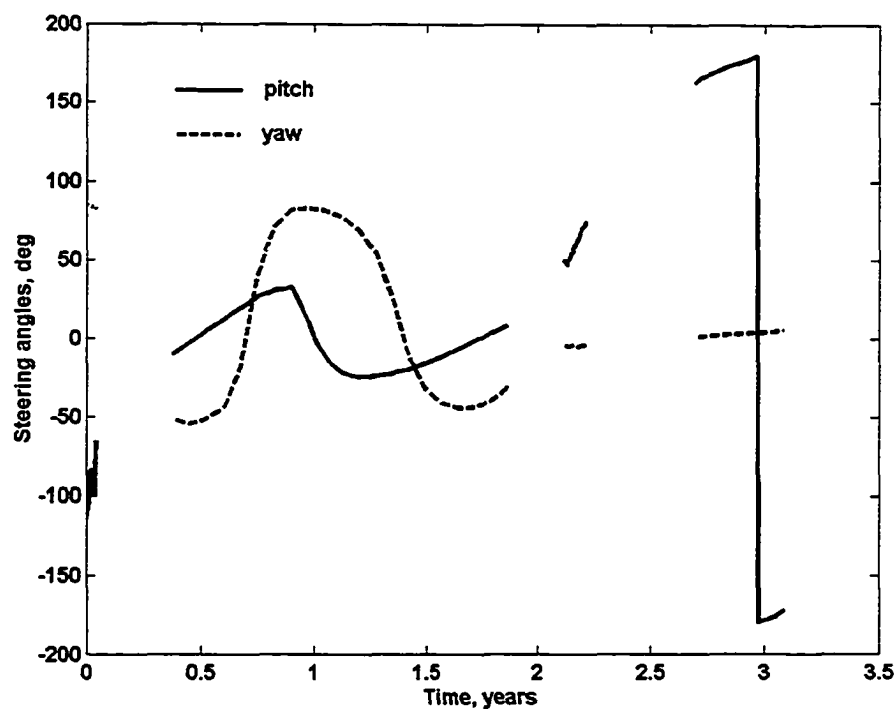


Figure 7.6 Time histories of control steering for optimal Eros sample return trajectory without gravity assist (parallel-burn)

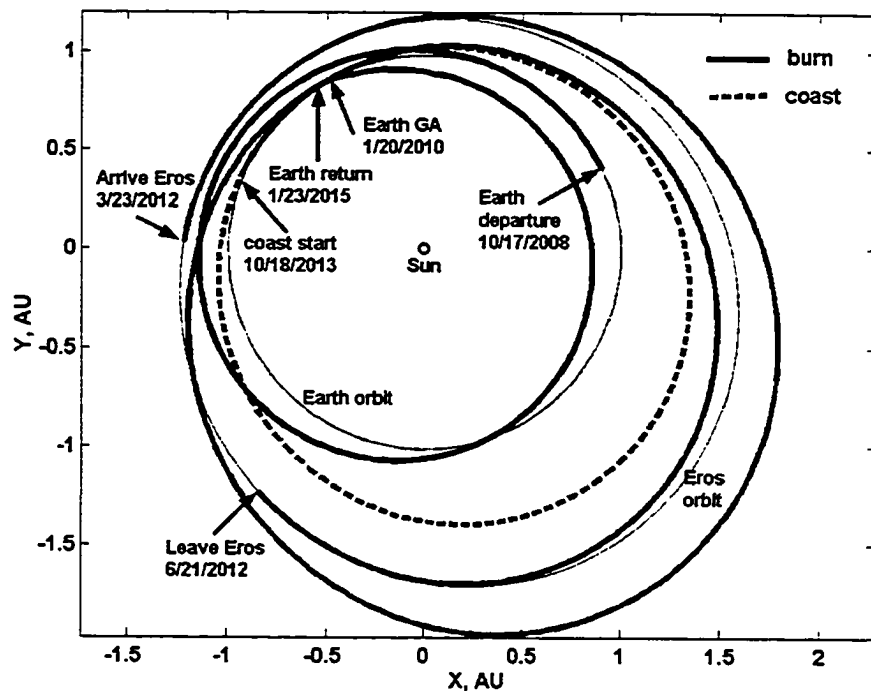


Figure 7.7 Optimal Eros sample return trajectory with Earth gravity assist (sequential-burn)

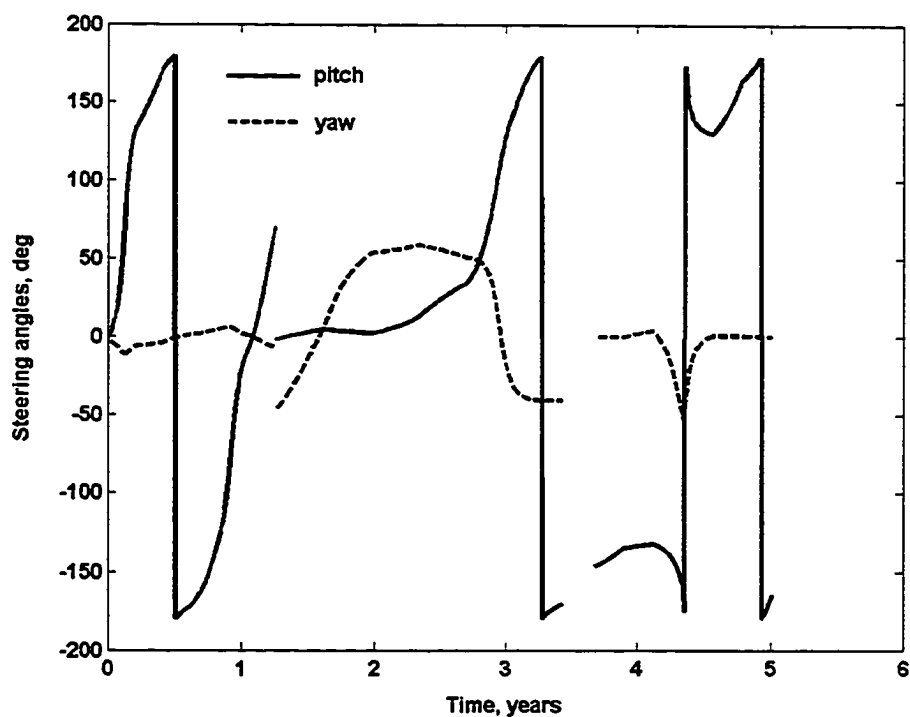


Figure 7.8 Time histories of control steering for optimal Eros sample return trajectory with Earth gravity assist (sequential-burn)

For the Eros sample return mission, we also consider dropping some devices to land on Eros for sampling. After the sampling work is done, the devices might be discarded to reduce the total mass of spacecraft in the return lag. In Table 7.2, we do not consider dropping mass at Eros, which is set to zero. To consider the dropped mass in optimization, we simply subtract a value of mass specified when the spacecraft leaves Eros, and then we obtained a series of payload mass with different values of the dropped mass. The results are shown in Fig. 7.9.

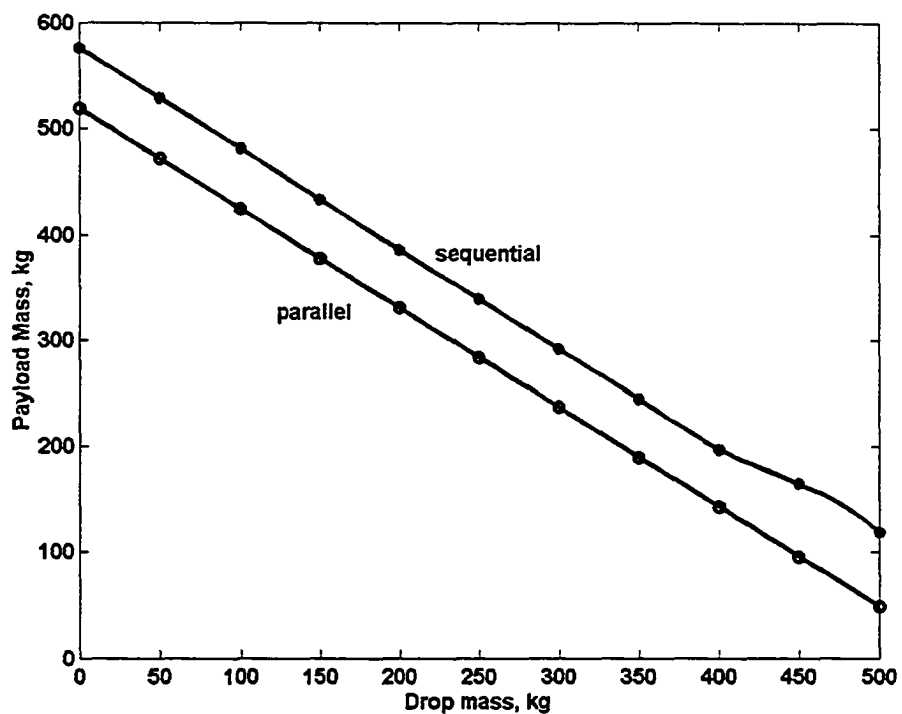


Figure 7.9 Payload mass vs. dropped mass (parallel-burn, sequential-burn)

7.1.5 Conclusions

The optimal Eros sample return trajectories have been presented. The operation of three engines in parallel and sequentially is also taken into consideration. Operation of

one engine at a time reduces the complexity of propulsion system and also gives satisfactory performance with the Earth gravity assist. The optimization of the final mass and payload mass for two cases has been investigated, respectively. The effect of mass dropped at Eros is also analyzed. The simulation results show that the SEP would be a viable option for this mission. These optimal trajectories could be considered for the base design of the future Eros sample return missions.

7.2 The Pluto-Flyby Mission Using SEP and Engine-Switching Logic

7.2.1 Introduction

The Pluto-flyby mission will help us understanding the world at the edge of our solar system by making the reconnaissance of Pluto and its satellite. Pluto is the only planet in the solar system, which has not been visited by the man-made spacecraft. Pluto is also the farthest planet from the sun. The orbital elements of Pluto are shown in Table 7.3. Pluto has a relatively large inclination and eccentricity, and its orbit also goes into the orbit of Neptune.

Table 7.3 Orbital Elements of Pluto

Orbital elements	Values
Semi-major axis	39.76 AU
Eccentricity	0.2583
Inclination	17.136 deg
Right ascension of ascending node	109.870 deg
Longitude of perihelion	222.894 deg

Based on current space technologies, scientists expect that the reconnaissance information could be sent back to the Earth by spacecraft in less than 15 years. Recently, the New Horizons, Pluto-Kuiper Belt mission, managed by the Johns Hopkins University - Applied Physics Laboratory, is designed to help us discover this mystery by making the

first flyby of Pluto and Charon – a "double planet" system. The mission would also visit one or more Kuiper belt objects, in the region beyond Pluto and observed a set of minor planets called "ice dwarfs" that have yet to be studied and could be connected with creation of the solar system.

The trajectory presented by the Applied Physics Laboratory is based on chemical propulsion. The spacecraft will gain the gravity assist of Jupiter and then reach Pluto. In this work, SEP propulsion is proved to be another option to perform the Pluto-Flyby mission. Due to the low-thrust feature of SEP and available power varying depending on the distance from the sun, multiple engines are equipped onboard. Both NSTAR and NEXT engines are utilized. It is also found that the engine switching needs to be considered due to the configurations of NSTAR and NEXT. Also it is shown that different engine-switching logic gives different performance.

7.2.2 System Dynamics and Engine-Switching Logic

The equinoctial elements (2.33)-(2.38) are utilized to avoid singularities for numerical integration. The equations of motion are also described by Eqs. (2.39)-(2.44), and the thrust magnitude is modeled as in Eq. (7.1). The total available power is expressed by Eq. (7.20) in an inverse square relation and P_0 is the power at 1 AU. The duty cycle is 0.92.

$$P_{\text{total}} = P_0 / r^2 \quad \text{and} \quad P_{\text{total}} \leq 2P_0 \quad (7.21)$$

In this case, the fixed SEP mass \bar{m}_{sep} is 257 kg. The other coefficients for payload mass computation are $K_t = 0.025$, $K_{st} = 0.09$, $K_h = 0.05$, $\alpha_{\text{power}} = 5.7471 \text{ kW/kg}$, and $K_{\text{res}} = 0.1$. In addition, we also consider the launch vehicle contingency $K_{\text{conty}} = 0.1$. The actual

delivered mass is $m_0(1-K_{conty})$, and m_0 is determined by the launch vehicle Delta IV 4450, whose performance is shown in Fig. 7.10.

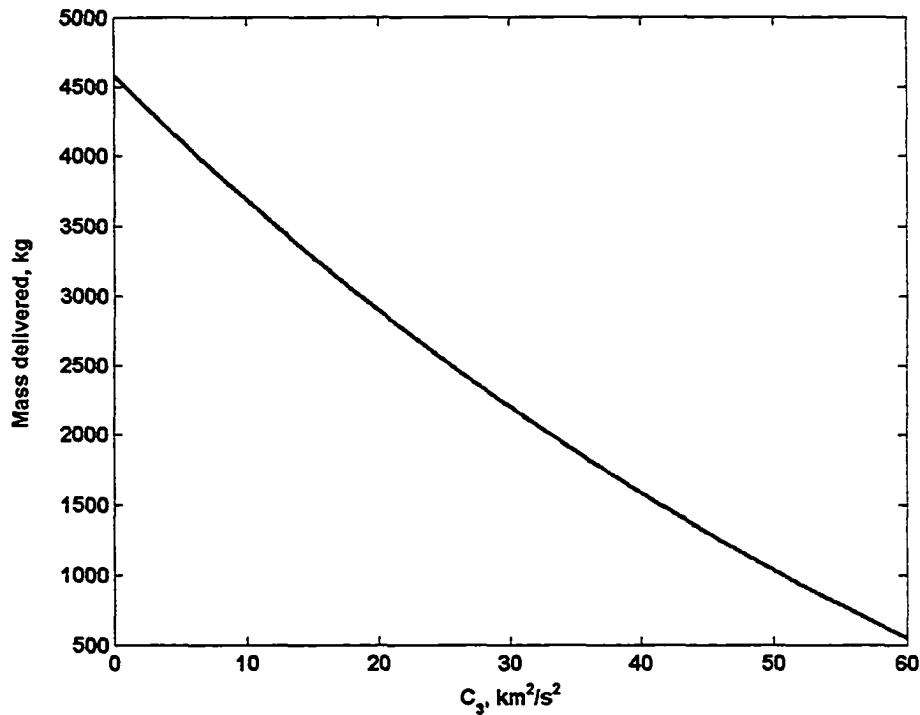


Figure 7.10 C_3 vs. delivered mass for Delta IV 4450

Multiple SEP engines are used to implement Pluto-flyby mission. We propose the question regarding how to operate multiple engines during the transfers – should they be fired simultaneously or is there a certain engine-switching logic? The natural way is that all engines mounted are used, and the available power is distributed equally for each engine. However, if the total available power is not large enough for distribution to all engines onboard (due to the lower limit of input power), we have to use fewer engines to handle the total available power. Furthermore, even when the total available power is large enough, using all onboard engines might not be optimal. With gravity assist of Venus, the Pluto-flyby trajectory has a feature that the spacecraft flies away from the sun,

then close to the sun, and finally reaches Pluto. Because the available power depends on the distance from the spacecraft to the sun, it is also changing from large values to small and then large. With the available power varying, we have to change the number of engines fired at the same time.

Suppose P_a is available power, P_i the input power for the i^{th} engine, P_{\min} the minimum input power for a single engine, P_{\max} the maximum input power for a single engine. There are total n engines mounted onboard. It is obvious that

$$\text{all } n \text{ engines operated if } P_a > nP_{\max} \quad (7.22)$$

$$\text{no engine operated if } P_a < P_{\min} \quad (7.23)$$

Excluding these two cases, the power level of P_a is limited

$$P_{\min} \leq P_a \leq nP_{\max} \quad (7.24)$$

and the power level of P_i is limited

$$P_{\min} \leq P_i \leq P_{\max} \quad (7.25)$$

Suppose the thrust generated is linear with respect to input power for each engine, that is

$$T_i = aP_i + b \quad (7.26)$$

If m engines are operated at the same time, the total thrust generated is

$$T_{\text{total}} = a \sum_{i=1}^m P_i + mb = aP_a + mb \quad (7.27)$$

If η and I_{sp} are constant, we can get $T_i = \frac{2\eta P_i}{gI_{sp}}$, which actually lead to the case $b = 0$

and $a = \frac{2\eta}{gI_{sp}}$. In order to produce largest thrust, we need to use as many engines as

possible if $b > 0$, use as few engines as possible if $b < 0$, and use any number of engines

if $b = 0$. Because of linear relation, the distribution of power for each engine is not significant. The engine switching logic for two cases is illustrated in Fig. 7.12.

If the thrust is strictly linear with respect to input power, the distribution of power in each engine does not necessarily have to be considered. However, an actual engine might not have this property. In addition, the engine switching logic is determined by maximizing thrust at a certain power level. How switching logic improves the mission performance is unknown in this section. However, it is concluded that different switching logic gives different performance. Since mission performance could be different variables, and mission could be complicated involving several dynamic stages, which switching logic is better is based on numerical simulations.

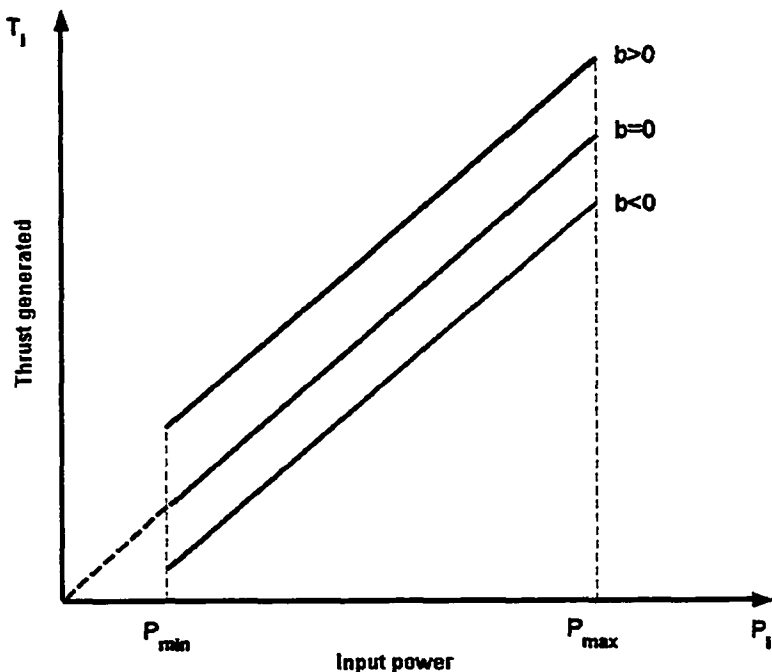


Figure 7.11 Relation between thrust and input power

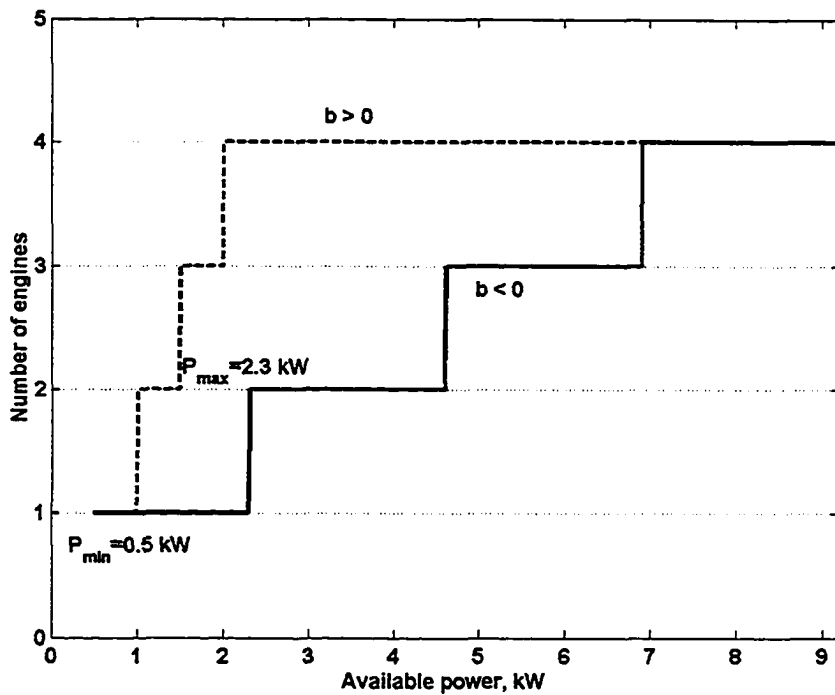


Figure 7.12 Engine-switching logic

In the Pluto-flyby mission, two types of SEP engine system, NSTAR and NEXT are used for Pluto-flyby mission. NSTAR is introduced in previous section for Eros sample retune mission .For a specific input power, I_{sp} and η of NSTAR could be obtained using Table 7.1. For the NEXT engine, I_{sp} and η have the lower and upper limits for a power level (refer to Table 7.4). There are 10 points to evaluate the upper limits for I_{sp} and η , and 9 points to evaluate the lower limits. A linear interpolation is employed to compute continuous bounds for a specific power level. The relation between I_{sp} , η and input power is shown in Figs. 7.13 and 7.14 where the mean values are plotted. Any values between upper and lower bounds are possible, and the actual values of I_{sp} , η are defined as

$$I_{sp} = I_{sp,lower} + a(I_{sp,upper} - I_{sp,lower}), \eta = \eta_{lower} + a(\eta_{upper} - \eta_{lower}), 0 \leq a \leq 1 \quad (7.28)$$

Unlike the NSTAR engines, I_{sp} and η of NEXT engines can be varying. In this work, the mean values are used for simulation that is $a = 0.5$. Obviously, the optimization of I_{sp} and η will eventually improve performance.

Table 7.4 I_{sp} and efficiency η of NEXT engine

Power (kW)	I_{sp} , sec. Upper limit	η Upper limit	Power (kW)	I_{sp} , sec. Lower limit	η Lower limit
1.485	2706	0.543	1.485	2706	0.543
1.675	2911	0.557	1.942	2895	0.592
1.936	3170	0.571	2.396	2965	0.614
2.142	3360	0.580	2.791	3008	0.628
2.423	3601	0.589	3.184	3041	0.640
3.193	3853	0.637	4.123	3302	0.663
3.960	3946	0.658	4.798	3596	0.675
4.628	4003	0.671	5.330	3811	0.683
5.295	4047	0.681	6.055	4086	0.691
6.055	4086	0.691	—	—	—

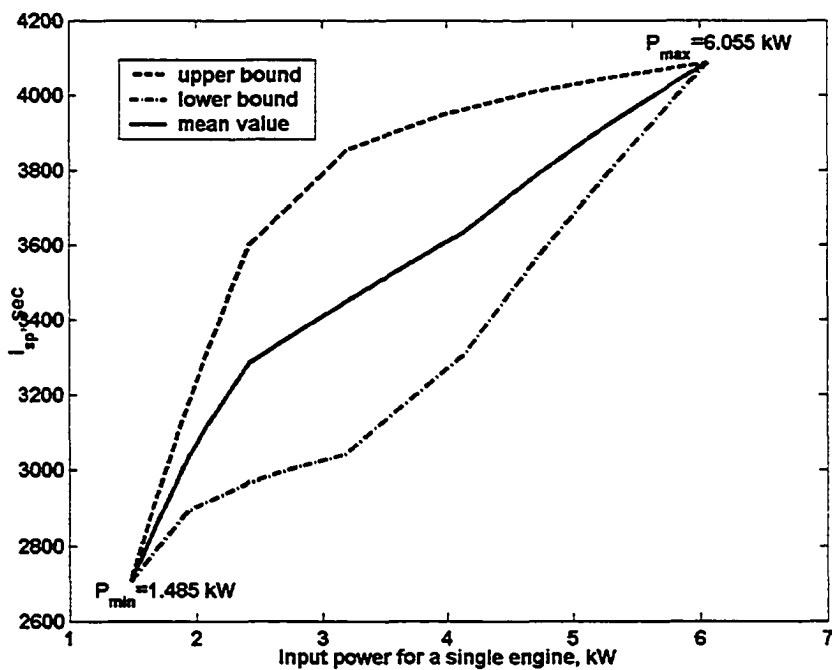


Figure 7.13 NEXT engine I_{sp} vs. power

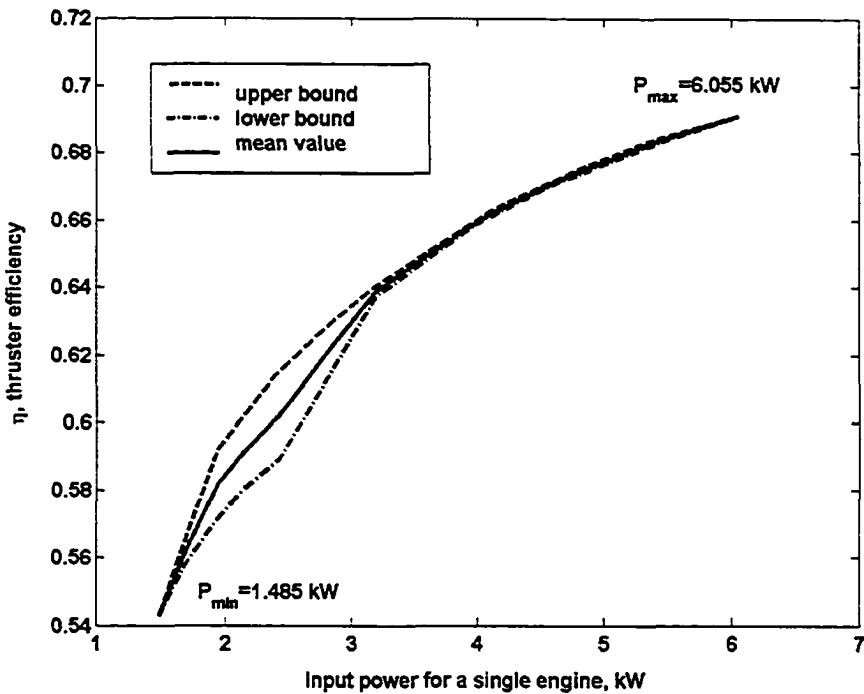


Figure 7.14 NEXT engine η vs. power

7.2.3 Numerical Results

The direct-shooting method is used for designing this mission. The flight sequence (burn-Venus flyby-burn-coast) is assumed a priori. In this work, the optimal trajectories with minimum transfer time and maximum final mass are obtained. Also the optimal trajectories using NSTAR and NEXT are analyzed.

Optimal trajectory with maximum final mass

In this case, the final mass is to be maximized. The sun will not supply sufficient power if the radius is greater than 3 AU since solar energy is too weak. The spacecraft will eventually coast to Pluto. The parameters needed for optimization are as follows. There are total 88 design variables for SQP: 78 variables are used for control steering nodes of direction cosines with 20 nodes for the first burn and 6 nodes for the second

burn. The other variables are two parameters for Venus flyby including flyby altitude and rotation angle, durations of two burns, duration of one coast, the launch date, escape energy C_3 , right ascending node and longitude at burnout point, and the initial power at 1 AU. The inclination at burnout point is fixed at 28.5 deg. The launch date is constrained within year 2008 and the arrival date is not later than August 29, 2019. The maximum radius of the burns is set to 3 AU. The switching logic I is to use as more engines as possible (dash line in Fig. 7.15) and the switching logic II is to use as fewer engines as possible (solid line in Fig. 7.15).

In Table 7.5, the solutions with maximized final mass using NSTAR engine are shown. The time histories of control steering, input power, and specific impulse I_{sp} for engine-switching logic I and II are presented in Fig. 7.15-7.17.

Table 7.5 Optimal Pluto-flyby trajectories with maximized final mass using NSTAR engine

Solutions	Switching logic I	Switching logic II
Launch date	Apr. 9, 2008	Apr. 7, 2008
Arrival date	Aug. 29, 2019	Aug. 29, 2019
Trip time (days)	4156.5145	4161.1736
Launch mass (kg)	1478.8857	1565.2163
C_3 (km^2/s^2)	41.7841	40.2785
Final mass (kg)	1006.1585	1093.4914
RAAN at burnout pt. (deg)	24.5808	25.2807
Longitude at burnout pt. (deg)	113.6283	116.4407
Payload mass (kg)	489.5487	565.3063
Propellant mass (kg)	520.00	520.00
Initial power (kW)	15.1085	16.69061
Venus GA date	April 28, 2010	April 28, 2010
Venus GA r_p (km)	350.0	350.0
Venus GA Δv (km/s)	4.7558	4.7977
V_∞ at Pluto arrival (km/s)	14.1757	14.1831

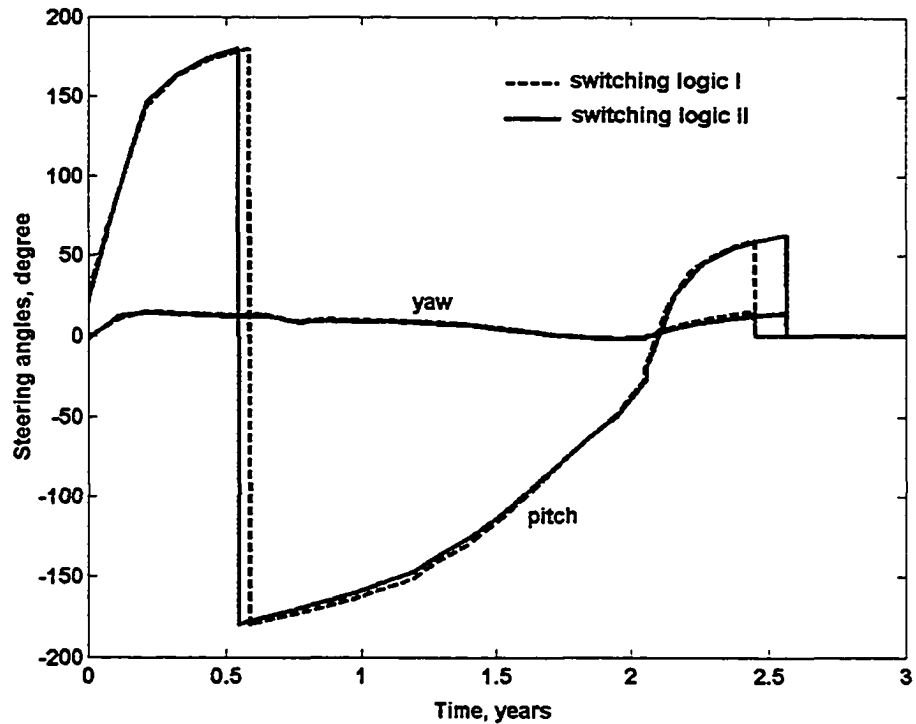


Figure 7.15 Control steering of optimal Pluto-flyby trajectories using NSTAR engine (maximum final mass)

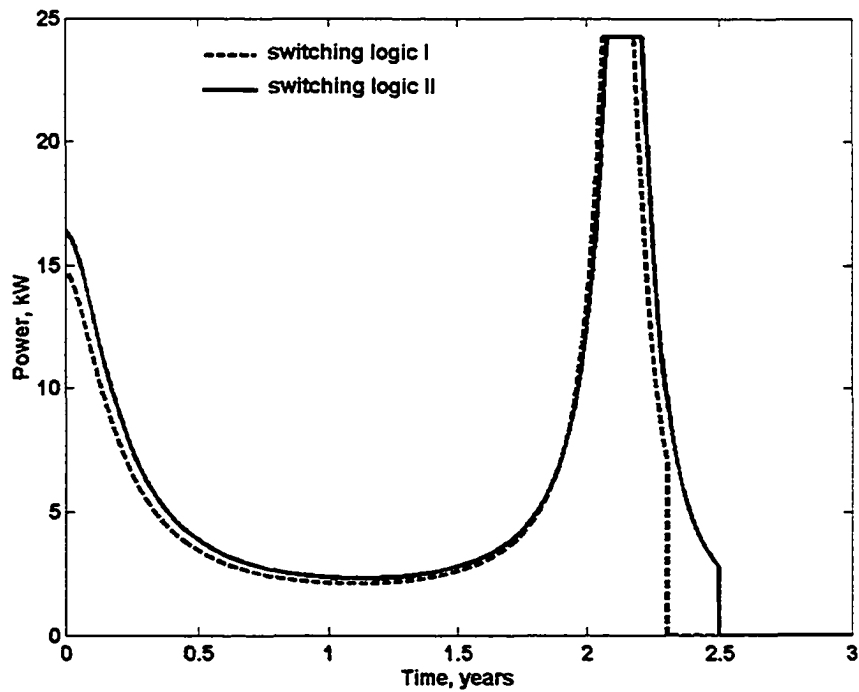


Figure 7.16 Time histories of input power for optimal Pluto-flyby trajectories using NSTAR engine (maximum final mass)

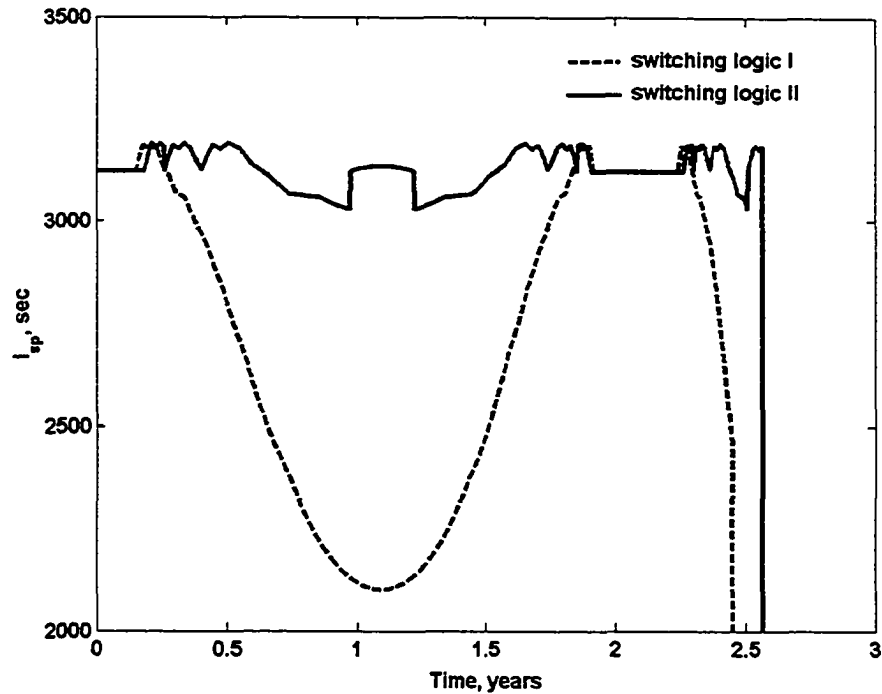


Figure 7.17 Time histories of I_{sp} optimal Pluto-flyby trajectories using NSTAR engine (maximum final mass)

In Table 7.6, the solutions with maximized final mass using NEXT engine are summarized. The time histories of control steering, input power, and specific impulse I_{sp} for engine-switching logic I and II are presented in Fig. 7.18-7.20.

Table 7.6 Optimal Pluto-flyby trajectories with maximized final mass using NEXT engine

Solutions	Switching logic I	Switching logic II
Launch date	March 31,2008	March 23, 2008
Arrival date	August 29, 2019	August 29, 2019
Trip time (days)	4168.4906	4176.4551
Launch mass (kg)	1832.1072	1998.7788
C_3 (km^2/s^2)	35.7896	33.1050
Final mass	1359.3799	1526.0515
RAAN at burnout pt. (deg)	12.7008	9.3824
Longitude at burnout pt. (deg)	115.7477	123.3729
Payload mass (kg)	843.9071	1001.1106
Propellant mass (kg)	520.00	520.00
Initial power (kW)	14.9383	16.3551
Venus GA date	April 28, 2010	April 29, 2010
Venus GA r_p (km)	350.0	350.0
Venus GA Δv (km/s)	4.7334	4.8787
V_∞ at Pluto arrival (km/s)	14.1620	14.1748

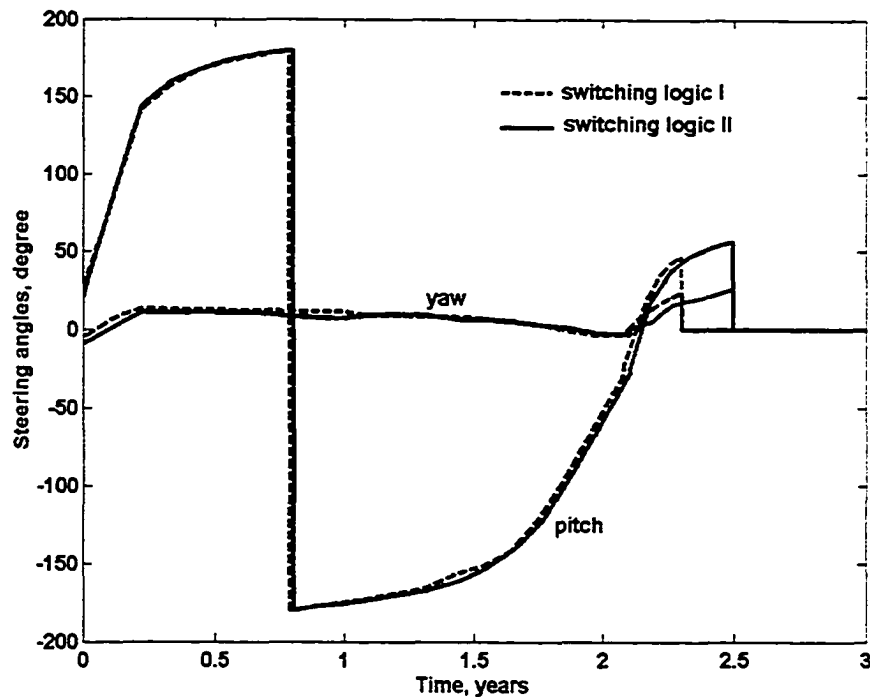


Figure 7.18 Time histories of control steering for optimal Pluto-flyby trajectories using NEXT engine (maximum final mass)

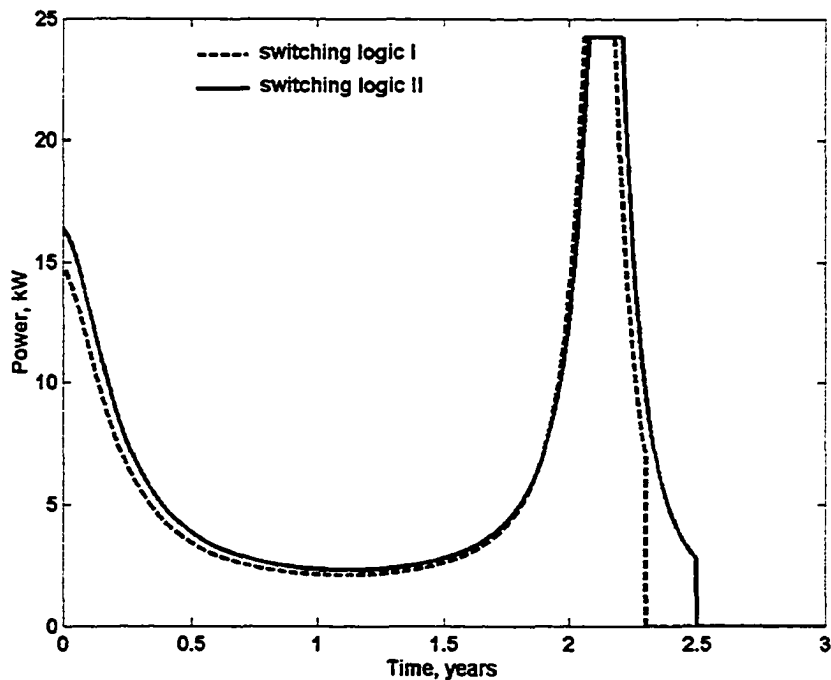


Figure 7.19 Time histories of input power for optimal Pluto-flyby trajectories using NEXT engine (maximum final mass)

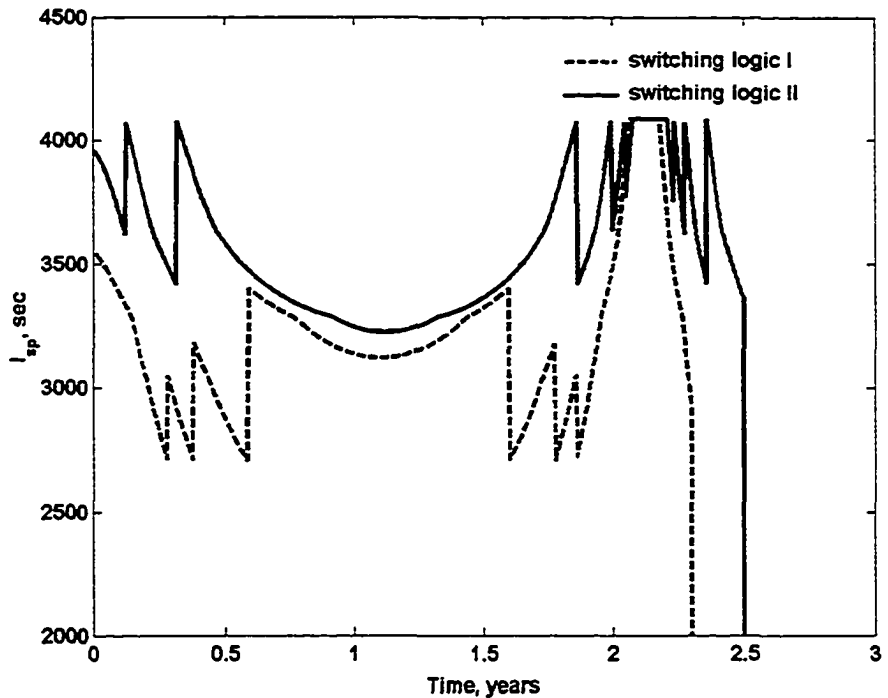


Figure 7.20 Time histories of I_{sp} for optimal Pluto-flyby trajectories using NEXT engine (maximum final mass)

Optimal trajectory with minimum transfer time

In this case, the transfer time is to be minimized. The spacecraft will eventually coast to Pluto. The parameters needed for DTOM are as follows: There are total 88 design variables for SQP. 78 variables are used for steering nodes of direction cosines with 20 nodes for the first burn and 6 nodes for the second burn. The other variables are two parameters for Venus flyby including flyby altitude and turn angle, durations of two burns, duration of one coast, the launch date, escape energy C_3 and right ascending node, longitude and the initial power at 1 AU. The launch date is constrained within year 2008, and the payload mass is not less than 250 kg. The maximum radius of burns is set 3 AU. The optimal solutions with maximized final mass using NSTAR engine are shown in

Table 7.7, and the time histories of control steering, input power, and specific impulse I_{sp} for engine-switching logic I and II are presented in Fig. 7.21-7.23.

Table 7.7 Optimal Pluto-flyby trajectories with minimized transfer time using NSTAR engine

Solutions	Switching logic I	Switching logic II
Launch date	April 20, 2008	April 22, 2008
Arrival date	January 17, 2018	October 15, 2017
Trip time (days)	3558.9931	3462.8814
Launch mass (kg)	1241.3128	1258.5566
C_3 (km^2/s^2)	46.0740	45.7550
Final mass (kg)	768.5855	785.8293
RAAN at burnout pt. (deg)	43.1152	51.8649
Longitude at burnout pt. (deg)	102.8986	99.1306
Payload mass (kg)	250.00	250.00
Propellant mass (kg)	520.00	520.00
Initial power (kW)	15.4041	17.9845
Venus GA date	April 26, 2010	April 26, 2010
Venus GA r_p (km)	350.0	350.0
Venus GA Δv (km/s)	4.4372	4.3778
V_∞ at Pluto arrival (km/s)	17.7044	18.4196

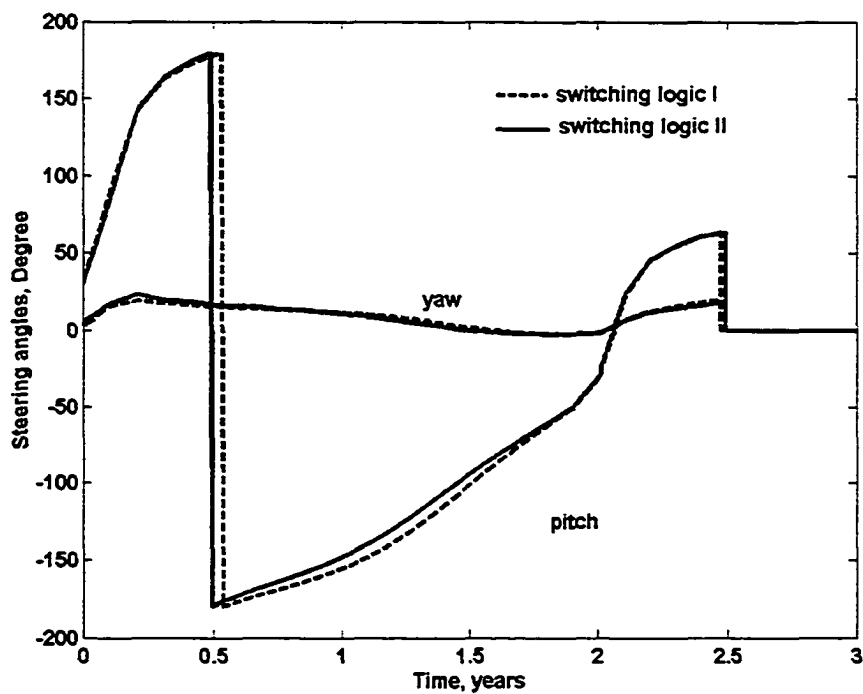


Figure 7.21 Time histories of control steering for optimal Pluto-flyby trajectories using NSTAR engine (minimum transfer time)

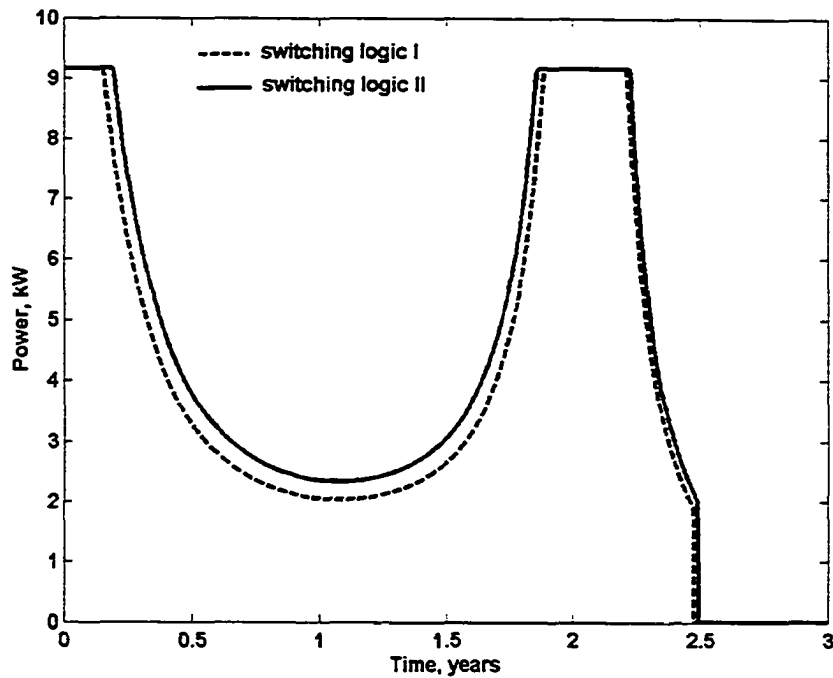


Figure 7.22 Time histories of input power for minimum-time Pluto-flyby trajectories using NSTAR engine (minimum transfer time)

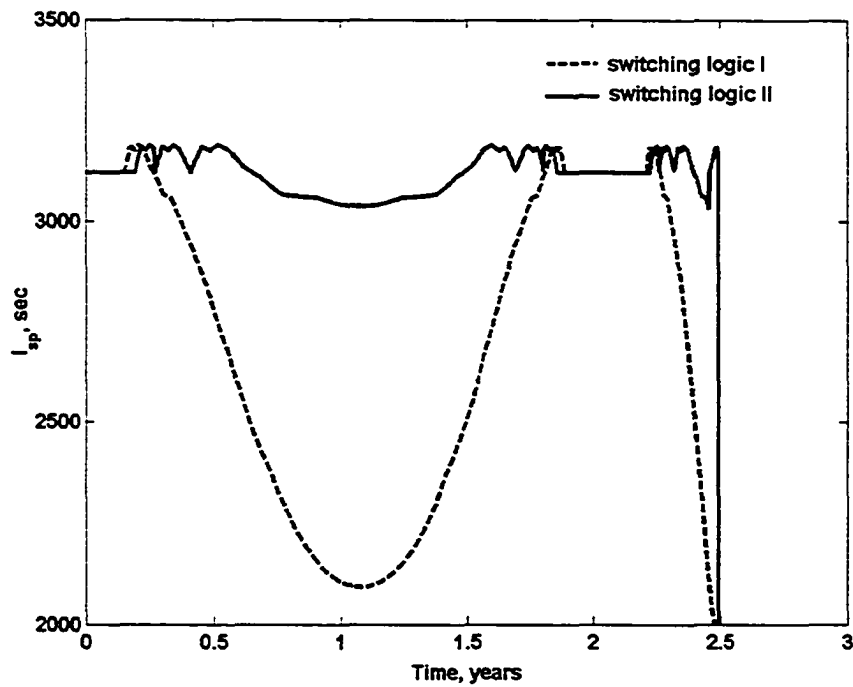


Figure 7.23 Time histories of I_{sp} for optimal Pluto-flyby trajectories using NSTAR engine (minimum transfer time)

In Table 7.8, the solutions with maximized final mass using NEXT engine are shown.

The time histories of control steering, input power and I_{sp} are shown in Figs. 7.24-7.26.

Table 7.8 Optimal Pluto-flyby trajectories with minimized transfer time using NEXT engine

Solutions	Switching logic I	Switching logic II
Launch date	April 21, 2008	April 22, 2008
Arrival date	June 7, 2016	February 28, 2016
Trip time (days)	2968.6676	2868.2295
Launch mass (kg)	1241.9686	1261.7350
C_3 (km^2/s^2)	46.0618	45.6964
Final mass (kg)	769.2414	789.0077
RAAN at burnout pt. (deg)	26.6418	41.2360
Longitude at burnout pt. (deg)	119.0064	111.4592
Payload mass (kg)	250.00	250.00
Propellant mass (kg)	520.00	520.00
Initial power (kW)	15.5022	18.4601
Venus GA date	April 20, 2010	April 19, 2010
Venus GA r_p (km)	350.0	350.0
Venus GA Δv (km/s)	3.8290	3.7642
V_∞ at Pluto arrival (km/s)	23.0350	24.2652

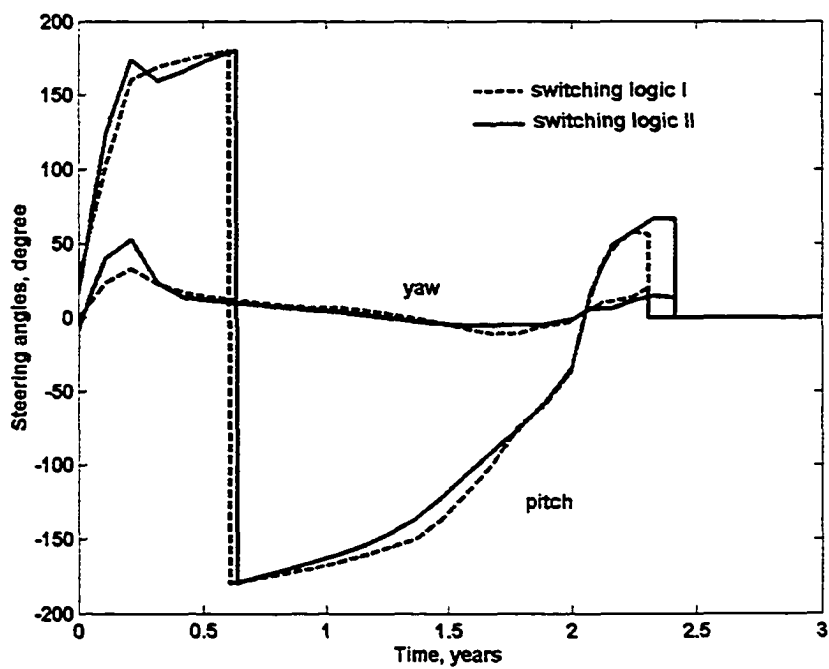


Figure 7.24 Time histories of control steering for optimal Pluto-flyby trajectories using NEXT engine (minimum transfer time)

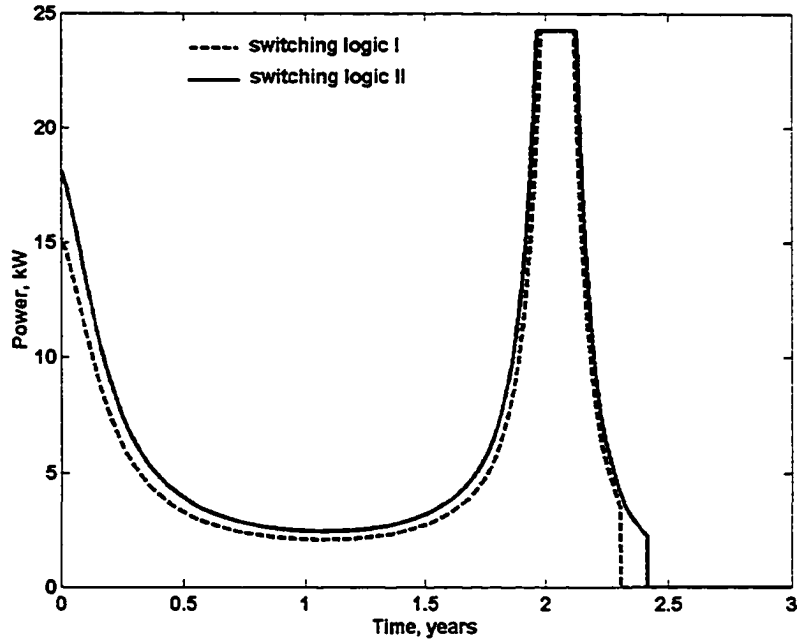


Figure 7.25 Time histories of input power for optimal Pluto-flyby trajectories using NEXT engine (minimum transfer time)

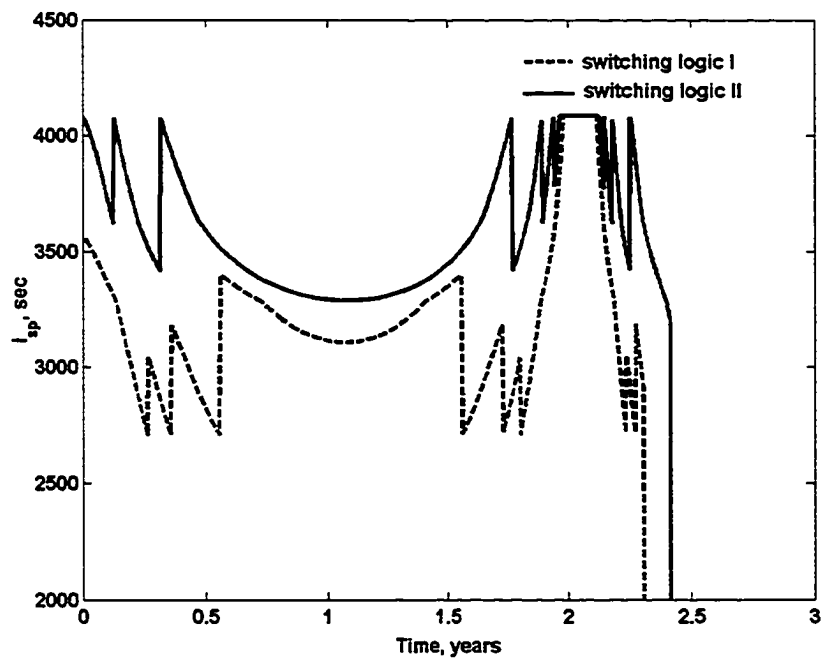


Figure 7.26 Time histories of I_{sp} for optimal Pluto-flyby trajectories using NEXT engine (minimum transfer time)

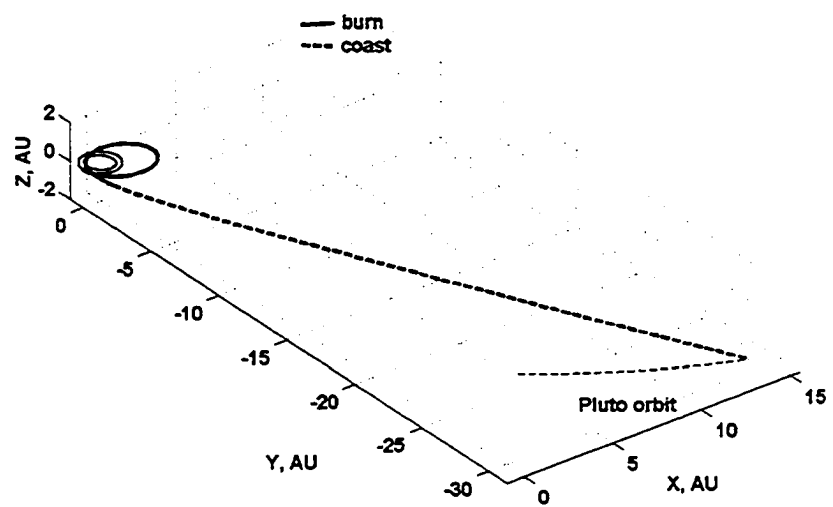


Figure 7.27 3-D Pluto-flyby trajectories (NEXT, maximum final mass, switching logic II)

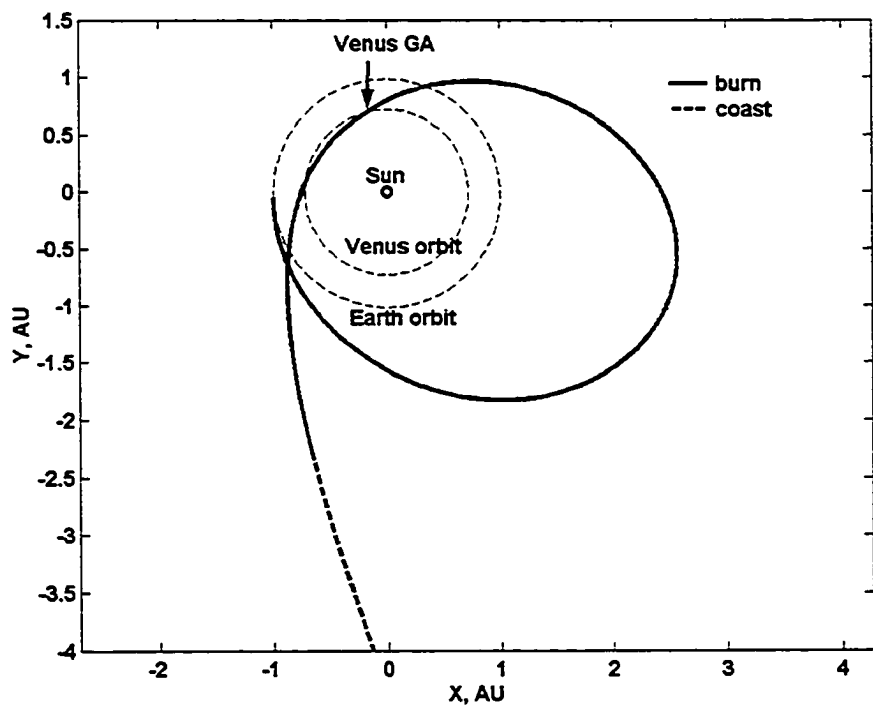


Figure 7.28 Pluto-flyby trajectory near the Earth (NEXT, maximum final mass, switching logic II)

The optimal Pluto-flyby trajectories using NEXT engine with maximum final mass is shown in Fig.7.27 and 7.28. From Tables 7.5-7.8, it is obvious that the arrival date in maximum-final-mass trajectories reach the boundary, and the payload mass in minimum-time trajectories is constrained by lower limit. By changing the constraints of arrival date or payload mass, a series of solutions having tradeoff between trip time and payload can be obtained.

7.2.4 Conclusions

The optimal Pluto-flyby trajectories using SEP have been presented. The maximized final mass and minimized trip time are considered. NSTAR and NEXT engines are used in optimization. The engine switching is employed in this mission due to its unique feature of trajectories, which is that the available power changes back and forth. The simulation results show that a proper engine switching logic is useful in order to obtain better performance. The future work would be analysis of distribution of power in each engine, which possibly changes the performance. Furthermore, the symmetric torque should be also taken into consideration if multiple engines are operated.

CHAPTER 8 ALTERNATIVE FORMULATIONS FOR EQUATIONS OF MOTION

In this chapter, two topics of alternative formulations for the equations of motion are to be discussed. The first one is on the transfers to circular orbits using inertial frame transformation in terms of three Euler angles. The LEO-GPS orbit transfer is demonstrated to verify the feasibility of this kind of transformation, and the convergence properties for the hybrid method are improved by this technique. The second topic is solving optimal orbit transfers using a modified set of equinoctial elements, in which the non-dimensional angular momentum is employed as the first element to describe the size of conic orbits. The costate equations are derived, and both state and costate equations seem simpler than other sets of equinoctial elements [19-22]. The perturbations, such as Earth oblateness and atmosphere drag, are also formulated in costate equations. In addition, the hybrid method is used to solve a LEO-GEO orbit transfer problem based on this set of equinoctial elements.

8.1 Transfers to Circular Orbits based on Inertial Frame Transformation

8.1.1 Introduction

Circular orbits are of great interest for satellites and spacecraft. Many researches presented this type of orbit transfers in the past decades. Kechichian [19-22] developed a

series of equations of motion using equinoctial elements to solve the LEO-GEO minimum-time transfers. Zondervan et al. [29] solved the three-burn transfer with a plane change using a combined direct/indirect method. Spencer and Culp [49] developed near-optimal 2-burn LEO-GEO transfers using equinoctial elements. In this scenario, a straightforward method of transfers to circular orbits is presented. If the final orbit is equatorial and circular, the constraints in spherical coordinate are quite simple.

$$r(t_f) = r_f, \theta(t_f) \text{ is free}, \phi(t_f) = 0, v_r(t_f) = 0, v_\theta(t_f) = \sqrt{\mu/r_f}, v_\phi(t_f) = 0 \quad (8.1)$$

The constraints in equinoctial elements are also simple.

$$p(t_f) = r_f, f(t_f) = g(t_f) = h(t_f) = k(t_f) = 0, \text{and } L(t_f) \text{ is free} \quad (8.2)$$

The constraints are state variables themselves so that performance of convergence could be improved. However, if the final orbit is not equatorial but inclined, we cannot simply set the above constraints. So is it possible that any transfer to an inclined circular orbits be converted to the transfer to an “equatorial” orbits by adopting constraint-based inertial coordinate transformation, and thus the terminal constraints (8.1) and (8.2) could be set easily? If an inertial coordinate is transformed from the J2000 frame by rotations about three axes, the expression of two-body dynamics is not changed only with states’ elements referenced in the different inertial frame. In the new inertial frame, the target orbit can be “equatorial”, and thus constraints are simple. An example of LEO-GPS orbital transfers is solved to demonstrate the use of inertial frame transformation. The J_2 perturbation expressed in the new inertial frame are developed and incorporated in state equations for numerical integration. The hybrid method is employed, and the optimal solutions are obtained only with a simple initial guess, which is one of the advantages for

inertial frame transformation. The other advantage is that singularities might be avoided, for example, $\phi = 90$ deg in spherical coordinate and $i = 180$ deg in equinoctial elements can be avoided by choosing an inclined inertial frame. For interplanetary orbital transfers, we can rotate the Earth equatorial frame to have the same orientation as the heliocentric frame so that at SOI of the Earth, it is not necessary to do the transformation between two frames. Furthermore, if TPBVP is employed, the terminal costates can be easily obtained (see Eqs. 3.18, 3.19 and 3.28).

8.1.2 Inertial Frame Transformation

The system dynamics with perturbations expressed in spherical coordinate and equinoctial elements are discussed in chapter 2 and chapter 3. Assuming that the original J2000 inertial coordinate frame is XYZ , an arbitrary inertial frame could be obtained by performing the following transformations in terms of three rotations. The three rotation angles are also called Euler angles.

- 1) Rotate about Z axis angle α to obtain $X_1Y_1Z_1$
- 2) Rotate about X_1 axis angle β to obtain $X_2Y_2Z_2$
- 3) Rotate about Z_2 axis angle γ to obtain $X_3Y_3Z_3$

This series of rotations is illustrated in Fig. 8.1. If $\alpha = \Omega_f$, $\beta = i_f$, and $\gamma = \omega_f$, the axis X_3 points to the direction of eccentricity vector, the X_3Y_3 plane is actually the final orbit plane, and Z_3 is perpendicular to the final orbit plane. If the final orbit is a circular orbit, the first two rotations are enough, and the third one is not used because the argument of perigee is undefined.

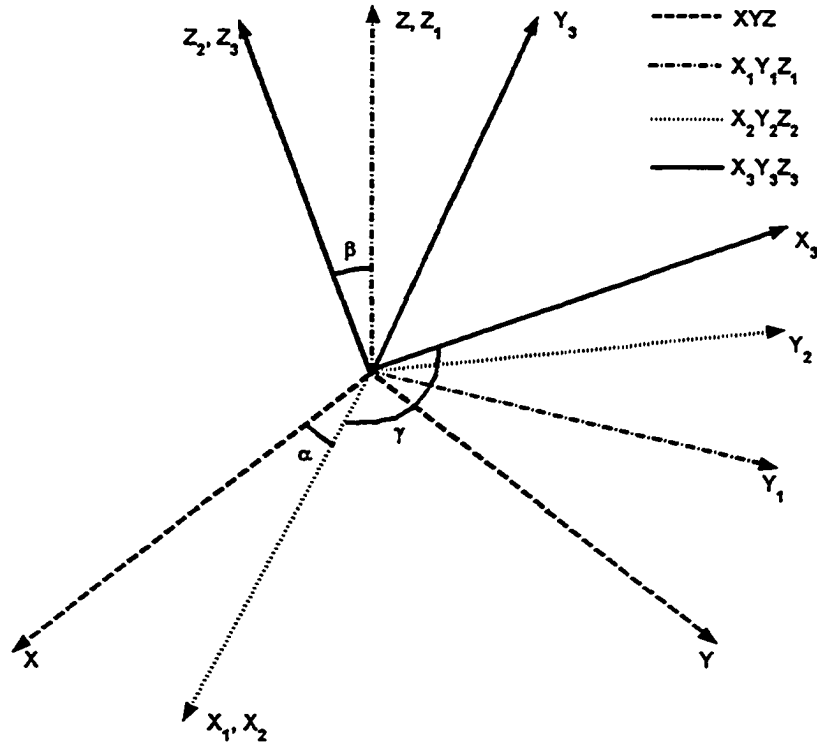


Figure 8.1 Coordinate transformation

The rotation matrix is as follows.

$$A = \begin{bmatrix} \cos \gamma \cos \alpha - \cos \beta \sin \gamma \sin \alpha & \cos \gamma \sin \alpha + \sin \gamma \cos \beta \cos \alpha & \sin \gamma \sin \beta \\ -\sin \gamma \cos \alpha - \cos \beta \cos \gamma \sin \alpha & -\sin \gamma \sin \alpha + \cos \gamma \cos \beta \cos \alpha & \cos \gamma \sin \beta \\ \sin \beta \sin \alpha & -\sin \beta \cos \alpha & \cos \beta \end{bmatrix} \quad (8.3)$$

and

$$\begin{bmatrix} X_3 \\ Y_3 \\ Z_3 \end{bmatrix} = A \begin{bmatrix} X \\ Y \\ Z \end{bmatrix} \text{ and } \begin{bmatrix} X \\ Y \\ Z \end{bmatrix} = A^{-1} \begin{bmatrix} X_3 \\ Y_3 \\ Z_3 \end{bmatrix} = A^T \begin{bmatrix} X_3 \\ Y_3 \\ Z_3 \end{bmatrix} \quad (8.4)$$

In the inertial frame $X_3Y_3Z_3$, the two-body dynamics expression is the same. However, the six states are all referenced in $X_3Y_3Z_3$ not XYZ . If we use \tilde{XYZ} to

denote $X_3Y_3Z_3$, we can find the relation between coordinate elements in two different frames.

$$(\tilde{\mathbf{r}}, \dot{\tilde{\mathbf{r}}}) = \text{sphe}(\tilde{r}, \tilde{\theta}, \tilde{\phi}, \tilde{v}_r, \tilde{v}_\theta, \tilde{v}_\phi) \text{ or } (\tilde{\mathbf{r}}, \dot{\tilde{\mathbf{r}}}) = \text{equi}(\tilde{p}, \tilde{f}, \tilde{g}, \tilde{h}, \tilde{k}, \tilde{L}) \quad (8.5)$$

$$(\mathbf{r}, \dot{\mathbf{r}}) = \text{sphe}(r, \theta, \phi, v_r, v_\theta, v_\phi) \text{ or } (\mathbf{r}, \dot{\mathbf{r}}) = \text{equi}(p, f, g, h, k, L) \quad (8.6)$$

$$\mathbf{r} = A^T \tilde{\mathbf{r}}, \dot{\mathbf{r}} = A^T \dot{\tilde{\mathbf{r}}} \text{ or } \tilde{\mathbf{r}} = A\mathbf{r}, \dot{\tilde{\mathbf{r}}} = A\dot{\mathbf{r}} \quad (8.7)$$

where $\text{sphe}(\cdot)$ and $\text{equi}(\cdot)$ are functions to transform spherical elements and equinoctial elements to position and velocity vectors, respectively.

8.1.3 The Earth Oblateness Expressed in the Transformed Inertial Frame

In the transformed inertial frame, J_2 effect has different expressions in the frame $\tilde{X}\tilde{Y}\tilde{Z}$. The J_2 perturbing function expressed in the frame XYZ can be written as:

$$U_{J_2} = \frac{\mu}{r^3} Re^2 J_2 \frac{1}{2} (3 \sin^2 \phi - 1) \text{ where } \sin \phi = \frac{z}{r} \quad (8.8)$$

According to the transform matrix A ,

$$z = \sin \gamma \sin \beta \cdot \tilde{x} + \cos \gamma \sin \beta \cdot \tilde{y} + \cos \beta \cdot \tilde{z} \quad (8.9)$$

$$c_1 = \sin \gamma \sin \beta \quad c_2 = \cos \gamma \sin \beta \quad c_3 = \cos \beta \quad (8.10)$$

$$r = \tilde{r} \quad \text{where } \tilde{r} = \sqrt{\tilde{x}^2 + \tilde{y}^2 + \tilde{z}^2} \quad (8.11)$$

The J_2 perturbing function expressed in frame $\tilde{X}\tilde{Y}\tilde{Z}$ can be written as

$$U_{J_2} = \frac{\mu}{\tilde{r}^3} Re^2 J_2 \frac{1}{2} \left[3 \frac{(c_1 \tilde{x} + c_2 \tilde{y} + c_3 \tilde{z})^2}{\tilde{r}^2} - 1 \right] \quad (8.12)$$

The J_2 expressed in Cartesian coordinate is as follows.

$$a_{J_2, \tilde{x}} = -\frac{\partial U_{J_2}}{\partial \tilde{x}} = \frac{1}{2} Re^2 J_2 \mu \left[\frac{15 \tilde{x} z^2}{\tilde{r}^7} - \frac{3 \tilde{x} + 6 c_1 z}{\tilde{r}^5} \right] \quad (8.13)$$

$$a_{J_2,\tilde{y}} = -\frac{\partial U_{J_2}}{\partial \tilde{y}} = \frac{1}{2} \text{Re}^2 J_2 \mu \left[\frac{15\tilde{y}z^2}{\tilde{r}^7} - \frac{3\tilde{y} + 6c_2 z}{\tilde{r}^5} \right] \quad (8.14)$$

$$a_{J_2,\tilde{z}} = -\frac{\partial U_{J_2}}{\partial \tilde{z}} = \frac{1}{2} \text{Re}^2 J_2 \mu \left[\frac{15\tilde{z}z^2}{\tilde{r}^7} - \frac{3\tilde{z} + 6c_3 z}{\tilde{r}^5} \right] \quad (8.15)$$

In the spherical coordinates, the derivation of J_2 perturbation is as follows.

$$z = c_1 \cdot \tilde{r} \cos \tilde{\phi} \cos \tilde{\theta} + c_2 \cdot \tilde{r} \cos \tilde{\phi} \sin \tilde{\theta} + c_3 \cdot \tilde{r} \sin \tilde{\phi} \quad (8.16)$$

$$r = \tilde{r} \quad (8.17)$$

$$\sin^2 \phi = \left(\frac{z}{r} \right)^2 = (c_1 \cos \tilde{\phi} \cos \tilde{\theta} + c_2 \cos \tilde{\phi} \sin \tilde{\theta} + c_3 \sin \tilde{\phi})^2 \quad (8.18)$$

$$U_{J_2} = \frac{\mu}{\tilde{r}^3} \text{Re}^2 J_2 \frac{1}{2} [3(c_1 \cos \tilde{\phi} \cos \tilde{\theta} + c_2 \cos \tilde{\phi} \sin \tilde{\theta} + c_3 \sin \tilde{\phi})^2 - 1] \quad (8.19)$$

The J_2 perturbation expressed in $\tilde{X}\tilde{Y}\tilde{Z}$ using spherical elements are:

$$a_{J_2,\tilde{r}} = -\frac{\partial U_{J_2}}{\partial \tilde{r}} = \frac{3\mu}{\tilde{r}^4} \text{Re}^2 J_2 \frac{1}{2} [3\sin^2 \phi - 1] \quad (8.20)$$

$$a_{J_2,\tilde{\theta}} = -\frac{1}{\tilde{r} \cos \tilde{\phi}} \frac{\partial U_{J_2}}{\partial \tilde{\theta}} = -\frac{3\mu}{\tilde{r}^4 \cos \tilde{\phi}} \text{Re}^2 J_2 [\sin \phi (-c_1 \cos \tilde{\phi} \sin \tilde{\theta} + c_2 \cos \tilde{\phi} \cos \tilde{\theta})] \quad (8.21)$$

$$a_{J_2,\tilde{\phi}} = -\frac{1}{\tilde{r}} \frac{\partial U_{J_2}}{\partial \tilde{\phi}} = -\frac{3\mu}{\tilde{r}^4} \text{Re}^2 J_2 [\sin \phi (-c_1 \sin \tilde{\phi} \cos \tilde{\theta} - c_2 \sin \tilde{\phi} \sin \tilde{\theta} + c_3 \cos \tilde{\phi})] \quad (8.22)$$

$$\text{where } \sin \phi = c_1 \cos \tilde{\phi} \sin \tilde{\theta} + c_2 \cos \tilde{\phi} \sin \tilde{\theta} + c_3 \sin \tilde{\phi} \quad (8.23)$$

We also can use the RTN frame to express the J_2 perturbation.

$$\sin \phi = \sin i \sin \varpi \quad \text{where } \varpi \text{ is longitude angle} \quad (8.24)$$

$$U_{J_2} = \frac{\mu}{r^3} \text{Re}^2 J_2 \frac{1}{2} \{3[c_1(c_{\bar{\Omega}} c_{\bar{\sigma}} - s_{\bar{\Omega}} s_{\bar{\sigma}} c_{\bar{\iota}}) + c_2(s_{\bar{\Omega}} c_{\bar{\sigma}} + c_{\bar{\Omega}} s_{\bar{\sigma}} c_{\bar{\iota}}) + c_3 \cdot s_{\bar{\sigma}} s_{\bar{\iota}}]^2 - 1\} \quad (8.25)$$

$$f_{J_2,\tilde{r}} = -\frac{\partial U_{J_2}}{\partial \tilde{r}} = \frac{3\mu}{\tilde{r}^4} \text{Re}^2 J_2 (3s_{\phi}^2 - 1) \quad (8.26)$$

$$f_{J_2,\tilde{r}} = -\frac{1}{\tilde{r}} \frac{\partial U_{J_2}}{\partial \tilde{w}} = -\frac{\mu}{\tilde{r}^4} \text{Re}^2 J_2 6s_\phi [c_1(-c_{\tilde{\Omega}} s_{\tilde{\omega}} - s_{\tilde{\Omega}} c_{\tilde{\omega}} c_{\tilde{i}}) - c_2(-s_{\tilde{\Omega}} s_{\tilde{\omega}} + c_{\tilde{\Omega}} c_{\tilde{\omega}} c_{\tilde{i}}) + c_3 c_{\tilde{\omega}} s_{\tilde{i}}] \quad (8.27)$$

$$f_{J_2,\tilde{r}} = -\frac{1}{\tilde{r} s_{\tilde{\omega}}} \frac{\partial U_{J_2}}{\partial \tilde{i}} = -\frac{\mu}{\tilde{r}^4} \text{Re}^2 J_2 6s_\phi (c_1 s_{\tilde{\Omega}} s_{\tilde{i}} - c_2 s_{\tilde{\Omega}} s_{\tilde{i}} + c_3 c_{\tilde{i}}) \quad (8.28)$$

where $s_\phi = c_1(c_{\tilde{\Omega}} c_{\tilde{\omega}} - s_{\tilde{\Omega}} s_{\tilde{\omega}} c_{\tilde{i}}) + c_2(s_{\tilde{\Omega}} c_{\tilde{\omega}} + c_{\tilde{\Omega}} s_{\tilde{\omega}} c_{\tilde{i}}) + c_3 \cdot s_{\tilde{\omega}} s_{\tilde{i}}$ (8.29)

The above expression is based on the classical orbital elements so that singularities occur at zero eccentricity and inclination. The equinoctial elements can be used to express the accelerations of J_2 effect using Eqs. (8.30)-(8.35).

$$\cos \Omega = h / \sqrt{h^2 + k^2} \quad (8.30)$$

$$\sin \Omega = k / \sqrt{h^2 + k^2} \quad (8.31)$$

$$\cos \varpi = (h \cos L + k \sin L) / \sqrt{h^2 + k^2} \quad (8.32)$$

$$\sin \varpi = (h \sin L - k \cos L) / \sqrt{h^2 + k^2} \quad (8.33)$$

$$\cos i = (1 - h^2 - k^2) / (1 + h^2 + k^2) \quad (8.34)$$

$$\cos i = 2\sqrt{h^2 + k^2} / (1 + h^2 + k^2) \quad (8.35)$$

The J_2 perturbation expressed in $\tilde{X}\tilde{Y}\tilde{Z}$ using equinoctial elements is as follows.

$$f_{J_2,\tilde{r}} = \frac{3\mu}{\tilde{r}^4} \text{Re}^2 J_2 \frac{1}{2} (3s_\phi^2 - 1) \quad (8.36)$$

$$f_{J_2,\tilde{r}} = -\frac{3\mu}{\tilde{r}^4} \text{Re}^2 J_2 s_\phi \frac{c_1[-(1 + \tilde{h}^2 - \tilde{k}^2)s_{\tilde{L}} + 2\tilde{h}\tilde{k}c_{\tilde{L}}] + c_2[(1 - \tilde{h}^2 + \tilde{k}^2)c_{\tilde{L}} - 2\tilde{h}\tilde{k}s_{\tilde{L}}] + c_3[2(\tilde{h}c_{\tilde{L}} + \tilde{k}s_{\tilde{L}})]}{1 + \tilde{h}^2 + \tilde{k}^2} \quad (8.37)$$

$$f_{J_2,\tilde{r}} = -\frac{3\mu}{\tilde{r}^4} \text{Re}^2 J_2 s_\phi \frac{c_1 \cdot 2\tilde{k} - c_2 \cdot 2\tilde{h} + c_3(1 - \tilde{h}^2 - \tilde{k}^2)}{1 + \tilde{h}^2 + \tilde{k}^2} \quad (8.38)$$

$$\text{where } s_4 = \frac{c_1[(1 + \tilde{h}^2 - \tilde{k}^2)c_L + 2\tilde{h}\tilde{k}s_L] + c_2[(1 - \tilde{h}^2 + \tilde{k}^2)s_L + 2\tilde{h}\tilde{k}c_L] + c_3[2(\tilde{h}s_L - \tilde{k}c_L)]}{1 + \tilde{h}^2 + \tilde{k}^2} \quad (8.39)$$

The J_2 effect formulation in costate equations can be obtained by computing the derivatives of accelerations caused by J_2 effect with respect to the coordinate elements. The J_2 effect accelerations are only determined by position elements and not related to velocity elements.

In the J2000 inertial frame, we simulate the orbit perturbed by J_2 effect [11]. The initial classical orbital elements in the J2000 inertial frame are $a_0 = 12,000 \text{ km}$, $e_0 = 0.3$, $i_0 = 20 \text{ deg}$, $\Omega_0 = 40 \text{ deg}$, $\omega_0 = 60 \text{ deg}$ and $\theta_0 = 80 \text{ deg}$. Three coordinates are used for integration, and the integration step of fixed-step fourth-order Runga-Kutta method is 2000. The time duration is 12 hours. We also simulate the same orbit in the inertial frame after transformation with three Euler angles $\alpha = 1.0 \text{ rad}$, $\beta = 1.0 \text{ rad}$, and $\gamma = 1.0 \text{ rad}$. Firstly, we transform the initial condition from the J2000 frame to the frame after rotations, then the numerical integration is performed in the new inertial frame, and the classical orbital elements at the final time are transformed back. This simulation is to verify the derivation of J_2 perturbation expressed by three different coordinate elements in the inertial frame after rotations. The results presented in Tables 8.1 and 8.2 could be compared to the solution in Ref. [11]. The time histories of semi-major axis, eccentricity, inclination, and right ascension of ascending nodes simulated in the J2000 frame and the frame after rotations are presented in Fig. 8.2. The two set of solutions are essentially the same, and it is hard to tell difference by eye.

Table 8.1 Terminal a , e , i , Ω and ω due to J_2 effect simulated in the J2000 frame

Coordinates	a_f , Re	e_f , deg	i_f , deg	Ω_f , deg	ω_f , deg
Cartesian	1.880882786	0.2995639786	19.9999252090	39.424096181	60.994379
Spherical	1.880882787	0.2995639792	19.9999252523	39.424096742	60.994377
Equinoctial	1.880882787	0.2995639792	19.9999252093	39.424096184	60.994377

Table 8.2 Terminal a , e , i , Ω and ω due to J_2 effect simulated in the frame after transformation

Coordinates	a_f , Re	e_f , deg	i_f , deg	Ω_f , deg	ω_f , deg
Cartesian	1.880882786	0.2995639786	19.9999252089	39.424096181	60.994379
Spherical	1.880882787	0.2995639740	19.9999252545	39.424095120	60.994380
Equinoctial	1.880882787	0.2995639792	19.9999252093	39.424096182	60.994377

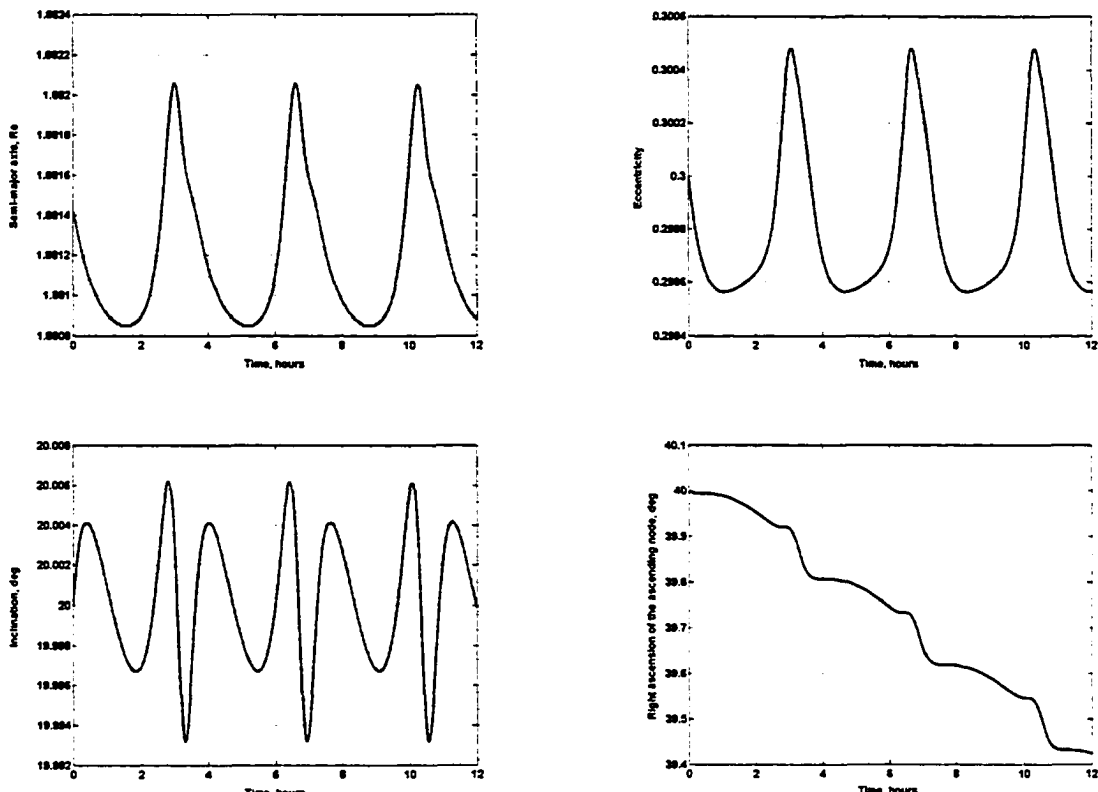


Figure 8.2 Time histories of a , e , i , Ω due to J_2 effect

8.1.4 Optimal LEO-GPS Orbit Transfers Using Inertial Frame Transformation

Global-position-system (GPS) satellites generally have large inclination and altitude so that they cannot be launched into orbit by rockets in one stage. For example, the GPS final orbit is a circular orbit with the altitude 20,000 km, inclination 60 deg, and right ascension of ascending node 30 deg. It is desired to propagate a satellite from LEO to GPS orbit so the terminal constraints are not in equatorial plane of the J2000 inertial coordinate. The transformation could be employed by setting rotation angles α, β, γ to be 60, 30, and 0 deg, respectively. In the new inertial frame, the GPS orbit is in an “equatorial” plane. The initial mass is 6100 kg, and the constant I_{sp} is 3800 seconds. The initial thrust-to-weigh ratio is 10^{-2} . In Table 8.3, the initial conditions in different inertial frame are shown.

Table 8.3 Initial orbital elements in different inertial frames

Orbital elements	J2000 frame	Frame after transformation
a (Re)	1.047	1.047
e	10^{-6}	10^{-6}
i (rad)	0.4974	0.6480
Ω (rad)	0.0	3.5479
ω (rad)	0.0	2.3416
θ (rad)	0.0	6.2832

Spherical coordinate elements and equinoctial elements are used to compute the optimal trajectories, and the solutions obtained can be compared. The converged solution is obtained from a simple guess of initial costates (8.40) and a reasonable transfer time if equinoctial elements are used for integration. The terminal constraints are simply set (8.41) such that the constraints are linear with the system states.

$$\lambda_p = 1, \lambda_f = 0, \lambda_g = 0, \lambda_h = 0, \lambda_k = 0, \lambda_L = 0 \quad (8.40)$$

$$p(t_f) = 20,000 \text{ km}, f(t_f) = g(t_f) = h(t_f) = k(t_f) = 0, \text{and } L(t_f) \text{ is free} \quad (8.41)$$

If spherical coordinates are used, a feasible converged solution is obtained by minimizing the sum of square of terminal constraints from a very simple initial guess (8.42) and a reasonable transfer time. The terminal constraints (8.43) are also simple. Then the better solution could be improved to optimize the final mass based on the feasible solution.

$$\lambda_r = 0, \lambda_\phi = 0, \lambda_{v_r} = 0, \lambda_{v_\theta} = -1, \lambda_{v_\phi} = 0 \quad (8.42)$$

$$r(t_f) = 20,000 \text{ km}, \phi(t_f) = v_r(t_f) = v_\phi(t_f) = 0, v_\theta(t_f) = \sqrt{\mu/r(t_f)}, \text{ and } \theta(t_f) \text{ is free}$$

$$(8.43)$$

The optimization results are summarized in Tables 8.4 and 8.5. The optimal trajectories without and with J_2 perturbation are obtained. For these two cases, the J_2 perturbation are included in state equations and not formulated in costate equations. Therefore, the solutions are considered to be sub-optimal but might be close to optimal ones because the two-body dynamics significantly affects the trajectories.

The numerical integration is performed and converged solutions are obtained in the transformed inertial frame not in the J2000 frame. An inverse transformation is performed so that the orbital elements in Tables 8.4 and 8.5 are referenced in the J2000 inertial frame. The optimal solutions computed by spherical and equinoctial elements are essentially the same. The time histories of control steering and orbital elements solved by equinoctial elements are presented in Fig. 8.3-8.7. We can see that the J_2 effect is not significant if the initial thrust-to-weight ratio is 10^{-2} .

Table 8.4 Optimal solutions of LEO-GPS orbit transfers without J_2 perturbation

Terminal states	Spherical	Equinoctial
$a(t_f)$ (Re)	3.13570818	3.13570818
$e(t_f)$	$4.0424(10^{-10})$	$1.8748(10^{-11})$
$i(t_f)$ (deg)	59.99999998	59.999999994
$\Omega(t_f)$ (deg)	30.000000008	29.999999994
Final mass $m(t_f)$ (kg)	5208.9060	5208.8940
Departure $\omega(t_0) + \theta(t_0)$ (deg)	180.1581	180.1581
Transfer time (hours)	7.7098	7.7099

Table 8.5 Optimal solutions of LEO-GPS orbit transfers with J_2 perturbation

Terminal states	Spherical	Equinoctial
$a(t_f)$ (Re)	3.13570818	3.13570781
$e(t_f)$	1.0483E-008	6.5030E-008
$i(t_f)$ (deg)	59.99999995	59.999998
$\Omega(t_f)$ (deg)	30.0000001	30.0000001
Final mass $m(t_f)$ (kg)	5205.1089	5205.0961
Departure $\omega(t_0) + \theta(t_0)$ (deg)	179.7743	-0.9591
Transfer time (hours)	7.7427	7.7428

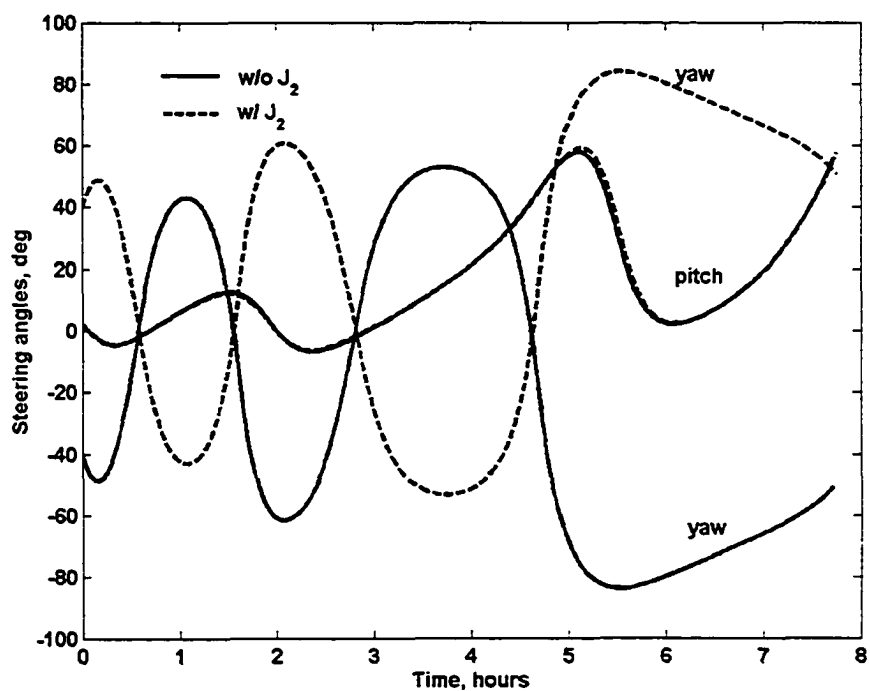


Figure 8.3 Control steering for optimal LEO-GPS transfers (equinoctial elements)

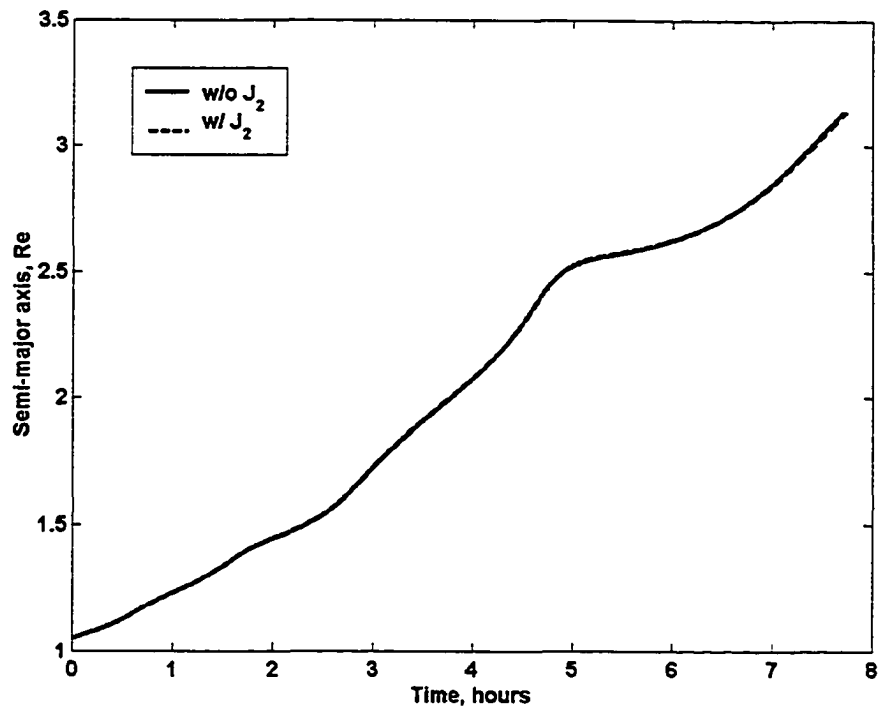


Figure 8.4 Time histories of semi-major axis for optimal LEO-GPS transfers (equinoctial elements)

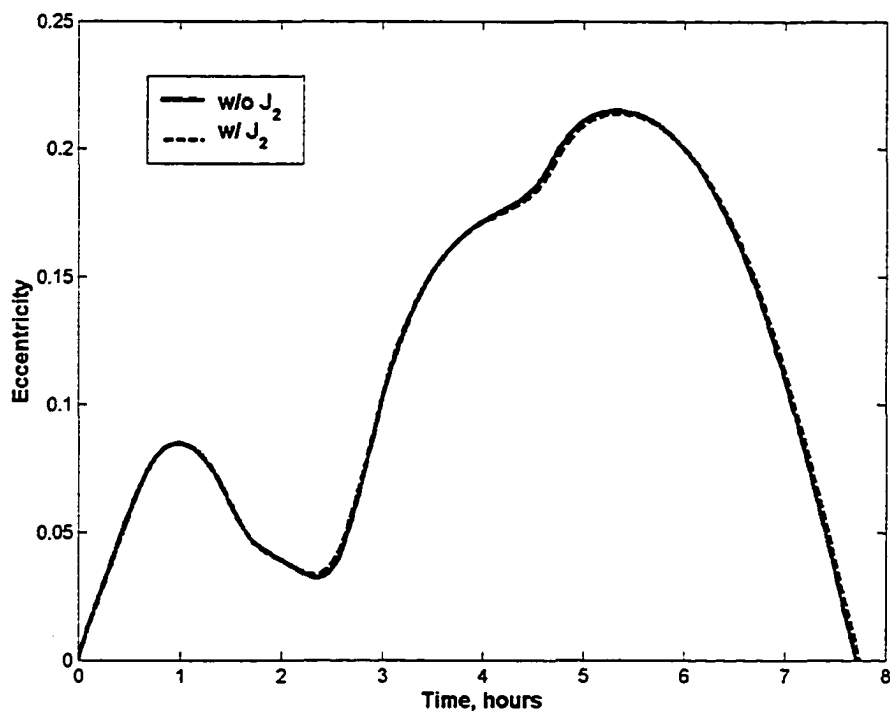


Figure 8.5 Time histories of eccentricity for optimal LEO-GPS transfers (equinoctial elements)

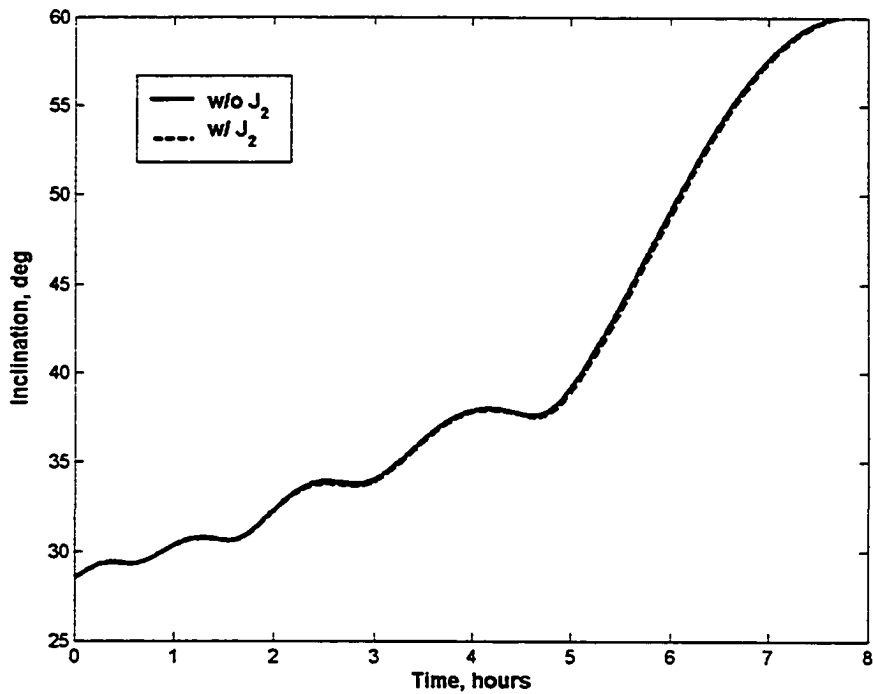


Figure 8.6 Time histories of inclination for optimal LEO-GPS transfers (equinoctial elements)

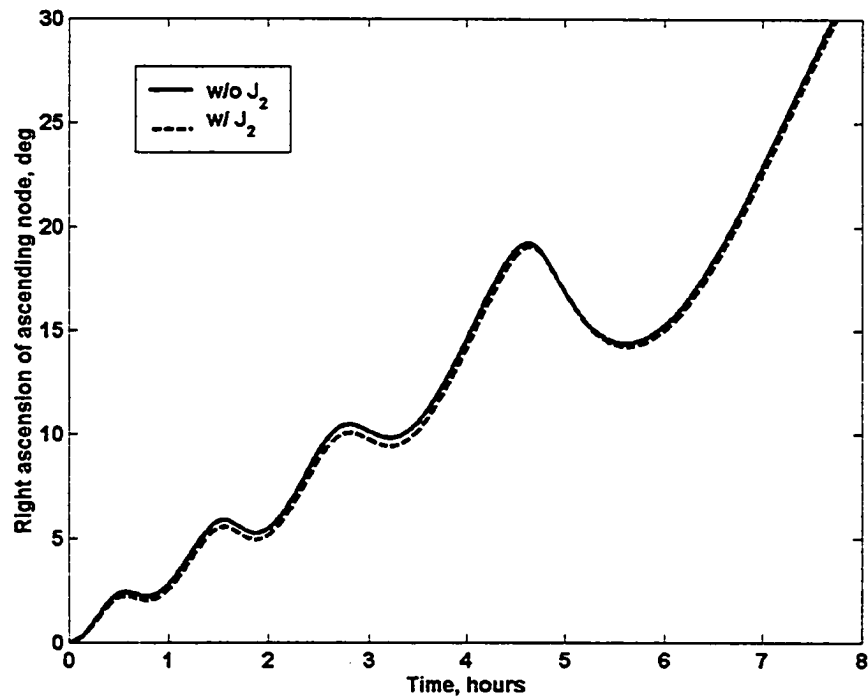


Figure 8.7 Time histories of RAAN for optimal LEO-GPS transfers (equinoctial elements)

8.1.5 Conclusions

Inertial frame transformation in terms of three Euler angles has been presented. The formulation of J_2 perturbation is derived in the new inertial frame. Any transfer to inclined circular orbit can be converted into the transfer to the “equatorial” circular orbit such that the terminal constraints expressed by spherical and equinoctial elements are simply defined. Furthermore, the convergence of performance using the hybrid method is also improved by this strategy. The LEO-GPS orbital transfers without and with J_2 perturbation are solved using spherical and equinoctial elements in the transformed inertial frame.

8.2 Trajectory Optimization Using Modified Equinoctial Elements

8.2.1 Introduction

It is known that the classical orbital elements exhibit singularities in numerical integration for some conditions such as zero eccentricity and zero inclination. Due to this reason, researchers hope to find another set of elements, which is also in a variational form but avoids singularities. In the past work, Broucke and Cefola [15] introduced a set of equinoctial elements. Battin [12] gave a set of equinoctial elements but used the true longitude for the sixth element. Walker [16] developed a set of modified equinoctial elements using the semi-latus rectum as the first element to accommodate all possible conic orbits. However, these researchers didn't use these elements to solve optimal orbital transfers.

Kechichian [19-22] also developed a series of equinoctial elements with different element as the sixth element and optimal LEO-GEO trajectories were presented by

solving TPBVP problem. The costate equations were developed and Earth-oblateness was considered. He used the semi-major axis as the first elements so that the parabolic orbits are excluded. Betts [17, 18] employed the Walker's equinoctial elements to solve the optimal interplanetary orbital transfer and Earth-Moon mission using the collocation method so he didn't need to derive the costate equations for integration. In this scenario, the general idea is presented to create a set of equinoctial elements that avoid singularities, and a new set of equinoctial elements based on Walker's solution by employing the non-dimensional angular momentum as the first element. This set of equinoctial elements can accommodate all conic orbits and seems relatively simpler than the others. Also the costate equations are developed, which have a much simpler expression. The trajectory optimization is demonstrated using this set of equinoctial elements and the hybrid method is employed.

8.2.2 Equinoctial Elements Avoiding Singularities

The orbital plane is only related to inclination and the nodal line where the orbital plane intercepts the X-Y plane. We use a two-dimensional vector to express the orbital plane.

$$\mathbf{i} = [i_x \ i_y] \quad (8.44)$$

The norm of vector \mathbf{i} is some function of the inclination and $f_i(*)$ should be a monotonic function, which means that one value of the inclination corresponds one value of $\|\mathbf{i}\|$.

$$\|\mathbf{i}\| = \sqrt{i_x^2 + i_y^2} = f_i(i) \quad (8.45)$$

$$i = f_i^{-1}(\|\mathbf{i}\|) = f_i^{-1}\left(\sqrt{i_x^2 + i_y^2}\right) \quad (8.46)$$

The nodal line is determined by the angle based on $\mathbf{i} = [i_x \ i_y]$.

$$i_x = f_i(i) \cos(f_\Omega(\Omega)) \quad (8.47)$$

$$i_y = f_i(i) \sin(f_\Omega(\Omega)) \quad (8.48)$$

$$\Omega' = f_\Omega(\Omega) = \tan^{-1}(i_x / i_y) \quad (8.49)$$

If $i_x = 0$ and $i_y = 0$, the inclination is zero, and Ω is undefined. Therefore, $\mathbf{i} = [i_x \ i_y]$ determine a set of orbits that are in a same orbital plane. We need two parameters to define the orbital plane pertains the inclination and nodal crossing. The next step is determining the shape of the orbit, which pertains to the eccentricity vector. We also use a vector $\mathbf{e} = [e_x \ e_y]$ to determine the shape of the orbit. The direction of the eccentricity could be determined by $\lambda = \tan^{-1}(e_x / e_y)$. The magnitude of eccentricity pertains to the the norm of $\|\mathbf{e}\|$

$$\|\mathbf{e}\| = \sqrt{e_x^2 + e_y^2} = f_e(e) \quad (8.50)$$

$$e = f_e^{-1}(\|\mathbf{e}\|) = f_e^{-1}(\sqrt{e_x^2 + e_y^2}) \quad (8.51)$$

$$e_x = f_e(e) \cos(f_\lambda(\lambda)) \quad (8.52)$$

$$e_y = f_e(e) \sin(f_\lambda(\lambda)) \quad (8.53)$$

If $e_x = 0$ and $e_y = 0$, the eccentricity is zero. To determine the size of the orbit, we could use several elements, such as semi-major axis, energy, semi-latus rectum and angular momentum.

The last element is to determine the position on the determined orbit. The inclined orbit could be projected onto the X-Y plane. Every point of the projected orbit is

corresponding a point in the inclined orbit. In X-Y plane, we use an angle measured from the +X axis to determine the position point of the spacecraft, and thus we also determine the position on the inclined orbit.

In summary, the first element determines the size of the orbit, the second and third elements determine the shape of the orbit (circular, elliptic, parabola or hyperbola), the fourth and fifth determine the orientation of the orbital plane, and the sixth element determines the angular displacement on the orbit. The former five elements could be considered so-called slow-changing variables and the sixth a fast-changing variable. The classical orbital elements can be related to the definition of the six elements. The first element could be semi-major axis, energy, semi-latus rectum, angular momentum or others. The second and third element could be $e\cos(\Omega + \omega)$, $e\sin(\Omega + \omega)$ or others. The fourth and fifth element could be $i\cos(\Omega)$, $i\cos(\Omega)$, $\tan(i/2)\cos(\Omega)$, $\tan(i/2)\sin(\Omega)$ and etc. The sixth element could be true longitude $L = \Omega + \omega + \theta$, eccentric longitude $L = \Omega + \omega + E$, mean longitude $L = \Omega + \omega + M$ and etc. For planar orbit transfers, we usually ignore the inclination and nodal crossing, and the fourth and fifth elements are not necessary.

8.2.3 Derivation of Differential Equations of Equinoctial Elements

A straightforward way to develop the ordinary differential equations (ODE) using equinoctial elements is introduced by Battin [12]. Kechichian [22] also used the similar method to give a general expression of the ODE, which is briefly introduced as below.

$$\frac{d\mathbf{x}}{dt} = \frac{\partial \mathbf{x}}{\partial \mathbf{v}}(f_T + f_d) \quad (8.54)$$

where \mathbf{x} is orbital element vector and \mathbf{v} is velocity vector. Equation (8.54) provides a direct method for determining ODE of equinoctial elements from position and velocity vectors in a specific inertial frame. The Lagrangian bracket and Poisson bracket are employed to derive this expression. The derivation could be found in Ref. [12, 22]. Another way to derive ODE of equinoctial elements is utilizing the Gauss planetary equations because equinoctial elements are always expressed in terms of classical orbital elements.

$$\frac{d\mathbf{x}}{dt} = \frac{\partial \mathbf{x}}{\partial a} \frac{da}{dt} + \frac{\partial \mathbf{x}}{\partial e} \frac{de}{dt} + \frac{\partial \mathbf{x}}{\partial i} \frac{di}{dt} + \frac{\partial \mathbf{x}}{\partial \Omega} \frac{d\Omega}{dt} + \frac{\partial \mathbf{x}}{\partial \omega} \frac{d\omega}{dt} + \frac{\partial \mathbf{x}}{\partial M} \frac{dM}{dt} \quad (8.55)$$

In Ref. [12], we can see that $h = \tan(i/2)\cos(\Omega)$, $k = \tan(i/2)\sin(\Omega)$. Why should we pick the term $\tan(i/2)$? The advantage of $\tan(i/2)$ could be revealed as follows.

$$\frac{dh}{dt} = \frac{\partial h}{\partial \Omega} \frac{d\Omega}{dt} + \frac{\partial h}{\partial i} \frac{di}{dt} \quad (8.56)$$

$$\frac{dh}{dt} = -\tan(i/2)\sin\Omega \frac{d\Omega}{dt} + \frac{1}{2\cos^2(i/2)} \cos\Omega \frac{di}{dt} \quad (8.57)$$

$$\frac{dh}{dt} = -\frac{\sin(i/2)}{\cos(i/2)} \sin\Omega \frac{r\sin(\omega+\theta)}{\bar{h}\sin i} f_n + \frac{1}{2\cos^2(i/2)} \cos\Omega \frac{r\cos(\omega+\theta)}{\bar{h}} f_n \quad (8.58)$$

$$\frac{dh}{dt} = \left[\frac{\sin i}{2\cos^2(i/2)} \frac{-\sin\Omega\sin(\omega+\theta)}{\sin i} + \frac{1}{2\cos^2(i/2)} \cos\Omega\cos(\omega+\theta) \right] \frac{r}{\bar{h}} f_n \quad (8.59)$$

$$\frac{dh}{dt} = \left\{ \frac{1}{2\cos^2(i/2)} [-\sin\Omega\sin(\omega+\theta) + \cos\Omega\cos(\omega+\theta)] \right\} \frac{r}{\bar{h}} f_n \quad (8.60)$$

Note that

$$1 + h^2 + k^2 = 1 + \tan^2(i/2) = \frac{1}{\cos^2(i/2)} \quad (8.61)$$

$$[-\sin\Omega\sin(\omega+\theta) + \cos\Omega\cos(\omega+\theta)] = \cos(\Omega + \omega + \theta) = \cos L \quad (8.62)$$

Then

$$\frac{dh}{dt} = \frac{1}{2}(1 + h^2 + k^2) \cos L \frac{r}{\bar{h}} f_n \quad (8.63)$$

where r is the radius and \bar{h} is the angular momentum. In this derivation, we can see that the term $\tan(i/2)$ is a perfect choice to define the element h and k , whose variational form is simple.

8.2.4 Equinoctial Elements Using Non-dimensional Angular Momentum

Based on Battin's [12] and Walker's definitions [16] of equinoctial elements, the non-dimensional angular momentum is employed as the first element to describe the size of a conic orbit.

$$h = \sqrt{\frac{p}{\mu}} = \frac{\|\mathbf{r} \times \mathbf{v}\|}{\mu} = \sqrt{\frac{a(1-e^2)}{\mu}} \quad (8.64)$$

The other elements remain the same as those of Battin's and Walker's definitions. The ODE of this set of equinoctial elements seems to be much simpler.

$$\dot{h} = h n \cdot f_r \quad (8.65)$$

$$\dot{f} = h \sin L \cdot f_r + [h \cos L + n(\cos L + f)] \cdot f_t - n X g \cdot f_n \quad (8.66)$$

$$\dot{g} = -h \cos L \cdot f_r + [h \sin L + n(\sin L + g)] \cdot f_t + n X f \cdot f_n \quad (8.67)$$

$$\dot{h} = \frac{1}{2} n s^2 \cos L \cdot f_n \quad (8.68)$$

$$\dot{k} = \frac{1}{2} n s^2 \sin L \cdot f_n \quad (8.69)$$

$$\dot{L} = n X \cdot f_n + \frac{1}{n^2 \bar{h} \mu} \quad (8.70)$$

where

$$n = \frac{\hbar}{1 + f \cos L + g \sin L} \quad (8.71)$$

$$X = h \sin L - k \cos L \quad (8.72)$$

$$s^2 = 1 + h^2 + k^2 \quad (8.73)$$

The acceleration due to thrust and perturbations are represented by three components f_r , f_i and f_n in the local RTN frame.

The transformation between equinoctial elements and classical orbital elements are easily obtained.

$$\cos \Omega = \frac{h}{\sqrt{h^2 + k^2}}, \sin \Omega = \frac{k}{\sqrt{h^2 + k^2}} \quad (8.74)$$

$$\cos i = \frac{1 - h^2 - k^2}{1 + h^2 + k^2}, \sin i = \frac{2\sqrt{h^2 + k^2}}{1 + h^2 + k^2} \quad (8.75)$$

$$\cos \omega = \frac{fh + gk}{\sqrt{(f^2 + g^2)(h^2 + k^2)}}, \sin \omega = \frac{gh - fk}{\sqrt{(f^2 + g^2)(h^2 + k^2)}} \quad (8.76)$$

$$\cos(\omega + \theta) = \frac{h \cos L + k \sin L}{\sqrt{h^2 + k^2}}, \sin(\omega + \theta) = \frac{h \sin L - k \cos L}{\sqrt{h^2 + k^2}} \quad (8.77)$$

The transformation from equinoctial elements to Cartesian elements is given by Battin [12] and Betts [17].

$$r_x = r(\cos \Omega \sin(\omega + \theta) - \sin \Omega \sin(\omega + \theta) \cos i) \quad (8.78)$$

$$r_y = r(\sin \Omega \cos(\omega + \theta) + \cos \Omega \sin(\omega + \theta) \cos i) \quad (8.79)$$

$$r_z = r \sin(\omega + \theta) \sin i \quad (8.80)$$

$$v_x = -\frac{1}{\hbar}[\cos \Omega (\sin(\omega + \theta) + e \sin \omega) + \sin \Omega (\cos(\omega + \theta) + e \cos \omega) \cos i] \quad (8.81)$$

$$v_y = -\frac{1}{\hbar} [\sin \Omega (\sin(\omega + \theta) + e \sin \omega) - \cos \Omega (\cos(\omega + \theta) + e \cos \omega) \cos i] \quad (8.82)$$

$$v_z = \frac{1}{\hbar} (\cos(\omega + \theta) + e \cos \omega) \sin i \quad (8.83)$$

By replacing the classical orbital element by equinoctial elements, the Cartesian elements could be expressed by equinoctial elements.

$$r_x = \frac{r}{s^2} [\cos L + (h^2 - k^2) \cos L + 2hk \sin L] \quad (8.84)$$

$$r_y = \frac{r}{s^2} [\sin L - (h^2 - k^2) \sin L + 2hk \cos L] \quad (8.85)$$

$$r_z = \frac{2r}{s^2} (h \sin L - k \cos L) \quad (8.86)$$

$$v_x = -\frac{1}{\hbar s^2} [\sin L + (h^2 - k^2) \sin L - 2hk \cos L + g - 2f hk + (h^2 - k^2) g] \quad (8.87)$$

$$v_y = -\frac{1}{\hbar s^2} [-\cos L + (h^2 - k^2) \cos L + 2hk \sin L - f + 2ghk + (h^2 - k^2) f] \quad (8.88)$$

$$v_z = \frac{2}{\hbar s^2} (h \cos L + k \sin L + fh + gk) \quad (8.89)$$

where $r = \frac{\hbar^2 \mu}{1 + f \cos L + g \sin L} \quad (8.90)$

The next step is to develop the costate equations for this set of equinoctial elements. As introduced in chapter two, the matrix form of ODE of equinoctial elements could be written as

$$\dot{\mathbf{x}} = \mathbf{M}f + \mathbf{D} \quad (8.91)$$

where $\mathbf{x} = [\hbar \ f \ g \ h \ k \ L]^T$, $\mathbf{f} = [f_r \ f_i \ f_n]^T$, \mathbf{M} is a 6×3 matrix and \mathbf{D} is 6×1 vector.

The elements in matrix \mathbf{M} and vector \mathbf{D} are described as follows.

$$M_{11} = 0 \quad M_{12} = \hbar n \quad M_{13} = 0 \quad (8.92)$$

$$M_{21} = \hbar \sin L \quad M_{22} = \hbar \cos L + n(\cos L + f) \quad M_{23} = -nXg$$

$$M_{31} = -\hbar \cos L \quad M_{32} = \hbar \sin L + n(\sin L + g) \quad M_{33} = nXf$$

$$M_{41} = 0 \quad M_{42} = 0 \quad M_{43} = \frac{1}{2}ns^2 \cos L$$

$$M_{51} = 0 \quad M_{52} = 0 \quad M_{53} = \frac{1}{2}ns^2 \sin L$$

$$M_{61} = 0 \quad M_{62} = 0 \quad M_{63} = nX$$

$$D = \frac{1}{n^2 \hbar \mu} \text{ and } \mathbf{D} = [0 \ 0 \ 0 \ 0 \ D]^T$$

The costate equation is derived by differentiate the Hamiltonian with respect to equinoctial elements.

$$\dot{\lambda} = -\frac{\partial H}{\partial \mathbf{x}} = -\left(\lambda^T \frac{\partial \mathbf{M}}{\partial \mathbf{x}} \frac{T}{m} \mathbf{a} + \lambda^T \frac{\partial \mathbf{D}}{\partial \mathbf{x}} \right) - \left(\lambda^T \frac{\partial \mathbf{M}}{\partial \mathbf{x}} \mathbf{f}_p + \lambda^T \mathbf{M} \frac{\partial \mathbf{f}_p}{\partial \mathbf{x}} \right) \quad (8.93)$$

The derivatives of elements of matrix \mathbf{M} and vector \mathbf{D} with respect to equinoctial elements are necessary to construct the costate equations, which are given in Appendix II.

8.2.5 The Perturbation Formulation in Costate Equations

Earth oblateness

For near Earth orbit transfer the perturbation is mainly the oblateness and atmospheric drag in low altitude. The J_2 perturbation has been shown by Kechichian [19] only with different notation as followed:

$$f_{ob} = -\frac{3\mu J_2 R_e^2}{2r^4} \left[1 - \frac{12(h \sin L - k \cos L)^2}{(1 + h^2 + k^2)^2} \right] \quad (8.94)$$

$$f_{ob_r} = -\frac{12\mu J_2 R_e^2}{r^4} \frac{(h \sin L - k \cos L)(h \cos L + k \sin L)}{(1+h^2+k^2)^2} \quad (8.95)$$

$$f_{ob_n} = -\frac{6\mu J_2 R_e^2}{r^4} \frac{(1-h^2-k^2)(h \sin L - k \cos L)}{(1+h^2+k^2)^2} \quad (8.96)$$

If we want to incorporate J_2 formulation in costate equations, we need derive the derivative of J_2 acceleration with respect to equinoctial elements as follows. Please note that f_r , f_t and f_n are used to represent f_{ob_r} , f_{ob_t} and f_{ob_n} .

$$\frac{\partial f_r}{\partial h} = 6 \frac{A}{r} \left(1 - \frac{12X^2}{s^4}\right) \frac{\partial r}{\partial h} \quad (8.97)$$

$$\frac{\partial f_r}{\partial f} = 6 \frac{A}{r} \left(1 - \frac{12X^2}{s^4}\right) \frac{\partial r}{\partial f}$$

$$\frac{\partial f_r}{\partial g} = 6 \frac{A}{r} \left(1 - \frac{12X^2}{s^4}\right) \frac{\partial r}{\partial g}$$

$$\frac{\partial f_r}{\partial h} = \frac{3A}{2} \left[\frac{24X \sin L}{s^4} - \frac{48X^2 h}{s^6} \right]$$

$$\frac{\partial f_r}{\partial k} = \frac{3A}{2} \left[\frac{-24X \cos L}{s^4} - \frac{48X^2 k}{s^6} \right]$$

$$\frac{\partial f_r}{\partial L} = \frac{6A}{r} \left(1 - \frac{12X^2}{s^4}\right) \frac{\partial r}{\partial L} + 36A \frac{XX_L}{s^4}$$

$$\frac{\partial f_t}{\partial h} = 48 \frac{A}{r} \frac{XY}{s^4} \frac{\partial r}{\partial h}$$

$$\frac{\partial f_t}{\partial f} = 48 \frac{A}{r} \frac{XY}{s^4} \frac{\partial r}{\partial f}$$

$$\frac{\partial f_t}{\partial g} = 48 \frac{A}{r} \frac{XY}{s^4} \frac{\partial r}{\partial g}$$

$$\frac{\partial f_t}{\partial h} = -12A \left[\frac{X \cos L + Y \sin L}{s^4} - \frac{4XYh}{s^6} \right]$$

$$\frac{\partial f_t}{\partial k} = -12A \left[\frac{X \sin L - Y \cos L}{s^4} - \frac{4XYk}{s^6} \right]$$

$$\frac{\partial f_t}{\partial L} = 48 \frac{A}{r} \frac{XY}{s^4} \frac{\partial r}{\partial L} - 12A \frac{X_L Y + X Y_L}{s^4}$$

$$\frac{\partial f_n}{\partial h} = 24 \frac{A}{r} \frac{(1-h^2-k^2)X}{s^4} \frac{\partial r}{\partial h}$$

$$\frac{\partial f_n}{\partial f} = 24 \frac{A}{r} \frac{(1-h^2-k^2)X}{s^4} \frac{\partial r}{\partial f}$$

$$\frac{\partial f_n}{\partial g} = 24 \frac{A}{r} \frac{(1-h^2-k^2)X}{s^4} \frac{\partial r}{\partial g}$$

$$\frac{\partial f_n}{\partial h} = -6A \left[\frac{-2hX + (1-h^2-k^2)\sin L}{s^4} - \frac{4h(1-h^2-k^2)X}{s^6} \right]$$

$$\frac{\partial f_n}{\partial k} = -6A \left[\frac{-2kX - (1-h^2-k^2)\cos L}{s^4} - \frac{4k(1-h^2-k^2)X}{s^6} \right]$$

$$\frac{\partial f_n}{\partial L} = 24 \frac{A}{r} \frac{(1-h^2-k^2)X}{s^4} \frac{\partial r}{\partial L} - 6A \frac{(1-h^2-k^2)X_L}{s^4}$$

where $A = \frac{\mu J_2 \text{Re}^2}{r^4}$, $Y = h \cos L + k \sin L$, $Y_L = -h \sin L - k \cos L$

$$\frac{\partial r}{\partial h} = \frac{2r}{h}, \frac{\partial r}{\partial f} = -n^2 \mu \cos L, \frac{\partial r}{\partial g} = -n^2 \mu \sin L, \frac{\partial r}{\partial h} = \frac{\partial r}{\partial k} = 0, \frac{\partial r}{\partial L} = -n^2 \mu w_L$$

Atmosphere drag

The spacecraft on the Low-Earth-Orbit is affected by the atmosphere drag, which could be described with an exponential function [24].

$$\mathbf{f}_d = -\frac{1}{2} \rho_0 e^{-\beta(r-r_0)} S C_D v \mathbf{v} \quad (8.98)$$

where $\mathbf{v} = [v_r, v_t, v_n]^T$ is the velocity of spacecraft, and v is the velocity magnitude.

Other parameters in Eq. (8.98) are constant factors associated with spacecraft. Three components of drag could be expressed easily in RTN frame

$$f_{d_r} = -\frac{1}{2} \rho_0 e^{-\beta(r-r_0)} S C_D v v_r \quad (8.99)$$

$$f_{d_t} = -\frac{1}{2} \rho_0 e^{-\beta(r-r_0)} S C_D v v_t \quad (8.100)$$

$$f_{d_n} = 0 \quad (8.101)$$

$$\text{where } v_r = \frac{1}{\hbar}(f \sin L - g \cos L), v_t = \frac{1}{\hbar}(1 + f \cos L + g \sin L) \text{ and } v_n = 0. \quad (8.102)$$

The derivative of the atmosphere drag with respect to equinoctial elements is as follows.

$$\frac{\partial \mathbf{f}_d}{\partial \mathbf{x}} = \frac{1}{2} \beta \rho_0 e^{-\beta(r-r_0)} \frac{\partial r}{\partial \mathbf{x}} S C_D v \mathbf{v} - \frac{1}{2} \rho_0 e^{-\beta(r-r_0)} S C_D \left(\frac{\partial v}{\partial \mathbf{x}} \mathbf{v} + \frac{\partial \mathbf{v}}{\partial \mathbf{x}} v \right) \quad (8.103)$$

The velocity magnitude can be expressed by modified equinoctial elements.

$$E = \frac{v^2}{2} - \frac{\mu}{r} = -\frac{\mu}{2a} = -\frac{1-f^2-g^2}{2\hbar^2} \quad (8.104)$$

$$\frac{v^2}{2} = \frac{\mu}{r} - \frac{1-f^2-g^2}{2\hbar^2} \quad (8.105)$$

$$v \frac{\partial v}{\partial \mathbf{x}} = -\frac{\mu}{r^2} \frac{\partial r}{\partial \mathbf{x}} - \frac{\partial}{\partial \mathbf{x}} \left(\frac{1-f^2-g^2}{2\hbar^2} \right) \quad (8.106)$$

The derivatives of the velocity magnitude with respect to equinoctial elements are as follows.

$$\frac{\partial v}{\partial \hbar} = \frac{1}{v} \left[-\frac{\mu}{r^2} \frac{\partial r}{\partial \hbar} + \frac{1-f^2-g^2}{\hbar^3} \right] \quad (8.107)$$

$$\frac{\partial v}{\partial f} = \frac{1}{v} \left[-\frac{\mu}{r^2} \frac{\partial r}{\partial f} + \frac{f}{\hbar^2} \right]$$

$$\frac{\partial v}{\partial g} = \frac{1}{v} \left[-\frac{\mu}{r^2} \frac{\partial r}{\partial g} + \frac{g}{\hbar^2} \right]$$

$$\frac{\partial v}{\partial h} = \frac{\partial v}{\partial k} = \frac{\partial v}{\partial L} = 0$$

The derivative of the radial velocity with respect to equinoctial elements is as follows.

$$\frac{\partial v_r}{\partial \hbar} = -\frac{2}{\hbar^2} (f \sin L - g \cos L), \quad (8.108)$$

$$\frac{\partial v_r}{\partial f} = \frac{\sin L}{\hbar}, \frac{\partial v_r}{\partial g} = -\frac{\cos L}{\hbar}, \frac{\partial v_r}{\partial h} = \frac{\partial v_r}{\partial k} = 0, \frac{\partial v_r}{\partial L} = \frac{f \cos L + g \sin L}{\hbar}$$

The derivative of the tangential velocity with respect to equinoctial elements is as below.

$$\frac{\partial v_t}{\partial \hbar} = -\frac{2}{\hbar^2} (1 + f \cos L + g \sin L) \quad (8.109)$$

$$\frac{\partial v_t}{\partial f} = \frac{\cos L}{\hbar}, \frac{\partial v_t}{\partial g} = \frac{\sin L}{\hbar}, \frac{\partial v_t}{\partial h} = \frac{\partial v_t}{\partial k} = 0, \frac{\partial v_t}{\partial L} = \frac{-f \sin L + g \cos L}{\hbar}$$

8.2.6 LEO-GEO Orbit Transfer Solved by Modified set of Equinoctial Elements

The LEO-GEO orbit transfer is to be solved using the modified set of equinoctial elements. The initial mass is 6100 kg and the initial thrust weight ratio is set $5(10^{-3})$. The I_{sp} is 3800 seconds. The hybrid method is employed. The SQP design variables include 6 initial costate, transfer time and longitude angle for starting the burn, which is considered due to existence of plane change. The optimal solutions with J_2 and without J_2 effect are obtained and shown in Tables 8.6. Due to the higher thrust compared with J_2 acceleration, two sets of solutions are very close. Only the longitude is slightly different.

The time histories of modified equinoctial elements for two cases are shown in Figs.8.8-8.13. For equinoctial elements \hbar , h and L , it is hard to tell difference by eye.

Table 8.6 Optimal solutions of LEO-GEO orbit transfers using modified set of equinoctial elements

	Without J_2	With J_2
$a(t_f)$ (Re)	6.6107001	6.6107002
$e(t_f)$	$1.1553(10^{-8})$	$2.0453(10^{-9})$
$i(t_f)$ (deg)	$2.5348(10^{-8})$	$2.6146(10^{-8})$
Final mass $m(t_f)$ (kg)	5237.8217	5236.7465
Departure $\omega(t_0) + \theta(t_0)$ (deg)	114.4322	104.0006
Transfer time (hours)	29.8386	29.8758

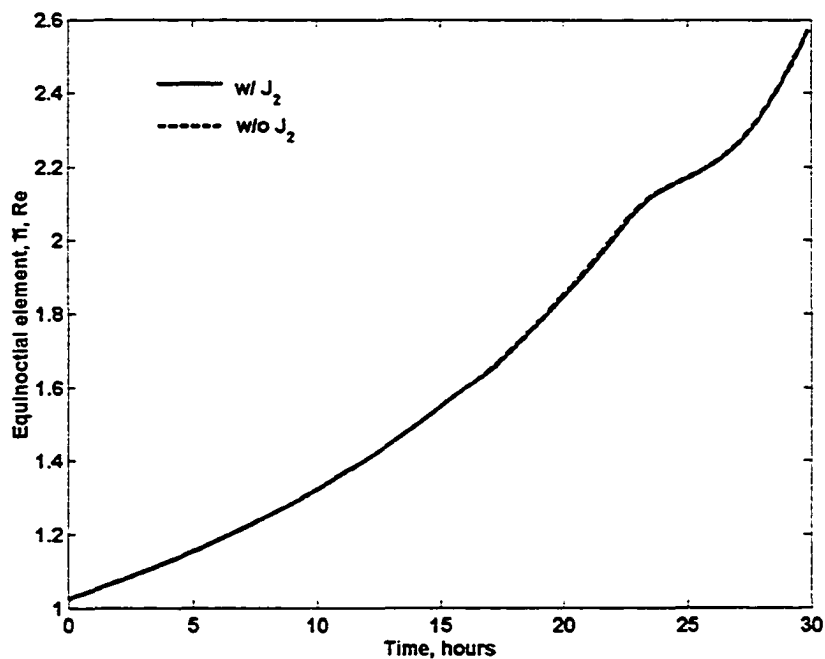


Figure 8.8 Time histories of equinoctial element \hbar

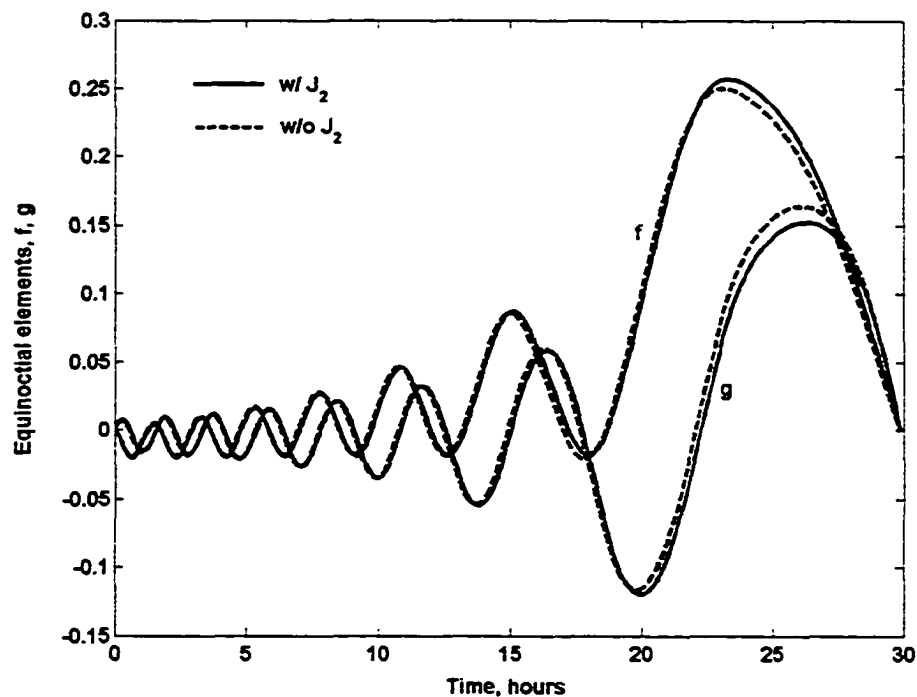


Figure 8.9 Time histories of equinoctial elements f and g

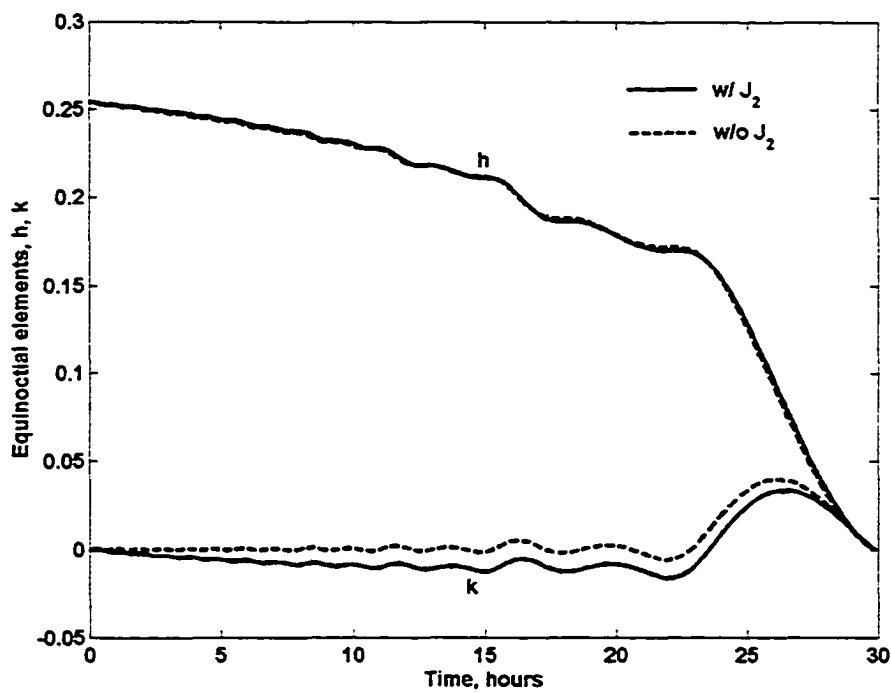


Figure 8.10 Time histories of equinoctial elements h and k

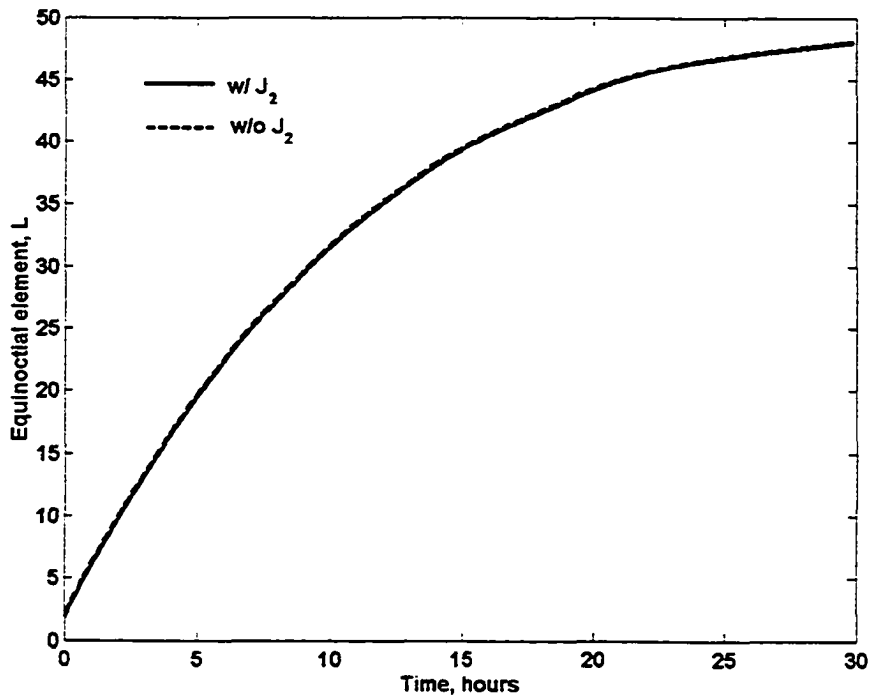


Figure 8.11 Time histories of equinoctial elements L

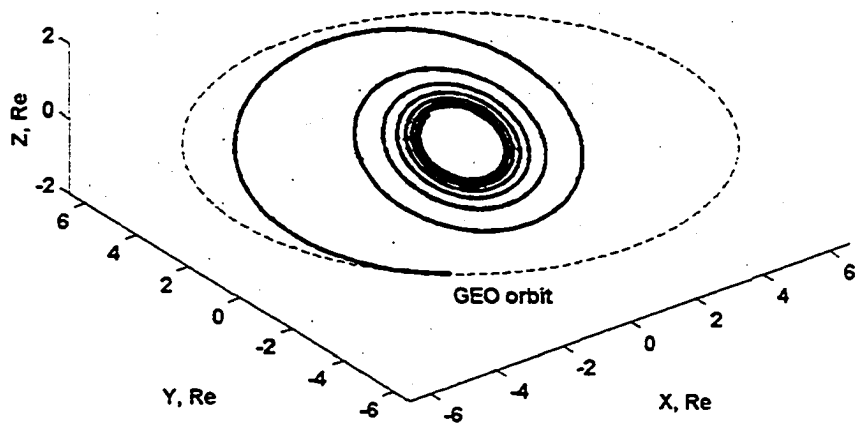


Figure 8.12 Optimal LEO-GEO trajectory w/ J_2 solved by modified equinoctial elements

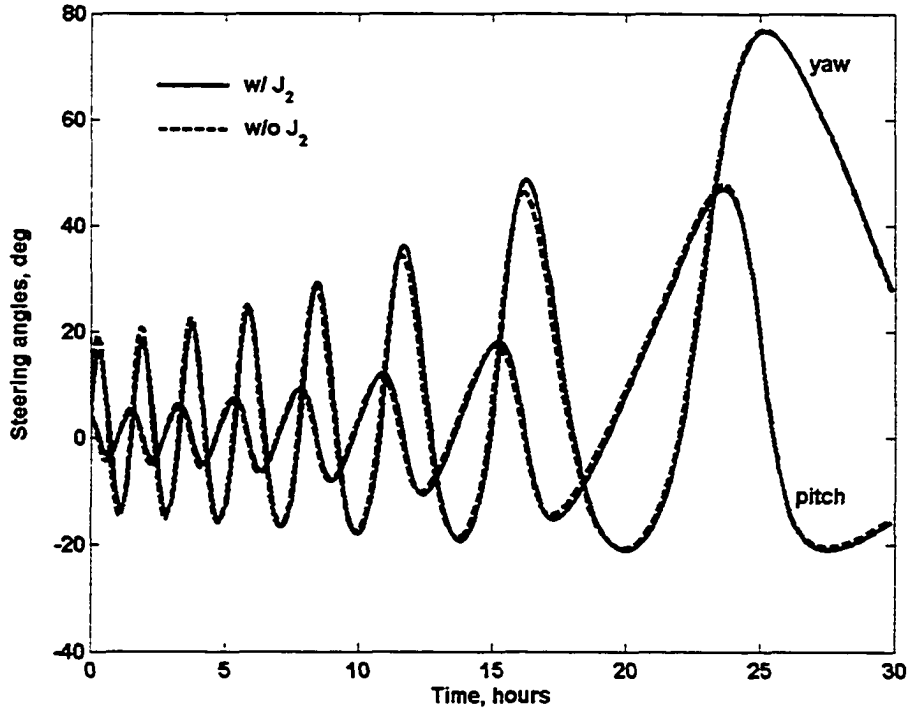


Figure 8.13 Optimal control steering solved by modified equinoctial elements

8.2.7 Conclusions

The non-dimensional angular momentum is employed as the first equinoctial elements. The state equations and costate equations have been developed, and both state and costate equations exhibit simple formulations. Furthermore, the perturbations such as J_2 effect and atmosphere drag are also formulated in both state and costate equations. A LEO-GEO orbit transfer is solved to demonstrate the use of the new set of equinoctial elements. This set of equinoctial elements is also a good choice for spacecraft dynamics.

CHAPTER 9 LOW-THRUST GUIDANCE SCHEME FOR EARTH-CAPTURE TRAJECTORIES

9.1 Introductions

As we know, trajectory optimization attempts to find an open-loop optimal control that optimizes a desired performance measure. This is usually to investigate the feasibility of desired missions or to choose a trajectory that saves time or fuel. However, due to uncertain perturbations during real transfers, open-loop control cannot guide spacecraft exactly to follow the pre-calculated trajectory. Therefore, guidance schemes are required to prevent spacecraft deviating from the desired orbit. Furthermore, simplicity, reliability, and autonomy are all desirable characteristics of a good guidance design. Compared to trajectory optimization, the volume of work involving the low-thrust guidance problem also appears to be limited. A series of guidance schemes were developed including blended control [81], inversed dynamics [82, 83], linear quadratic regulator [84-86], and Lyapunov-based guidance [45-47].

In this chapter, a guidance scheme based on application of time-rate of orbital elements is utilized for Earth-capture trajectories. There is no reference trajectory and control stored onboard, and the task is how to guide the spacecraft to return to low-Earth orbit from a hyperbolic orbit, which is different from the trajectory optimization described in previous chapters. The controllers using optimal time-rate of energy and eccentricity are employed. Also the blended control is developed, which is implemented periodically by onboard calculations.

Deep Space 1 (DS1) demonstrated that solar electric propulsion (SEP) is a viable propulsion option for interplanetary space missions [1]. An interplanetary mission design may include using SEP for the Earth-return leg of a sample return mission. For example, Vadali et al. [87] investigated the use of low-thrust propulsion for a Mars sample return mission. In a sample return scenario, SEP would eventually perform the capture maneuver from hyperbolic approach to a closed Earth orbit. It appears that research involving optimal SEP capture trajectories, especially transfers involving hundreds of orbital revolutions, is somewhat limited. Battin [88] presented a feasible scheme for performing capture trajectories into a low lunar orbit with a variable low-thrust engine. Vadali et al. [87] demonstrated a Lyapunov feedback control law for performing a low-thrust capture into a high-altitude Earth elliptical orbit. Recently, Kluever [67], and Kluever and Gao [89] presented a method for computing optimal low-thrust Earth-capture trajectories. The trajectory optimization method in Ref. [67, 89] simultaneously considered the initial high-energy transfer to a closed orbit and the subsequent quasi-circular spiral transfer (with hundreds of revolutions) to a low-Earth orbit (LEO).

Low-thrust guidance may be defined as the determination of the thrust-steering program that is required to attain a target orbit. This guidance problem presents a challenge since the thrust magnitude is small (SEP thrust-to-weight ratio is typically around 10^{-5} to 10^{-4}) and the continuous steering commands must be determined over a long transfer time (possibly hundreds of days). In addition, trajectory optimization methods typically determine an open-loop steering program that may be difficult or impractical to store onboard for use by a guidance system. Furthermore, the low control

authority characteristic of SEP may preclude the use of traditional path-following guidance designs that rely on stored trajectory and control profiles.

Desai et al. [90] developed an autonomous guidance system for DS1 that targeted flyby conditions with an asteroid and a comet. The DS1 guidance computed steering corrections based on a linear combination of deviations between a reference (stored) target state and a numerically projected trajectory. This linear guidance design was used only for small trajectory deviations (small steering corrections); significant deviations required a complete redesign of the reference trajectory and steering profiles, which was performed on the ground.

In this work, we present a new predictive guidance scheme for performing an Earth-capture maneuver using low-thrust propulsion. We assume that the capture trajectory begins with hyperbolic conditions near the Earth's sphere of influence (SOI) and that the terminal target is a circular LEO. Our guidance design is comprised of two major stages. The first phase reduces orbital energy and eccentricity in order to establish a closed orbit at the first perigee passage. The second guidance phase reduces energy, eccentricity, and inclination so that the resulting trajectory terminates on a surface defined by universal low-thrust planar spiral trajectory solutions. Once the spacecraft has reached the spiral solution surface, a simple open-loop thrust-steering profile can be used to guide the vehicle on an inward winding spiral path to the target LEO. Both initial guidance phases alter the capture trajectory by adjusting a single guidance parameter. Numerical results are presented for the guided capture trajectories.

9.2 System Model

The Earth-capture trajectory is governed by the following dynamical equations:

$$\dot{\mathbf{r}} = \mathbf{v} \quad (9.1)$$

$$\dot{\mathbf{v}} = -\frac{\mu \mathbf{r}}{r^3} + \mathbf{a}_P + \mathbf{a}_T \quad (9.2)$$

$$\dot{m} = \frac{-2\eta P}{(gI_{sp})^2} \quad (9.3)$$

where \mathbf{r} and \mathbf{v} are the position and velocity vectors of the spacecraft in an Earth-centered inertial (ECI) Cartesian frame, μ is the Earth gravitational constant, \mathbf{a}_P is an acceleration vector due to perturbations, and \mathbf{a}_T is the thrust acceleration vector. Eq. (9.3) defines the mass loss due to the low-thrust engine where m is spacecraft mass, P is input power to the SEP system, η is engine efficiency, g is Earth gravitational acceleration, and I_{sp} is specific impulse. Perturbation vector \mathbf{a}_P in Eq. (9.2) accounts for Earth oblateness (J_2) effects and lunar and solar gravitational acceleration. Thrust acceleration \mathbf{a}_T in the ECI frame is

$$\mathbf{a}_T = \frac{2\eta P}{mgI_{sp}} \hat{\mathbf{u}}_{\text{ECI}} \quad (9.4)$$

where $\hat{\mathbf{u}}_{\text{ECI}}$ is a unit vector along the thrust direction. It is advantageous to define the thrust-direction unit vector in a local-vertical local-horizontal (LVLH) frame in terms of local pitch and yaw steering angles:

$$\hat{\mathbf{u}}_{\text{LVLH}} = [\sin \alpha \cos \beta \quad \cos \alpha \cos \beta \quad \sin \beta]^T \quad (9.5)$$

Pitch angle (α) is measured from the local horizon to the projection of the thrust vector onto the orbit plane, and yaw angle (β) is measured from the orbit plane to the thrust vector. A coordinate transformation from the LVLH to ECI frame determines the thrust direction required in Eq. (9.4).

9.3 Capture Guidance Scheme

The goal of the guidance design is to determine the thrust-steering angle program such that the vehicle will follow a capture trajectory to circular LEO. It is assumed that the SEP vehicle is on a return path to Earth (perhaps the end of a sample return mission), and the capture phase begins near the Earth's SOI with hyperbolic conditions with respect to the Earth's gravity field.

We choose to develop a predictive guidance system instead of a path-following guidance design that relies on a stored reference trajectory. Furthermore, we wish to keep our guidance design simple, and therefore the scheme determines the steering-angle commands by selecting a single guidance parameter. The capture guidance is separated into three basic phases: 1) initial energy and eccentricity reduction, 2) transition to spiral boundary surface, and 3) spiral transfer to target LEO.

9.3.1 Initial Energy and Eccentricity Reduction Guidance Phase

The goal of the initial guidance phase is to reduce orbital energy and eccentricity such that a closed (elliptic) orbit is established at the first perigee passage. Our initial guidance phase accomplishes this task by blending two control laws that reduce the instantaneous rates of change of energy and eccentricity. We assume that no out-of-plane (yaw) steering is employed, so that all propulsive force can be used to alter orbital energy and eccentricity. A desired inclination-change maneuver can be efficiently performed at nodal crossings after a closed orbit is established. The first control law, which minimizes the rate of energy change, is derived from the governing energy-rate equation

$$\dot{E} = a_T \sqrt{\frac{\mu}{p}} [e \sin \theta \sin \alpha + (1 + e \cos \theta) \cos \alpha] \quad (9.6)$$

where E is orbital energy, p is the semilatus parameter, e is eccentricity, and θ is true anomaly. Optimal pitch steering that minimizes energy rate is determined by setting the partial derivative of Eq. (9.6) equal to zero:

$$\frac{\partial \dot{E}}{\partial \alpha} = a_T \sqrt{\frac{\mu}{p}} [e \sin \theta \cos \alpha - (1 + e \cos \theta) \sin \alpha] = 0 \quad (9.7)$$

The resulting extremal control law is

$$\tan \alpha = \frac{e \sin \theta}{1 + e \cos \theta} \quad (9.8)$$

The optimal control law that minimizes energy rate is determined by taking the second partial derivative of Eq. (9.6) and selecting the proper sign to ensure $\partial^2 \dot{E} / \partial \alpha^2 \geq 0$. The optimal control law is

$$\sin \alpha = \frac{-e \sin \theta}{\sqrt{1 + e^2 + 2e \cos \theta}} \quad (9.9)$$

$$\cos \alpha = \frac{-(1 + e \cos \theta)}{\sqrt{1 + e^2 + 2e \cos \theta}} \quad (9.10)$$

This control law aligns the thrust vector in the opposite direction of the instantaneous velocity vector (“anti-tangent steering”).

The second control law reduces eccentricity during the capture maneuver. Eccentricity can be determined from orbital energy and angular momentum, h :

$$e = \sqrt{1 + \frac{2Eh^2}{\mu^2}} \quad (9.11)$$

At the start of the Earth-capture phase (near the SOI), the orbit is hyperbolic with eccentricity slightly greater than one and energy slightly positive, and the velocity vector

is nearly aligned with the radial direction. Therefore, anti-tangent steering will reduce energy to some extent, but the subsequent orbit will approach a degenerate conic where all kinetic energy is radial velocity and perigee radius is zero. In order to avoid this degenerate case, the thrust acceleration must have a component in the horizontal direction in order to increase angular momentum. Eq. (9.11) shows that increasing h after a capture orbit is established ($E < 0$) decreases eccentricity. Therefore, the simple inertial thrust-steering control law is proposed:

$$\alpha = \pi + \theta, \quad -\pi \leq \theta < 0 \text{ rad} \quad (9.12)$$

Control law (9.12) fixes the thrust vector perpendicular to the line of apses, so that angular momentum is increased when the spacecraft is near apogee. Steering law (9.12) is essentially the “inertial-fixed” steering program for decreasing eccentricity proposed by Spitzer for Earth orbit-raising maneuvers [91].

The “blended” steering direction is determined from a linear combination of the minimum-energy rate and inertial steering programs

$$\hat{\mathbf{u}} = \hat{\mathbf{u}}_E + \lambda \hat{\mathbf{u}}, \quad (9.13)$$

where λ is a constant scalar. Unit vectors $\hat{\mathbf{u}}_E$ and $\hat{\mathbf{u}}$, are the thrust directions for the minimum-energy rate and inertial steering control laws, respectively, as regulated by Eqs. (9.9), (9.10), and (9.12). The respective thrust-direction unit vectors in the LVLH frame are determined by Eq. (9.5) with the appropriate pitch angle and zero yaw angle ($\beta = 0$). This method was employed in Ref. [48] to compute optimal trajectories.

The initial guidance phase adjusts the single guidance parameter λ so that a desirable closed orbit is established at the first perigee passage. Desirable orbital conditions at perigee are low eccentricity and radius greater than some acceptable lower

bound (r_{\min}). Therefore, the guidance scheme selects the best parameter λ by minimizing the following augmented performance index

$$J = e_p + \Phi(r_p) \quad (9.14)$$

where e_p and r_p are eccentricity and radius at perigee, respectively. The penalty function $\Phi(r_p)$ is

$$\Phi(r_p) = \begin{cases} 0 & \text{if } r_p \geq r_{\min} \\ A(r_{\min} - r_p) & \text{if } r_p < r_{\min} \end{cases} \quad (9.15)$$

where A is a penalty function constant. The guidance algorithm predicts the capture trajectory by numerically integrating the planar two-body equations of motion from the current state to the predicted perigee passage. Numerical integration by the guidance scheme is performed by a fourth-order, fixed-step Runge-Kutta routine. Thrust steering during the capture is solely determined by the guidance constant λ . Therefore, “shooting” several trajectories to perigee for a range of λ values and sorting the resulting values of performance index J performs a simple one-dimensional minimization search. This simple minimization approach currently uses six candidate λ values. If the minimizing parameter λ^* is either the upper or lower boundary of the range of candidate values, then the search is expanded about that boundary value until the optimal λ^* is bracketed. The initial search range for λ is fairly broad in order to locate the global minima. Once an optimal λ^* is determined, then it is held constant and the “true” spacecraft trajectory is propagated forward by numerically integrating Eqs. (9.1)-(9.3), which include lunar and solar gravitational perturbations. Thrust steering is determined by λ^* and Eq. (9.13) during integration of the “true” trajectory. The guidance parameter

λ is updated at regular intervals by re-solving the one-dimensional minimization problem with the trajectory shooting approach. The previous optimal λ^* is used as the mid-point for the range of candidate values for λ . We refer to re-solving the minimization problem as the “guidance update” for parameter λ . The initial guidance phase ends when the spacecraft reaches perigee.

9.3.2 Spiral Target Guidance Phase

The goal of the second phase is to guide the spacecraft to a target energy-eccentricity state defined by acceptable inward spiral trajectories. Although the initial guidance phase will establish a closed orbit at first perigee passage, eccentricity and energy (and therefore apogee radius) will be quite high. A trajectory with a high apogee radius and large eccentricity will be perturbed by lunar and solar gravity, which will complicate trajectory planning and guidance calculations. Therefore, a robust guidance strategy would be to establish a nearly circular high-altitude orbit, so that the low-thrust spacecraft can subsequently follow a quasi-circular inward spiral transfer to LEO by using a simple anti-tangent thrust-steering program. Such a steering and trajectory profile is easy to implement in an open-loop fashion and would provide nearly autonomous operation for the majority of the transfer to LEO.

The target boundary state is derived from Perkins’ set of universal low-thrust spiral trajectory solutions, which hold for a wide range of thrust-to-weight ratios [92]. Perkins [92] developed universal solutions for low-thrust planar spiral transfers with a constant, continuous thrust force aligned with the velocity vector (i.e., “tangent steering”). Perkins’ solutions for dimensionless velocity magnitude (V), flight-path angle

(γ), and dimensionless time parameter (T) are presented in Fig. 1 with dimensionless radial distance (R) as the independent variable. If an inward spiral trajectory is desired, then the flight-path angle from Fig. 1b is set as a negative value. Dimensionless time parameter (T) is the time beyond local escape conditions, and therefore the vertical dashed line with $T = 0$ indicates local escape (parabolic orbit) conditions. Dimensional values of radius, velocity magnitude, and spiral time to a point on the unwinding (or, inward winding) spiral can be computed from the dimensionless values (R , V , and T) and the appropriate scaling equations that involve the central body gravitational parameter, initial circular orbit radius, and thrust-to-weight ratio (see Refs. [67, 89, 92] for details).

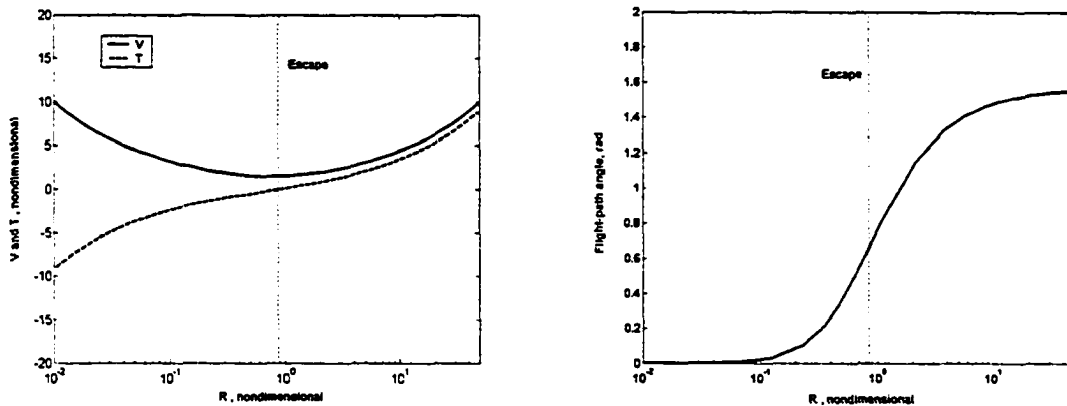


Figure 9.1 Perkins' low-thrust spiral solutions. (a) Velocity and spiral time (b) Flight-path angle

The target spiral boundary for the second guidance phase is the energy-eccentricity phase plane that can be mapped from Perkins' universal spiral solutions presented in Fig. 9.1. A specific energy-eccentricity state can be determined from the values for radius, velocity magnitude, and flight-path angle that exist on the universal spiral trajectory. Fig. 9.2 shows the energy-eccentricity phase plane mapped from Perkins' spiral solutions (energy has been transformed to dimensional units by using the

Earth's gravitational parameter, initial LEO, and initial thrust-to-weight ratio). The curve presented in Fig. 9.2 represents the osculating values of energy and eccentricity that exist on an outward or inward winding spiral trajectory. At the first perigee passage, the vehicle will have an energy-eccentricity state in Fig. 9.2 that is below the zero-energy horizontal line and to the left of the unity-eccentricity vertical line.

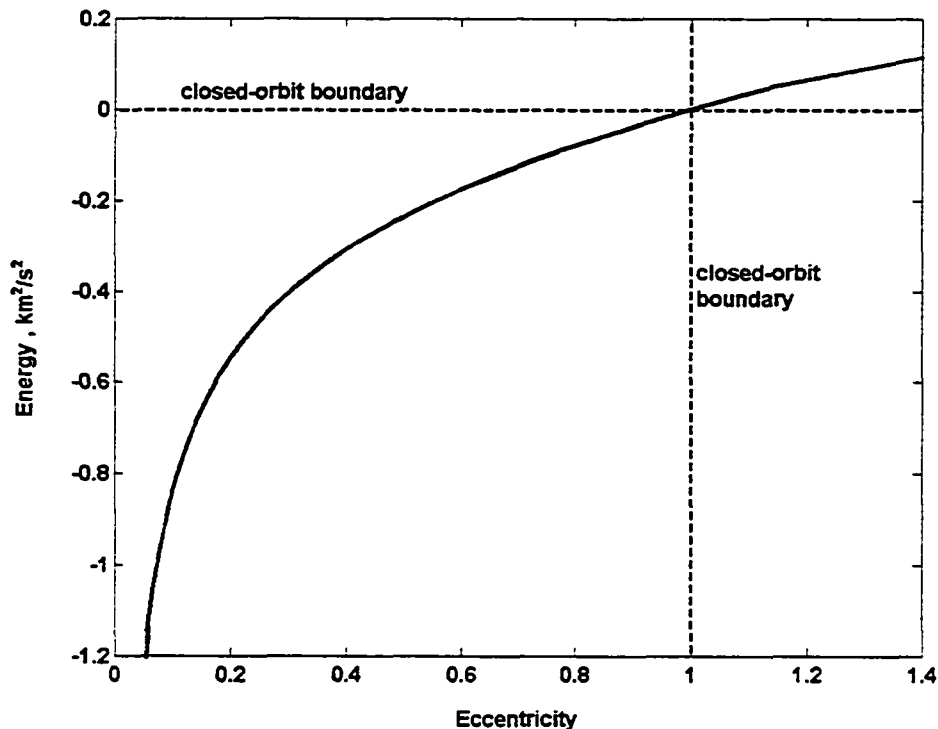


Figure 9.2 Perkins' low-thrust spiral solutions in energy-eccentricity space

The second guidance phase blends two optimal control laws (minimum energy-and eccentricity-rate steering programs) so that the predicted capture trajectory terminates on the spiral target boundary presented by Fig. 9.2. Minimum eccentricity-rate steering is derived from the governing equation for eccentricity

$$\dot{e} = a_T \sqrt{\frac{p}{\mu}} [\sin \theta \sin \alpha + (\cos \theta + \cos \psi) \cos \alpha] \quad (9.16)$$

where ψ is eccentric anomaly. Following the derivation for minimum energy-rate steering, the first derivative $\partial\dot{e}/\partial\alpha$ is set to zero, and a positive second derivative is ensured. The resulting optimal control for minimum eccentricity-rate is

$$\sin \alpha = \frac{-\sin \theta}{\sqrt{1+2\cos \theta \cos \psi + \cos^2 \psi}} \quad (9.17)$$

$$\cos \alpha = \frac{-(\cos \theta + \cos \psi)}{\sqrt{1+2\cos \theta \cos \psi + \cos^2 \psi}} \quad (9.18)$$

The “blended” steering direction is determined from a linear combination of the minimum energy-rate and minimum eccentricity-rate steering programs

$$\hat{\mathbf{u}} = \hat{\mathbf{u}}_E + \lambda \hat{\mathbf{u}}_e \quad (9.19)$$

Unit vectors $\hat{\mathbf{u}}_E$ and $\hat{\mathbf{u}}_e$ are the thrust directions for the minimum energy- and eccentricity-rate control laws, respectively. Similar to the previous phase, the second guidance phase adjusts guidance parameter λ so that the predicted trajectory terminates on the spiral boundary shown in Fig. 9.2. Because several values of λ will lead to interception with the desired energy-eccentricity boundary curve, the guidance scheme selects the best λ by minimizing

$$J = t_{spiral} \quad (9.20)$$

where t_{spiral} is the subsequent inward spiral time to LEO (moving *along* the curve in Fig. 2) as predicted by Perkins’ universal spiral solutions. As before, testing a range of λ values by employing a trajectory shooting method solves this 1-D minimization problem. Robustness is improved by excluding λ values that do not produce trajectories that reach the boundary curve before a specified lower energy threshold. If all λ values produce trajectories that do not reach the Perkins’ boundary curve before the designated

lower energy threshold, then the candidate trajectory with the lowest eccentricity at the energy threshold is selected (recall that λ is periodically updated, so the latter update trials will produce trajectories that reach the Perkins boundary).

During the initial guidance phase, no out-of-plane (yaw) steering is employed since we want to establish a closed orbit at the first perigee pass. However, it is possible to perform a desired plane change during the spiral target guidance phase and terminate on the Perkins' boundary curve. The yaw-steering guidance can be determined by considering the variational equations for inclination and argument of perigee

$$\frac{di}{dt} = \frac{r}{\sqrt{\mu p}} \cos(\omega + \theta) a_T \sin \beta \quad (9.21)$$

$$\dot{\omega} = -\frac{1}{e} \sqrt{\frac{p}{\mu}} a_T [\cos \theta \sin \alpha - (1 + \frac{r}{p}) \sin \theta \cos \alpha] \quad (9.22)$$

where i is the orbital inclination, r is the radial distance, and ω is the argument of perigee. Obviously, the inclination rate is maximized when the yaw steering angle is $\beta = \pm\pi/2$. Furthermore, the inclination rate is maximized when r is large (apogee) and when the spacecraft is at a nodal crossing (longitude angle $\omega + \theta = 0$ or π). However, the nodal crossing may not coincide with apogee, so the argument of perigee profile must be obtained in order to find the orbital location for maximum inclination rate. Therefore, the guidance scheme numerically integrates Eq. (9.22) in order to propagate the argument of perigee. This auxiliary propagation is performed *after* the optimal λ^* value is determined via the planar propagation to the Perkins boundary (recall that the initial propagation and search for λ^* is completely planar). Propagating Eq. (9.22) is straightforward since the planar states and pitch histories are known. After propagating

$\omega(t)$ forward in time, the switch time t^* which produces the maximum inclination rate can be determined from Eq. (9.21). Time t^* determines when to switch from in-plane (pitch) steering to out-of-plane (yaw) steering.

Once the optimal λ^* and t^* are determined, the “true” trajectory is determined by numerically integrating Eqs. (9.1)-(9.3) with the pitch steering program determined by Eq. (9.19). When time reaches the predicted switch time t^* , the yaw angle is stepped to $\pm\pi/2$ (the sign depends on the cosine of the longitude) and pure yaw steering is employed until the desired plane change is performed. Note that the energy-eccentricity state will (theoretically) remain at a fixed point in Fig. 9.2 for two-body motion. The need to propagate ω is eliminated once the spacecraft begins the yaw-steering phase. As with the first guidance phase, the parameter λ is periodically updated until the vehicle reaches the spiral target boundary. The osculating values of energy and eccentricity are monitored, and the spiral target guidance phase is terminated when the energy-eccentricity state intercept the boundary presented in Fig. 9.2.

9.3.3 Inward Spiral Guidance Phase

The third guidance phase begins on the spiral target boundary, or an energy-eccentricity state defined by Fig. 9.2. However, the spacecraft may not be in the proper orbital position to begin following the inward spiral trajectory defined by Perkins’ solution. Therefore, the vehicle may need to coast to the appropriate true anomaly (between apogee and perigee) such that the flight-path angle γ matches the appropriate value for the given orbital energy (which is determined by an (R,V) combination in Fig. 9.1a). Once the vehicle has reached the appropriate (negative) flight-path angle, the

inward spiral guidance may employ a simple “anti-tangent” thrust steering program for the majority of the trajectory to LEO (recall that Perkins’ universal solutions are unwinding spirals with tangential thrust). If a plane change is required, then a simple yaw steering strategy may be employed during the inward spiral. For example, nominal out-of-plane steering could be commanded near nodal crossings in order to change orbital inclination, and the amplitude of the yaw steering angle could be reduced as the inclination error and orbital radius decrease.

Perkins’ universal low-thrust solutions predict the inward spiral time, but these solutions assume uninterrupted continuous thrust. An SEP vehicle will experience increasing periods of Earth-shadow conditions (with total loss of thrust) as the orbital energy decreases. Shadow eclipses produce asymmetric thrusting arcs, which result in residual eccentricity as the spacecraft approaches the orbital energy for LEO. Therefore, a terminal guidance steering strategy should be employed near LEO so that eccentricity can be reduced simultaneously with orbital energy.

9.4 Numerical Results

We present numerical simulations in order to demonstrate the proposed capture guidance scheme. The initial condition for the Earth-capture trajectory is taken from the latter stage of a minimum-propellant Mars-Earth transfer, which could be the return phase of a low-thrust sample return mission. Table 9.1 presents the initial Earth-relative state, which is from Klueve [67]. Note that the initial flight-path angle is $\gamma_0 = -85.79$ deg, for a nearly radial descent trajectory. Initial spacecraft mass is $m_0 = 315$ kg. The constant spacecraft system parameters are $P = 3$ kW, $\eta = 0.68$, and $I_{sp} = 3800$ s, which represent the current level of SEP technology. Numerical integration of the trajectory

dynamics [Eqs. (9.1)-(9.3)] is performed by a fourth-order Runge-Kutta method with a variable integration step. Both absolute and relative error tolerances are set as 10^{-8} in non-dimensional time units and the states are recorded every 13.45 min.

Table 9.1 Initial spacecraft state for capture trajectory

Parameter	Initial value
r_0	$[-1.9376(10^5) \quad -9.6272(10^5) \quad -1.0861(10^6)]^T$ km
v_0	$[0.1924 \quad 0.6384 \quad 0.6866]^T$ km/s
E_0	0.1858 km 2 /s 2
e_0	1.0123
γ_0	-85.79 deg
i_0	53.28 deg
Ω_0	23.08 deg
θ_0	194.09 deg

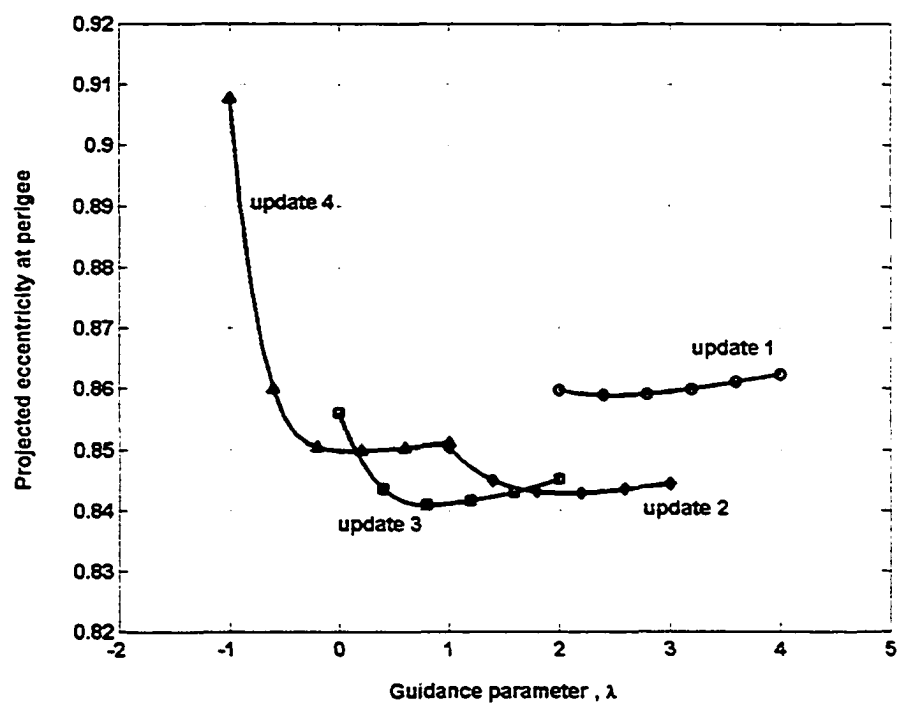


Figure 9.3 Projected eccentricity at perigee for guidance parameter update trials

The powered capture begins with the initial energy and eccentricity reduction guidance phase. Six trial λ values are used during the 1-D minimization (trajectory shooting to perigee), and the guidance update period is 4.67 days. Lower radius bound (r_{\min}) is set at 20 Earth radii. Fig. 9.3 presents the minimization results of each update cycle for parameter λ . Note that the optimal λ^* decreases with each update as the spacecraft approaches the first perigee passage, and that the predicted eccentricity at perigee changes between update periods. The variation in predicted eccentricity is due to the solar and lunar gravitational perturbations, since the onboard guidance algorithm utilizes a two-body model for simplicity and computational efficiency. The spacecraft reaches perigee in 15.69 days, and resulting eccentricity is 0.847 at perigee.

Several initial capture trajectories were simulated for a range of update cycle periods, and the results are summarized in Table 9.2. The initial capture phase appears to be relatively insensitive to the λ update frequency (note that the last table entry involves only a single λ update during the capture). Eccentricity at perigee is consistently around 0.85 and the time to perigee is around 15.7 days. Perigee radius approaches the lower boundary of 20 Earth radii as the update cycle frequency increases; therefore, a high λ update rate may be necessary if a particular target perigee radius is desired.

Table 9.2 Initial capture trials with various guidance update frequencies

Update period (days)	Eccentricity at perigee	Energy at perigee (km ² /s ²)	Perigee radius (Earth radii)	Time to perigee (days)
0.93	0.8499	-0.2269	20.17	15.669
1.87	0.8494	-0.2259	20.31	15.669
3.73	0.8480	-0.2181	21.16	15.679
4.67	0.8472	-0.2164	22.06	15.688
9.33	0.8478	-0.2122	22.41	15.688

The spiral target guidance phase begins at the first perigee passage. Fig. 9.4 shows the predicted trajectories in the energy-eccentricity phase space for λ test values, as computed by the onboard guidance scheme. Figure 4 shows the first shooting trials to select the optimal λ as the second guidance phase is initiated. The lower energy bound is set at $-1.0416 \text{ km}^2/\text{s}^2$ (i.e., the corresponding energy from Perkins' solution when $R = 30$ Earth radii), and therefore test trajectories 5 and 6 are discarded during the shooting trials since they do not reach Perkins' spiral trajectory curve before this energy threshold. Shooting trial 4 results in the minimum predicted spiral time (t_{spiral}), and therefore the respective λ value is used for the initial steering program until the next update cycle.

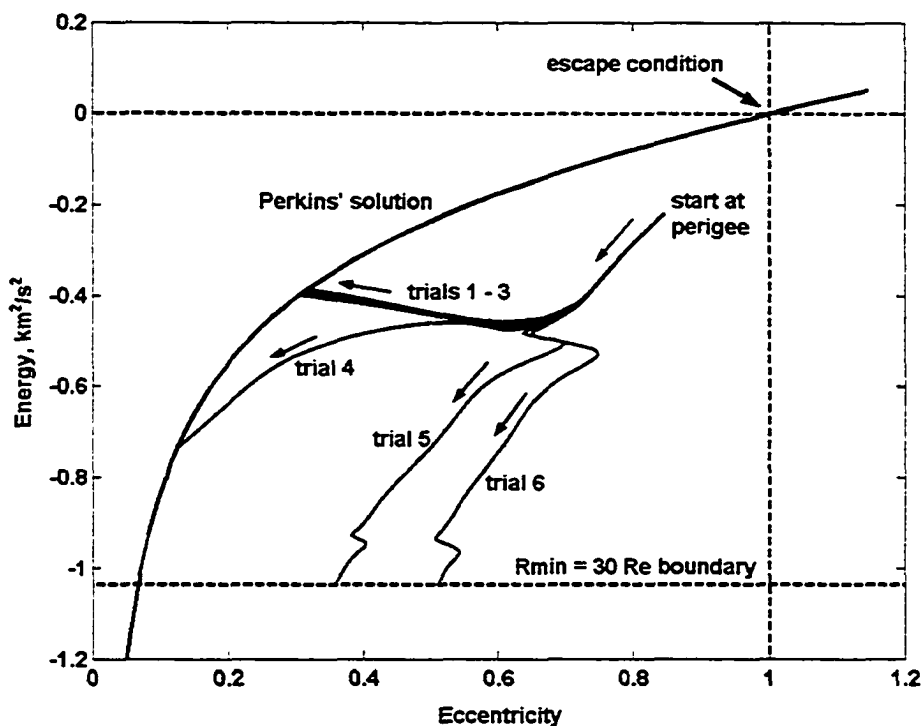


Figure 9.4 Guidance parameter λ update trials at start of second guidance phase

Once the optimal λ^* and propagated planar trajectory is obtained, the guidance needs to compute the time t^* when the inclination rate is maximized. Fig. 9.5 shows the time history of the predicted inclination rate using the optimal λ^* and propagated planar trajectory from the first shooting trial. The predicted t^* for maximum negative di/dt is about 26 days for the first update cycle (start of second guidance phase). The update cycle for this second guidance phase was set at 9.33 days, and therefore λ^* and t^* are re-computed at $t = 25$ days. Therefore, t^* is re-computed during the second update cycle, and t^* is slightly greater than the initial estimate of 26 days (see Fig. 9.5). Once the yaw-steering phase is initiated, guidance ceases to propagate Eq. (9.22) and instead focuses on updating the in-plane steering parameter λ .

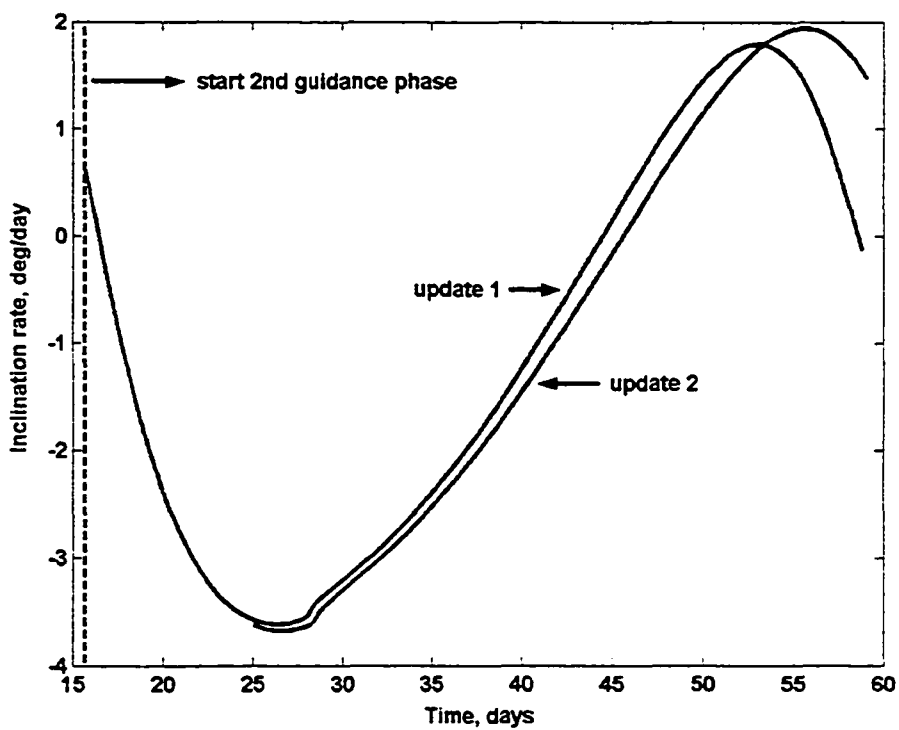


Figure 9.5 Predicted inclination rate for two update cycles in second guidance phase

Table 9.3 summarizes the performance of the second guidance phase for a range of lower energy threshold values (energy threshold from the Perkins solution is presented in terms of radius R_{\min}). All trajectory results use a nominal 9.33-day update period for λ . Orbit parameters pertaining to the energy-eccentricity curve intersection point are denoted by the subscript “end,” and t_{G_2} denotes the powered transit time of the second guidance phase (from perigee to target spiral boundary). Note that in each case the spacecraft intersects the energy-eccentricity curve at a radial distance that is close to the respective lower bound on energy (radius). This characteristic demonstrates that the update scheme is driving the vehicle to the lowest possible energy-eccentricity state in order to minimize the subsequent inward spiral time. Eccentricity at the target spiral intersection is also presented in Table 9.3, and the initial inward spiral becomes more circular as the semimajor axis threshold is decreased. Table 9.3 also presents the true anomaly of the spacecraft at the boundary curve intersection (θ_{end}), as well as the true anomaly required for proper initiation of the inward spiral (θ_{spiral}). Recall that the energy-eccentricity boundary curve in Fig. 9.2 merely defines the instantaneous size and shape of the orbit for the initiation of an inward spiral trajectory without regard for position in the orbit. Orbital position is dictated by the respective flight-path angle (shown in Fig. 9.1b), with the proper quadrant determined by the sign of γ (outward or inward spiral). The guided trajectories for $R_{\min} = 40$ and 20 Earth radii intersect the boundary curve such that the subsequent coast angle is less than 180 deg, and therefore a relatively short coast phase (t_{coast}) is needed before the vehicle has the proper radius, velocity, and flight-path angle to initiate the inward spiral. On the other hand, the three

trials with $R_{\min} = 50$, 30, and 10 Earth radii show that the vehicle has intersected the boundary curve “beyond” the required orbital position, and therefore a significant coasting arc (greater than 180 deg) is necessary. Lunar and solar gravitational effects will perturb the orbit during the coast phase, and the onboard guidance system could monitor the vehicle’s osculating orbital elements and initiate the inward spiral phase at the appropriate conditions. Table 9.3 also presents the duration of the yaw-steering phase (t_β) and the final inclination at interception of the Perkins boundary. The time required for the yaw-steering phase (with 26-deg inclination change) is relatively short (7-10 days) and the yaw phase occurs near apogee. As a final note, Table 9.3 shows that the total powered time from first perigee passage to LEO (i.e., $t_{G2} + t_{spiral}$) is between 231 to 248 days, and that the total powered time increases as R_{\min} (energy threshold) decreases.

Table 9.3 Second guidance phase trials with various energy (radius) thresholds

R_{\min} (Re)	r_{end} (Re)	e_{end}	θ_{end} (deg)	θ_{spiral} (deg)	t_β (days)	i_{end} (deg)	t_{G2} (days)	t_{coast} (days)	t_{spiral} (days)
50	43.63	0.140	341.3	276.9	6.90	28.36	34.5	15.23	197.0
40	37.59	0.106	119.1	276.0	6.81	28.55	37.2	6.91	194.0
30	30.77	0.071	337.3	272.1	6.81	28.31	46.5	8.28	189.8
20	22.38	0.038	117.4	272.4	6.81	28.36	54.9	2.88	182.1
10	10.03	0.008	3.317	277.2	10.45	28.55	91.3	1.43	156.8

Figure 6 shows the guided trajectory from the initial conditions (near SOI) to the spiral target boundary, as presented in the energy-eccentricity space. The trajectory shown in Fig. 6 uses a lower radius bound of 30 Re for the second guidance phase. The dashed arc represents the initial guidance phase (SOI to first perigee passage), and the solid arc represents the second guidance phase (perigee to spiral target). Note that eccentricity initially increases during the first guidance phase until it reaches a maximum

value and is then reduced to 0.847 at perigee. In general, energy and eccentricity steadily decrease during the second guidance phase as the spacecraft reaches the Perkins' solution boundary. Note that a “zig-zag” in energy and eccentricity occurs when eccentricity is near 0.65. This deviation is a result of the yaw-steering phase, when no thrust component is in the orbit plane ($\beta = 90$ deg) and the orbit is perturbed by third-body effects. Fig. 9.7 presents the inclination change during the capture maneuver. Third-body perturbation effects are noticeable during the start of the capture, and the 7-day yaw-steering phase quickly reduces inclination to the desired value of 28.5 deg. Fig. 9.8 presents the pitch and yaw steering programs, $\alpha(t)$ and $\beta(t)$, during the powered capture to the Perkins' boundary. Longitude angle ($\omega + \theta$) is superimposed on the steering profile, and the coast phase is also presented. Discontinuities in the pitch program mark the guidance updates to λ during the first guidance phase. Note that pitch angle is near ± 90 deg when the spacecraft is in the vicinity of apogee and the yaw-steering phase is employed. Radial thrust on both sides of the yaw phase exists because the guidance parameter λ is approximately unity, and the horizontal components of the two steering laws essentially cancel [see Eqs. (9.9), (9.10), (9.17), and (9.18)] leaving a component along the radial direction. Radial thrust near apogee has a small effect on both energy and eccentricity, so switching to pure out-of-plane steering is a beneficial strategy. Fig. 9.9 presents the three-dimensional capture trajectory, and shows that the SEP spacecraft completes about 2.5 revolutions during the capture trajectory to Perkins' boundary (point 2). The coast arc to the proper inward spiral (the inner arc on Fig. 9.9) requires more than three-quarters of a revolution.

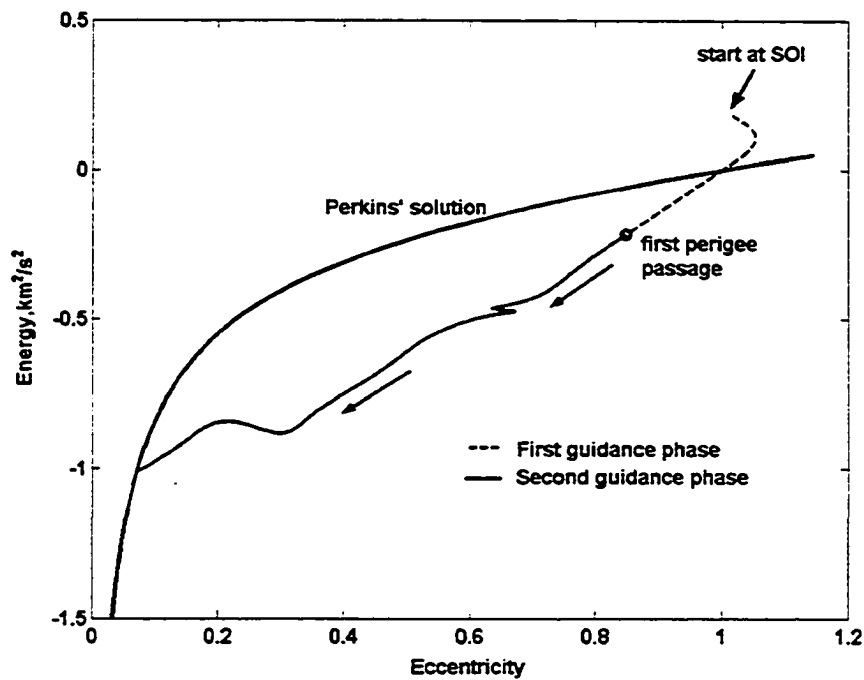


Figure 9.6 Guided trajectory from SOI to spiral target boundary

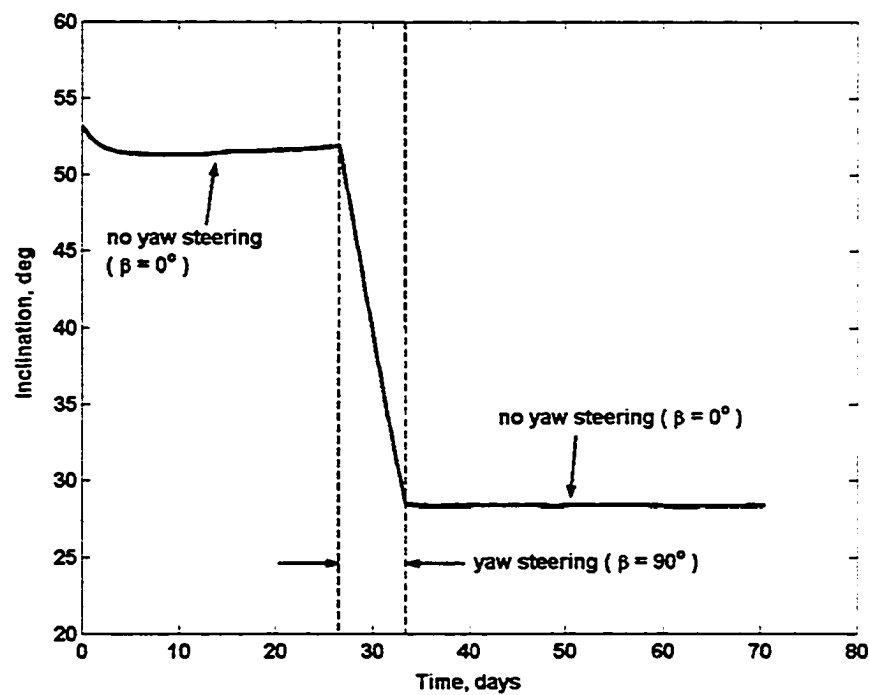


Figure 9.7 Time history of inclination

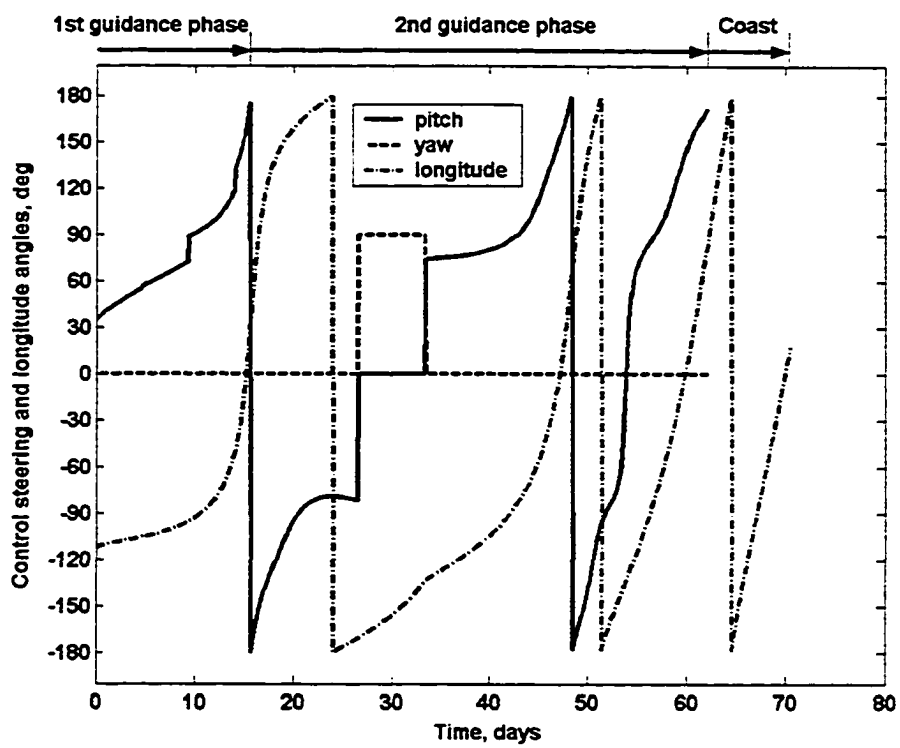


Figure 9.8 Steering program from SOI to spiral target boundary

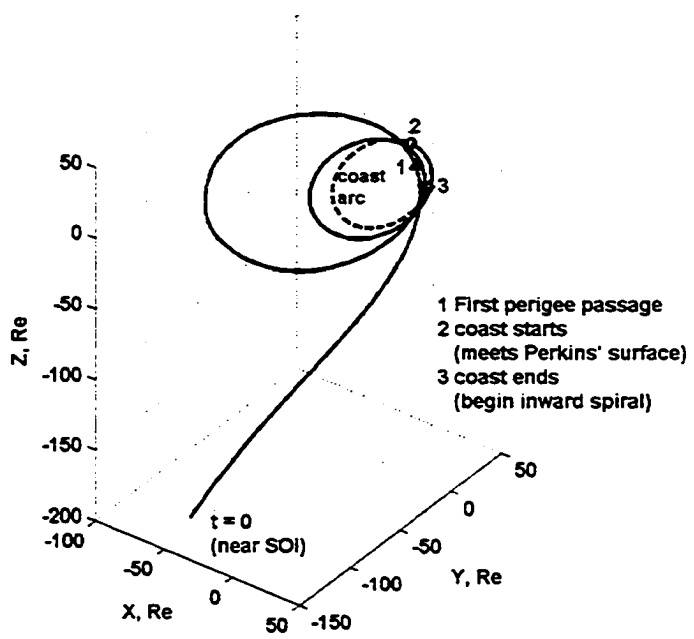


Figure 9.9 The Earth-capture trajectories to Perkins' universal solution

9.5 Conclusions

A new guidance scheme for Earth-capture SEP trajectories has been developed. The guidance design divides the capture maneuver into three phases: 1) initial energy and eccentricity reduction, 2) transition to spiral boundary surface, and 3) spiral transfer to target LEO. Thrust steering programs for the first two phases are based on a linear combination of two control laws that reduce energy and eccentricity. The control laws are blended using a single guidance constant, λ . During the initial phase, the guidance algorithm iterates on the guidance constant such that eccentricity is minimized at the first perigee passage. During the second phase, the guidance algorithm adjusts the guidance constant so that the projected trajectory reaches an energy-eccentricity state that ensures a subsequent quasi-circular inward spiral to LEO. In addition, the guidance scheme predicts the best time to switch to out-of-plane steering in order to maximize the inclination rate. Once the vehicle has reached the spiral target state, a simple open-loop anti-tangent steering profile can be used to guide the spacecraft to LEO.

The guidance design is simple, reliable, and can be implemented onboard for autonomous operation. Our technique makes novel use of Perkins' universal low-thrust spiral trajectory solutions as a convenient target state. The choice of control laws coupled with the spiral trajectory boundary target provides a robust method for guiding the vehicle from a high-energy trajectory to a benign inward spiral mode. The simplicity and performance of our guidance design makes it a viable candidate for onboard implementation.

CHAPTER 10 SUMMARY AND CONCLUSIONS

Several advances in low-thrust trajectory optimization and flight mechanics have been presented. Low-thrust trajectories discussed in this dissertation refer to maneuvers where long burn arcs exist, and numerical integration (whether explicit or implicit) is needed for optimization. The equations of motion are expressed in three different coordinates and the corresponding costates or Euler-Lagrange differential equations are also developed. The relatively simple calculations for planetary escape, capture, gravity assist, and perturbations were introduced.

Two direct optimization approaches (the hybrid and direct-shooting methods) are successfully applied to solving low-thrust orbit transfer problems. The hybrid method is also employed to solve interplanetary orbit transfer problems. These two methods are capable of constructing multiple dynamic stages for solving complex, real-world missions. The numerical examples solved by these two methods are presented in the previous chapters. Furthermore, the hybrid method needs fewer design variables in NLP problem, and users can choose which initial costate to optimize. Because the optimal control is governed by costate differential equations in the hybrid method, it has a smoother profile and is first-order differentiable. For the direct-shooting method, the time histories of the control steering for burn phases are represented by a finite number of discrete nodes, which are converted to free variables in NLP problem. In summary, for both approaches (the hybrid and direct-shooting methods), the optimal control problem is

converted into the parameter optimization problem. The solutions obtained by the hybrid method have higher accuracy and exhibit better performance than those obtained by the direct-shooting method. The drawback of both methods is the possibility of locating a local minimum, which is also the problem for all direct optimization approaches. However, the hybrid method leads fewer design variables and thus less computation time, more trials of initial guesses can be employed to find the global optimum. The multiple-shooting techniques discussed in the dissertation differ from previous approaches in several aspects. The state and costate nodes can be inserted during burn arcs, which are divided into several segments. The state nodes could be expressed by a subset of the classical orbital elements, which results in intuitive initial guesses and fewer design variables. It is demonstrated in Chapter 6 that multiple-shooting techniques improve convergence properties for both the hybrid and direct-shooting methods. In general, with the aid of multiple-shooting techniques, the hybrid and direct-shooting methods can be employed to solve a wide range of complex low-thrust orbit transfer problems. In Table 10.1, several mission types and suggested methods are listed, which is helpful to find optimal solutions more efficiently.

Two complex “real world” mission designs, optimal Eros sample return and Pluto-flyby missions are analyzed in detail. These two missions also involve many free variables and real constraints. The operation of multiple engines and engine switching logic are taken into consideration. Two realistic engine’s configurations (NSTAR and NEXT) are used for the mission design.

Table 10.1 Mission types and suggested methods

Mission types	Suggested methods
2-D near-circular transfers	direct-shooting method with simple initial guesses
Transfers with large eccentricity changes	multiple shooting in both the hybrid and direct-shooting methods
Transfers with large inclination changes	multiple shooting in both the hybrid and direct-shooting methods
Many-revolution transfers without inclination changes	direct-shooting method with simple initial guesses
Many-revolution transfers with inclination changes	hybrid method
Interplanetary transfers with few revolutions	hybrid method, direct-shooting method with simple initial guesses
2-burn transfers	hybrid method, direct-shooting method, split the time histories of control steering of optimal single-burn solutions
Earth-orbit transfers with higher thrust levels	verify many-burn trajectories
Interplanetary transfers with large eccentricity changes	verify 2-burn trajectories and gravity assists
Transfers with constraints	hybrid method, direct-shooting method, optimize the penalty function first, and then optimize the performance based on the feasible solution
Complex interplanetary transfers	hybrid method, direct-shooting method, divide the mission into sub-missions and solve one by one

Alternative formulations of the equations of motion are discussed. Inertial frame transformation in terms of three Euler angles makes it possible to convert transfers to arbitrary inclined orbits to transfers to “equatorial” orbits. In addition, for transfers to circular orbits, the terminal constraints are very simple if the final orbit is “equatorial”. Optimal LEO-GPS orbit transfers are demonstrated to illustrate the inertial frame transformation. The non-dimensional angular momentum is used to construct a new set of equinoctial elements. The perturbations are also developed using this set of equinoctial elements, and their formulations in the costate equations are derived. The LEO-GEO orbit transfers are successfully solved by the new equinoctial elements.

Finally, a new low-thrust Earth-capture guidance scheme is discussed in chapter 9. Instead of finding the optimal trajectories, the guidance scheme is developed and provides the appropriate thrust-steering program to transfer the vehicle to a desired target orbit. Control steering based on the time-rate of orbital elements is employed in the guidance scheme. The onboard periodic guidance calculations and the novel use of Perkins' solution form the basis of the simple guidance method, which doesn't require a stored reference trajectory or control profile.

In summary, this dissertation advances state-of-the-art of low-thrust flight mechanism, trajectory optimization, and guidance algorithms. This work will be used to help realize new space missions of the future.

APPENDIX I: DERIVATIVES OF M, D WITH RESPECT TO WALKER'S EQUINOCTIAL ELEMENTS

The elements of the matrix **M** and vector **D** are as follows:

$$M_{11} = 0, M_{12} = \frac{2p}{w} \sqrt{\frac{p}{\mu}}, M_{13} = 0$$

$$M_{21} = \sqrt{\frac{p}{\mu}} \sin L, M_{22} = \sqrt{\frac{p}{\mu}} [(w+1) \cos L + f] \frac{1}{w}, M_{23} = -\sqrt{\frac{p}{\mu}} [h \sin L - k \cos L] \frac{g}{w}$$

$$M_{31} = -\sqrt{\frac{p}{\mu}} \cos L, M_{32} = \sqrt{\frac{p}{\mu}} [(w+1) \sin L + g] \frac{1}{w}, M_{33} = \sqrt{\frac{p}{\mu}} [h \sin L - k \cos L] \frac{f}{w}$$

$$M_{41} = M_{42} = 0, M_{43} = \sqrt{\frac{p}{\mu}} \frac{s^2}{2w} \cos L$$

$$M_{51} = M_{52} = 0, M_{53} = \sqrt{\frac{p}{\mu}} \frac{s^2}{2w} \sin L$$

$$M_{61} = M_{62} = 0, M_{63} = \frac{1}{w} \sqrt{\frac{p}{\mu}} (h \sin L - k \cos L)$$

$$\mathbf{D} = [0 \ 0 \ 0 \ 0 \ 0 \ D]^T, \quad D = \sqrt{\mu p} \left(\frac{w}{p} \right)^2$$

The derivatives of elements of the matrix **M** and vector **D** with respect to the modified equinoctial elements are as follows:

$$\frac{\partial M_{11}}{\partial p} = \frac{\partial M_{11}}{\partial f} = \frac{\partial M_{11}}{\partial g} = \frac{\partial M_{11}}{\partial h} = \frac{\partial M_{11}}{\partial k} = \frac{\partial M_{11}}{\partial L} = 0$$

$$\frac{\partial M_{12}}{\partial p} = \frac{3}{w} \sqrt{\frac{p}{\mu}}, \frac{\partial M_{12}}{\partial f} = -\frac{\cos L}{w} M_{12}, \frac{\partial M_{12}}{\partial g} = -\frac{\sin L}{w} M_{12}, \frac{\partial M_{12}}{\partial h} = \frac{\partial M_{12}}{\partial k} = 0,$$

$$\frac{\partial M_{12}}{\partial L} = -\frac{2p}{w^2} \sqrt{\frac{p}{\mu}} (-f \sin L + g \cos L)$$

$$\frac{\partial M_{13}}{\partial p} = \frac{\partial M_{13}}{\partial f} = \frac{\partial M_{13}}{\partial g} = \frac{\partial M_{13}}{\partial h} = \frac{\partial M_{13}}{\partial k} = \frac{\partial M_{13}}{\partial L} = 0$$

$$\frac{\partial M_{21}}{\partial p} = \frac{1}{2p} M_{21}, \frac{\partial M_{21}}{\partial f} = \frac{\partial M_{21}}{\partial g} = \frac{\partial M_{21}}{\partial h} = \frac{\partial M_{21}}{\partial k} = \frac{\partial M_{21}}{\partial L} = 0, \frac{\partial M_{21}}{\partial L} = \sqrt{\frac{p}{\mu}} \cos L$$

$$\frac{\partial M_{22}}{\partial p} = \frac{1}{2p} M_{22}, \frac{\partial M_{22}}{\partial f} = \sqrt{\frac{p}{\mu}} \{(\cos^2 L + 1) \frac{1}{w} - \frac{1}{w^2} \cos L [(w+1) \cos L + f]\},$$

$$\frac{\partial M_{22}}{\partial g} = \sqrt{\frac{p}{\mu}} \{\sin L \cos L \frac{1}{w} - \frac{1}{w^2} \sin L [(w+1) \cos L + f]\}, \frac{\partial M_{22}}{\partial h} = \frac{\partial M_{22}}{\partial k} = 0,$$

$$\frac{\partial M_{22}}{\partial L} = \sqrt{\frac{p}{\mu}} [\cos L (-f \sin L + g \cos L) - w \sin L - \sin L] \frac{1}{w} - \sqrt{\frac{p}{\mu}} \frac{1}{w^2} (-f \sin L + g \cos L) [(w+1) \cos L + f]$$

$$\frac{\partial M_{23}}{\partial p} = \frac{1}{2p} M_{23}, \frac{\partial M_{23}}{\partial f} = -\frac{\cos L}{w} M_{23},$$

$$\frac{\partial M_{23}}{\partial g} = \sqrt{\frac{p}{\mu}} [h \sin L - k \cos L] \frac{g}{w^2} \cos L - \sqrt{\frac{p}{\mu}} [h \sin L - k \cos L] \frac{1}{w},$$

$$\frac{\partial M_{23}}{\partial h} = -\sqrt{\frac{p}{\mu}} \sin L \frac{g}{w}, \frac{\partial M_{23}}{\partial k} = \sqrt{\frac{p}{\mu}} \cos L \frac{g}{w},$$

$$\frac{\partial M_{23}}{\partial L} = -\sqrt{\frac{p}{\mu}} (h \cos L + k \sin L) \frac{g}{w} + \sqrt{\frac{p}{\mu}} \frac{g}{w^2} (-f \sin L + g \cos L) (h \sin L - k \cos L)$$

$$\frac{\partial M_{31}}{\partial p} = \frac{1}{2p} M_{31}, \frac{\partial M_{31}}{\partial f} = \frac{\partial M_{31}}{\partial g} = \frac{\partial M_{31}}{\partial h} = \frac{\partial M_{31}}{\partial k} = 0, \frac{\partial M_{31}}{\partial L} = \sqrt{\frac{p}{\mu}} \sin L$$

$$\frac{\partial M_{32}}{\partial p} = \frac{1}{2p} M_{32}, \frac{\partial M_{32}}{\partial f} = \sqrt{\frac{p}{\mu}} \{\cos L \sin L \frac{1}{w} - \frac{1}{w^2} \cos L [(w+1) \sin L + g]\},$$

$$\begin{aligned}
\frac{\partial M_{32}}{\partial g} &= \sqrt{\frac{p}{\mu}} \{(\sin^2 L + 1) \frac{1}{w} - \frac{1}{w^2} \sin L [(\omega + 1) \sin L + g]\}, \frac{\partial M_{32}}{\partial h} = \frac{\partial M_{32}}{\partial k} = 0, \\
\frac{\partial M_{32}}{\partial L} &= \sqrt{\frac{p}{\mu}} [\sin L (-f \sin L + g \cos L) + w \cos L + \cos L] \frac{1}{w} - \sqrt{\frac{p}{\mu}} \frac{1}{w^2} (-f \sin L + g \cos L) [(\omega + 1) \sin L + g] \\
\frac{\partial M_{33}}{\partial p} &= \frac{1}{2p} M_{33}, \frac{\partial M_{33}}{\partial f} = -\sqrt{\frac{p}{\mu}} [h \sin L - k \cos L] \frac{f}{w^2} \cos L + \sqrt{\frac{p}{\mu}} [h \sin L - k \cos L] \frac{1}{w}, \\
\frac{\partial M_{33}}{\partial g} &= -\frac{\sin L}{w} M_{33}, \frac{\partial M_{33}}{\partial h} = \sqrt{\frac{p}{\mu}} \sin L \frac{f}{w}, \frac{\partial M_{33}}{\partial k} = -\sqrt{\frac{p}{\mu}} \cos L \frac{f}{w}, \\
\frac{\partial M_{33}}{\partial L} &= \sqrt{\frac{p}{\mu}} (h \cos L + k \sin L) \frac{f}{w} - \sqrt{\frac{p}{\mu}} \frac{f}{w^2} (-f \sin L + g \cos L) (h \sin L - k \cos L) \\
\frac{\partial M_{41}}{\partial p} &= \frac{\partial M_{41}}{\partial f} = \frac{\partial M_{41}}{\partial g} = \frac{\partial M_{41}}{\partial h} = \frac{\partial M_{41}}{\partial k} = \frac{\partial M_{41}}{\partial L} = 0 \\
\frac{\partial M_{42}}{\partial p} &= \frac{\partial M_{42}}{\partial f} = \frac{\partial M_{42}}{\partial g} = \frac{\partial M_{42}}{\partial h} = \frac{\partial M_{42}}{\partial k} = \frac{\partial M_{42}}{\partial L} = 0 \\
\frac{\partial M_{43}}{\partial p} &= \frac{1}{2p} M_{43}, \frac{\partial M_{43}}{\partial f} = -\frac{\cos L}{w} M_{43}, \frac{\partial M_{43}}{\partial g} = -\frac{\sin L}{w} M_{43}, \\
\frac{\partial M_{43}}{\partial h} &= \sqrt{\frac{p}{\mu}} \frac{h}{w} \cos L, \frac{\partial M_{43}}{\partial k} = \sqrt{\frac{p}{\mu}} \frac{k}{w} \cos L \\
\frac{\partial M_{43}}{\partial L} &= -\sqrt{\frac{p}{\mu}} \frac{s^2}{2w} \sin L - \frac{1}{w^2} \sqrt{\frac{p}{\mu}} \frac{s^2}{2} \cos L (-f \sin L + g \cos L) \\
\frac{\partial M_{51}}{\partial p} &= \frac{\partial M_{51}}{\partial f} = \frac{\partial M_{51}}{\partial g} = \frac{\partial M_{51}}{\partial h} = \frac{\partial M_{51}}{\partial k} = \frac{\partial M_{51}}{\partial L} = 0 \\
\frac{\partial M_{52}}{\partial p} &= \frac{\partial M_{52}}{\partial f} = \frac{\partial M_{52}}{\partial g} = \frac{\partial M_{52}}{\partial h} = \frac{\partial M_{52}}{\partial k} = \frac{\partial M_{52}}{\partial L} = 0 \\
\frac{\partial M_{53}}{\partial p} &= \frac{1}{2p} M_{53}, \frac{\partial M_{53}}{\partial f} = -\frac{\cos L}{w} M_{53}, \frac{\partial M_{53}}{\partial g} = -\frac{\sin L}{w} M_{53},
\end{aligned}$$

$$\frac{\partial M_{53}}{\partial h} = \sqrt{\frac{p}{\mu}} \frac{h}{w} \sin L, \quad \frac{\partial M_{53}}{\partial k} = \sqrt{\frac{p}{\mu}} \frac{k}{w} \sin L,$$

$$\frac{\partial M_{53}}{\partial L} = \sqrt{\frac{p}{\mu}} \frac{s^2}{2w} \cos L - \frac{1}{w^2} \sqrt{\frac{p}{\mu}} \frac{s^2}{2} \sin L (-f \sin L + g \cos L)$$

$$\frac{\partial M_{61}}{\partial p} = \frac{\partial M_{61}}{\partial f} = \frac{\partial M_{61}}{\partial g} = \frac{\partial M_{61}}{\partial h} = \frac{\partial M_{61}}{\partial k} = \frac{\partial M_{61}}{\partial L} = 0$$

$$\frac{\partial M_{62}}{\partial p} = \frac{\partial M_{62}}{\partial f} = \frac{\partial M_{62}}{\partial g} = \frac{\partial M_{62}}{\partial h} = \frac{\partial M_{62}}{\partial k} = \frac{\partial M_{62}}{\partial L} = 0$$

$$\frac{\partial M_{63}}{\partial p} = \frac{1}{2p} M_{63}, \quad \frac{\partial M_{63}}{\partial f} = -\frac{\cos L}{w} M_{63}, \quad \frac{\partial M_{63}}{\partial g} = -\frac{\sin L}{w} M_{63},$$

$$\frac{\partial M_{63}}{\partial h} = \frac{1}{w} \sqrt{\frac{p}{\mu}} \sin L, \quad \frac{\partial M_{63}}{\partial k} = -\frac{1}{w} \sqrt{\frac{p}{\mu}} \cos L,$$

$$\frac{\partial M_{63}}{\partial L} = -\frac{1}{w^2} (-f \sin L + g \cos L) \sqrt{\frac{p}{\mu}} (h \sin L - k \cos L) + \frac{1}{w} \sqrt{\frac{p}{\mu}} (h \cos L + k \sin L)$$

APPENDIX II: DERIVATIVES OF M, D WITH RESPECT TO EQUINOCTIAL ELEMENTS USING NON- DIMENSIONAL ANGULAR MOMENTUM

The elements of the matrix **M** and vector **D** are described as follows:

$$M_{11} = 0$$

$$M_{12} = \hbar n$$

$$M_{13} = 0$$

$$M_{21} = \hbar \sin L$$

$$M_{22} = \hbar \cos L + n(\cos L + f)$$

$$M_{23} = -nXg$$

$$M_{31} = -\hbar \cos L$$

$$M_{32} = \hbar \sin L + n(\sin L + g)$$

$$M_{33} = nXf$$

$$M_{41} = 0$$

$$M_{42} = 0$$

$$M_{41} = \frac{1}{2}ns^2 \cos L$$

$$M_{51} = 0$$

$$M_{52} = 0$$

$$M_{51} = \frac{1}{2}ns^2 \sin L$$

$$M_{61} = 0$$

$$M_{62} = 0$$

$$M_{63} = nX$$

$$D = \frac{1}{n^2 \hbar \mu}$$

The derivatives of elements of the matrix **M** and vector **D** with respect to the modified equinoctial elements are as follows:

$$\frac{\partial M_{11}}{\partial h} = \frac{\partial M_{11}}{\partial f} = \frac{\partial M_{11}}{\partial g} = \frac{\partial M_{11}}{\partial h} = \frac{\partial M_{11}}{\partial k} = \frac{\partial M_{11}}{\partial L} = 0$$

$$\frac{\partial M_{12}}{\partial h} = 2n, \frac{\partial M_{12}}{\partial f} = -n^2 \cos L, \frac{\partial M_{12}}{\partial g} = -n^2 \sin L, \frac{\partial M_{12}}{\partial h} = \frac{\partial M_{12}}{\partial k} = 0, \frac{\partial M_{12}}{\partial L} = -n^2 w_L$$

$$\frac{\partial M_{13}}{\partial h} = \frac{\partial M_{13}}{\partial f} = \frac{\partial M_{13}}{\partial g} = \frac{\partial M_{13}}{\partial h} = \frac{\partial M_{13}}{\partial k} = \frac{\partial M_{13}}{\partial L} = 0$$

$$\frac{\partial M_{21}}{\partial h} = \sin L, \quad \frac{\partial M_{21}}{\partial f} = \frac{\partial M_{21}}{\partial g} = \frac{\partial M_{21}}{\partial h} = \frac{\partial M_{21}}{\partial k} = \frac{\partial M_{21}}{\partial L} = 0, \quad \frac{\partial M_{21}}{\partial L} = -M_{31}$$

$$\frac{\partial M_{22}}{\partial h} = \frac{1}{\hbar} M_{22}, \quad \frac{\partial M_{22}}{\partial f} = -\frac{n}{w} (\cos^2 L + f \cos L) + n, \quad \frac{\partial M_{22}}{\partial g} = -\frac{n}{w} (\sin L \cos L + f \sin L)$$

$$\frac{\partial M_{22}}{\partial h} = \frac{\partial M_{22}}{\partial k} = 0, \quad \frac{\partial M_{22}}{\partial L} = -(\hbar + n) \sin L - \frac{n w_L}{w} (\cos L + f)$$

$$\frac{\partial M_{23}}{\partial h} = \frac{1}{\hbar} M_{23}, \quad \frac{\partial M_{23}}{\partial f} = -\frac{\cos L}{w} M_{23}, \quad \frac{\partial M_{23}}{\partial g} = -\frac{\sin L}{w} M_{23} - n X$$

$$\frac{\partial M_{23}}{\partial h} = -n g \sin L, \quad \frac{\partial M_{23}}{\partial k} = n g \cos L, \quad \frac{\partial M_{23}}{\partial L} = -\frac{w_L}{w} M_{23} - n g X_L$$

$$\frac{\partial M_{31}}{\partial h} = -\cos L, \quad \frac{\partial M_{31}}{\partial f} = \frac{\partial M_{31}}{\partial g} = \frac{\partial M_{31}}{\partial h} = \frac{\partial M_{31}}{\partial k} = \frac{\partial M_{31}}{\partial L} = 0, \quad \frac{\partial M_{31}}{\partial L} = M_{21}$$

$$\frac{\partial M_{32}}{\partial h} = \frac{1}{\hbar} M_{32}, \quad \frac{\partial M_{32}}{\partial f} = -\frac{n}{w} (\sin L \cos L + g \cos L), \quad \frac{\partial M_{32}}{\partial g} = -\frac{n}{w} (\sin^2 L + g \sin L) + n$$

$$\frac{\partial M_{32}}{\partial h} = \frac{\partial M_{32}}{\partial k} = 0, \quad \frac{\partial M_{32}}{\partial L} = (\hbar + n) \cos L - \frac{n w_L}{w} (\sin L + g)$$

$$\frac{\partial M_{33}}{\partial h} = \frac{1}{\hbar} M_{33}, \quad \frac{\partial M_{33}}{\partial f} = -\frac{\cos L}{w} M_{33} + n X, \quad \frac{\partial M_{33}}{\partial g} = -\frac{\sin L}{w} M_{33}$$

$$\frac{\partial M_{33}}{\partial h} = n f \sin L, \quad \frac{\partial M_{33}}{\partial k} = -n f \cos L, \quad \frac{\partial M_{33}}{\partial L} = -\frac{w_L}{w} M_{33} + n f X_L$$

$$\frac{\partial M_{41}}{\partial h} = \frac{\partial M_{41}}{\partial f} = \frac{\partial M_{41}}{\partial g} = \frac{\partial M_{41}}{\partial h} = \frac{\partial M_{41}}{\partial k} = \frac{\partial M_{41}}{\partial L} = 0$$

$$\frac{\partial M_{42}}{\partial h} = \frac{\partial M_{42}}{\partial f} = \frac{\partial M_{42}}{\partial g} = \frac{\partial M_{42}}{\partial h} = \frac{\partial M_{42}}{\partial k} = \frac{\partial M_{42}}{\partial L} = 0$$

$$\frac{\partial M_{43}}{\partial \hbar} = \frac{1}{\hbar} M_{43}, \quad \frac{\partial M_{43}}{\partial f} = -\frac{\cos L}{w} M_{43}, \quad \frac{\partial M_{43}}{\partial g} = -\frac{\sin L}{w} M_{43},$$

$$\frac{\partial M_{43}}{\partial h} = nh \cos L, \quad \frac{\partial M_{43}}{\partial k} = nk \cos L, \quad \frac{\partial M_{43}}{\partial L} = -M_{53} - \frac{w_L}{w} M_{43}$$

$$\frac{\partial M_{51}}{\partial \hbar} = \frac{\partial M_{51}}{\partial f} = \frac{\partial M_{51}}{\partial g} = \frac{\partial M_{51}}{\partial h} = \frac{\partial M_{51}}{\partial k} = \frac{\partial M_{51}}{\partial L} = 0$$

$$\frac{\partial M_{52}}{\partial \hbar} = \frac{\partial M_{52}}{\partial f} = \frac{\partial M_{52}}{\partial g} = \frac{\partial M_{52}}{\partial h} = \frac{\partial M_{52}}{\partial k} = \frac{\partial M_{52}}{\partial L} = 0$$

$$\frac{\partial M_{53}}{\partial \hbar} = \frac{1}{\hbar} M_{53}, \quad \frac{\partial M_{53}}{\partial f} = -\frac{\cos L}{w} M_{53}, \quad \frac{\partial M_{53}}{\partial g} = -\frac{\sin L}{w} M_{53},$$

$$\frac{\partial M_{53}}{\partial h} = nh \sin L, \quad \frac{\partial M_{53}}{\partial k} = nk \sin L, \quad \frac{\partial M_{53}}{\partial L} = M_{43} - \frac{w_L}{w} M_{53}$$

$$\frac{\partial M_{61}}{\partial \hbar} = \frac{\partial M_{61}}{\partial f} = \frac{\partial M_{61}}{\partial g} = \frac{\partial M_{61}}{\partial h} = \frac{\partial M_{61}}{\partial k} = \frac{\partial M_{61}}{\partial L} = 0$$

$$\frac{\partial M_{62}}{\partial \hbar} = \frac{\partial M_{62}}{\partial f} = \frac{\partial M_{62}}{\partial g} = \frac{\partial M_{62}}{\partial h} = \frac{\partial M_{62}}{\partial k} = \frac{\partial M_{62}}{\partial L} = 0$$

$$\frac{\partial M_{63}}{\partial \hbar} = \frac{X}{w}, \quad \frac{\partial M_{63}}{\partial f} = -\frac{\cos L}{w} M_{63}, \quad \frac{\partial M_{63}}{\partial g} = -\frac{\sin L}{w} M_{63},$$

$$\frac{\partial M_{63}}{\partial h} = n \sin L, \quad \frac{\partial M_{63}}{\partial k} = -n \cos L, \quad \frac{\partial M_{63}}{\partial L} = -\frac{w_L}{w} M_{63} + n X_L$$

$$\frac{\partial D}{\partial \hbar} = -\frac{3}{n^2 \hbar^2 \mu}, \quad \frac{\partial D}{\partial f} = -\frac{2 \cos L}{\hbar^2 n \mu}, \quad \frac{\partial D}{\partial g} = -\frac{2 \sin L}{\hbar^2 n \mu}, \quad \frac{\partial D}{\partial h} = \frac{\partial D}{\partial k} = 0, \quad \frac{\partial D}{\partial L} = \frac{2 w_L}{\hbar^2 n \mu}$$

where $w = 1 + f \cos L + g \sin L$

$$w_L = -f \sin L + g \cos L$$

$$X_L = h \cos L - k \sin L$$

LIST OF REFERENCES

- [1] Rayman, M. D., Varghese, P., Lehman, D. H., and Livesay, L. L., "Results from the Deep Space 1 Technology Validation Missions," *Acta Astronautica*, Vol. 47, No. 2-9, 2000, pp. 475-487.
- [2] Rayman, M. D., Williams, S. N., "Design of the First Interplanetary Solar Electric Propulsion Mission," *Journal of Spacecraft and Rockets*, Vol. 39, No. 4, 2002, pp. 589-595.
- [3] Powers, R. B. and Coverstone, V. L., "Optimal Solar Sail Orbit Transfers to Synchronous Orbits," *The Journal of the Astronautical Sciences*, Vol. 49, No. 2, 2001, pp. 269-281.
- [4] Colasurdo, G. and Casalino, L., "Optimal Control Law for Interplanetary Trajectories with Nonideal Solar Sail," *Journal of Spacecraft and Rockets*, Vol. 40, No. 2, 2003, pp. 260 – 265.
- [5] Hughes, G. W. and McInnes, C. R., "Solar Sail Hybrid Trajectory Optimization for Non-Keplerian Orbit Transfers," *Journal of Guidance Control & Dynamics*, Vol. 25, No. 3, 2002, pp. 602-604.
- [6] Otten, M. and McInnes, C. R., "Near Minimum-Time Trajectories for Solar Sails," *Journal of Guidance, Control, and Dynamics*, Vol. 24 No. 3, 2000, pp. 632 – 634.
- [7] Oleson, S., Benson, S., Gefert, L., Patterson, M., and Schreiber, J., "Radioisotope Electric Propulsion For fast Outer Planetary Orbiters," AIAA-2002-3967.
- [8] Noble, R. J., "Radioisotope Electric Propulsion of Sciencecraft to the Outer Solar System and Near-Interstellar Space," *Acta Astronautica*. Vol. 44 No. 2, 1999, pp. 193-199.
- [9] Mailhe, L. M. and Heister, S. D., "Design of a Hybrid Chemical/Electric Propulsion Orbital Transfer Vehicle," *Journal of Spacecraft and Rockets*, Vol. 39, No. 1, 2001, pp. 131-139.
- [10] Bate, R. R., Mueller, D. D., and White, J. E., *Fundamentals of Astrodynamics*, Dover Publications, Inc., New York, 1971.
- [11] Sidi, M. J., *Spacecraft Dynamics & Control, a practical engineering approach*, Cambridge University Press, 1997.

- [12] Battin, R. H., *An Introduction to the Mathematics and Methods of Astrodynamics*, AIAA Education Serials, AIAA, Washington, DC, 1987.
- [13] Kluever, C. A. and Pierson, B. L., "Optimal Low-Thrust Earth-Moon Transfers with a Switching Function Structure," *The Journal of the Astronautical Sciences*, Vol. 42, No. 3, 1994, pp. 269-283.
- [14] Kluever, C.A. and Pierson, B.L., "Optimal Low-Thrust Three-Dimensional Earth-Moon trajectories," *Journal of Guidance, Control, and Dynamics*, Vol. 18, No.4, 1995, pp.830-837.
- [15] Broucke, R.A. and Cefola, P.J., "On the Equinoctial Orbit Elements," *Celestial Mechanics*, Vol. 5, No. 3, 1972, pp.303-310.
- [16] Walker, M.J.H., Ireland, B., and Owens, J., "A set of Modified Equinoctial Orbit Elements," *Celestial Mechanics*, Vol. 36, 1985, pp.409-419.
- [17] Betts, J. T., "Optimal Interplanetary Orbit Transfers by Direct Transcription," *The Journal of the Astronautical Sciences*, Vol. 42, No. 3, 1994, pp. 247-268.
- [18] Betts, J. T. and Erb, S. O., "Optimal Low Thrust Trajectories to the Moon," *SIAM Journal of Applied Dynamical Systems*, Vol. 2, No. 2, 2003, pp. 144 - 170.
- [19] Kechichian, J. A., "The Optimization of Continuous Constant Acceleration Transfer Trajectories in the Presence of the J_2 Perturbation," AAS 99-405, Aug. 1999
- [20] Kechichian, J. A., "Optimal Low-Thrust-Orbit-Geostationary-Earth-Orbit Intermediate Acceleration Orbit Transfer," *Journal of Guidance, Control and Dynamics*, Vol.20, No.4, 1997, pp.803-811.
- [21] Kechichian. J. A., "Mechanics of Trajectory Optimization Using Nonsingular Variation Equations in Polar Coordinates," *Journal of Guidance, Control and Dynamics*, Vol.20, No.4, 1997, pp.812-818.
- [22] Kechichian, J. A., "Minimum-Time Low-Thrust Rendezvous and Transfer Using Epoch Mean Longitude Formulation," *Journal of Guidance, Control, and Dynamics*, Vol. 22 No. 3, 1999, pp. 421-432.
- [23] McInnes, C. R., "Dynamics, Stability, and Control of Displaced Non-Keplerian Orbits," *Journal of Guidance, Control and Dynamics*, Vol.21, No.5, 1997, pp.799-805.
- [24] Chuang, Jason C.H., Goodson, T. D., Hanson, J., "Multiple-Burn Families of Optimal Low-and-Medium-Thrust Orbit Transfer," *Journal of Spacecraft and Rocket*, Vol.36, No.6, 1999, pp.866-874.

- [25] Hanson, J. M., and Duckman, G. A., "Optimization of Many-Burn Orbital Transfers," *The Journal of the Astronautical Sciences*, Vol. 45, No. 1, 1997, pp. 1-40.
- [26] Yan, H. and Wu, H., "Initial adjoint-Varaible Guess Technique and Its Application in Optimal Orbit Trajectory," *Journal of Guidance, Control, and Dynamics*, Vol. 22, No. 3, 1999, pp.490-492.
- [27] Seywald, H. and Kumar, R. R., "Finite Difference Scheme for Automatic Costate Calculation," *Journal of Guidance Control & Dynamics*, Vol. 19, No. 1, 1996, pp. 231-239.
- [28] Ilgen, M. R., "Hybrid Method for Computing Optimal Low Thrust OTV Trajectories," *Advances in the Astronautical Sciences. Publ, by Univelt Inc, San Diego, CA, USA.* Vol. 87, No. 2, 199, pp. 941-958.
- [29] Zondervan, K.P., Wood, L.J., and Caughey, T.K., "Optimal Low-Thrust, Three-Burn Orbit Transfers with Large Plane Changes," *Journal of the Astronautical Sciences*, Vol. 32, No. 3, 1984, pp. 407-427.
- [30] Da Silva Fernandes S., "Generalized Canonical System Applications to Optimal Trajectory Analysis," *Journal of Dynamics, Guidance and Control*, Vol. 22, No. 6, 1999, pp. 918-921.
- [31] Kluever, C. A., "Optimal Low-Thrust Interplanetary Trajectories by Direct Method Techniques," *The Journal of the Astronautical Sciences*, Vol. 45, No. 3, 1997, pp. 247-262.
- [32] Betts, J. T., "Using Sparse Nonlinear Programming to Compute Low Thrust Orbit Transfers," *Journal of the Astronautical Science*, Vol. 41, No. 3, 1993, pp. 349-371.
- [33] Betts, J. T., "Very Low-Thrust Trajectory Optimization using a Direct SQP Method," *Journal of Computational & Applied Mathematics*, Vol. 120, No. 1, 2000, pp. 27-40.
- [34] Tang, S. and Conway, B. A., "Optimization of Low-Thrust Interplanetary Trajectories Using Collocation and Nonlinear Programming," *Journal of Guidance, Control, and Dynamics*, Vol. 18, No.3, 1995, pp.600-604.
- [35] Herman, A. L. and Conway, B. A., "Optimal, Low-Thrust, Earth-Moon Orbit Transfer," *Journal of Guidance, Control, and Dynamics*, Vol. 21, No. 1, 1998, pp.141-148.

- [36] Herman, A. L. and Conway, B. A., "Direct Optimization Using Collocation Based on High-Order-Gauss-Lobatto Quadratic Rules," *Journal of Guidance, Control, and Dynamics*, Vol. 17, No. 3, 1994, pp.480-487.
- [37] Herman, A. L. and Spencer, D. B., "Optimal, Low-Thrust Earth-Orbit Transfers Using Higher-Order Collocation Methods," *Journal of Guidance, Control, and Dynamics*, Vol. 25, No. 1, 2002, pp. 40-47.
- [38] Scheel, W. A. and Conway, B. A., "Optimization of Very-Low-Thrust, Many-Revolution Spacecraft Trajectories," *Journal of Guidance, Control, and Dynamics*, Vol. 17, No. 6, 1994, pp.1185-1192.
- [39] Seywald, H., "Trajectory Optimization Based on Differential Inclusion," *Journal of Guidance, Control, and Dynamics*, Vol. 17, No. 3, 1994, pp.480-487.
- [40] Kuma, B. R. and Seywald, H., "Fuel-Optimal Stationkeeping via Differential Inclusions," *Journal of Guidance, Control, and Dynamics*, Vol. 18, No. 5, 1995, pp.1156-1161.
- [41] Coverstone C. V. and William, S. N., "Optimal Low-Thrust Trajectories Using Differential Inclusion Concept," *Journal of Astronautical Sciences*, Vol. 19, No. 3, 1996, pp.592-599.
- [42] Conway, B.A. and Larson, K.M., "Collocation Versus Differential Inclusion in Direct Optimization," *Journal of Guidance, Control, and Dynamics*, Vol. 21, No. 5, 1998, pp.780-785.
- [43] Betts, J. T., "Survey of Numerical Methods for Trajectory Optimization," *Journal of Guidance, Control, and Dynamics*, Vol. 21, No. 2, 1998, pp.193-207.
- [44] Hull, D. G., "Conversion of Optimal Control Problems into Parameter Optimization Problems," *Journal of Guidance, Control, and Dynamics*, Vol. 20, No. 1, 1997, pp.57-60.
- [45] Ilgen, M. R., "Low Thrust OTV Guidance Using Lyapunov Optimal Feedback Control Techniques," *Advances in the Astronautical Sciences*, 85, 1980, pp.1527 – 1545.
- [46] Chang D.E., Chichka, D. F., and Marsden J. E., "Lyapunov-Based Transfer Between Elliptic Keplerian Orbits," *Discrete and Continuous Dynamical System – Series B*, Vol. 2, No. 1, February 2002, pp. 57-67.
- [47] Schaub, H., Vadali, S. R., Junkinsz, J. L., and Alfriend, K. T., "Spacecraft Formation Flying Control Using Mean Orbit Elements," *The Journal of the Astronautical Sciences*, Vol. 48, No. 1 2001, pp. 69-87.

- [48] Kluever, C.A. and Oleson, S.R., "Direct Approach for Computing Near-Optimal Low-Thrust Earth-Orbit Transfers," *Journal of Dynamics, Guidance and Control*, Vol. 35, No. 4, 1998, pp. 509-515.
- [49] Spencer, D.B. and Culp, R.D., "Designing Continuous-Thrust Low-Earth-Orbit to Geosynchronous-Earth-Orbit Transfers," *Journal of Spacecraft and Rockets*, Vol.32, No.6, 1995, pp.1033-1038.
- [50] Kechichian, J. A., "Low-Thrust Eccentricity-Constrained Orbit Raising," *Journal of Spacecraft & Rockets*, Vol. 35, No. 3, May-Jun 1998, pp 327-335.
- [51] Kechichian, J. A., "Optimum Thrust Pitch Profiles for Certain Orbit Control Problems," *Journal of Spacecraft and Rockets*, Vol. 40, No. 2, 2003, pp. 253-259.
- [52] Kechichian, J. A., "Low-Thrust Inclination Control in Presence of Earth Shadow," *Journal of Spacecraft and Rockets*, Vol. 35 No. 4, 1998, pp. 526 – 532.
- [53] Fahroo, F. and Ross, I. M., "Direct Trajectory Optimization by a Chebyshev Pseudospectral Method," *Journal of Guidance Control & Dynamic*, Vol. 25, No. 1, 2002, pp. 160-166.
- [54] Jacobson, D.H., "New Second-Order and First-Order Algorithms for Determining Optimal Control: A Differential Dynamic Programming Approach," *Journal of Optimization Theory and Application*, Vol. 2, No. 6, 1968. pp. 411-440.
- [55] Jacobson, D.H., "Second-order and Second-variation Methods for Determining Optimal Control: A Comparative Study using Differential Dynamic Programming," *International Journal of Control*, Vol. 7, No. 2, 1968, pp.175-196.
- [56] Kim, Y. H. and Spencer, D. B., "Optimal Spacecraft Rendezvous Using Genetic Algorithms," *Journal of Spacecraft and Rockets*, Vol. 39, No. 6, 2002, pp. 859-865.
- [57] Hartmann, J. W. and Coverstone-Carroll V., L., Williams, S. N. "Optimal Interplanetary Spacecraft Trajectories via a Pareto Genetic Algorithm," *Journal of the Astronautical Science*. Vol. 46 No. 3, 1998, pp. 267-282.
- [58] Luo, J. and Kluever, C. A., "Fuzzy Logic Controller for Orbital Rendezvous," *ASME Dynamic Systems and Control Division American Society of Mechanical Engineers, Dynamic Systems and Control Division (Publication) DSC*. Vol. 61 1997. ASME, Fairfield, NJ, USA, pp 283-292.
- [59] Redding, D.C., and Breakwell, J.V., "Optimal Low-Thrust Transfers to Synchronous Orbit," *Journal of Guidance, Control, and Dynamics*, Vol. 7, No. 2, 1984, pp.148-155.

- [60] Cirić, C., "Optimal Strategy for Geostationary Orbit Acquisition Using Ion Propulsion," *Journal of Guidance Control & Dynamic*, Vol. 26 No. 4, 2003, pp. 608-614.
- [61] Guelman, M. and Kogan, A., "Electric Propulsion for Remote Sensing from Low Orbit," *Journal of Guidance, Control, and Dynamics*, Vol. 22 No. 2, 1999, pp. 313-321.
- [62] Guelman, M. "Earth-Moon Transfer with a Limited Power Engine," *Journal of Guidance, Control, and Dynamics*, Vol. 18, No. 5, 1995, pp.1133-1138.
- [63] Vadali, S. R., Nah, R., Braden, E., and Johnson, I. L. Jr., "Fuel-Optimal, Low-Thrust, Three-Dimensional Earth-Mars Trajectories," *Journal of Guidance, Control, and Dynamics*, Vol. 24, No. 6, 2001, pp. 476-482.
- [64] Axelrod, A. M. and Guelman, D. M., "Optimal Control of Interplanetary Trajectories Using Electrical Propulsion with Discrete Thrust Levels," *Journal of Guidance, Control, and Dynamics*, Vol. 25, No. 5, 2002, pp. 932-939.
- [65] Colasurdo, G., Casalino L., and Fantino E., "Minimum-Fuel Escape from Two-Body Sun-Earth System," Minimum-Fuel Escape from Two-Body Sun-Earth System," *Journal of Guidance, Control, and Dynamics*, Vol. 22 No. 5, pp. 632 – 636.
- [66] Casalino, L., Colasurdo, G. and Pastrone, D. "Optimal Low-Thrust Escape Trajectories Using Gravity Assist," *Journal of Guidance, Control, and Dynamics*, Vol. 22, No. 5, pp. 637 – 642.
- [67] Kluever, C.A., "Optimal Earth-Capture Trajectory Using Solar Electrical Propulsion," *Journal of Dynamics, Guidance and Control*, Vol. 25, No. 3, 2002, pp. 604-606.
- [68] Ivashkin, V. V., Chernov, A V., and Zaytsev, A. V. "Optimal Flights to Near-Earth Asteroid," *Acta Astronautica*. Vol. 44, No. 5-6, 1999, pp. 219-225.
- [69] Kluever, C.A. "Comet Rendezvous Mission Design Using Solar Electric Propulsion Spacecraft," *Journal of Spacecraft and Rockets*, Vol. 37, No. 5, 2000, pp.698-700.
- [70] Gath, P. F. and Calise, A. J., "Optimization of Launch Vehicle Ascent Trajectories with Path Constraints and Coast Arcs," *Journal of Guidance, Control, and Dynamics*, Vol. 24, No. 2, 2001, pp. 296-304.
- [71] Zimmermann, F. and Calise, A. J., "Numerical Optimization Study of Aeroassisted Orbital Transfer," *Journal of Dynamics, Guidance and Control*, Vol. 21, No. 1, 1995, pp. 127-133.
- [72] Horis, K. and Conway, B., "Optimal Aeroassisted Orbit Interception," *Journal of Guidance, Control, and Dynamics*, Vol. 22, No. 5, 1999, pp.625-631.

- [73] Park, S. Y. and Ross, I. M., "Two-Body Optimization for Deflecting Earth-Crossing Asteroids," *Journal of Guidance, Control, and Dynamics*, Vol.22, No. 3, 1999, pp. 415 – 420.
- [74] Bryson, A. E. Jr. and Ho, Y. C., *Applied Optimal Control*, Blaisdell Publishing Company, 1969.
- [75] Lewis, Frank L., *Optimal Control*, A wiley-interscience publication, 1986.
- [76] Bazaraa, M. S., Sherali, H. D. and Shetty, C.M., *Nonlinear Programming: Theory and Algorithms*, John Wiley & Sons, Inc, 1979.
- [77] Wirthman, D.J., Park, S. Y. and Vadali, S.R., "Trajectory Optimization using Parallel Shooting Method on Parallel Computer," *Journal of Dynamics, Guidance and Control*, Vol. 18, No. 2, pp. 377-379.
- [78] Goodson, T. D., Chuang Jason C. H., and Hanson J., "Optimal Finite Thrust Orbit Transfers with Large Numbers of Burns," *Journal of Guidance, Control, and Dynamics*, Vol. 22, No. 1, 1999, pp. 139 – 148.
- [79] Vadali, S. R., Nah, R., Braden, E. and Johnson, I. L. Jr., "Fuel-Optimal Planar Earth-Mars Trajectories Using Low-Thrust Exhaust-Modulated Propulsion," *Journal of Guidance Control & Dynamic*, Vol. 23, No. 3, 2000, pp. 476-482.
- [80] Veverka, J., Farquhar, B. et al., "The landing of the NEAR-Shoemaker spacecraft on asteroid 433 Eros," *Nature*, Vol. 413, 27, September 2001.
- [81] Kluever, C.A., "Simple Guidance Scheme for Low-Thrust Orbit Transfer," *Journal of Dynamics, Guidance and Control*, Vol. 21, No.6, 1998, pp.1015-1017.
- [82] Kluever, C. A., "Low-Thrust Transfer Guidance Using an Inverse Dynamics Approach," *Journal of Dynamics, Guidance and Control*, Vol. 22, No.4, pp.609-611.
- [83] Lu, P., "Inverse Dynamics Approach to Trajectory Optimization for an Aerospace Plane," *Journal of Dynamics, Guidance and Control*, Vol. 16, No.4, 1993, pp.726-732.
- [84] Kluever, C. A., "Optimal Feedback Guidance for Low-Thrust Orbit Insertion," *Optimal Control Applications & Methods*. Vol. 16 No. 3, Jul-Sep 1995, pp. 155-173.
- [85] Kluever, C. A. and Tanck, G. S., "A Feedback Guidance Scheme for Orbital Rendezvous," *Advances in the Astronautical Sciences*, Vol. 47, No.3 and 4, 1999, pp.229-237.

- [86] Kluever, C. A., "Feedback Control for Spacecraft Rendezvous and Docking," *Journal of Guidance Control & Dynamics*, Vol. 22, No. 4, 1999, pp. 609-611.
- [87] Vadali, S.R., Aroonwilairut, K., and Braden, E., "A Hybrid Trajectory Optimization Technique for the Mars Sample Return Mission," American Astronautical Society, Paper AAS 01-466, Aug. 2001.
- [88] Battin, R.H., *Astronautical Guidance*, 1st ed., McGraw-Hill, New York, 1964, pp. 344-354.
- [89] Kluever, C.A. and Gao, Y., "Earth-Capture Trajectories Using Solar Electric Propulsion," *Proceedings of 12th AAS/AIAA Space Flight Mechanics Meeting*, Jan. 2002.
- [90] Desai, S.D., Bhaskaran, S., Bollman, W.E., Halsell, C.A., Riedel, J.E., and Synnott, S.P., "The DS-1 Autonomous Navigation System: Autonomous Control of Low Thrust Propulsion Systems," AIAA Paper 97-38819, Aug. 1997.
- [91] Spitzer, A., "Near Optimal Transfer Orbit Trajectory Using Electric Propulsion," American Astronautical Society, Paper AAS 95-215, Feb. 1995.
- [92] Perkins, F.M., "Flight Mechanics of Low Thrust Spacecraft," *Journal of the Aerospace Sciences*, Vol. 26, No. 5, 1959, pp. 291-297.

VITA

Yang Gao was born on November 30, 1974, in Xi'an Shaanxi, China. After attending public schools in China and United States, he received the following degrees: B.S. in Automatic Control department, Beijing University of Aeronautics and Astronautics at Beijing, China (1997); M.S. in Satellite Remote Sensing Ground Station, Chinese Academy of Sciences at Beijing, China (2000); Ph.D. in Mechanical and Aerospace Engineering department, University of Missouri-Columbia.